Massachusetts Institute of Technology
Lincoln Laboratory

EO-1 Technology Validation Report

Advanced Land Imager

August 1, 2001

C.J. Digenis
D.R. Hearn
D.E. Lencioni
J.A. Mendenhall

MIT Lincoln Laboratory
244 Wood St.
Lexington, MA
02420-9185

NASA/GSFC

Table of Contents

1 INTRODUCTION

The primary instrument on the first Earth Observing satellite (EO-1) under the New Millennium Program (NMP) is the Advanced Land Imager (ALI) multispectral instrument [17] (Figure 1-1). Overall direction of the EO-1 mission and acquisition of the spacecraft is being carried out by the Goddard Space Flight Center (GSFC) of NASA. MIT Lincoln Laboratory developed the Advanced Land Imager with NMP instrument team members Raytheon Systems Santa Barbara Remote Sensing (focal plane) and SSG Inc. (optical system). This instrument includes an optical system, a focal plane system, a calibration system, and the structural, thermal, and electrical components required to form an integrated unit. Lincoln Laboratory was responsible for the design, fabrication, test and development of the instrument, the software and databases for calibration, and is responsible for on-orbit performance assessment.

This document provides a detailed overview of the instrument, preflight calibration techniques and results, and pre-flight environmental testing. In-flight calibration techniques and results are also reviewed and lessons learned related to the transfer of ALI technology to the Landsat Data Continuity Mission (LDCM) are provided.
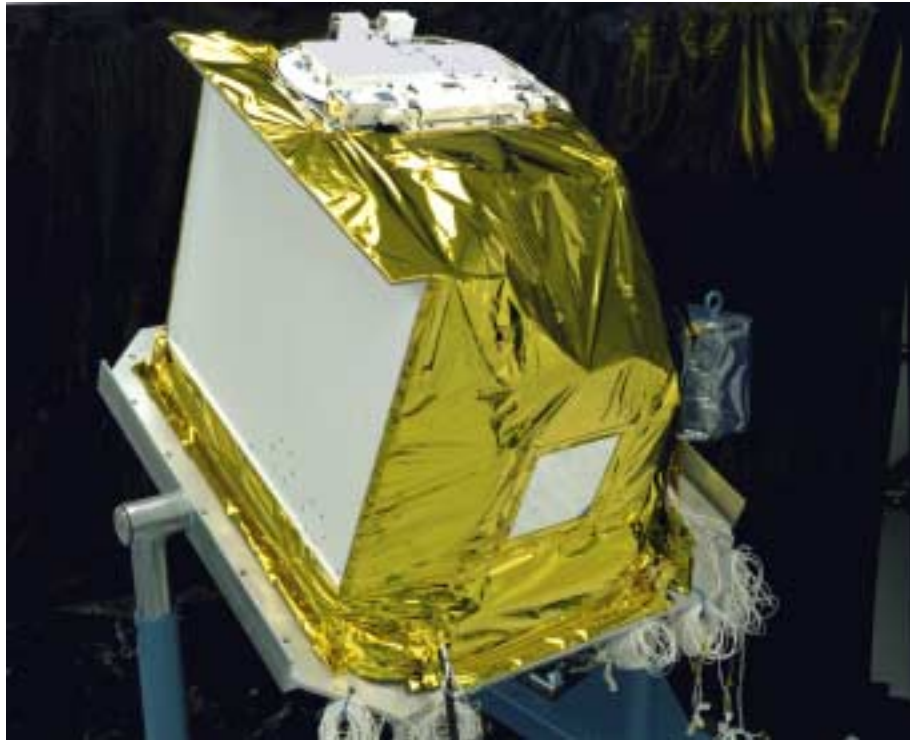

Figure 1-1. Photograph of the Earth Observing-1 Advanced Land Imager.

2   ADVANCED LAND IMAGER INSTRUMENT DESCRIPTION

The overall envelope and configuration of the Advanced Land Imager is depicted in Figure 2-1. The instrument is approximately 0.9m (X) x 0.9m (Y) x 0.7m (Z) and sits on an aluminum pallet that attaches to the spacecraft. The instrument has a velocity vector in the +X direction with the base pallet mounted on the nadir deck of the spacecraft so that earth is in the +Z direction.   The focal plane and focal plane electronics each have radiators to help regulate the thermal environment of these components. The telescope is under multi-layer insulation (MLI) and is surrounded by a thin (~1mm) aluminum housing that supports an aperture cover.   The ALI Control Electronics and the Focal Plane Electronics (FPE) packages are supported on the pallet outside the telescope housing.
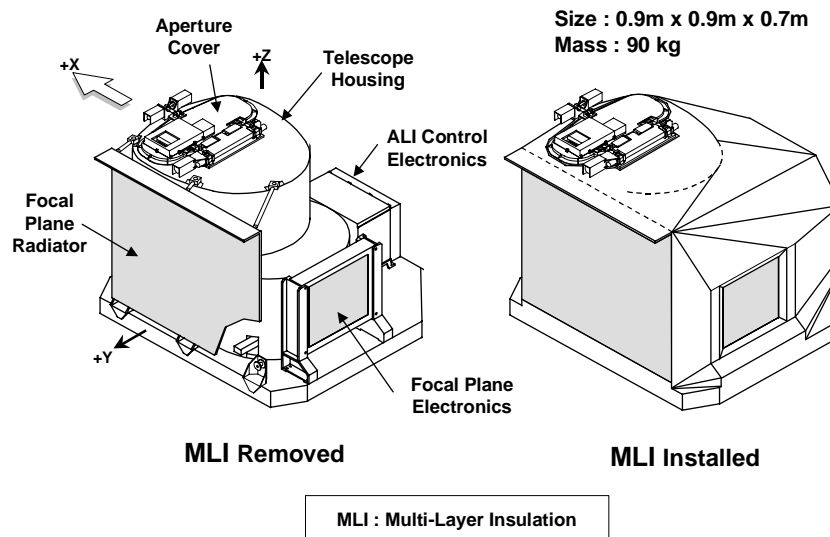

Figure –2-1. ALI instrument configuration showing the main thermal, mechanical, and electronic components.

2.1   Telescope

A conceptual sketch of the interior of the ALI illustrating the major design features is shown in Figure 2-2 The telescope is a f/7.5 reflective triplet design with a 12.5 cm unobscured entrance pupil and a FOV of 15° cross-track by 1.256° in-track. It employs reflecting optics throughout, to cover the fullest possible spectral range. The design uses four mirrors: the primary is an off-axis asphere, the secondary is an ellipsoid, the tertiary is a concave sphere, and the fourth is a flat folding mirror. The optical design features a flat focal plane and telecentric performance, which greatly simplifies the placement of the filter and detector array assemblies. The focal plane consists of five modules, only one of which is populated with detectors (for cost reasons). When the focal plane is fully

populated, the detector arrays will cover an entire 185 km swath on the ground, equivalent to Landsat, in a 'push-broom' mode.

SiC Optics
Low mass
Thermally stable

Main Focal Plane Assembly

Innovative in-flight calibration
Solar calibration
Lunar calibration
Internal lamps

15°

Wide FOV 1.256° x 15°
All reflective telescope
Push broom data collection
No scan mirror

1.256°

Multispectral/ Panchromatic Sensor Assembly
Ten VNIR/SWIR bands on common readout
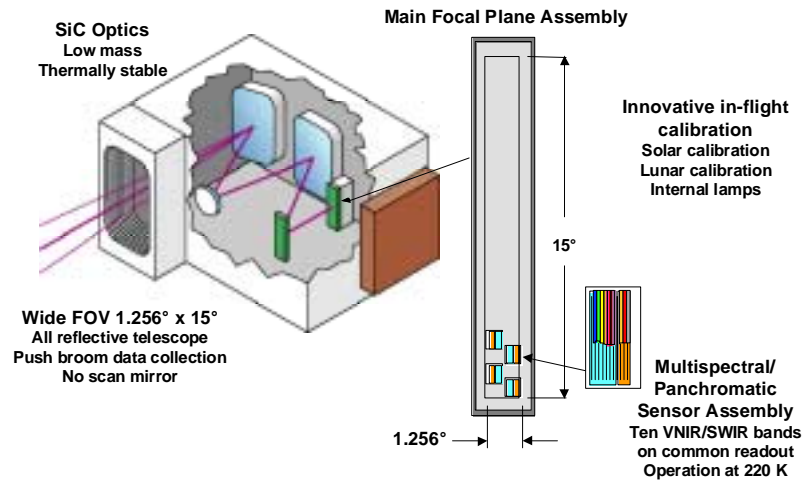Operation at 220 K

Figure 2-2. A conceptual sketch of the ALI telescope and Focal Plane Assembly.

The telescope design incorporates silicon carbide mirrors and an Invar truss structure with appropriate mounting and attachment fittings. Silicon carbide has many favorable properties for space optical systems. It possesses a high stiffness to weight ratio and a low coefficient of thermal expansion. Although it has been used for space optical elements previously, it has not been used for such large mirrors. A photograph of the silicon carbide mirrors that are held in place by the Invar metering truss is shown in Figure 2-3.

Telescope features

- 12.5 cm entrance pupil
- 15° x 1.26° field-of-view
- Telecentric, f/7.5 design
- Unobscured, reflective optics
- Silicon carbide mirrors
- Wavefront error = $0.11\,\lambda$ RMS @ 633 nm

Figure 2-3. Photograph of the silicon carbide mirrors supported by the Invar metering truss.

2.2 Focal Plane

Although the optical system supports a 15° wide FOV, only 3° was populated with detector arrays, as illustrated in Figures 2-4, 2-5, 2-6. The multispectral panchromatic (MS/Pan) array has 10 spectral bands in the visible, near infrared (VNIR), and short wave infrared (SWIR) (Figures 2-7 and 2-8). The pan detectors subtend 10 m square pixels on the ground and are sampled every 10 m as the earth image moves across the array. The MS detectors subtend 30 m and are sampled every 30 m. The wavelength coverage and ground sampling distance (GSD) are summarized in Table 2-1. Six of the nine multispectral bands are the same with those of the Enhanced Thematic Mapper (ETM+) on Landsat 7 [1] for direct comparison. The additional bands, indicated with primes, were chosen for other science objectives.
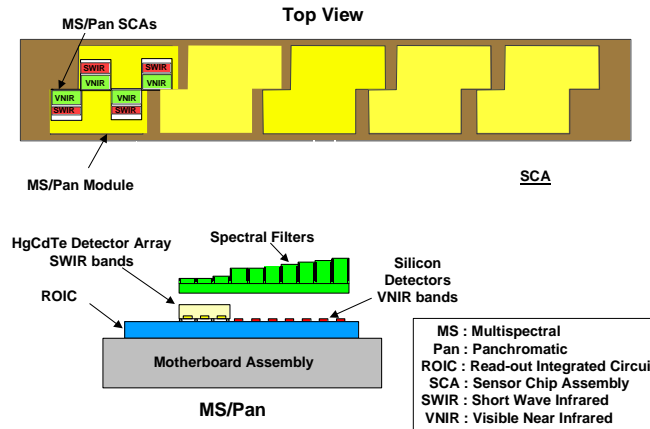

Figure 2-4. ALI Focal Plane Assembly.

Four sensor chip assemblies (SCAs) populate the 3° cross-track segment of the focal plane to form the focal plane array or FPA. Each MS band on each SCA contains 320 detectors in the cross-track direction, while each pan band contains 960 detectors. The total cross-track coverage from the single MS/Pan module is 37 km.

The MS/Pan arrays use silicon-diode VNIR detectors fabricated on the silicon substrate of the Readout Integrated Circuit (ROIC). The SWIR detectors are mercury-cadmium-telluride (HgCdTe) photo-diodes that are indium bump-bonded onto the ROIC that services the VNIR detectors. These SWIR detectors promise high performance over the 0.9 to 2.5 μm wavelength region at temperatures that can be reached by passive or thermoelectric cooling. The nominal focal plane temperature is 220K and is maintained by the use of a radiator and heater controls.

Application of detectors of different materials to a single readout integrated circuit (ROIC) enables a large number of arrays covering a broad spectral range to be placed

closely together. This technology is extremely effective when combined with the wide cross-track FOV optical design being used on the ALI.

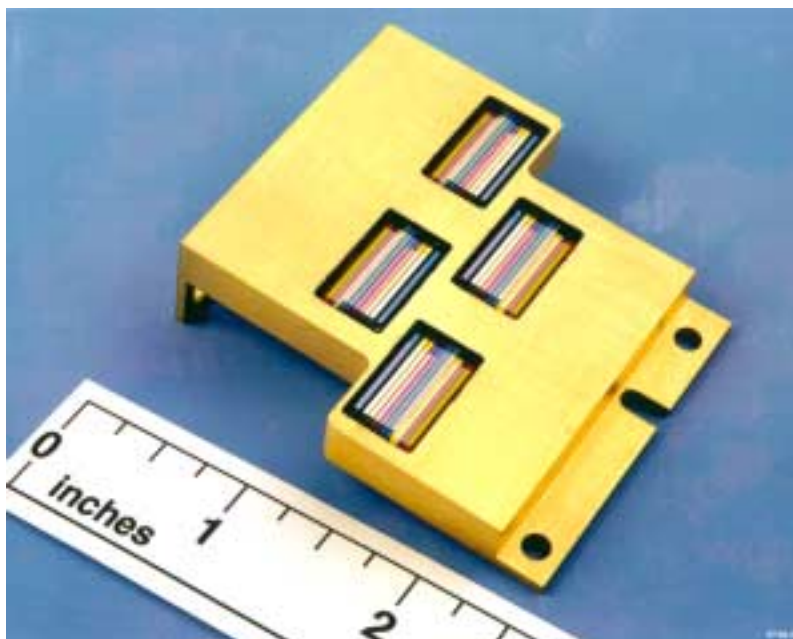*Figure 2-5. Photograph of ALI Focal Plane Assembly.*

Figure 2-6. Photograph of populated Sensor Chip Assembly.

TABLE 2-1

ALI Spectral Coverage and Ground Sample Distances

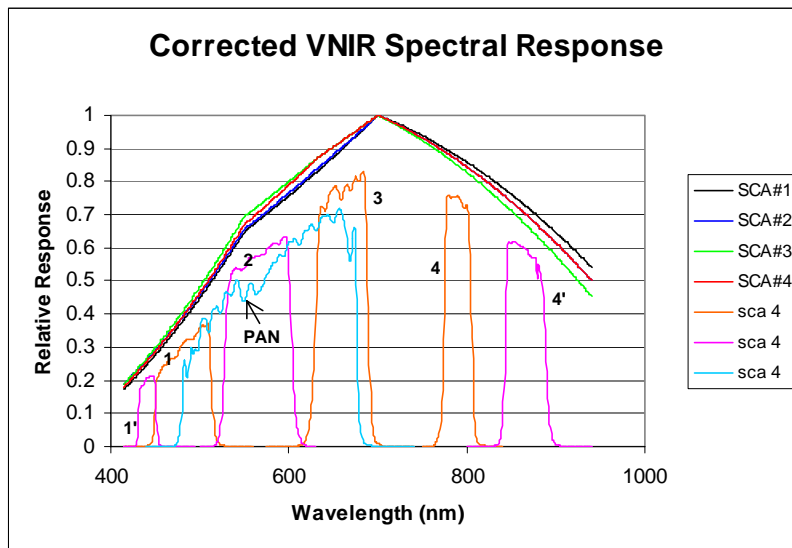| Band	Wavelength (µm)	GSD (m)
Pan	0.480-0.690	10
MS-1'	0.433-0.453	30
MS-1	0.450-0.515	30
MS-2	0.525-0.605	30
MS-3	0.630-0.690	30
MS-4	0.775-0.805	30
MS-4'	0.845-0.890	30
MS-5'	1.200-1.300	30
MS-5	1.550-1.750	30
MS-7	2.080-2.350	30

Figure 2-7. ALI spectral response functions for the visible and near infrared bands obtained from component level measurements. The smoothly varying curves at the top represent the responsivities of the silicon detectors for each SCA. The final responses for each band, considering mirror reflectivities, filter transmissions, and detector responsivities are shown in the lower curves.
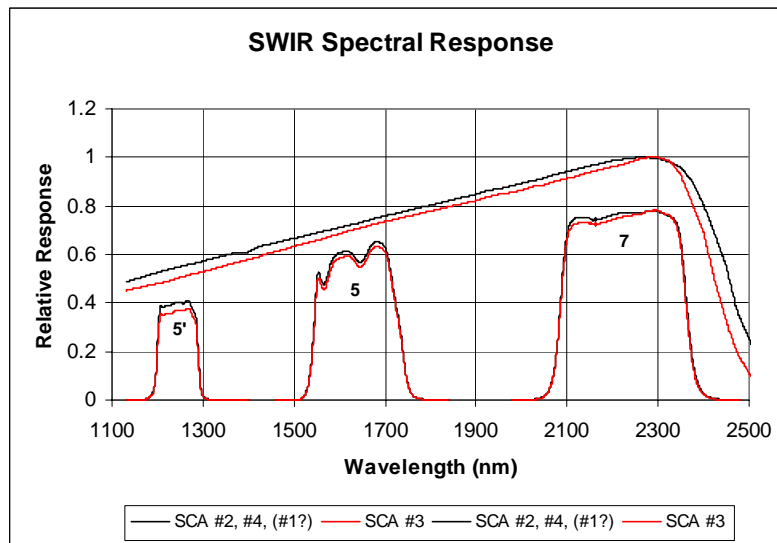
Figure 2-8. ALI spectral response functions for the short wave infrared bands obtained from component level measurements. The smoothly varying curves at the top represent the responsivities of the HgCdTe detectors for each SCA. The final responses for each band, considering mirror reflectivities, filter transmissions, and detector responsivities are shown in the lower curves.

The focal plane electronics (FPE) provides the necessary bias and clock voltages to operate and control the FPA. Both the array frame rate and the detector integration times can be set by commands to the FPE. The nominal frame rate is 226 frames/sec. The nominal integration time for the MS detectors is 4.05 msec while 1.35 msec for the Pan. The frame rate can be adjusted in 312.5 nsec increments to synchronize frame rate with ground scan velocity variations due to altitude and velocity variations during orbit.

The FPE samples the output of each detector with a 12-bit converter. The samples are then multiplexed into a 32-bit parallel word (two detector samples plus an 8 bit header), RS-422 output channel that streams the data at a 102.4 Mbit/sec rate to a 44 Gbit capacity, Wideband Advanced Recorder-Processor (WARP) onboard the spacecraft.

2.3 Internal Reference Source

Daily in-flight radiometric checks of the Advanced Land Imager will be conducted by observing the on-board internal reference source (Figures 2-9, 2-10). This source consists of three Welch Allyn 997418-7 (modified) gas-filled lamps mounted on a small, 0.8-inch diameter integrating sphere. Light emerging from the exit slit of the sphere passes through a BK 7 lens and infrared filter, is reflected off the ALI flat mirror, and floods the focal plane. This source should provide better that 2% absolute radiometric calibration for the instrument. Extensive stability and lifetime testing of the internal reference source for spaceflight operation was conducted at Lincoln Laboratory.
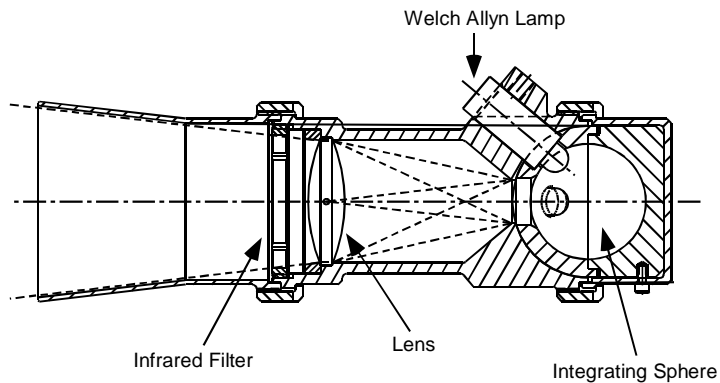
Figure 2-9. EO-1 ALI internal reference source.
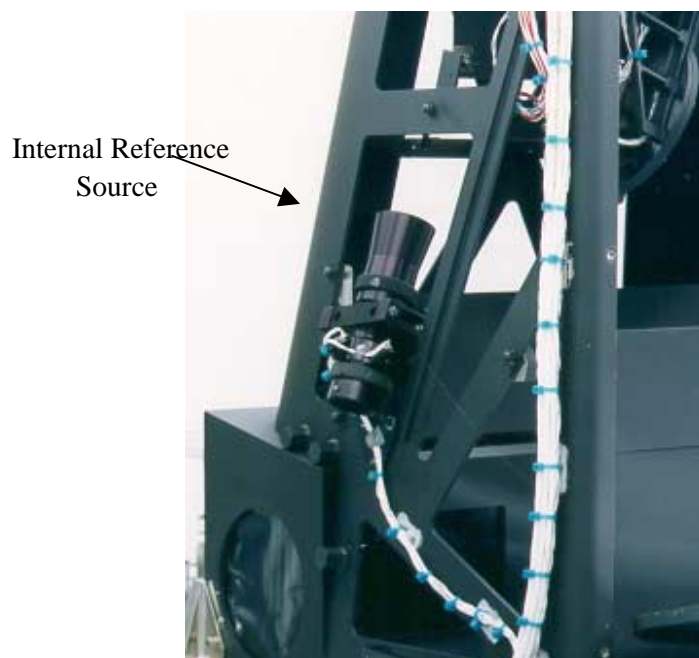
Figure 2-10. Photograph of internal reference source.

Following each observation, after the aperture cover has been closed, the three internal calibration lamps are powered by the ALI Control Electronics. After an eight-second stabilization period the lamps are sequentially powered down in a staircase fashion, with two-second exposures between each step. In this manner, the focal plane will receive a three point radiometric calibration after each observation.

2.4 Mechanisms

Figure 2 -11 illustrates three motor-driven mechanisms employed by the ALI. The aperture cover opens for a data collection event and closes after data collection. The cover is driven by a two-phase stepper motor and four LEDs are mounted near the cover for discrete status monitoring (open, closed, launch latch released, fail safe released). There is also an aperture cover throwback spring that is enabled by firing a High Output Paraffin Actuator (HOPA). The throwback spring would be used in case of motor failure; however, shutting the aperture cover would not be possible after invoking this option.
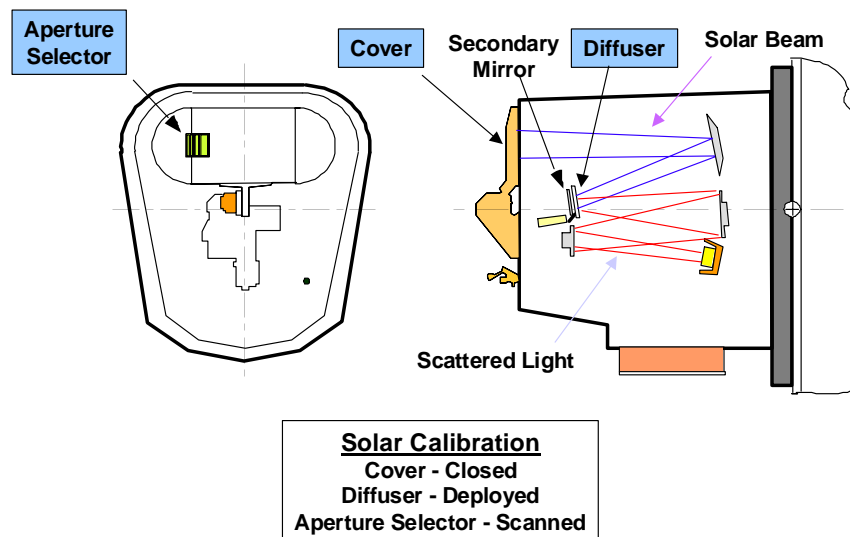

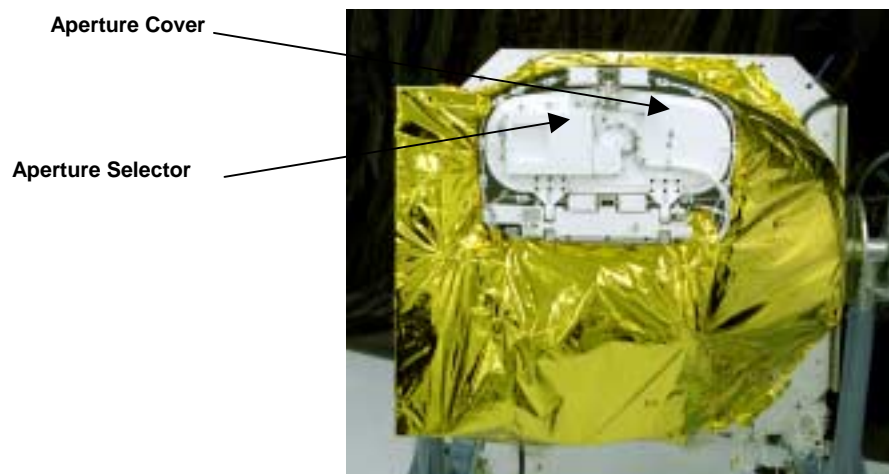*Figure 2-11. Mechanisms used in ALI*

Figure 2-12. Photograph of the ALI Aperture Cover Assembly.

For solar calibration, the aperture cover is closed and a Spectralon diffuser plate is swung over the secondary mirror by a second stepper motor (Figure 2-13). Four LEDs are mounted near the diffuser assembly for discrete status monitoring (deployed, stowed, launch latch released, fail safe released). Fully deployed, the diffuser panel will reflectively scatter any sunlight that would otherwise impinge on the secondary. Once the diffuser is in place, an Aperture Selector Assembly, contained within the Aperture Cover Assembly, is activated. The aperture selector is a two-phase stepper motor that moves an opaque slide over a row of small to increasingly larger slit openings, exposing the diffuser to increasing amounts of sunlight. Fully open, the aperture selector then reverses the slide motion to eventually block all light. Two LEDs are used to monitor the position of the selector (fully extended, fully retracted). Additionally, a resolver is used for continuous position readout. During solar calibration the reflectively scattered sunlight exposes the FPA to an irradiance that is equivalent to earth-reflected sunlight for an earth albedo ranging from 0 to 90%.

Figure 2-13. Photograph of the Spectralon diffuser plate and motor. The diffuser is stowed in the left image and deployed in the right image.

2.5   HIGH OUTPUT PARAFFIN ACTUATORS

The ALI employs six high output paraffin actuators or HOPAs. Four of the HOPAs are used as launch latches and fail safe latches for the aperture cover (Figure 2-14). The remaining two HOPAs are used as a single string launch latch and fail safe latch for the solar diffuser. The launch latches are used to secure the aperture cover and solar diffuser during ascent. The fail safe latches are only to be used if the aperture cover or solar diffuser motors fail and cannot be recovered. Once the fail-safe latches are fired, the associated mechanism can never be used again.
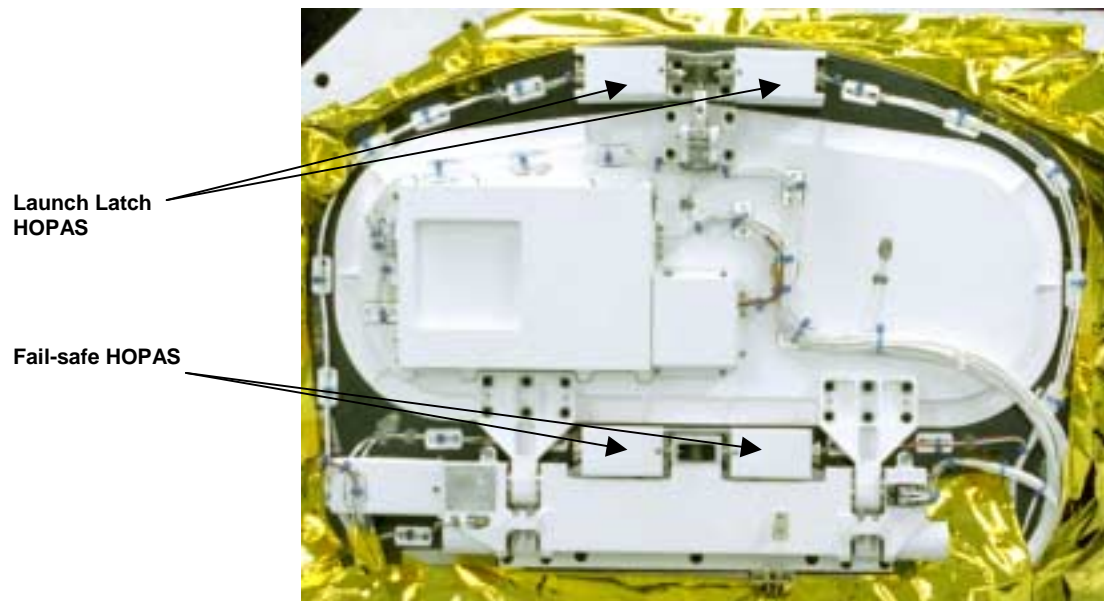
Launch Latch HOPAS

Fail-safe HOPAS

Figure 2-14: Location of aperture cover HOPAs.

3. ADVANCED LAND IMAGER VALIDATION

3.1 Ground Test Verification

The ALI instrument was thoroughly tested and calibrated at Lincoln Laboratory prior to delivery to GSFC for integration with the spacecraft. The following sections describe first, the functional verification tests, then the various calibrations: spatial, spectral, and radiometric. Some of the functional tests, and all of the calibrations took place in a Class 1000 clean room at Lincoln Laboratory. Most of the calibrations were performed with the instrument at nominal operating temperatures in a thermal vacuum chamber.

3.1.1 Functional Verification

Functional verification tests are intended to show that the instrument or subsystem operates as intended, and produces results within nominal design limits. The functional tests described here include assembly and engineering tests; detector tests for dark current, noise, and anomalous detectors; a description of the Leaky Detector phenomenon; contamination; focus adjustment; and end-to-end imaging.

3.1.1.1 Instrument Assembly And Engineering Test Results

The flight telescope was delivered by SSG to MIT Lincoln Laboratory in April 1998. The Focal Plane System was delivered by Raytheon SBRS in June 1998. ALI sub-systems were assembled, integrated, and tested over a 9-month period in preparation for delivery to the spacecraft integrator (Swales Aerospace) in March 1999. The integration and assembly followed a set of NASA processes specially tailored for the program quality control, documentation, and cleanliness of space-qualified components and sub-systems. During this time period testing was undertaken for subsystem alignment, for space flight qualification, and for performance measurement.

3.1.1.1.1 Thermal and Mechanical Testing

A number of successful tests were conducted to establish the qualification of the ALI for launch and space operation. Table 3-1 summarizes these tests.

TABLE 3-1

Thermal and Mechanical Tests During Development

Test	Test Conditions
Sine burst acceleration along each axis • ALI Structural Thermal Model • Flight units box level	• Qualification[*] • Protoflight[†]
Sine sweep • Flight units box level • ALI flight unit	• Protoflight[†] • Protoflight[†]
Random vibration along each axis • Flight units box level • ALI Flight Unit Note: Acceleration spectrum was notched as necessary to insure 3 σ acceleration loads did not exceed Qualification Level loads at any frequency for non-electronics box level testing.	• Protoflight[‡] • Protoflight[‡]
Mechanism Life Testing • Mechanism's Engineering Development Unit	1.5 times design life Aperture Selector and Calibration Diffuser: 240 cycles Aperture Cover: 3900 cycles Survive 50°C to -10°C thermal cycle before and after test
Thermal Cycle Testing • ALI Flight Unit	50°C to –30°C survival hot-to-cold soak cycle Four thermal cycles 40°C to –10°C Checked operation before, during, and after each cycle.

[*]Qualification levels = 1.5 × flight levels (2 oct/minute)   [‡]Protoflight levels = flight level + 3 dB (1 minute/axis)

[†]Protoflight levels = 1.25 × flight levels (4 oct/minute)

To facilitate testing, an ALI Structural Thermal Model (STM) and an Engineering Development Unit (EDU) of the ALICE and mechanisms were developed during the course of fabrication and assembly of the instrument. The STM was subjected to qualification level testing, while flight box and instrument level testing was restricted to protoflight levels.

After being fully assembled, the ALI also underwent thermal vacuum testing to 1) validate the ALI thermal model and 2) demonstrate survivability of the instrument within an environment more severe than expected on orbit. This testing was conducted at Lincoln Laboratory and included thermal soaking and thermal cycling while under vacuum. Figure 3-1 shows the instrument being placed into the thermal vacuum test chamber. Figure 3-2 provides a summary of ALI thermal vacuum testing, compared to on-orbit expectations. Testing at Lincoln Laboratory is included in the ALI I&T region.

Figure 3-1. ALI being placed into thermal-vacuum test chamber.
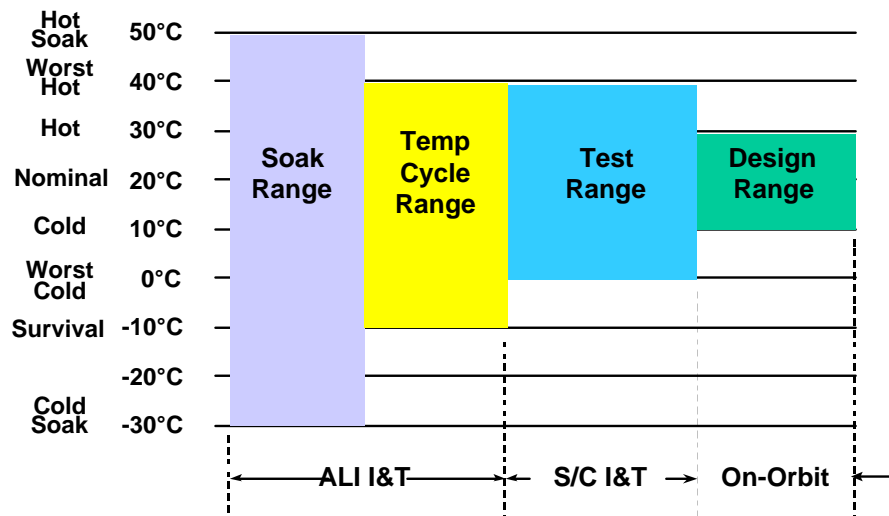

Figure 3-2. ALI thermal vacuum testing temperature ranges.

3.1.1.2 Dark Current, Noise, and Anomalous Detectors

This section provides a review of three key Advanced Land Imager (ALI) instrument [17] performance parameters: dark current, noise, and anomalous detectors. The dark current and noise of the ALI are closely coupled. The dark current defines the background level for each detector, and frame-to-frame fluctuations of this current is a major contributor to the noise of the instrument.[†] Results obtained while operating the focal plane at the nominal integration times (4.05 ms for multispectral bands and 1.35 ms for the panchromatic band) at 220 K will be provided. It should also be noted that all results are referenced to the 12-bit system the ALI employs.

This section also provides a review of anomalous detectors of the instrument. These detectors have been selected based on unusual dark current and noise characteristics, as well as gain and cross-talk peculiarities. The behavior of anomalous detectors should be carefully considered when selecting targets of small spatial extent or scientifically assessing the quality of particular scenes.

Additional results with the focal plane operating at 215 & 225k may be found elsewhere [21].

3.1.1.2.1 Dark Current And Noise Characterization

3.1.1.2.1.1 Dark Current

The ALI dark current is a measure of the background level of each detector. It is a combination of thermally excited electrons within the detector and the gain of the associated electronics. The dark current for each detector of every band has been calculated as the mean of 512 multispectral and 1536 panchromatic frames (2 seconds). The dark current levels calculated from data collected during calibration at MIT Lincoln Laboratory are provided in Figures 3-3 and 3-4. The focal plane was operating at 220 K during this period. Expected detector to detector and Sensor Chip Assembly to Sensor Chip Assembly (SCA to SCA) variations are present. Five of the six ALI inoperable detectors are clearly evident in the dark current data and are listed in Table 3-2. Nine ALI detectors have been identified as having excessive dark current (>1.25 times the mean dark current for that band and SCA) and are listed in Table 3-3. The observed large dark current offsets between odd and even detectors on SCA 4 band 2 and SCA 3 band 3 are the result of two 'leaky' detectors. Detector 1149 on band 2 and detector 864 on band 3 have significant cross-talk with neighboring odd and even detectors respectively. As a result, even under dark conditions, over 300 digital number (DN) units (out of 4096) of induced signal are present on the corrupted detectors. This effect is covered in more detail elsewhere [6]. Finally, bands 5p, 5, and 7 exhibit large increases in dark current centered on detector 1200. These regions of enhanced dark

---

[†] All SWIR detectors have a transient effect associated with the initial data collected following the focal plane turn-on. As a result, the first ten frames from all data sets have been excluded from dark current and noise analysis

current, therwise referred to as 'hot spots', are stable and repeatable, and may be accounted for by using normal dark current subtraction techniques.
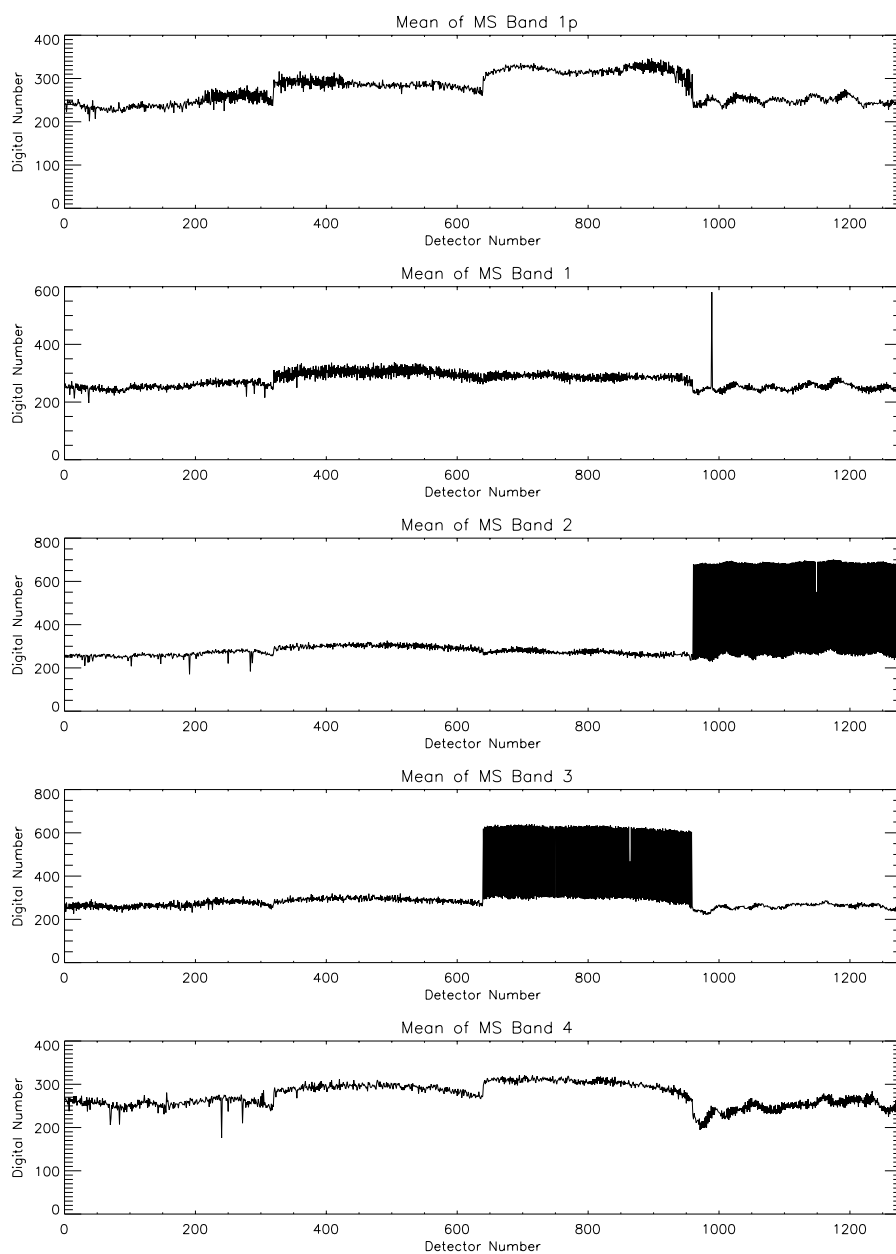

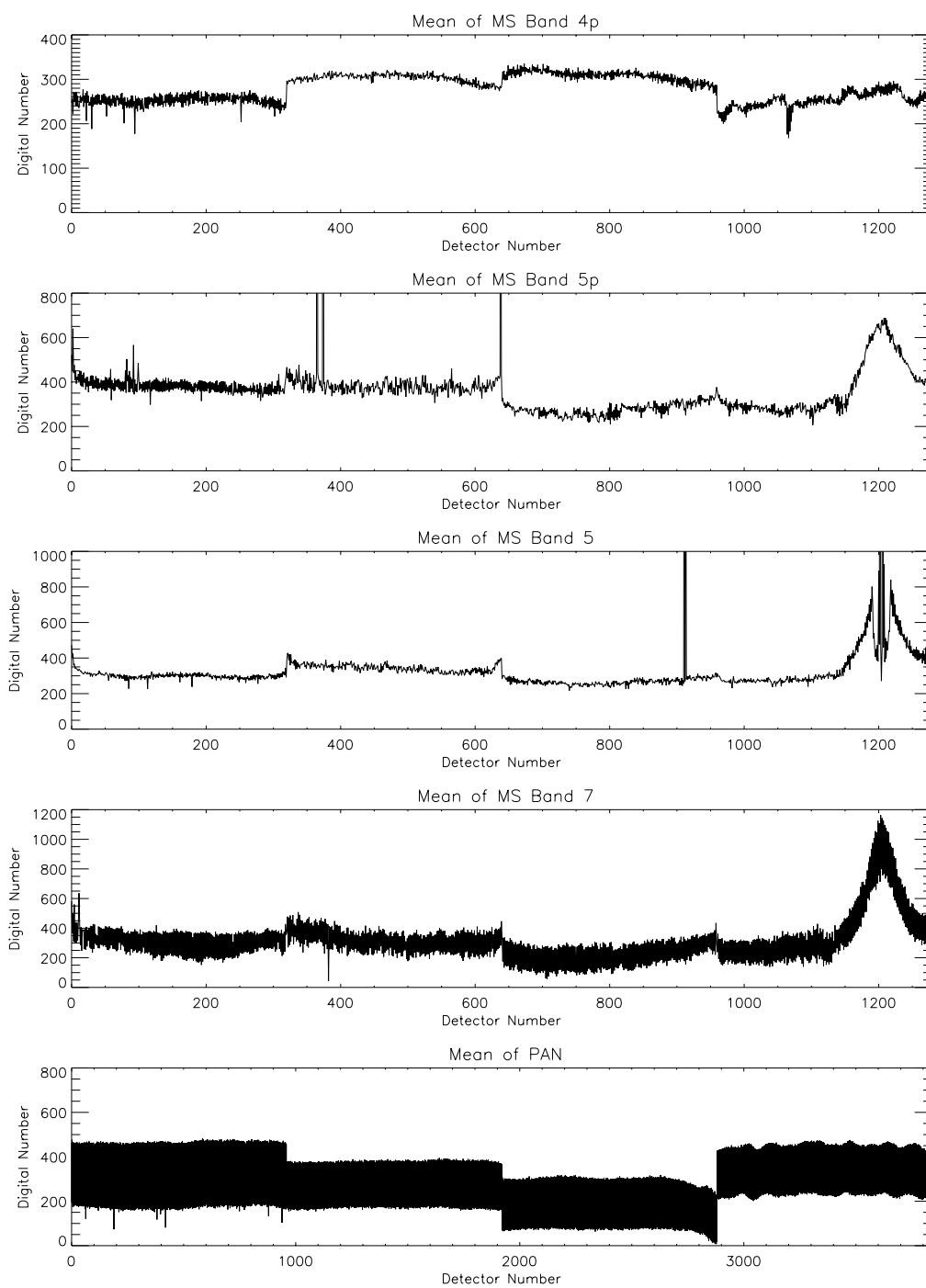*Figure 3-3. Band 1p, 1, 2, 3, 4 dark current values at 220 K.*

Figure 3-4. Band 4p, 5p, 5, 7 and pan band dark current values at 220 K.

Table 3-2:

Inoperable Detectors with Marked Dark Current.

Band	Detector	Comment
5p	374	HOT
5p	638	HOT
5	1202	HOT
5	1204	HOT
5	1206	HOT

Table 3-3:

Detectors with Marked Dark Current.

Band	Detector	Comment
1	989	--
5p	365	Excessive noise
5p	374	Excessive noise, Inoperable detector
5p	638	Excessive noise, Inoperable detector
5	911	Excessive noise
5	913	Excessive noise
5	1202	Excessive noise, Inoperable detector
5	1204	Inoperable detector
5	1206	Excessive noise, Inoperable detector

3.1.1.2.1.2 Noise

The overall noise of the ALI is a combination of random, coherent, and pseudo-random fluctuations (PRF) in a detector's dark current value. For a standard Earth scene, the effects of these noise sources will be varied. The random or white noise component will establish the

overall noise floor on a detector-to-detector basis. Coherent or pick-up noise will manifest itself as recognizable rippling or patterns in an otherwise 'clean' image. Pseudo-random or drifting dark current could affect the quality of an image on a frame-by-frame (high frequency) basis and as a function of time (low frequency) during an observation. Each of these sources will be discussed, and their contributions noted. For this document, only the white noise contributions will be discussed. A discussion of pseudo-random and coherent noise contributions may be found elsewhere[21]

The random or white noise of the ALI has been calculated for each detector as the standard deviation of dark current data collected over 500 multispectral and 1500 panchromatic frames (~2 seconds). Results from these calculations are provided in Figures 3-5 and 3-6 for the focal plane operating at 220 K. The mean of white noise values is ≤ 1.2 DN for all bands and all sensor chip assemblies. Detectors with white noise values greater than three times the mean noise value for each sensor chip assembly or detectors with zero white noise, have been flagged as unusual. Fifteen ALI detectors have more than three times the average white noise values for all three focal plane operating temperatures and are listed in Table 3-4. All but one of these detectors are SWIR detectors and are associated with high dark current and/or high pseudo-random noise.
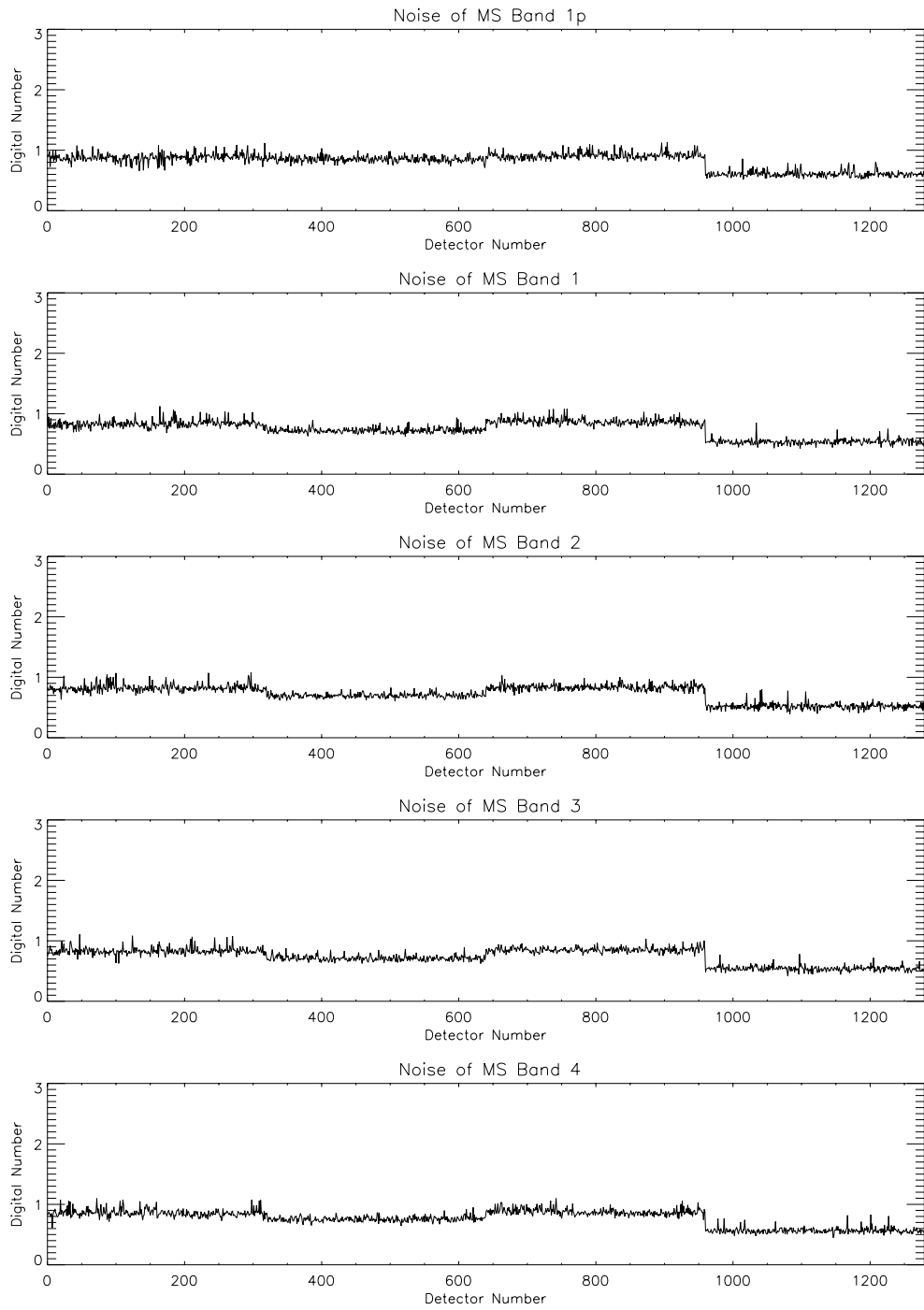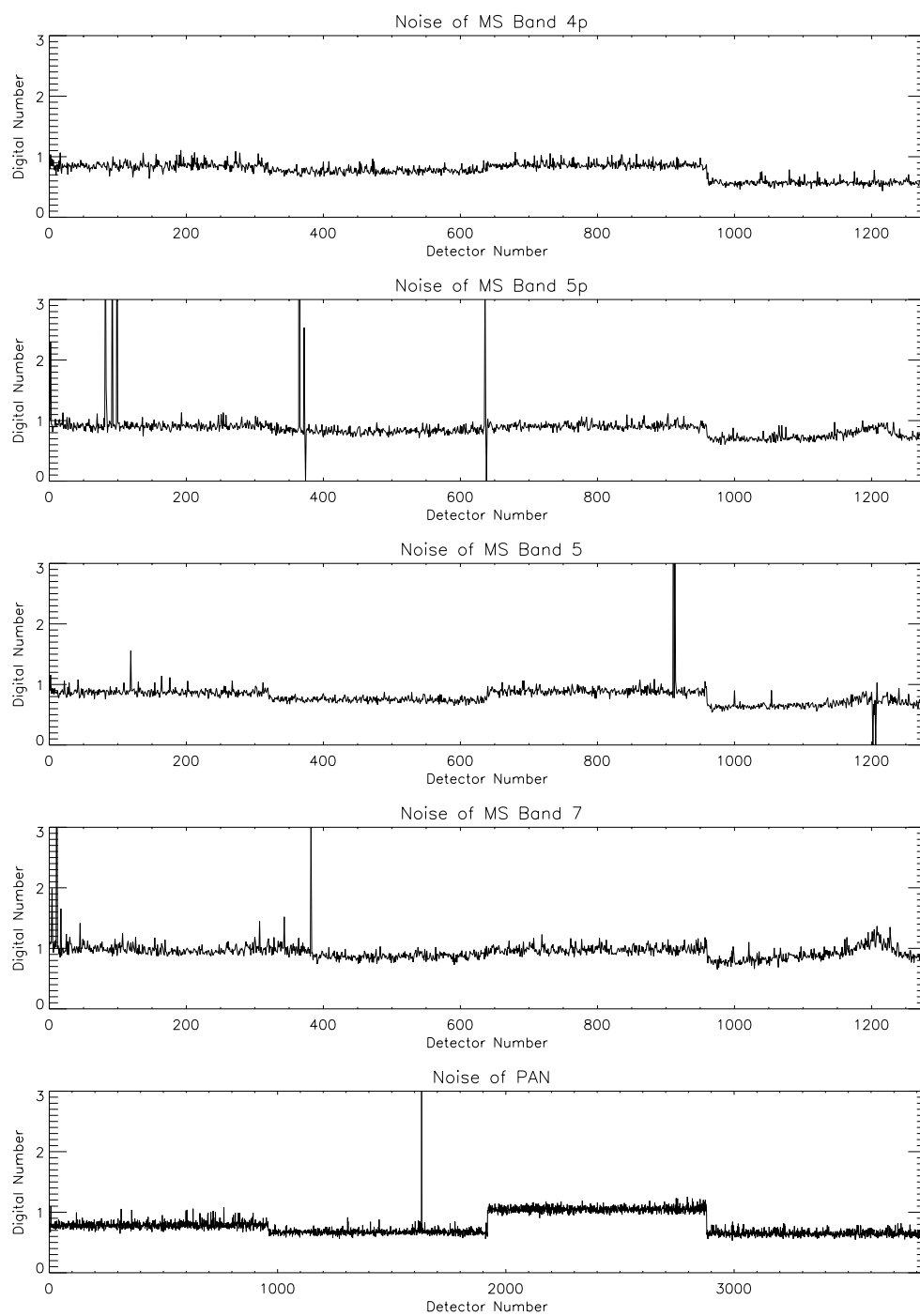
Figure 3-5. Band 1p, 1, 2, 3, 4 noise values at 220 K.

Figure 3-6. Band 4p, 5p, 5, 7 and pan band noise values at 220 K.

Table 3-4

Detectors with Marked Random or White Noise

Band	Detector	Comment
5p	82	--
5p	92	--
5p	99	--
5p	365	Excess dark current
5p	372	--
5p	374	Excess dark current , Inoperable
5p	636	Noise value <3x mean with FPA @ 225 K
5p	638	Excess dark current, Inoperable
5	911	Excess dark current
5	913	Excess dark current
5	1202	Excess dark current , Inoperable
5	1206	Excess dark current , Inoperable
7	11	--
7	382	--
Pan	1631	--

3.1.1.2.1.3 Repeatability

Focal planes with highly repeatable dark current and noise properties are very desirable. This repeatability simplifies the normalization of background signal and the prediction for future scenes' signal to noise ratios. The Advanced Land Imager repeatability has been characterized by measuring the dark current and noise of each detector for ten data sets spanning ten days. For each of these data, the focal plane was maintained at 220 K, and the nominal integration time (4.05 ms for multispectral detectors, 1.35 ms for panchromatic detectors) was used.

Plotted in Figures 3-7 and 3-8 are the overlaid differences between dark current for each band collected over a ten-day period during ground calibration at Lincoln Laboratory. The dark

current was found to be repeatable to within ±2 digital numbers for all VNIR and panchromatic detectors. SWIR detectors are repeatable to within -20/+100 digital numbers. Of particular interest are the sensitivities of the SWIR bands on SCA 1 and the good repeatability of the hot spot centered on detector 1200 of bands 5p, 5 and 7.

Plotted in Figures 3-9 and 3-10 are the overlaid differences between mean white noise levels for data collected over a ten-day period during ground calibration. The mean noise levels were found to be repeatable to within 0.1 digital numbers for all bands. Fourteen ALI detectors demonstrating noise differences $> \pm 0.5$ digital numbers are listed in Table 3-5. All but two of these detectors have been previously flagged as having high dark current or excessive noise values.

The above results indicate the VNIR and panchromatic dark current values and all detector noise levels of the ALI are highly repeatable. However, SWIR dark current levels have shown up to 100 DN variability. It is therefore recommended that dark reference scenes should be used to determine actual dark current and noise levels at the time of each earth scene such that small day-to-day variations will not add to the uncertainties of the measurements.
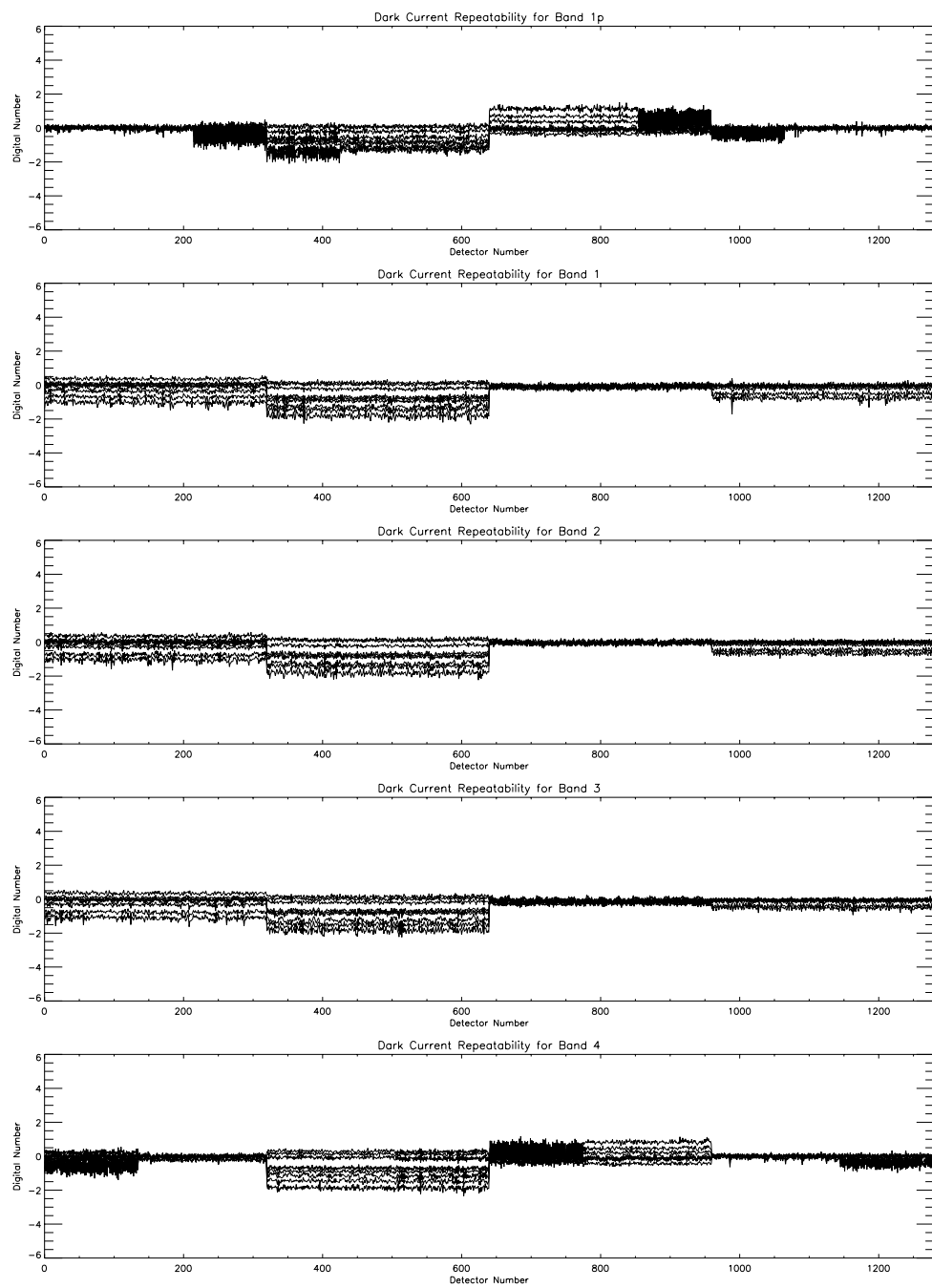
Figure 3-7. Bands 1p, 1, 2, 3, 4 dark current repeatability at 220 K.
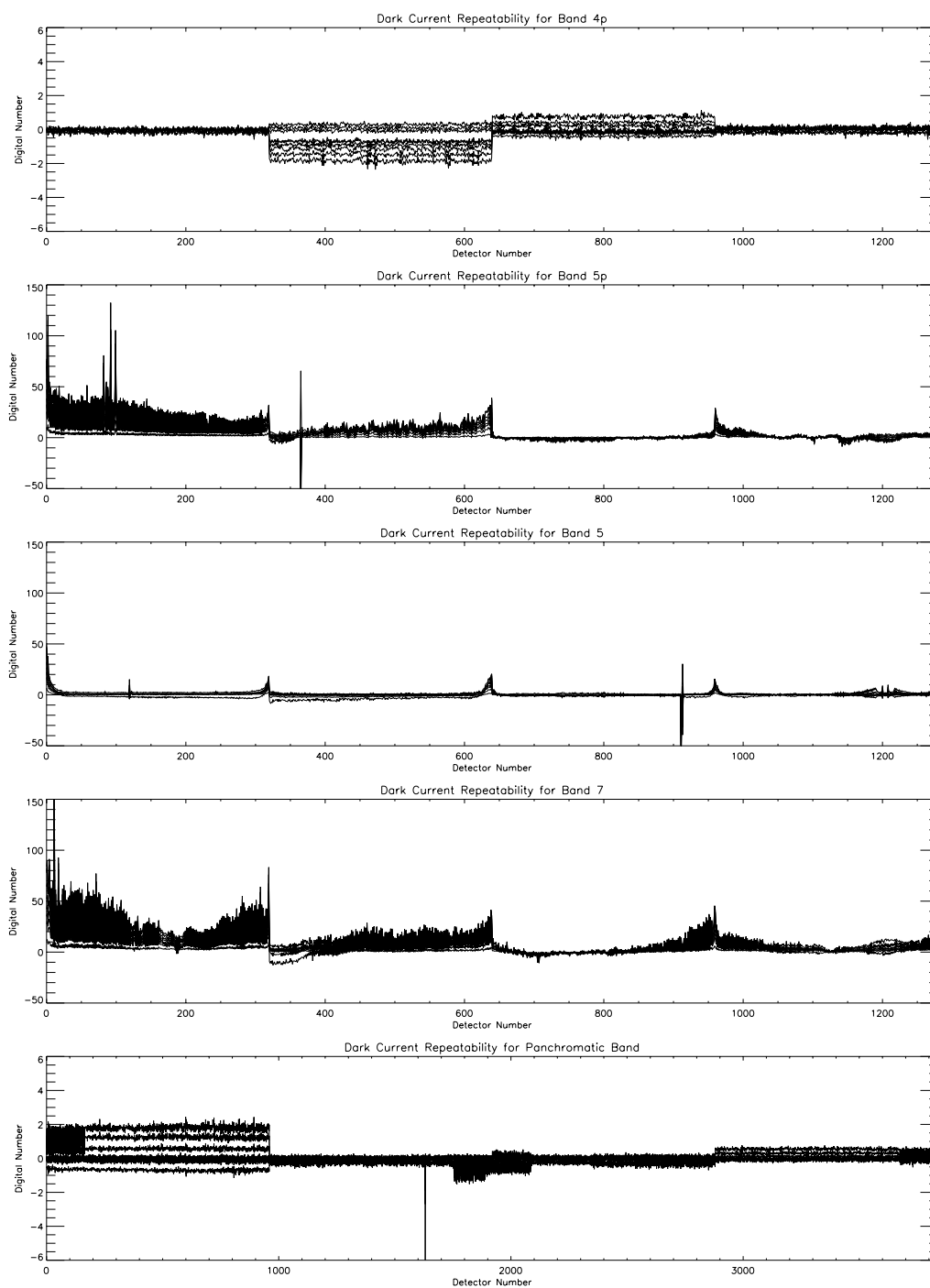
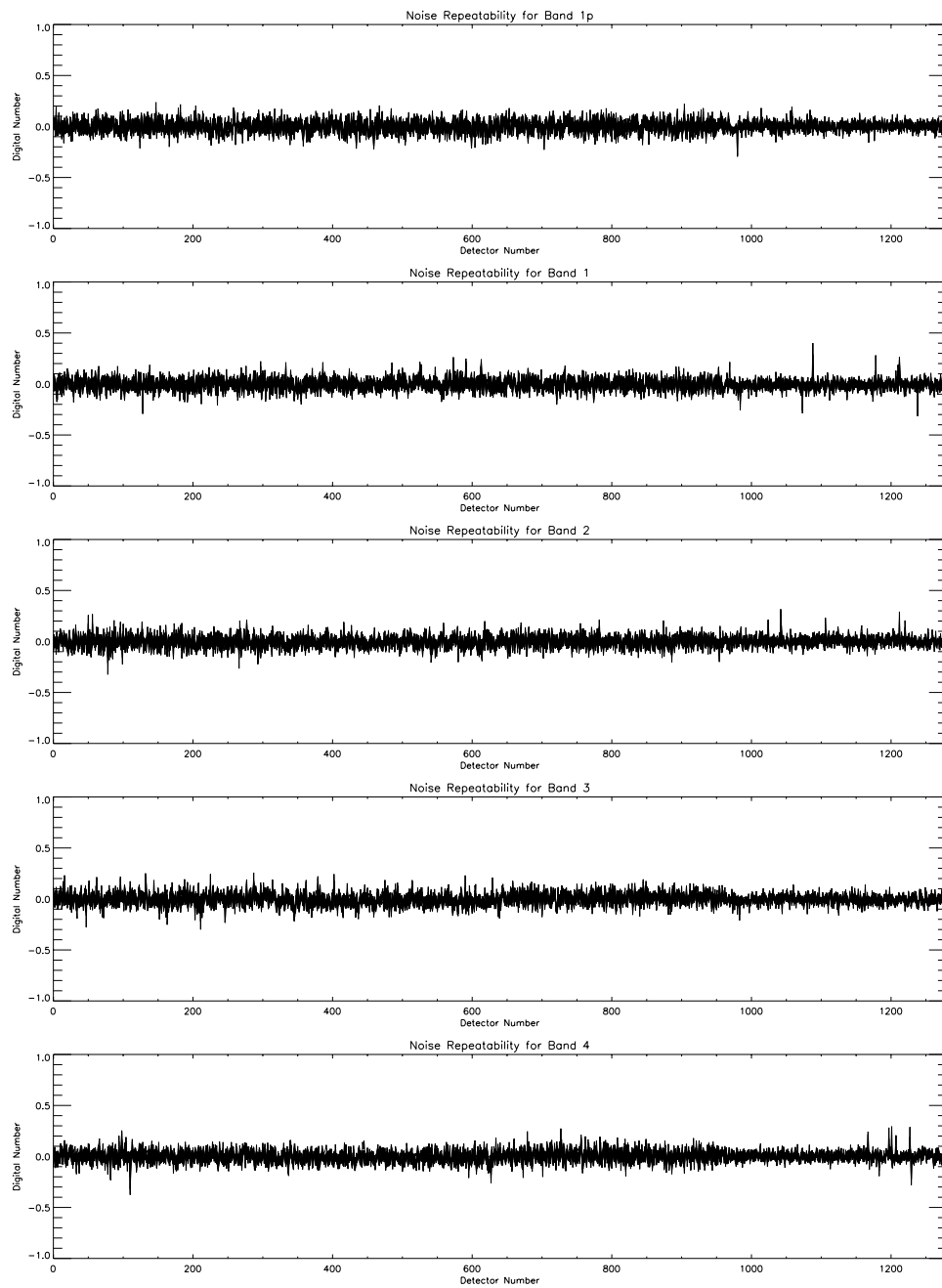*Figure 3-8. Bands 4p, 5p, 5, 7 and pan band dark current repeatability at 220 K.*

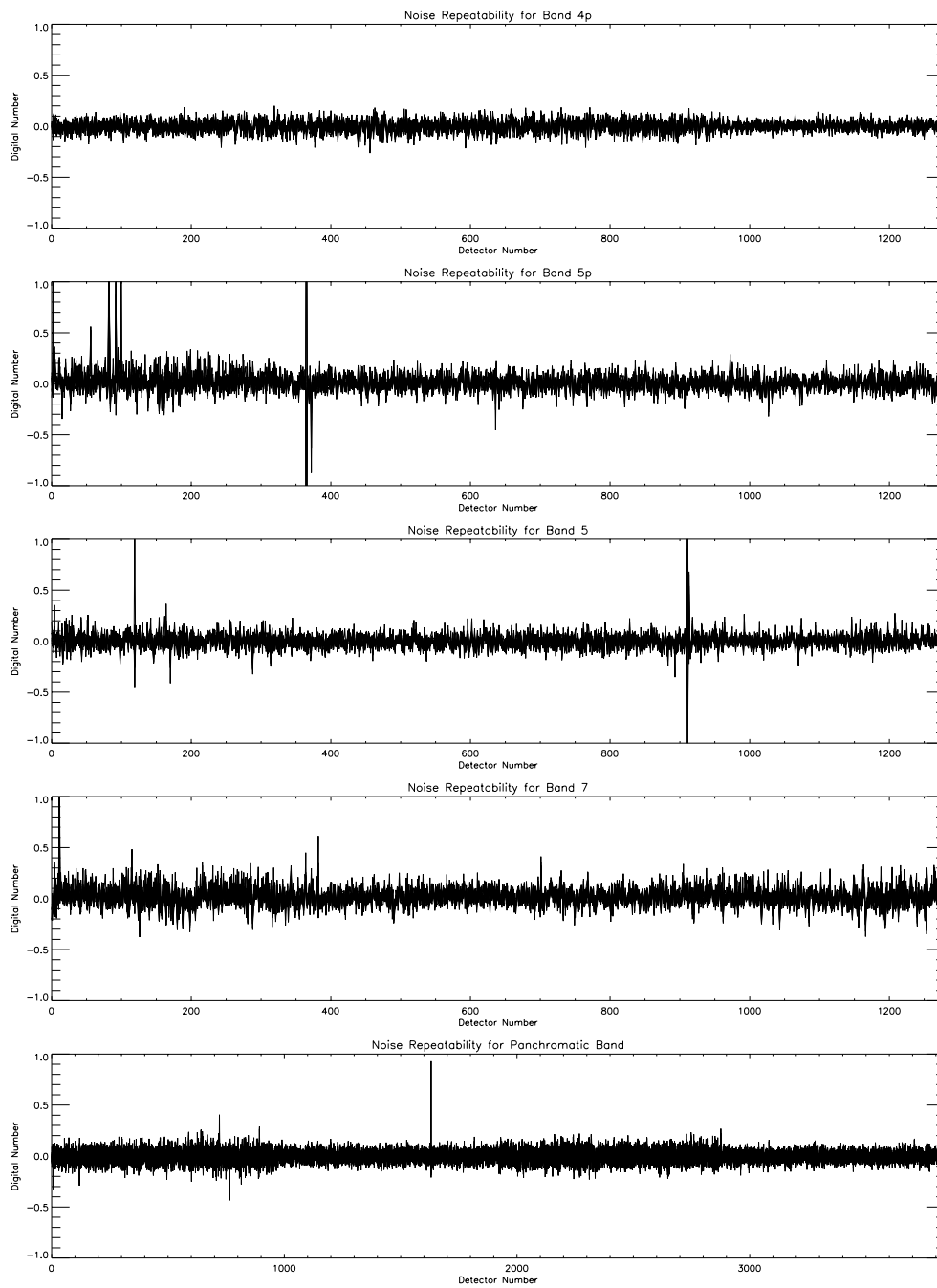*Figure 3-9. Bands 1p, 1, 2, 3, 4 noise repeatability at 220 K.*

Figure 3-10. Bands 4p, 5p, 5, 7 and pan band noise repeatability at 220 K.

Table 3-5

Detectors with Variable Noise Levels at 220 K

Band	Detector	Comment
5p	2	Excess PRF[*]
5p	56	--
5p	82	Excess PRF, Excess white noise
5p	83	Excess PRF
5p	92	Excess PRF, Excess white noise
5p	99	Excess PRF, Excess white noise
5p	365	Excess dark current, Excess PRF, Excess White Noise
5p	372	Excess PRF, Excess white noise
5	119	Excess PRF
5	911	Excess dark current, Excess PRF, Excess White Noise
5	913	Excess dark current, Excess PRF, Excess White Noise
7	11	Excess PRF, Excess white noise
7	382	Excess PRF, Excess white noise
Pan	1631	Excess white noise

[*] PSR = Pseudo-Random Fluctuation.

3.1.1.2.1.4 Dark Current and Noise Characterization Summary

The dark current and noise characteristics for the EO-1 Advanced Land Imager have been characterized. Six inoperable detectors were identified indicating that 99.96% of the ALI focal plane is functional.

All SWIR detectors have a transient effect associated with the initial data collected following the focal plane turn-on. As a result, the first ten frames of the first dark image should be excluded from on-orbit dark current and noise analysis.

Ground calibration data indicate the VNIR and panchromatic dark current values and all detector noise levels of the ALI are highly repeatable. However, SWIR dark current levels have shown significant day-to-day variability. Additionally, the dark current is dependent on focal plane temperature, more particularly for the SWIR bands. It is therefore recommended that concurrent dark reference scenes should be used to determine actual dark current and noise levels at the time of each Earth scene.

The noise levels of the ALI focal plane are excellent (less than 1.2 digital number for the mean of all bands and sensor chip assemblies). Twenty-two detectors were identified as having higher than average noise values. All but one of these were SWIR detectors and associated with high dark current or pseudo-random noise. The overall noise of the ALI is dominated by white noise with little contribution from coherent or pseudo-random fluctuation components.

It is recommended that a single one-minute dark scene be collected once every 14 days to characterize and track the dark current and noise of the Advanced Land Imager. Repeatability may be characterized by assessing the dark scenes obtained with each observation over a two-week period.

3.1.1.2.2 Anomalous Detectors

This section provides a summary listing of all Advanced Land Imager detectors that exhibit anomalous behavior. Anomalous detectors have been selected based on the following criteria:

1. Inoperable detector
2. Excessive dark current
3. Excessive noise
4. Anomalous gain value
5. High cross-talk

Detectors identified for each of the above criteria are listed in subsequent sections. All data used to generate this list were taken with the focal plane at 220 K and the nominal integration times: 1.35 ms for panchromatic detectors and 4.05 ms for multispectral detectors. Some detectors may be listed in several sections (e.g., a high noise detector may be temporally unstable). It must also be noted that although detectors may be marked 'anomalous', most of the characteristics noted in this document are accounted for during instrument calibration. Only the inoperable detectors are

definite problems that need to be addressed by nearest neighbor interpolation or other schemes during image reconstruction. However, in the interest of fully understanding the ALI instrument, it is important to list all interesting focal plane array characteristics.

3.1.1.2.2.1 Inoperable Detector

An inoperable detector is one that has zero dark current or zero gain ('dead') or is saturated at all times ('hot'). Six ALI detectors have been identified as inoperable and are listed in Table 3-6.

Table 3-6

Inoperable Detectors

Band	Detector	Comment
5p	374	HOT
5p	638	HOT
5	982	Gain = 0
5	1202	HOT
5	1204	HOT
5	1206	HOT

3.1.1.2.2.2 Excessive Dark Current

Detectors with dark current values greater than 1.25 times the mean dark current for that band and SCA are flagged as having excessive dark current. Nine ALI detectors have been identified as having excessive dark current and are listed in Table 3-7.

Table 3-7

Detectors with Marked Dark Current

Band	Detector	Comment
1	989	--
5p	365	Excess white noise, Excess PRF[*]
5p	374	Excess white noise, Inoperable
5p	638	Excess white noise, Inoperable
5	911	Excess white noise, Excess PRF
5	913	Excess white noise, Excess PRF
5	1202	Excess white noise, Inoperable
5	1204	Inoperable
5	1206	Excess white noise, Inoperable

[*] PSR = Pseudo-Random Fluctuation.

3.1.1.2.2.3 Excessive Noise

Detectors with noise values (standard deviation of dark current) greater than three times the mean noise value for that band and sensor chip assembly or detectors with more than 1 DN shift in dark current over a forty-second period have been flagged as having excessive noise. Twenty-

two detectors have been noted as having excessive noise by the above criteria and are listed in Table 3-8. Fifteen ALI detectors have higher than average random (white) noise values, and sixteen ALI detectors have been noted as temporally unstable (low frequency pseudo-random fluctuations or high frequency pseudo-random fluctuations).

Table 3-8

Detectors with Marked Noise.

Band	Detector	Comment
5p	2	Excess PRF
5p	82	Excess white noise, Excess PRF
5p	83	Excess PRF
5p	92	Excess white noise, Excess PRF
5p	99	Excess white noise, Excess PRF
5p	365	Excess white noise, High dark current, Excess PRF
5p	372	Excess white noise
5p	374	Excess white noise, Inoperable, Excess dark current
5p	636	Excess white noise, Excess PRF
5p	638	Excess white noise, Inoperable, Excess dark current
5	119	Excess PRF
5	911	Excess white noise, Excess dark current, Excess PRF
5	913	Excess white noise, Excess dark current, Excess PRF
5	1202	Excess white noise, Inoperable, Excess dark current
5	1206	Excess white noise, Inoperable, Excess dark current
7	4	Excess PRF
7	11	Excess white noise, Excess PRF
7	17	Excess PRF
7	126	Excess PRF
7	307	Excess PRF
7	382	Excess white noise, Excess PRF
Pan	1631	Excess white noise

3.1.1.2.2.4 Anomalous Gain Value

An anomalous gain value will either lead to lower dynamic range of the detector (early saturation), if too high, or low signal to noise ratios over the range of scene radiances expected, if too low. Four ALI detectors are found to exhibit anomalous gain values and are listed in Table 3–9.

Table 3-9

Detectors with Anomalous Gain Values.

Band	Detector	Comment
5p	365	Gain too high
5	911	Gain too high
5	913	Gain too high
5	982	Gain = 0

3.1.1.2.2.5 High Cross-Talk or Leaky Detectors

Detectors with high cross-talk are problematic in that they add signal to adjacent detectors. Correcting for this effect may be difficult, especially for scenes with high spatial frequencies covering a large dynamic range. Two ALI detectors have been identified as being leaky, i.e., having high cross-talk characteristics, and are listed in Table 3-10.

Table 3-10

Detectors with Marked Cross Talk

Band	Detector
2	1149
3	864

3.1.1.2.2.6 Anomalous Detectors Summary

Six inoperable detectors were identified, indicating 99.96% of the ALI focal plane is functional. Twenty-one additional detectors have been observed with degraded performance due to such effects as noted dark current values and/or white, low frequency pseudo-random fluctuation, or high frequency pseudo-random fluctuation noise. The remaining 99.82% of the focal plane have excellent dark current stability and noise characteristics. Finally, a master list of anomalous detectors is provided in Table 3-11.

Table 3-11

Master Anomalous Detector List

Band	Detector	Inoperable	Excess Dark Current	Excess Noise White	Excess Noise PRF	High Cross-Talk	Anomalous Gain
1	989		X				
2	1149					X	
3	864					X	
5p	2				X		
5p	82			X	X		
5p	83				X		
5p	92			X	X		
5p	99			X	X		
5p	365		X	X	X		X
5p	372			X			
5p	374	X	X	X			
5p	636			X	X		
5p	638	X	X	X			
5	119				X		
5	911		X	X	X		X
5	913		X	X	X		X
5	982	X					X
5	1202	X	X	X			
5	1204	X	X				
5	1206	X	X	X			
7	4				X		
7	11			X	X		
7	17				X		
7	126				X		
7	307				X		
7	382			X	X		
Pan	1631			X			

3.1.1.3 Leaky Detector

The Earth Observing-1 Advanced Land Imager focal plane contains two *leaky* detectors (1149 of Band 2 and 864 of band 3). When illuminated, these detectors leak or induce signal onto detectors of the same band and row. By row, we mean the odd or even detector row in which the *leaker* is contained (odd row for band 2 and even row for band 3). Detectors of the opposing row are not affected. Additionally, when the leaky detector is not illuminated, residual cross-talk remains but is effectively removed by dark-current subtraction. Detectors that are affected by leakage will be referred hereafter as *corrupted* detectors. Detectors that are not affected by leakage will be referred hereafter as *standard* detectors.

The optical or electrical cross-talk of leaky detectors results in the corruption of portions of images when the leaky detector is illuminated. Figures 3-11 and 3-12 depict images of Lincoln Laboratory in bands 2 and 3 respectively, before the effects of the leaky detectors are accounted for. The approximate location of the leaky detector column is indicated by an arrow. Furthermore, abutting sensor chip assemblies are included in these images to demonstrate the quality of the data in non-leaky regions.

Boundary between SCA 3
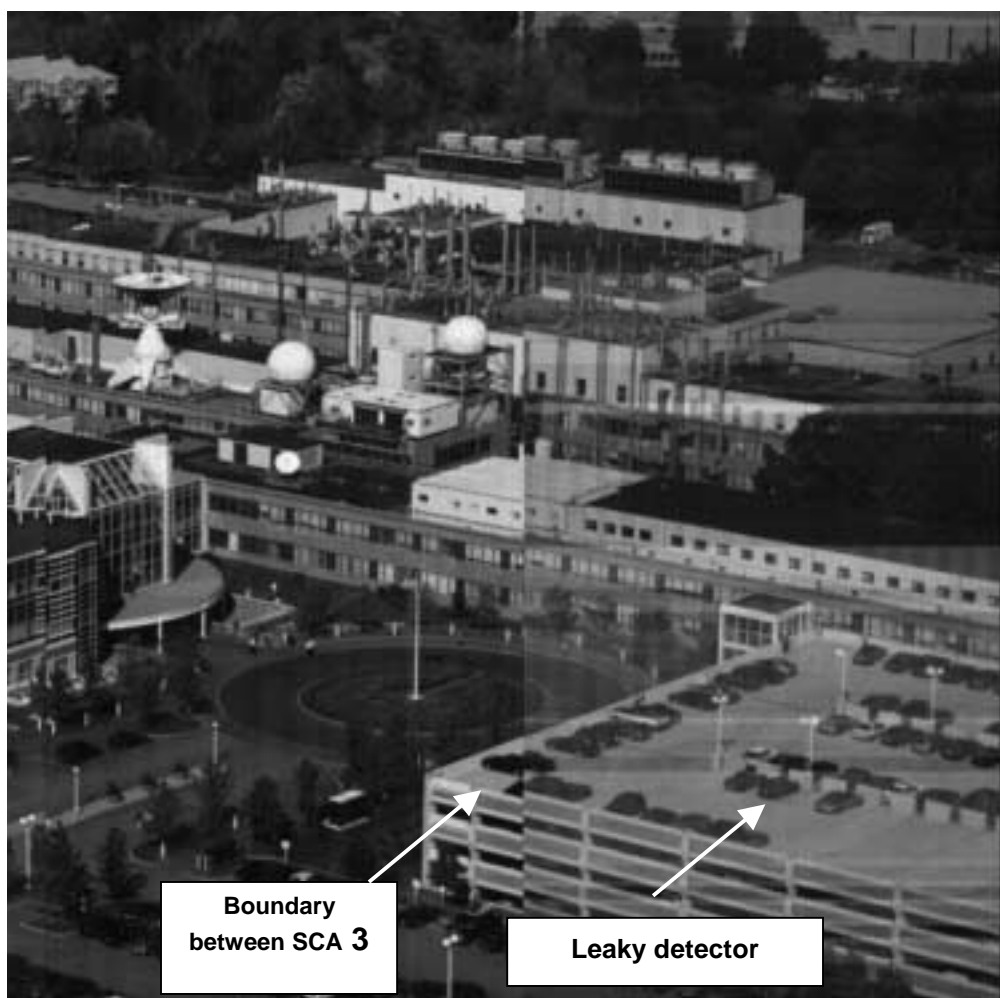
Leaky detector

Figure 3-11. Band 2 image of Lincoln Laboratory before the effects of the leaky detector (1149) are corrected. The left portion of the image is from sensor chip assembly 3, which does not contain a leaky detector for this band.
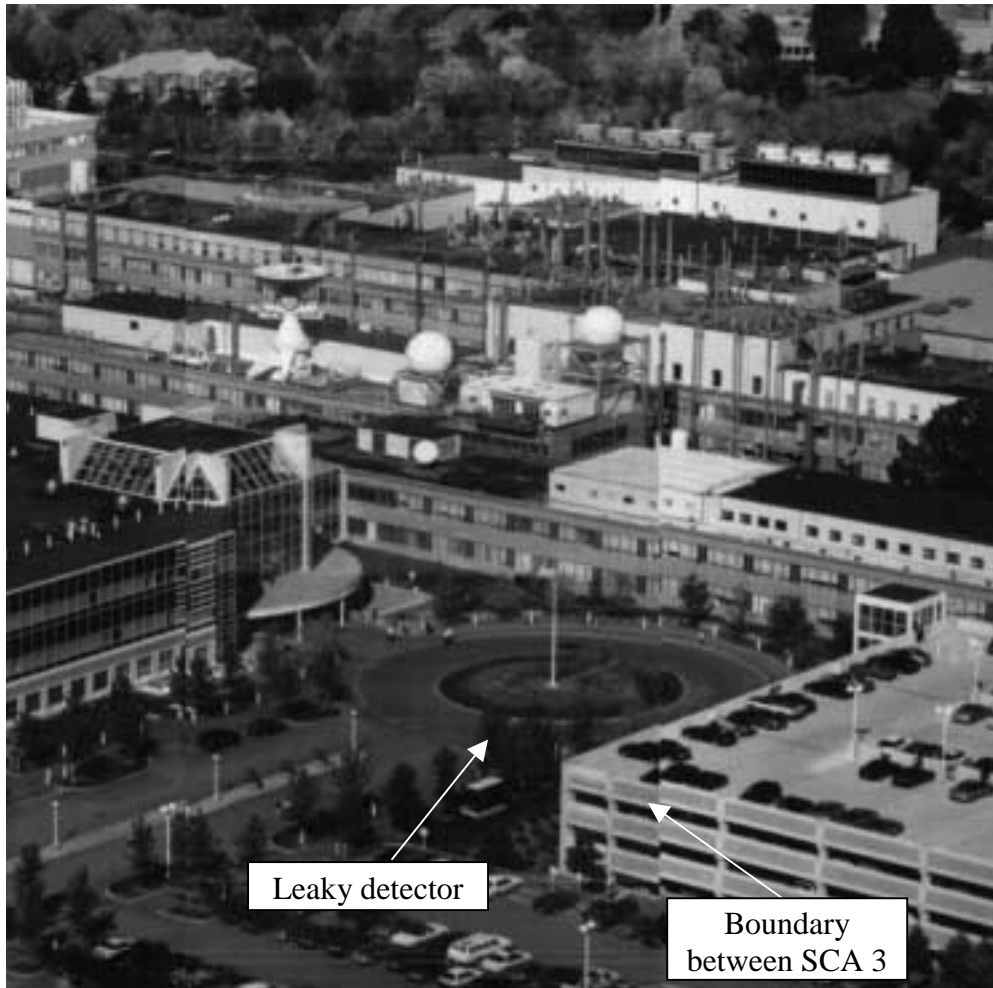
Figure 3-12. Band 3 image of Lincoln Laboratory before the effects of the leaky detector (864) are corrected. The right portion of the image is from sensor chip assembly 4, which does not contain a leaky detector for this band.

3.1.1.3.1 Radiometric Correction Methodology

The radiometric response of corrupted detectors is highly dependent on leaky detector illumination. As a result, a correction procedure must be followed to radiometrically account for the effects of leakage on affected regions. Initially, an algorithm was developed to correct images for leaky detector artifacts by associating the amount of leakage with the dark subtracted value of the leaky detector on a frame-by-frame basis. This algorithm may be represented analytically as

$$L_N = ADN_N + BDN_L \qquad \text{Equation 1}$$

Where L_N is the apparent radiance of corrupted detector N, DN_N is the true detector value for detector N, A is the radiometric gain coefficient for detector N, DN_L is the detector value for the

leaky detector, and B is a constant which describes the fraction of the leaky detector corrupting detector N. This algorithm correctly accounted for leaky detector effects for most portions of images. However, it was quickly realized that all regions where the algorithm failed were associated with sharp edges crossing the leaky detector during the push-broom imaging of a scene. For regions with uniform illumination, the leaky detector and defect are fully illuminated and equation 1 is correct. For regions with no illumination, no leakage exists and equation 1 is again correct. However, if the leaky detector is partially illuminated, the defect within this detector may have no illumination, partial illumination, or full illumination. As a result, the dependence on the leaky detector illumination is no longer valid and the original image correction process breaks down. *This leads us to the conclusion that the amount of leakage for any frame is dependent on the illumination of the leaky detector defect and not the leaky detector itself. Additionally, since we do not know the precise illumination of the defect apriori, we have adopted an empirical correction method to eliminate the effects of leaky detectors on ALI images.*

The empirical correction method we have adopted is implemented on a frame-by-frame basis and uses the differences between each corrupted detector and its nearest neighbor uncorrupted (standard) detector to derive a leakage function. The leakage function is then used to correct corrupted detectors while maintaining the unique detector-to-detector radiometric variations for that frame. This method is then repeated for all frames. The empirical correction method is implemented in the following manner:

- Geometrically correct odd and even detector offsets and SCA to SCA offsets for the entire image
- Radiometrically correct entire image using calibration coefficients
- Begin frame-by-frame loop
  - Generate difference array between corrupted detectors and nearest neighbors
  - Compute leakage function
  - Correct frame
- End frame-by-frame loop
- Save corrected image

3.1.1.3.1.1 Geometrically correct image

The first step in correcting the effects of leaky detector corruption is to geometrically correct the entire image for odd and even detector and SCA to SCA offsets. The ALI focal plane is composed of four sensor chip assemblies, positioned in a staggered formation to provide overlap between arrays (Figure 3-13). Within each array, detectors are aligned in odd and even rows for each band (Figure 3-14). The SCAs are offset by 5 mm and each odd and even row is separated by 80μm.
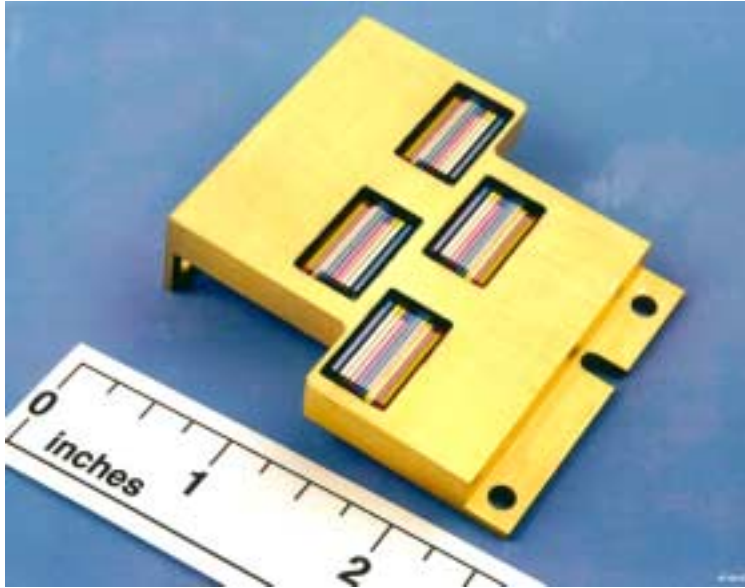
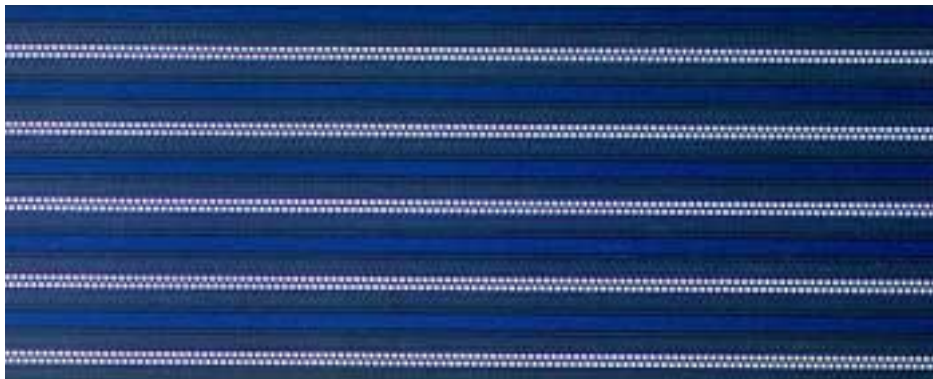*Figure 3-13. Photograph of ALI filter assembly.*

Figure 3-14. Photograph of detector rows for Bands 1-4p. Odd and even rows for each band are evident.

To reconstruct an ALI image, even numbered SCAs and detector columns are shifted down an integral number of frames (correction factor is different for SCAs and columns), depending on the frame rate used during the data collection. Small effects from telescope distortion must also be accounted for when properly reconstructing an image but these effects are second order when correcting for leaky detector corruption. To illustrate the effects of detector offset shifting, subframes of the Band 2 image of Lincoln Laboratory are displayed in Figure 3-15.
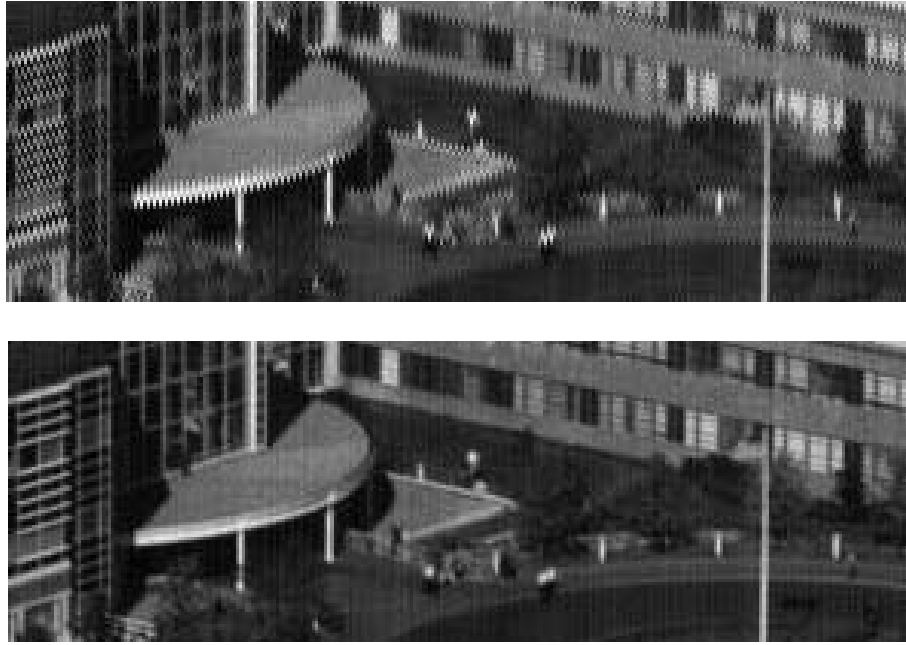
Figure 3-15. Example of geometric correction performed on images before the leaky detector correction is implemented. The top figure is before correction. The bottom figure is after correction.

3.1.1.3.1.2 Radiometrically Correct Image

The second step in accounting for leaky detector effects is to radiometrically calibrate the image. This involves applying radiometric calibration coefficients to transform data from digital numbers to W/cm^2/sr/μ. For ALI data this transform is linear and maybe expressed analytically as

$$L_N = A_N + B_N DN_N \qquad \text{Equation 2}$$

Here, L_N is the radiance observed by detector N, A_N and B_N are the offset and gain calibration coefficients for detector N, and DN_N is the dark subtracted focal plane response for detector N. The calibration coefficients have been derived from laboratory measurements of the radiometric response of the focal plane to diffuse scenes of varying radiance (see *Earth Observing-1 Advanced Land Imager: Radiometric Response Calibration* [19]). Although the response of corrupted detectors is influenced by the leaky detectors, we have found the adoption of incorrect radiometric response coefficients for these detectors are effectively accounted for during leaky detector correction. As an example of this step in the leaky detector correction process, frame 1050 of the Lincoln Laboratory image, before and after radiometric correction, are graphically displayed in Figure 3-16.
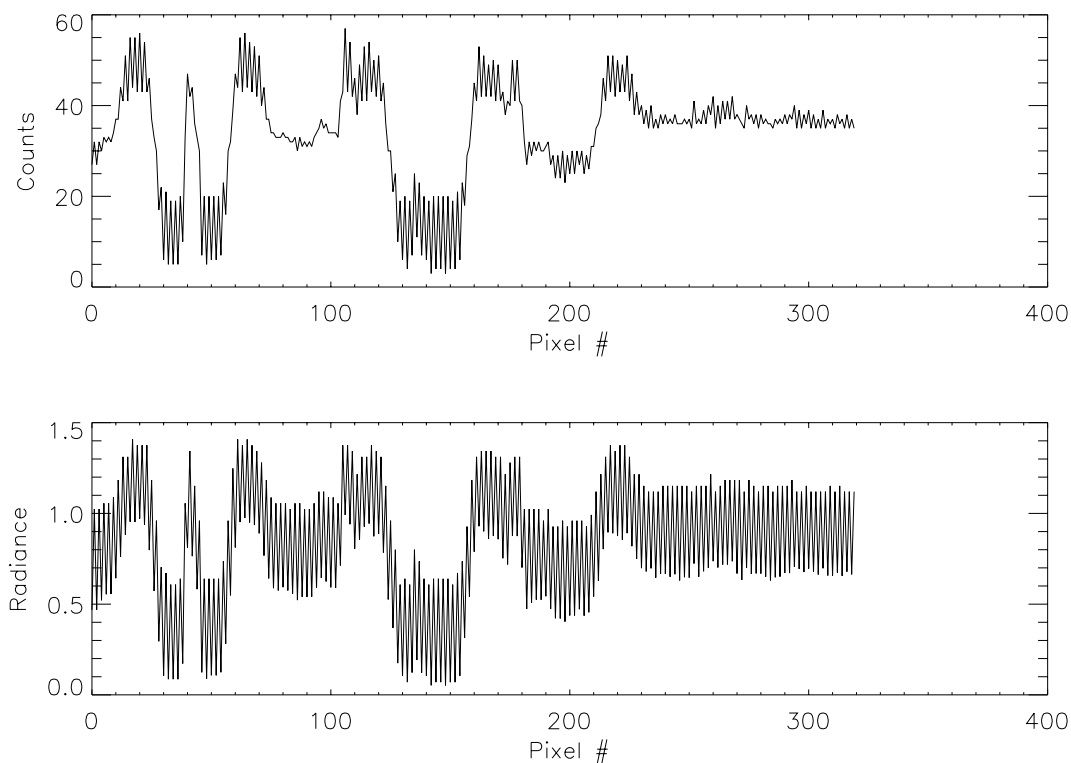
Figure 3-16. Effects of leaky detector corruption of frame 1050 of the Band 2 image of Lincoln Laboratory. The top figure is dark subtracted data. The bottom figure has been radiometrically corrected.

3.1.1.3.1.3 Generate Difference Array Between Corrupted Detectors and Nearest Neighbors

Once an image has been geometrically corrected and radiometrically calibrated, the leaky detector correction methodology focuses on a frame-by-frame correction. This correction begins with the generation of a *difference* array between corrupted detectors and nearest uncorrupted or *standard* neighbors. After an image has been geometrically corrected, each corrupted detector is abutted on either side by an uncorrupted or standard detector. A difference array between corrupted and standard detectors creates a database of leakage for a given frame. A trend of leakage verses radiance is then formed if the weighted standard detector radiance is plotted against the difference array. The difference array against radiance for frame 1050 is plotted in Figure 3-17.
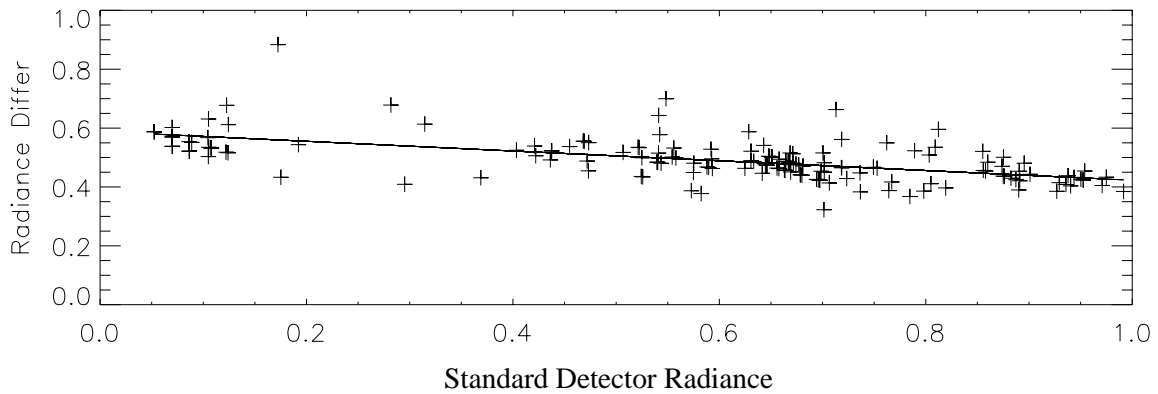
Figure 3-17: Frame 1050 difference array as a function of weighted standard detector radiance.

3.1.1.3.1.4 Compute Correction Function

The leakage correction function for each frame is calculated as a polynominal fit to the standard detector radiance and difference array data. This fit identifies the leakage observed as a function of radiance by statistically averaging the inherent standard-to-corrupted detector variations in geometrically varying scenes. The correction function for frame 1050 is shown in Figure 3-18.
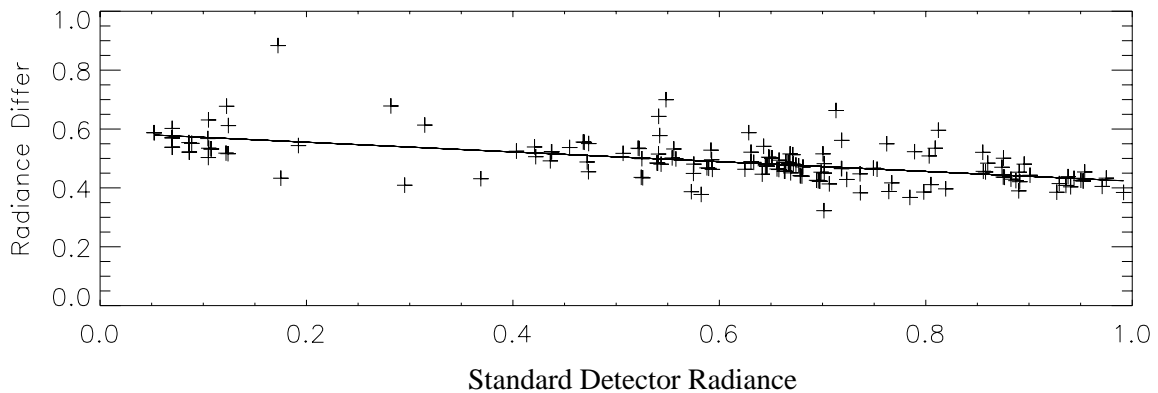
Figure 3-18: Frame 1050 difference array as a function of weighted standard detector radiance. Overlaid is the linear fit leakage function that is used to correct corrupted detectors for this frame.

3.1.1.3.1.5 Correct Image

The final step in leaky detector correction is the application of the leakage correction function to individual detectors. For a given corrupted detector, a correction factor is calculated, based on the correction function and neighboring standard detector value:

$$C_N = A_{CF} + B_{CF}(R_S) + C_{CF}(R_S)^2 \qquad\qquad \text{Equation 3}$$

Here, C_N is the correction factor for detector N, A_{CF}, B_{CF}, C_{CF} the correction factors, and R_S is the radiance of the neighboring standard detectors. Once a correction factor has been calculated, it is simply subtracted from the original radiometrically calibrated corrupted detector value. Figure 3-19 depicts the effects of leaky detector correction for frame 105. As one may see, the leakage has been effectively removed, while maintaining the intrinsic detector to detector variability of the scene. This is demonstrated graphically in Figures 3-20 and 3-21. The images on the left are the original corrupted Band 2 and Band 3 images respectively. The images on the right are the images after leaky detector correction has been implemented.
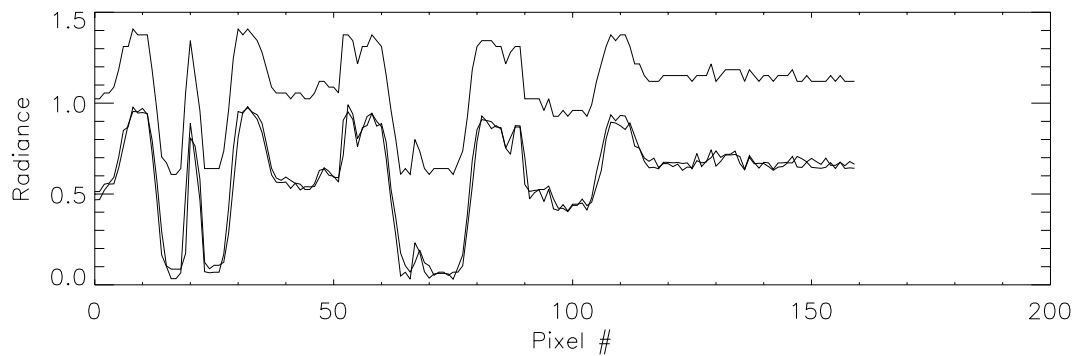

Figure 3-19. Frame 1050 with leaky detector correction applied. The data set at the top is the original radiometrically corrected corrupted detector data. The data at the bottom is an overlay of uncorrupted detector data and leaky detector corrected data.

Figure 3-20. Band 2 image of Lincoln Laboratory before (left) and after (right) leaky detector correction applied.

Figure 3-21. Band 3 image of Lincoln Laboratory before (left) and after (right) leaky detector correction applied.

3.1.1.3.1 Discussion

The radiometric responses of corrupted detectors are highly dependent on leaky detector illumination. As a result, an empirical correction method has been developed to effectively eliminate the addition of optical or electrical cross-talk induced by leaky detectors. This method centers on the generation of a *difference* array between corrupted and neighboring *standard* detectors. This array is used to fit a correction function on a frame-by-frame basis and calculate correction factors on a detector-by-detector basis. This method has been used on various scenes collected during ground calibration at Lincoln Laboratory with excellent results.

Using the above method on a variety of scenes, one area of concern has been identified: scenes with uniform high (low) radiance levels, sparsely intermixed with a very low number of small, low (high) radiance regions. Examples of these scenes include snow covered scenes with a single

road cutting across the image or ocean scenes with small, sparsely distributed clouds. The root of the problem lies in the generation of the correction function. For the above examples, an overwhelming number of detectors will have nearly the same high (low) radiances with only a handful of detectors exhibiting low (high) radiances. If the difference array for the handful of detectors cluster is not correctly calculated or has a large scatter, the resulting correction function will not be correct, resulting in poor correction for those detectors. This danger only exists for scenes where the distribution of radiance across the scene is split into large and small groups. Fortunately, by the nature of the problem, only the handful of detectors whose correction function is incorrect will be affected.

3.1.1.4   Contamination

Contamination of the focal plane by an unknown substance was recognized in October 1998 during the characterization and calibration of the Advanced Land Imager at Lincoln Laboratory. This contaminant may be completely eliminated by raising the temperature of the focal plane to above 260 K. Prior to launch, several bake outs occurred in an attempt to eliminate the source of the contaminant. In January 1999, the entire instrument was baked out at 303 K while under vacuum for one week and then later for an additional two days. The focal plane was baked out for three hours at 273 K in October 1999 and for one day at 273 K in July 2000 during spacecraft thermal vacuum testing at Goddard Space Flight Center.

In the event that on-orbit bake outs would become necessary, an additional heater was added to the focal plane radiator in February 1999. This heater, along with others on the instrument, will raise the temperature of the focal plane to 270 K in the space environment.

3.1.1.4.1   Detection

The monitoring of contaminant deposition on the ALI focal plane during ground testing and on-orbit is performed using the internal reference lamps mounted on the telescope metering truss. These lamps provide three levels of stable, repeatable reference illumination of the focal plane (Figure 3-22). However, because the internal reference lamp assembly has a much higher f-number (40) compared to the telescope (7.5), the assembly acts as a microscope for detecting contamination effects. This magnification must be considered when assessing the impact of focal plane contamination on image quality and radiometry. Generally, any apparent spatial variations caused by focal plane contamination should be reduced by a factor of 4 when applied to imagery collected by the ALI.
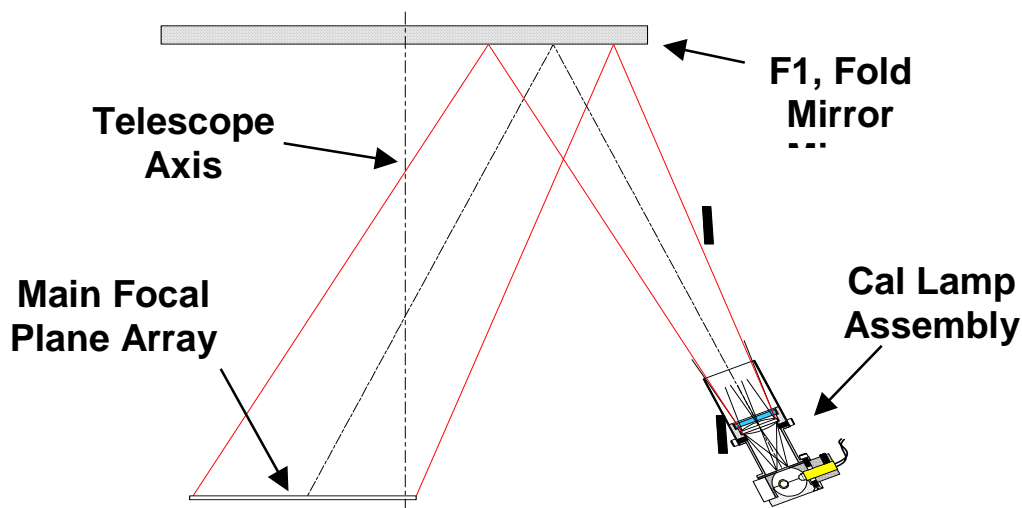
Figure 3-22. Illumination of the ALI focal plane using the internal reference lamp assembly.

The first step in detecting contaminants is to collect data using the internal reference lamp assembly when the focal plane is considered 'clean'. The dark current subtracted response of the focal plane for each band using the clean data is considered the baseline. Data is then collected once per day over a period of interest. All data are then divided by the baseline data, and the mean and standard deviations of the ratio are then computed for each band. The mean and standard deviations are considered figures of merit for focal plane contamination. If the reference lamps and focal plane are stable, and it no contamination occurs, the mean of the ratios for each day should be unity and the standard deviations should be equivalent to the noise of the detectors.

3.1.1.4.2 *Location of Contamination*

The location of ALI contamination has been identified as the top surfaces of the spectral filters overlaying the focal plane detectors. A CCD camera was placed at the focus of a collimator and images of the filter surfaces were obtained. The left side of Figure 3-23 shows a portion of the focal plane filters during a period when contamination had been detected. The image on the right is of the same portion of the filter after the instrument had been baked out. Clearly, a residue had formed on the surface of the filters during contamination build-up. Additionally, all evidence of the residue has been eliminated as a result of the bake out. This conclusion is supported by the levels of post-bake out data returning to baseline levels once the focal plane had been heated above 260 K.
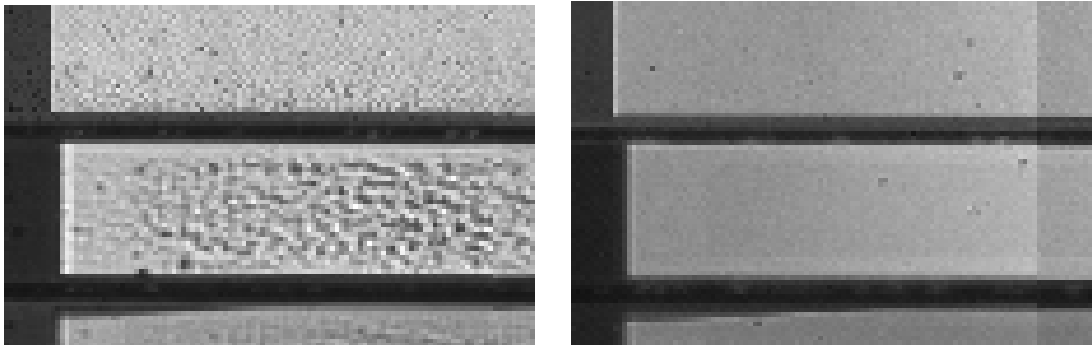
Figure 3-23. Image of a portion of the top surface of the focal plane filters when contaminated (left) and after a bake out (right).

3.1.1.4.3 Characteristics

Focal plane contamination appears in three forms: pixel-to-pixel variation, mean level shifts, and bowing. Pixel-to-pixel variation refers to an apparent random shifting in individual detector responses either above or below the original reference values. As deposition continues, the pixel-to-pixel variations increase and the standard deviations between observations increase.

Another characteristic of contamination is mean level shifting. This refers to the gradual shifting of the apparent mean level response of an SCA as contaminants are accumulated on the filter surfaces. This shifting usually occurs negative to the baseline response. However, in some instances, positive and even changing mean level responses have been observed.

Bowing is also observed in cases of significant focal plane contamination. As an SCA becomes contaminated, the mean apparent response of the detectors may change as a function of detector position. Detectors near the edges of SCAs have a larger change in apparent response, relative to those near the middle of the SCA, resulting in a bowing appearance for some bands.

Figure 3-24 depicts history of focal plane contamination for Band 4 for two periods. The left column shows rapid contamination of the focal plane over a six data period. Clearly evident are the effects of pixel-to-pixel variations, as well as mean level shifting and bowing. The right column shows a significantly reduced contaminant build-up after the first instrument bake out at Lincoln Laboratory.
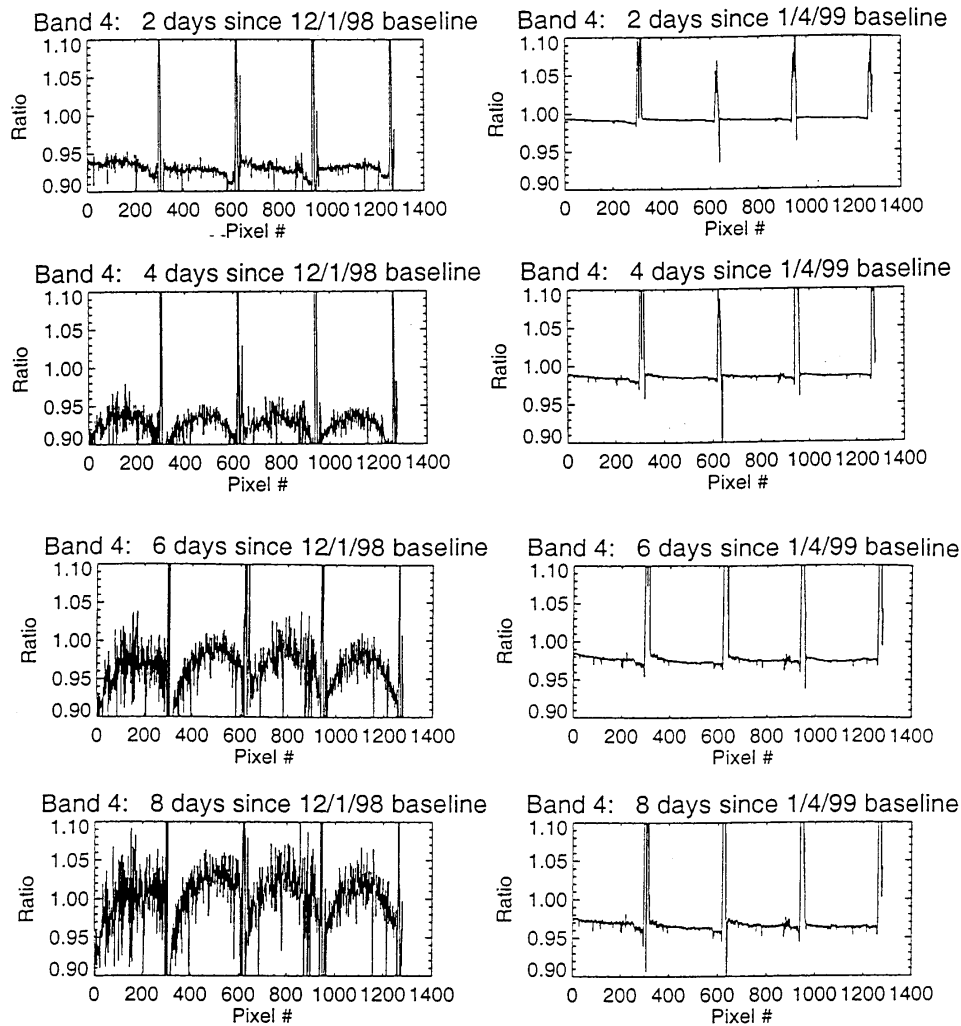
Figure 3-24: History of focal plane contamination for two periods during instrument characterization at Lincoln Laboratory.

3.1.1.4.4 Discussion

Much information pertaining to the contamination of the Advanced Land Imager focal plane has been obtained during ground testing between October 1998 and November 2001. The contaminant appears to condense on the surfaces of the spectral filters lying above the detectors when the focal plane is operated at 220K. However, once the focal plane is warmed above 260 K the contaminant 'boils off' and detector responses return to baseline levels. This implies that

mirror surfaces, maintained above 273 K at all times, will not collect contaminants during ground testing or during orbital operations.

Although the source of the contamination is not known, the leading suspect is the black paint (Z306) coating the inside of the telescope to reduce stray light. Bake out of the telescope surround structure by SSG was not completed in the interest of schedule and it is believe residual outgassing of the paint may be sticking onto the filter surfaces when the focal plane is cold. Future work at Lincoln Laboratory is to characterize the properties of Z306 to further evaluate the possibility of this paint as the source of contamination.

3.1.1.5 Focus Shim Adjustment

Following integration of the Focal Plane System with the instrument optics, a set of measurements were made to determine what correction, if any, was needed to the focus shim in order to put the focal plane detectors at the best focus. For these measurements, the ALI was

 supported on a fixture in a Class 1000 clean room, with its Z axis horizontal. In front of the ALI was the imaging collimator developed for imaging simulations and MTF testing (see Figure 3-25).
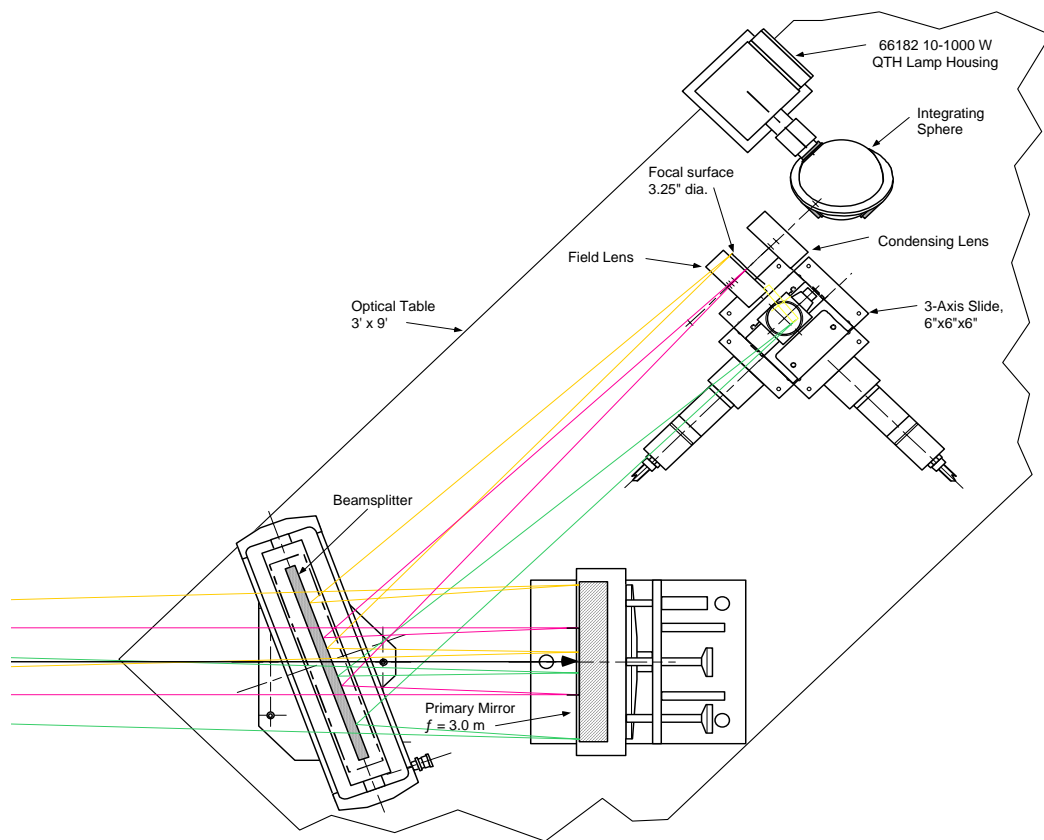
Figure 3-25. Top view of Imaging Collimator. A LUPI takes the place of the lamp, integrating sphere, and condensing lens during collimation testing.

The procedure was as follows: After the collimator had been set up for infinite focus, a series of knife-edge scans were performed as described under MTF calibration below. Data from a detector were recorded as the image of the knife edge passed across the detector. The scan was repeated with the knife edge shifted along the axis of the collimator at a series of positions known distances from the infinite focus reference position.

For each knife-edge scan, the sharpness of the edge in the detector data was computed. In this case, the figure of merit was the length (in frames at a constant speed) of the transition from dark to light. The figure of merit was plotted *vs*. the focus offset of the collimator. The value of focus offset at the minimum of the curve was determined. The corresponding ALI focus error was proportional to this collimator focus offset.

The ALI focus error was estimated for many of the VNIR detectors at widely-separated locations on the focal plane. From this set of data, a best shim correction was derived. A large piston correction of 823 µm was required, but no tip or tilt correction was necessary. The shim was then

removed and corrected, and the focal plane re-installed. The focus tests were repeated. This time no further corrections were found to be necessary.

3.1.1.6   End-to-End Imaging Tests

A major functional verification test of the ALI was the End-to-End Imaging test. For this test, a reticle or target, typically the negative "USAF 1951" target, was mounted at the focal plane of the collimator. A vertical slide moved the target at the correct speed to simulate apparent ground motion from orbit. Focal plane data were recorded at the nominal frame rates and integration times. The data were then processed and reconstructed as planned for on-orbit data. The resulting digital images from all of the VNIR bands were examined, and the instrument was found to be basically working correctly. In the process, it was also found that two detectors caused significant cross-talk. Those "leaky pixels" (in band 3 of SCA 3 and band 2 of SCA 4) were the cause of a major effort in calibration to correct the resulting artifacts.

The original End-to-End Imaging tests were performed soon after the instrument was integrated at Lincoln Laboratory. A final test was performed in a clean room at GSFC after integration with the spacecraft and thermal vacuum testing. A starburst pattern was scanned in the early tests and in the final test. There was no perceptible difference between the original images and the final image.

3.1.2   Spatial Calibration

3.1.2.1   Modulation Transfer Functions

The spatial response of the ALI instrument was calibrated in the laboratory during the period July to December, 1998, prior to its integration with the spacecraft. This section presents the final results for the calibrations of the Modulation Transfer Function (MTF). Details of the MTF model developed for the instrument are described. Results for selected bands are shown graphically. Fuller details of the MTF calibration, including numerical values of the MTF's have been reported elsewhere [16].

Spatial response is fully characterized by a spatial transfer function (STF). The full STF of the instrument is a two-dimensional complex function, which depends on the wavelength band, and to a lesser degree, on the position within the field of view. The STF is the Fourier transform of the point-spread function (PSF). The modulation transfer function is normally defined as the magnitude of the STF, a real, non-negative quantity. An additional phase transfer function (PTF) is then required to describe the spatial response completely.

In the ALI, as in most good imaging instruments, the PSF is essentially symmetrical. As a result, the imaginary part of the STF (Im(STF)) is very small, compared to the real part (Re(STF)). The conventional MTF then looks like the absolute value of Re(STF). For simplicity, we prefer to work with the STF, rather than the MTF and a PTF. We have habitually called the STF the

"complex MTF," or simply the MTF while working on the ALI calibration. In the rest of this document, the terms have been used interchangeably.

The approach we used to measure the MTF's of the ALI was to project the image of a knife-edge into the instrument, and scan the edge slowly across a selected set of detectors while the instrument records the image data at its nominal rates. The knife-edge was physically located at the focus of a collimator and the scan was performed by translating its support stage slowly in the plane of best focus. For each pixel in the set, the detected signal vs. time, after normalization, yields an edge-spread function (ESF). Differentiation of the ESF gives the line-spread function (LSF). Fourier transformation of the LSF results in the STF, or complex MTF, along one axis.

All measurements reported here were made while the instrument was in a thermal vacuum chamber, at its normal operating temperatures. For each of the four sensor chip assemblies (SCA's), the knife-edge was scanned across a set of pixels near the middle of that SCA, for each band. Scans were performed in both the cross-track and in-track directions of the instrument by using two sides of the 9 mm open square in a negative "USAF 1951" target as our knife-edges. (The rest of the target was covered by black plastic.) When switching from one SCA to the next, the instrument was re-positioned on an azimuthal rotation stage in the vacuum chamber in order to scan each SCA with the knife-edge within ~0.5° of the collimator axis.

The knife-edge was moved at 200 µm/s, which translates to 127.4µm/s at the ALI focal plane. The frame rates were 226 s^{-1} for the multispectral (MS) bands, and 678 s^{-1} for the panchromatic (Pan) band. The spatial sampling intervals were 0.564 µm and 0.188 µm for the MS and Pan bands, respectively, or approximately 70 samples per pixel width in all cases.

Analysis of the data from the knife-edge scans proceeded in several steps. While the scans were being performed in the thermal vacuum chamber in the clean room, a portion of the data was analyzed and graphically displayed on a monitor next to the control computer. The data files were stored on the hard drives of a Silicon Graphics R-10000 workstation (called the Performance Assessment Machine (PAM)), and periodically backed up on DLT cartridges.

After all of the knife-edge scan files were recorded, preliminary processing was done on the PAM. A program was run to de-scramble the raw data. Next, running under IDL♦, a procedure read the full MS or Pan data file and wrote a much more compact file (*.kes)[†], containing only the data from the SCA and bands of that particular scan.

The next step was to analyze the signal from each detector to derive its edge-spread function. A sigmoid curve (hyperbolic tangent) was fitted to each pixel's ESF, in order to resample the ESF's to co-align all of the edge-crossing times. In the process, automatic selection criteria were

---

♦ Interactive Data Language, from Research Systems, Inc., 4990 Pearl East Circle, Boulder, CO 80301, (see www.rsinc.com).
† In this context, * represents a "wildcard," substituting for the root name of the data file.

applied to reject pixels that had data artifacts or incomplete scans. An intermediate file (*.kes.fit) was written to facilitate the further processing steps.

To transform the ESF's to MTF's, another procedure was developed to read the *.kes and *.kes.fit files, then derive the LSF and MTF functions from them. For each SCA and band combination, the complex MTF was computed on a pixel-by-pixel basis, then the mean and standard deviation was derived. These are written to an IDL data file (*.mtf) for further reference, and plots are generated to display the results of each step in the analysis.

Finally, for each band the complex MTF's for the individual SCA's are averaged and plotted together, along with a curve representing the MTF model. Again, the results are written to an IDL data file.

A typical page of plots generated in the analysis of one scan file is shown in Figures 3-26 to 3-29.
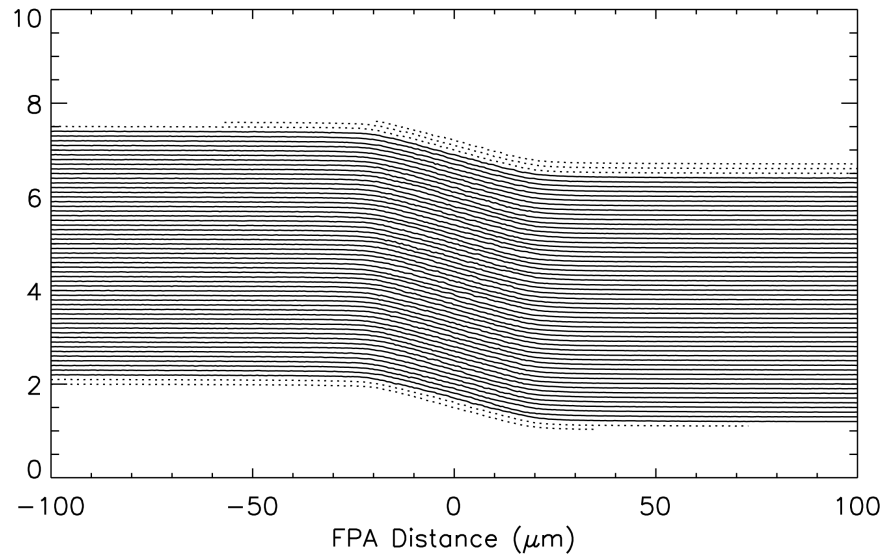
Figure 3-26. Edge-spread functions of SCA2, Band 4 pixels scanned in the cross-track direction, from file no. 16638. Pixels not used in further analysis are shown with dotted lines
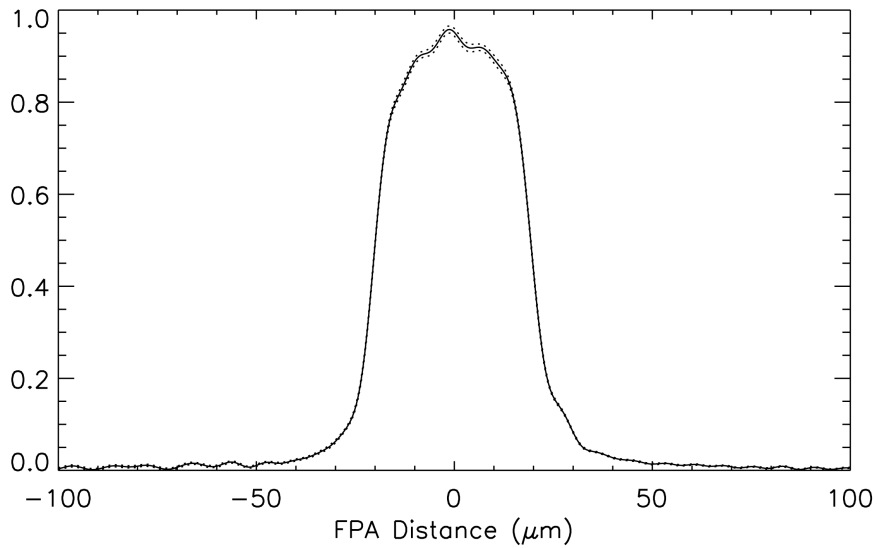
Figure 3-27. Average line-spread function derived from the data shown in figure 1. The dotted lines are one standard deviation above and below the mean
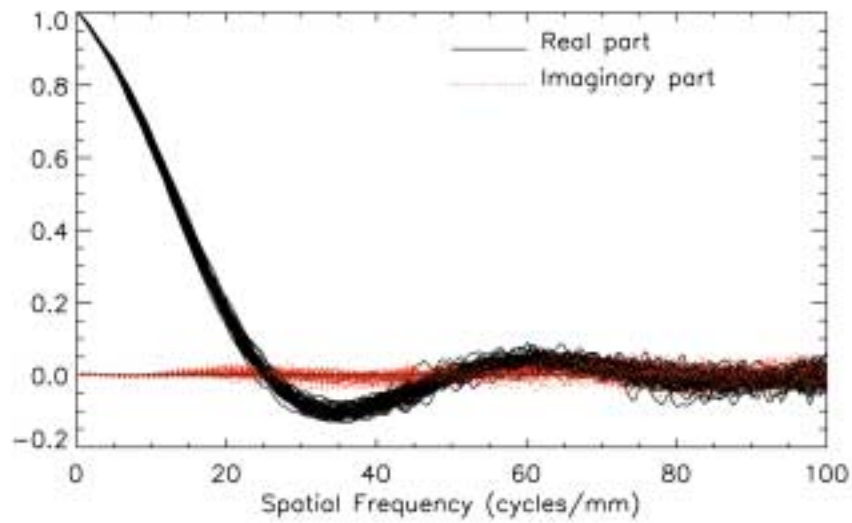
Figure 3-28. Normalized transfer functions derived from the data shown in figure 1.
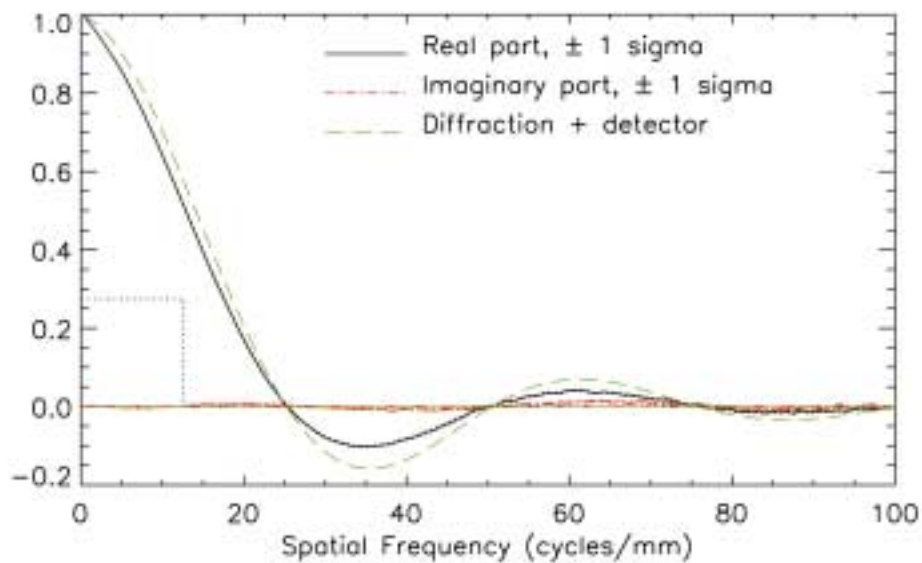
Figure 3-29. Average normalized transfer function derived from the data shown in figure 1. The dotted lines are one standard deviation above and below the mean. The curve labeled "Diffraction + detector" is computed from the simplest model of diffraction by a circular aperture and a sharp-edged detector response. The specified MTF at the Nyquist frequency is indicated with dotted lines.

We describe the MTF of the instrument with a model which contains only enough parameters to fit the measurement data within the experimental uncertainties, and which will enable other investigators to compute the MTF for their own needs. It is important to have a model for the MTF, since the knife-edge scan measurements can only produce one-dimensional cross-sections of the MTF, which is a two-dimensional function. The following subsections describe the various factors which, when multiplied together, yield the system MTF of the ALI instrument. These are the optical system MTF, the detector MTF, and the MTF of the scan motion of the instrument as it collects images on orbit.

The optical MTF estimated from our laboratory measurements results from the combined optical transfer functions (OTF's) of the ALI telescope and the collimator. It is modified by the effects of light scattering from the imperfect surfaces of the ALI mirrors.

SSG, Inc., the builder of the ALI optical system, has used a laser unequal-path interferometer (LUPI) to characterize the WFE of the ALI. They obtained interferograms at a dozen points distributed over the 1.26°x15° field of view of the optical system. The WFE derived from each interferogram was fitted with a set of 37 Zernike polynomials. The first three Zernike polynomials, representing piston, tip, and tilt, are set to zero. The fourth coefficient represents a focus error. We use the Zernike coefficients from SSG to obtain an interpolated set of coefficients for any given point within the MS/Pan array of the ALI.

To ascertain the amount of focus error in the integrated system, MTF scans were performed with varying amounts of defocus applied at the collimator. The figure of merit (FoM) chosen to test the defocus was the integral of the MTF from zero to the detector sampling frequency of the FPA. A plot of this FoM as a function of the axial displacement of the knife-edge from the collimator focus is shown in Figure 3-30. The plot also shows a parabola fitted to the highest values, to derive the focus error. These results indicate that the ALI FPA, at operating temperature, is approximately 75±20 µm away from the optimum focus position. This does not seriously degrade the optical resolution, but must be taken into account when modeling the system MTF.

The collimator, and the methods used to set it to best focus, are described in a paper by Willard. The spherical aberration of the collimator is calculated to be 0.007 µm rms, when the collimator and ALI pupils are correctly aligned. The remaining rms WFE, caused mainly by the beamsplitter, is approximately 0.032 µm.

The spatial response of the detectors was initially modeled as unity within a defining rectangular mask (39.6 µm x 40 µm for the MS pixels, and 13.2 µm square for the Pan pixels), and zero outside of that area. The corresponding pixel MTF is a product of two sinc functions: MTF_{PIX} (f_x, f_y) = $sinc(wf_x)$ $sinc(h, f_y)$ where w and h are the width and height of the detector mask, respectively, and (f_x, f_y) are the components of the spatial frequency.
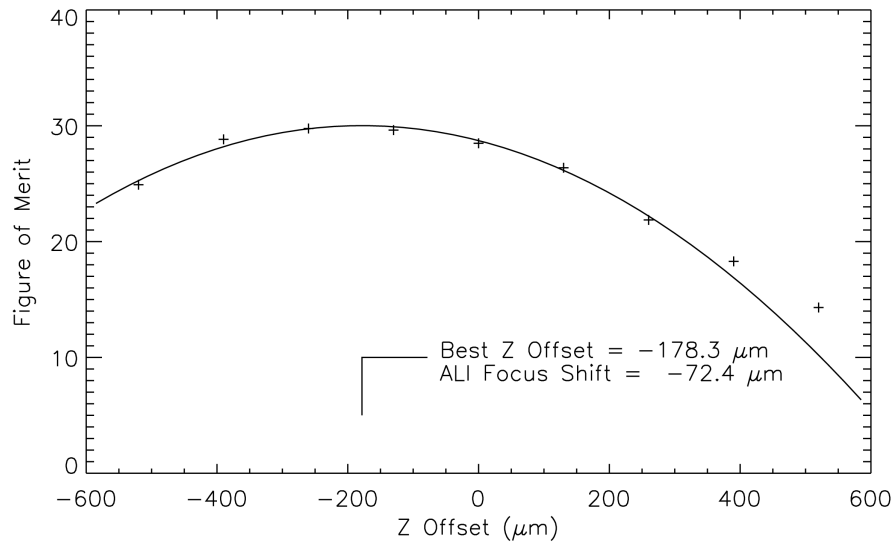
Figure 3-30. *ALI focus figure of merit vs. axial displacement of the knife-edge from the collimator focus (Z Offset). Data symbols represent individual MTF scans. The curve is a parabola fitted to the points within 500 μm of the peak.*

Measured values of the ALI system MTF tended to decrease approximately linearly, in comparison with the system MTF computed using this simple detector model, after adjustment of the free optical parameters. Good fits between measured and modeled MTF's are only obtained when a *carrier diffusion MTF* is included in the model.

Motion of the satellite as it collects image data in push-broom mode causes a slight smearing of the image in the in-track direction. The geometric footprint of each detector on the ground is convolved with a vector representing the motion of the view axis during the integration time of a single frame. The MTF of this motion is another sinc function in the in-track direction only: $MTF_{INT} = sinc\ (\alpha v)$ where v is the angular frequency and α is the angle subtended by the ground motion vector.

Procedures written in IDL are used to construct the ALI WFE from the adjusted set of Zernike coefficients derived from interferograms by SSG. From the WFE, the optical point-spread function (PSF) and MTF of the ALI telescope are obtained, by use of the Fourier transform procedure in IDL.

A surface plot of the WFE near the middle of the MS/Pan array, excluding tip, tilt, and focus, is shown in Figure 3-31. There are small differences in WFE from place to place on the focal plane, caused by the fact that the beam footprint covers different parts of the M1 and M3 mirrors for different points in the field of view.
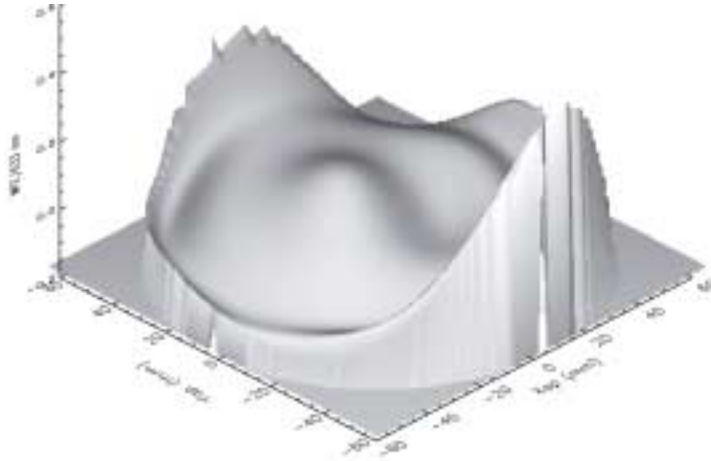
Figure 3-31. Surface plot of the wavefront error near the middle of the MS/Pan array. The focus term is not included here.

The optical point-spread function of the Pan band, computed from the WFE, is shown in Figure 3-32. The real part of the corresponding OTF is shown in Figure 3-33.
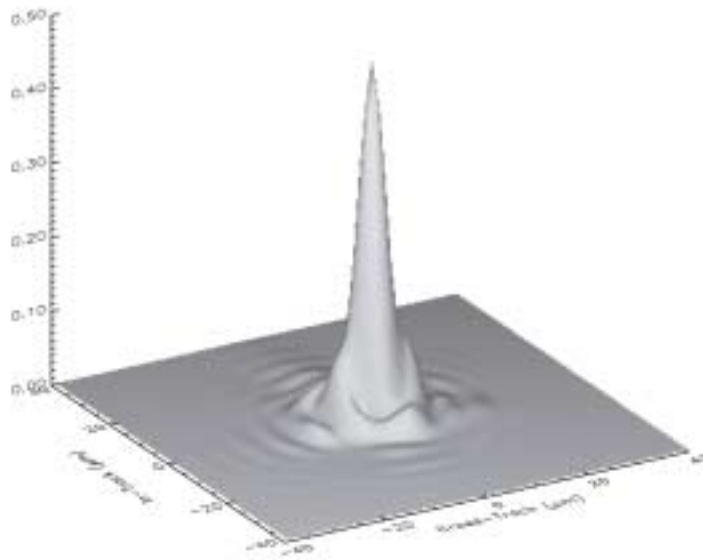

Figure 3-32. Optical point-spread function of the Pan band, computed from the full wavefront error, including the focus term.
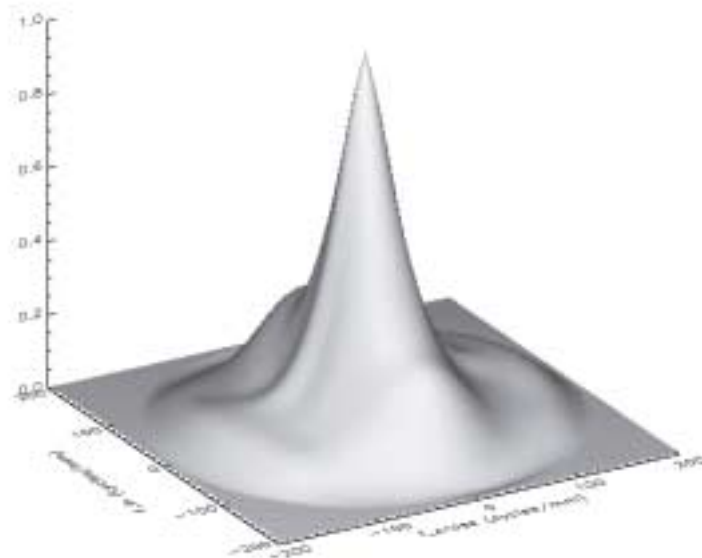
Figure 3-33. Optical transfer function of the Pan band (real part), computed from the wavefront error, including the focus term.

Figure 3-34 shows the MTF curves derived from scans of the four Pan arrays, along with the average, modeled MTF curve.
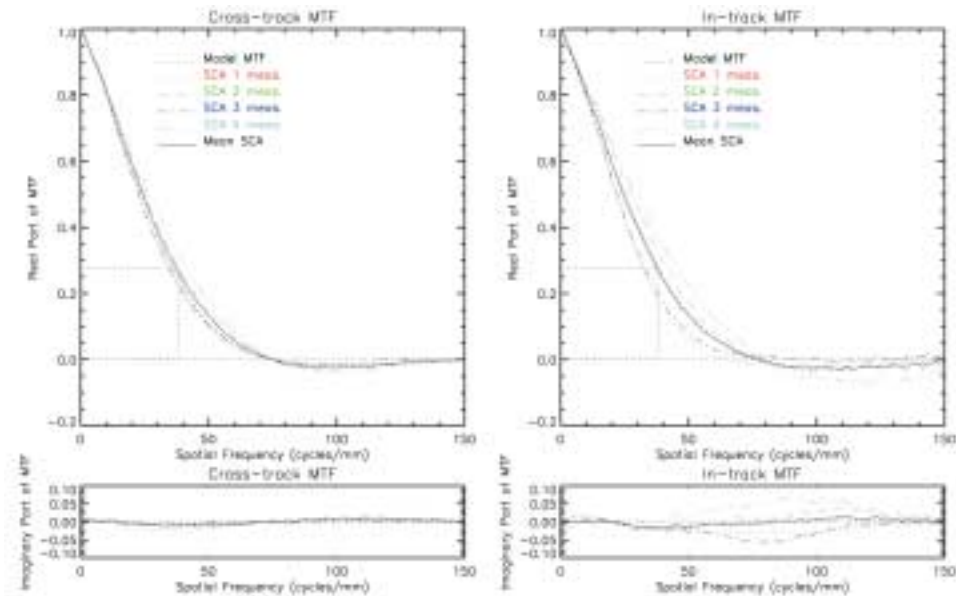
Figure 3-34. Measure and modeled Average MTF's for the Pan band, and measured MTF's for the individual SCA's.

3-48

The real part of the two-dimensional Pan MTF at the center of the array computed from our model is shown in Figure 3-35. The small imaginary part can be neglected, given the uncertainties in our fitting of the model to the measurements. The real part of the MTF is symmetric in both axes, the imaginary part anti-symmetric.
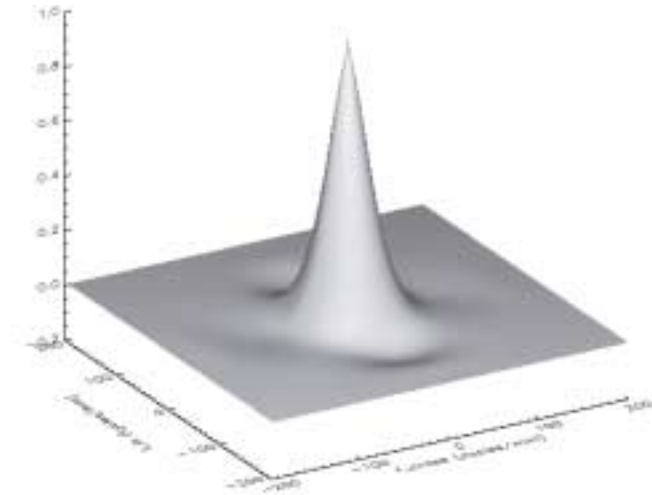
Figure 3-35. System MTF of the Panchromatic band near the center of the detector array.

Figure 3-36 give a representation of the Panchromatic system point-spread function (PSF), not including scan motion spreading.
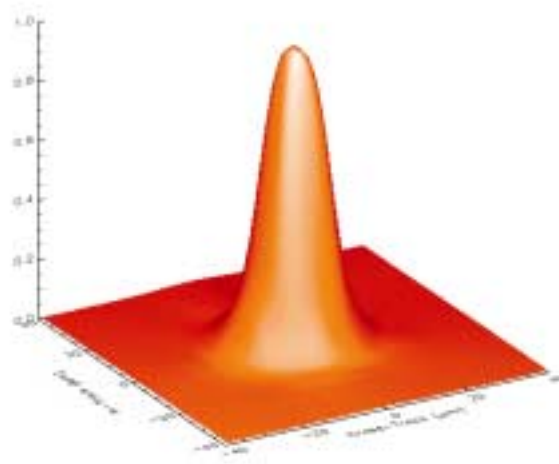
Figure 3-36. System PSF of the Panchromatic band near the center of the detector array.

The real part of the two-dimensional average MTF's for bands 1', 4', and 7 are plotted in Figures 3-37 to 3-39.
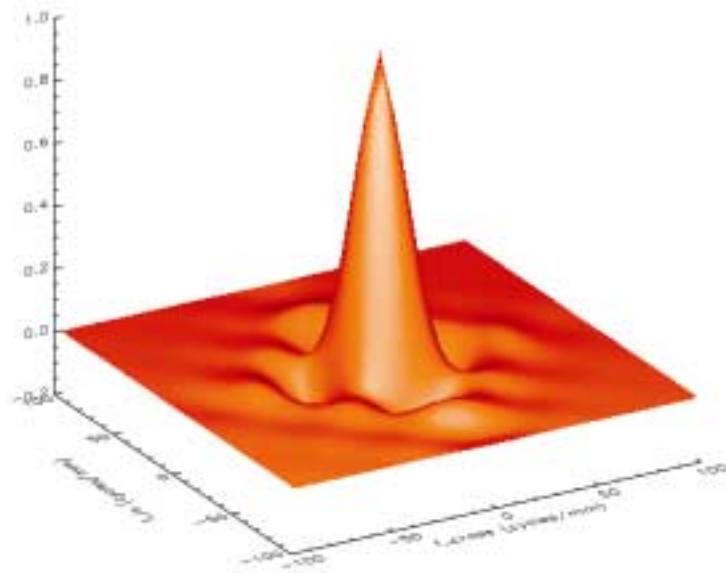

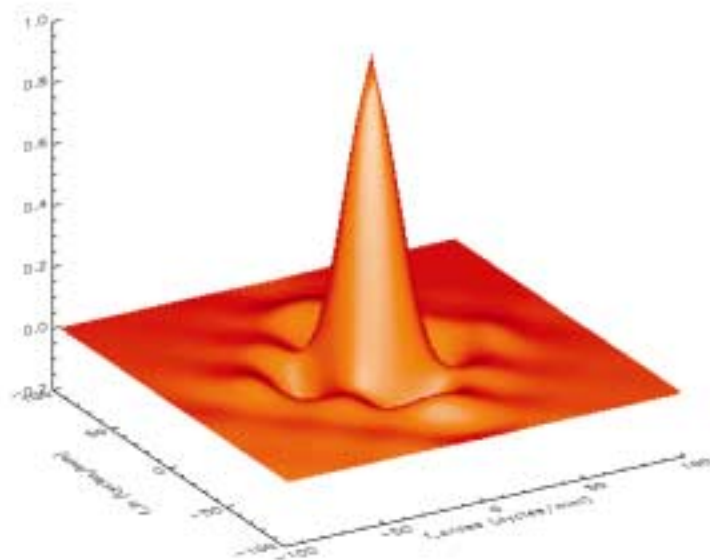*Figure 3-37. System MTF of band 1' near the center of the detector array.*

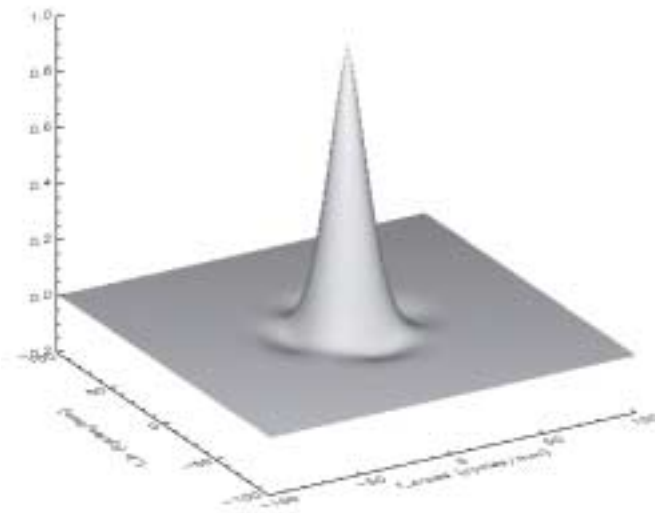*Figure 3-38. System MTF of band 4' near the center of the detector array.*

Figure 3-39. System MTF of band 7 near the center of the detector array.

Representative point-spread functions computed from the model MTF's are shown in Figures 3-40, 3-41, and 3-42. The in-track spreading caused by scan motion is not included in these PSF's.
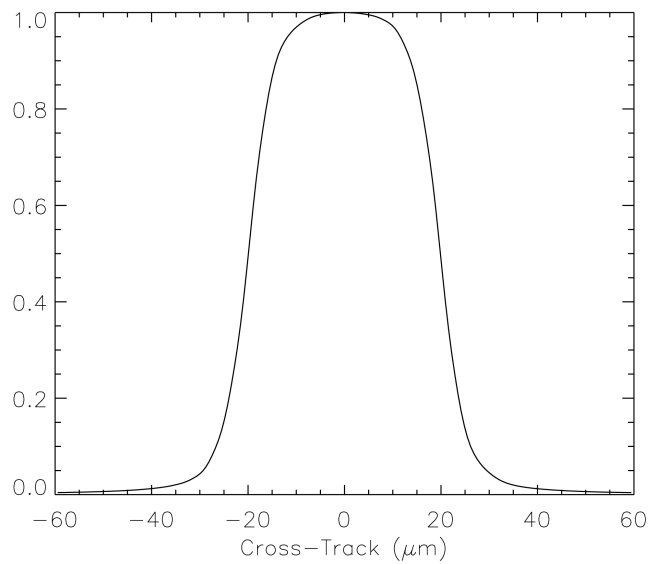

Figure 3-40. System PSF of band 1' near the center of the detector array. This cross-section is through center in the cross-track direction.
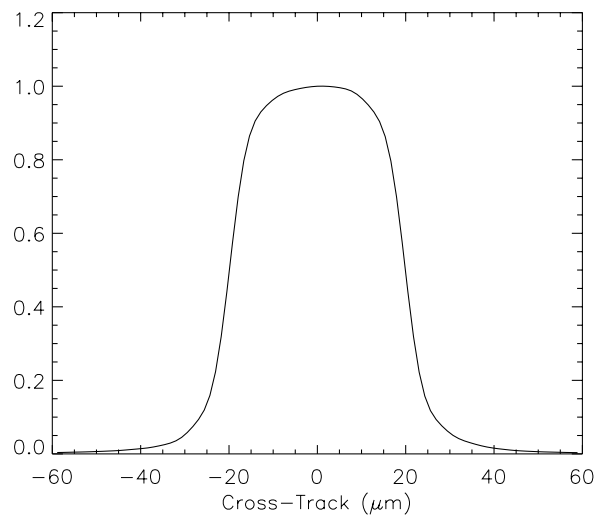
Figure 3-41. System PSF of band 4' near the center of the detector array. This cross-section is through center in the cross-track direction.
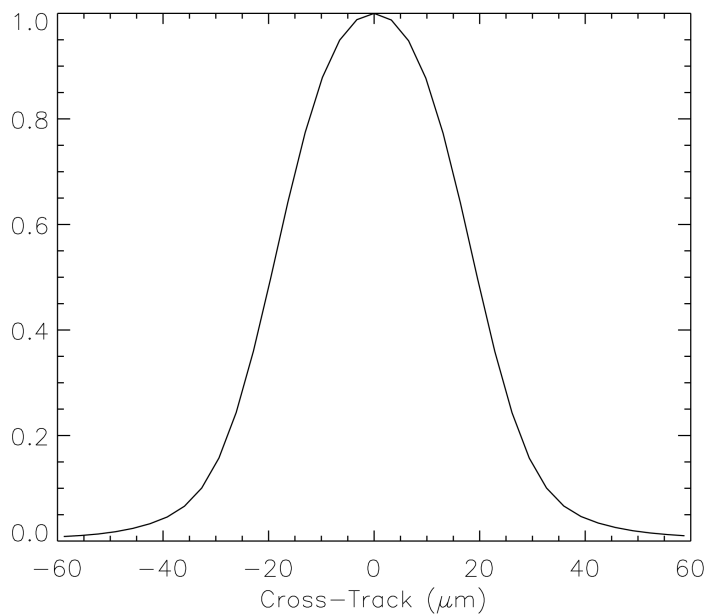

Figure 3- 42. System PSF of band 7 near the center of the detector array. This cross-section is through center in the cross-track direction.

3.1.2.2   Detector Lines of Sight

In order to reconstruct the ALI image data in reference to the geographic coordinates of the land scene, the lines-of-sight (LOS) of the many detectors relative to the satellite body axes must be known. That information is contained in the LOS map. The LOS map is a tabulation of the sight direction of each detector on the ALI focal plane, relative to a set of reference axes. A parameterized model was developed to describe the apparent position of each detector on the focal plane, as seen through the telescope. The detector LOS map is a tabulation of those apparent positions. To obtain the angular LOS of any detector, we treat the telescope as an ideal imaging system, with a given focal length. The LOS calibration performed at Lincoln Laboratory was reported by Hearn [20].

The focal length of the telescope is one key parameter. The physical position of a detector on the focal plane is described by the positions of fiducial marks on the SCA, and the layout design of the SCA. Here, we assume that the geometric precision of the photolithographic process used to make the ROIC/detector chip is on the order of 0.1 µm, far greater than our ability to discern errors. Each VNIR detector thus far has four uncertain parameters to determine its position: focal length of the telescope, X–offset, Y–offset, and rotation offset of the SCA. In the case of the SWIR bands, three additional parameters describe the offset of the SWIR detector array chip relative to the ROIC.

The ALI telescope design produces some optical distortion. Owing to the asymmetry of the design, the distortion is not axisymmetric. Thus we are unable to apply a simple radial distortion model. Instead, we resort to a general third-order polynomial in X (the in-track axis) and Y (the cross-track axis). There are actually two polynomials, one for the X component of the distortion, and one for the Y component. This leads potentially to 32 polynomial coefficients to be determined. Some of the coefficients can be eliminated, such as the zero-power term, representing a fixed offset.

The ALI includes an optical reference cube fixed to its base pallet. The measurements that were made by theodolite to determine the orientation of the optical axes of the ALI telescope relative to this ALI reference cube are described in a following section. After final integration with the spacecraft, additional theodolite measurements were made to relate the ALI reference cube to the other sensors on board the spacecraft.

3.1.2.2.1   Subsystem Measurements

Four distinct sets of measurements were made in order to estimate the values of the line-of-sight parameters. This section describes the measurements made on the major subsystems of the instrument. Section 3.1.2.2.2 describes the end-to-end calibration measurements of the complete instrument to establish the detector lines-of-sight relative to the telescope axes. Finally, Section 3.1.2.3 discusses the theodolite measurements at Lincoln Laboratory to establish the angles from the reference cube to the telescope axes.

Santa Barbara Remote Sensing (SBRS) measured the locations of the SCA's on the assembled MS/Pan module. The measurements on the assembled focal plane used a coordinate-measuring machine to establish the locations of fiducial marks in the metallization of each SCA, to an accuracy of ~ ± 1 µm. The location of the pixels within each SCA, determined by photolithography, is believed to have an accuracy of ~ ± 0.1 µm.

SSG used a theodolite to measure the telescope for focal length and distortions. For this purpose, a fixture bearing scribed lines was mounted at the focal plane location. These lines were measured at Lincoln Laboratory on a coordinate-measuring machine. A precision theodolite was used to measure the angles of the scribe-line intersections when seen through the telescope, to ± 1 arc sec. These angular readings were then fitted to cubic polynomial functions to describe the cross-track and in-track optical distortion. A vector map of the measured distortions is shown in in Figure 3-43. The axes are labeled in millimeters and encompass the entire 15°x 1.2° field of view of the telescope. The residuals from the fits are shown in Figure 3-44. The fitted focal lengths are 942.41 mm and 945.15 mm in the cross-track and in-track directions, respectively. The scale of the vectors is greatly enlarged in comparison with Figure 3-43
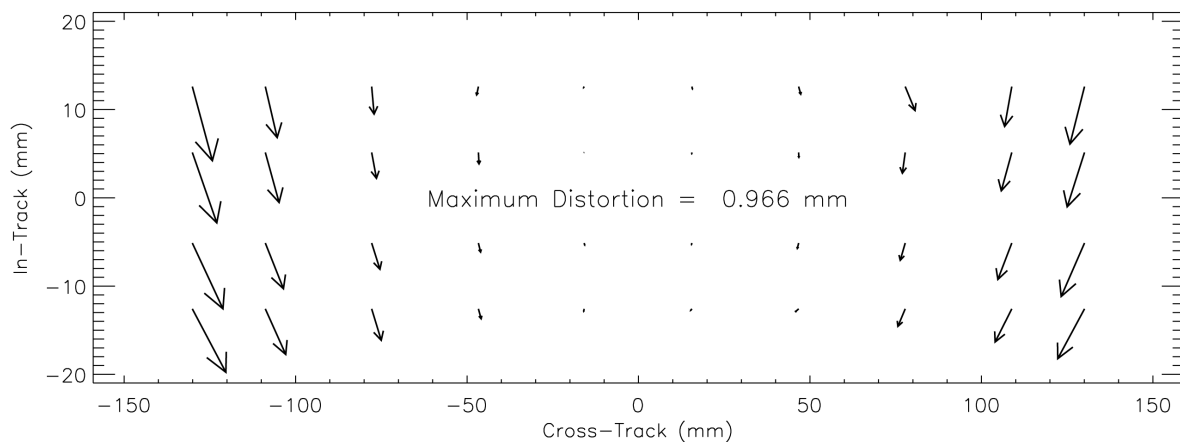
.

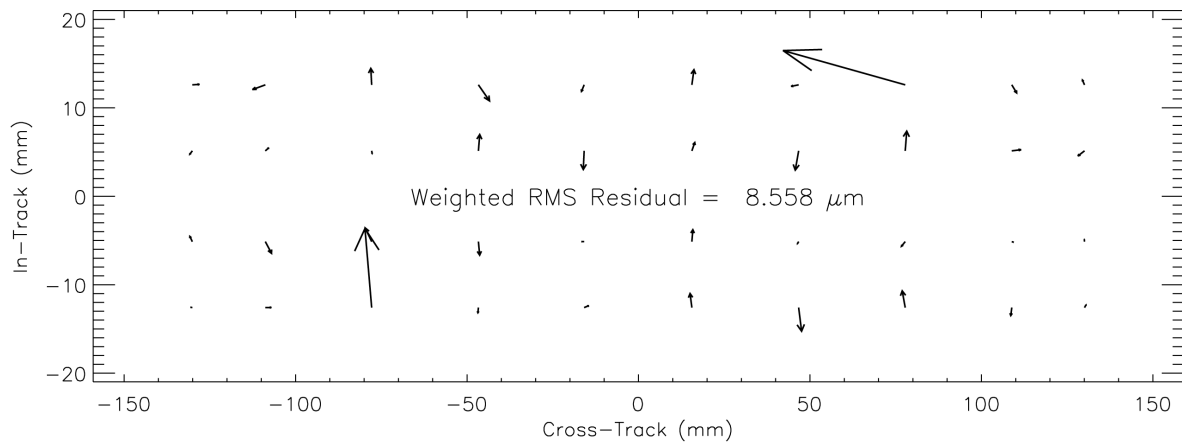*Figure 3-43 ALI telescope optical distortion, from SSG measurement data*

.

Figure 3-44. Residual ALI optical distortion, after subtracting a cubic polynomial fit from the measurement data.

3.1.2.2.2 End-to-End LOS Calibration

A precision target was placed at the focal plane of the imaging collimator. Ordinarily, a standard grid target would be used, giving apparent displacements of the grid points as seen by the instrument. The ALI detectors are arranged on the focal plane in staggered rows, not in a simple two-dimensional grid. It is only capable of forming two-dimensional images by scanning. It was undesirable to scan the target with the vertical slide, as was done to test end-to-end image formation, since that would introduce the uncertainties of the scan speed and direction. The approach chosen was to record static images of a Ronchi ruling placed at the collimator focal plane. The orientation of the ruling was changed from one image to the next. First, the lines were vertical, in the in-track direction to the ALI. Two more images were recorded with the lines at approximately 60° and 120° from vertical. The three static images of the Ronchi ruling which were later analyzed consisted of averages of 1,000 frames of MS/Pan detector signals. An image was also recorded with the Ronchi ruling removed from the collimator, to establish the "white" level signals. Similarly, dark levels were recorded, with the aperture cover of the instrument closed.

Relative lines of sight of the detectors were estimated from the Ronchi ruling images by using a linearized, least-squares fitting process to adjust the LOS parameters until numerically modeled detector signals matched the measured signals. The frequency of the Ronchi ruling target mounted in the collimator was 2.000 mm^{-1}. At the ALI focal plane, this became approximately 3.18 mm^{-1}. Thus there were 40.2 cycles of the ruling across each SCA detector row for the vertical ruling, and 20.1 cycles for the 60° and 120° rulings. This was expected to provide great precision in determining the relative detector lines-of-sight.

The data from the ALI were recorded and pre-processed on a Silicon Graphics workstation. The raw files were archived to digital linear tape. Additional analysis was performed with the IDL language, running on a 500 MHz Power Macintosh G4.

Results from the laboratory modulation transfer function measurements [16] were used to predict the appearance of the Ronchi ruling to the ALI. In IDL, the product of the detector transfer function with the component amplitudes of the square-wave was inverse-Fourier transformed to construct the detector response as a function of phase within the Ronchi cycle. This was stored as a look-up table. The remainder of the calculations then used vector algebra to find the expected phase of the Ronchi cycle at each detector.

The raw detector signals were radiometrically corrected with a two-point calibration. A normalization was performed on the detector signals to cause the peaks to be near one, and the valleys near zero. The theoretical response *vs*. Ronchi phase array (which did not range from zero to one) was modified to match.

In the standard IDL package is a linearized, least-squares fitting procedure called *curvefit.pro*. It requires the user to supply a function of the independent variables to be fitted to a given set of measured data values. Any number or type of parameters may be used to describe the user's function. In this case, the data values are the (normalized) measured detector signals for *all three* static Ronchi images, and the independent variables are the identities of the detectors to be fitted. The SCA 4 fiducial position was selected to be fixed, to anchor the coordinate system of the telescope.

Vector algebra was used to trace the ray from the center of each detector through the ALI telescope, and through the collimator to its intersection with the Ronchi ruling target. Both the ALI optical system and the collimator were treated as ideal imaging systems with added distortion. Angular rotations of the vectors to different reference frames were accomplished in IDL by matrix multiplication.

It proved essential to plot the modeled detector signals over the measured ones, in order to verify whether or not the fitting process was converging to a valid set of parameters. This we did for each static image, one band at a time. All four SCA's were plotted, but the odd and even-numbered detectors were plotted separately, making eight plots per band. Samples of these diagnostic plots are shown in Figure 3-45.
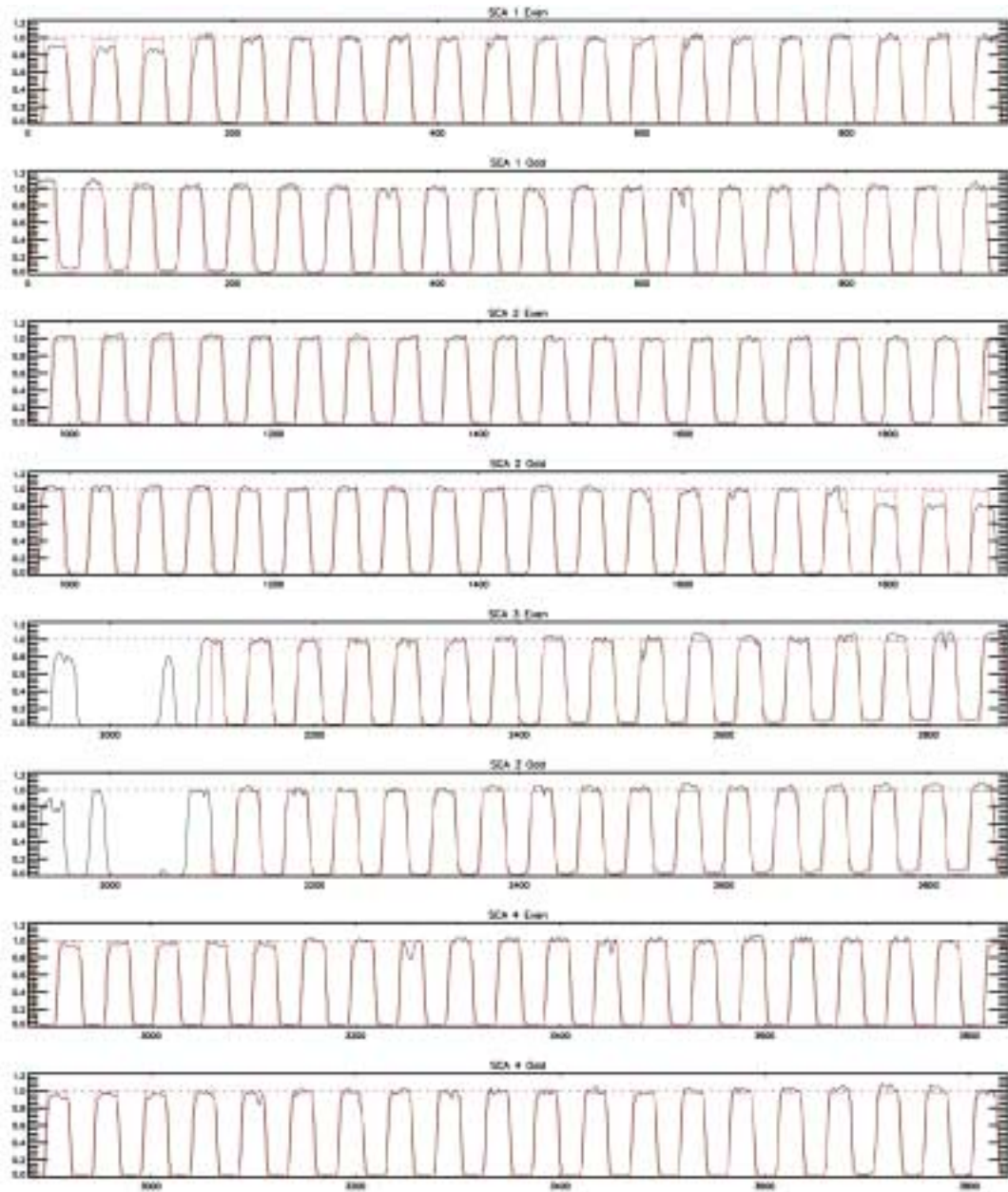
Figure 3-45. Measured detector signals and modeled signals (in red) for the Pan Band, 59.47° Ronchi orientation.

The focal length of the ALI telescope can not be determined from the image fits independently of the collimator focal length. The fits can only tell us that the ratio of the ALI focal length to the collimator focal length is 0.63445. If we use the design value of the collimator focal length, which is 1485.94 mm, then the ALI focal length is 942.761 ± 0.003 mm. Theodolite

3-57

measurements of the ALI telescope indicated a focal length of 942.436 ± 0.005 mm. The discrepancy between these two values probably arises from an error of 0.5 mm in the collimator focal length. Analysis of images from on-orbit operations may permit a refinement of the ALI focal length determination.

Distortion polynomial coefficients for the linear terms in X and Y are highly correlated with the telescope focal length. We have generally fixed those terms at zero. The telescope however, could be anamorphic. In the final analysis, the in-track (X) distortion term linear in X position was left free.

To visualize the meaning of the parameters resulting from the fit to the Ronchi images, plots have been constructed to show the vector difference between actual LOS positions on the focal plane and corresponding ideal LOS positions in the absence of distortions or alignment errors. The scales of the vectors are much larger than the position scales, and are generally indicated by drawing a multispectral detector at the scale of the vectors. There is excellent agreement between the subsystem measurement and the Ronchi fit.

Figure 3-46 is a plot showing only the region of the focal plane near the MS/Pan array. It shows locations of the detector rows, the offsets of the SCA's, and the optical distortion field, all at the same scale, indicated by the 40 µm square detector "pixel." The offsets of the SCA's from their nominal locations are shown as vectors. The origins of the SCA vectors are at the positions of fiducial marks. The black arrows are from the subsystem measurement, and the red arrows resulted from the end-to-end fit.
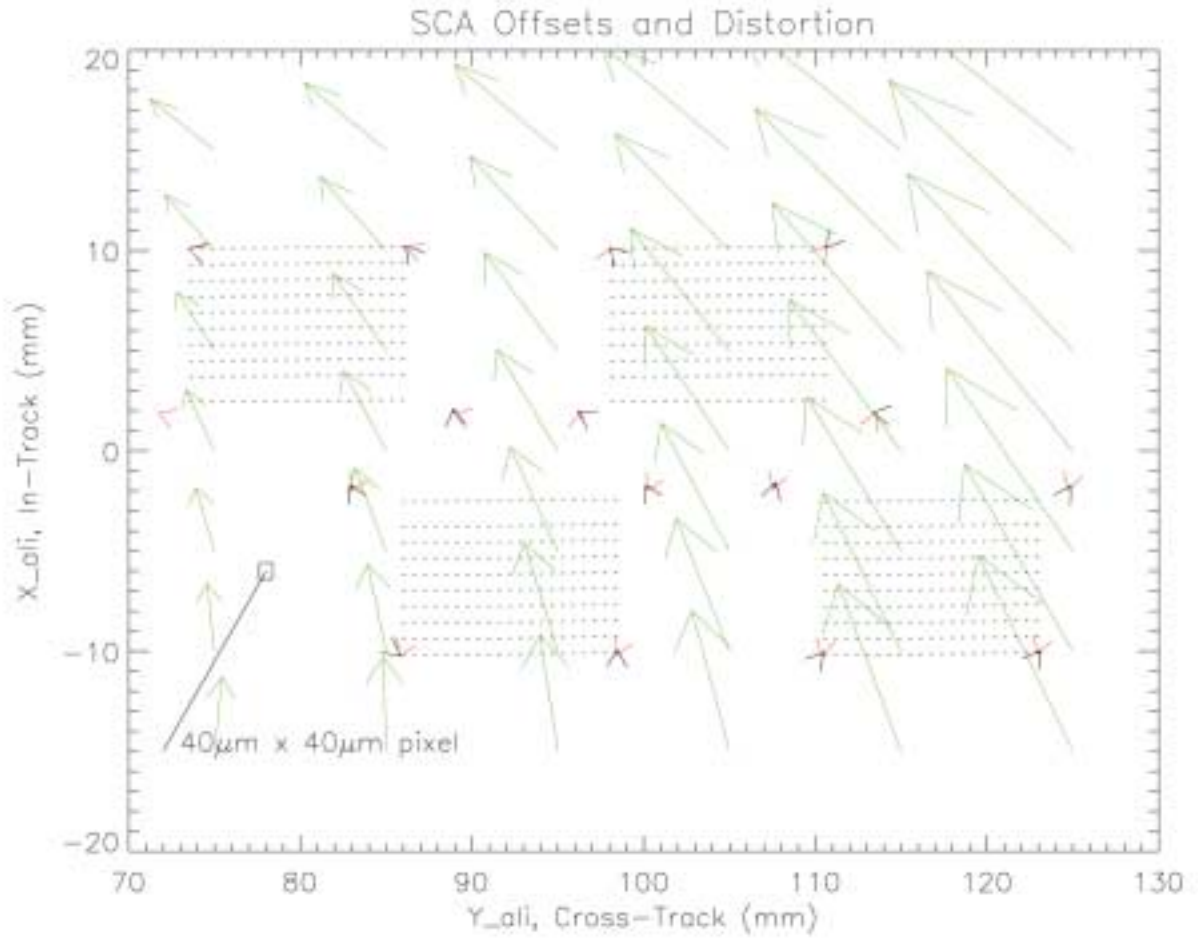
Figure 3-46. Vector plot of the MS/Pan end of the focal plane.

3.1.2.2.3 Detector Line-of-Sight Map

The end product of our line-of-sight calibrations is a data file to be used for the reconstruction of ALI images. An IDL procedure was developed to read the output data from the end-to-end parameter fitting procedure, and apply those parameters to reconstruct the LOS of every detector. The LOS map file lists the ALI focal length, and the *apparent* positions of the detectors on the ALI focal plane, in units of millimeters. The angular lines of sight are constructed as vectors. For example, given a detector position (x_d, y_d) on the focal plane, the corresponding (non-normalized) line-of-sight vector is $(-x_d, -y_d, f_{ALI})$. Such vectors are used in image reconstruction and geo-referencing procedures.

3.1.2.3 Reference Cube Alignment

The end-to-end measurements described in the preceding sections provided the detector lines of sight relative to the ALI telescope axes. This section describes the measurements made on the ALI instrument to determine the angular relationships of the telescope axes relative to the external reference cube. That cube is mounted on the ALI pallet, and is intended to provide an angular reference during satellite integration for alignment with the inertial reference unit and the other optical instruments.

All measurements took place with the ALI in a fixed position in the clean room. It was placed on the Flotron fixture under the Class 100 hood, with the *X*-axis pointing down and the *Z*-axis horizontal. The reference cube was approximately 43 inches above the floor, and the center of the entrance pupil approximately 51 inches from the floor.

Equipment used for these measurements included an electronic autocollimating theodolite (Zeiss model Eth 2), a sturdy tripod for the theodolite, a 12-inch flat mirror in a gimbaled mount, and a stable portable platform for the mirror. A pair of Maglite flashlights were also mounted to a bar supported on a tripod in front of the theodolite in order to illuminate the focal plane. A plan view of the equipment positions is shown in Figure 3-47.
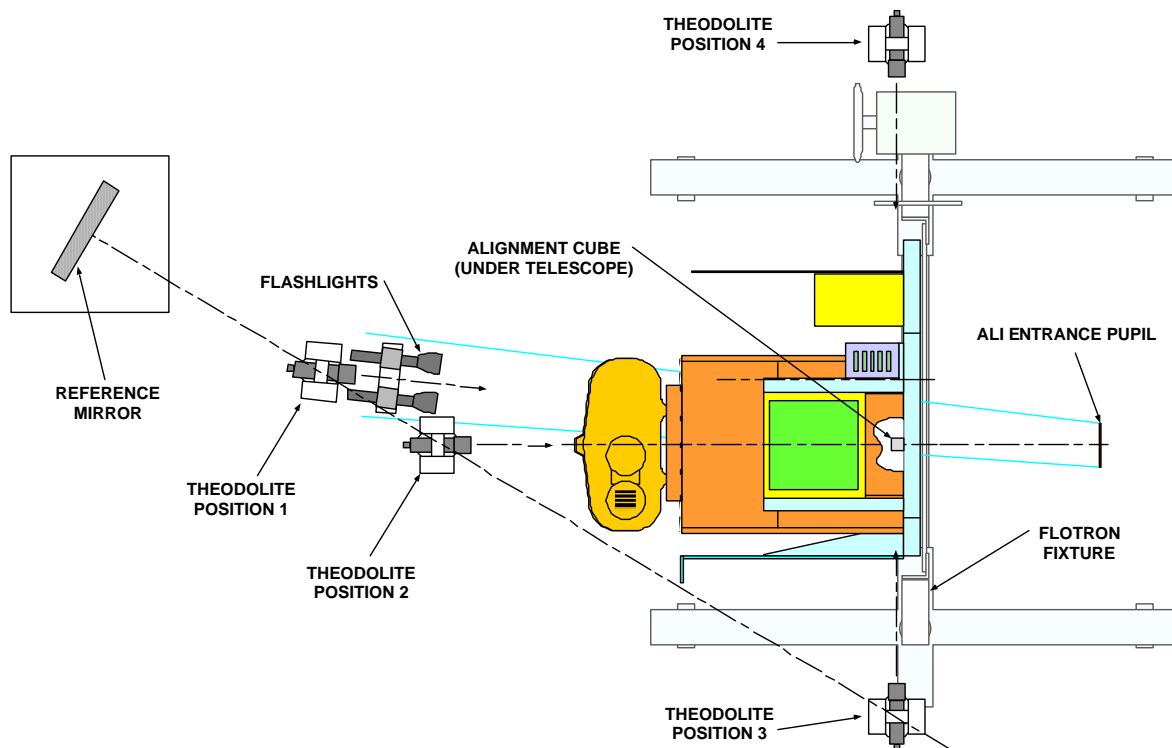

Figure 3-47. Plan view of clean room setup to measure alignment of the ALI reference cube

There were four distinct positions of the theodolite. Positions 1, 2, and 3 were along a line normal to the center of the reference flat mirror, which was kept in a fixed position. The detectors were sighted from position 1. The front of the reference cube was sighted from position 2, and the right side of the cube from position 3. The left side of the cube was sighted from position 4.

In position 1, the focal plane was sighted through the telescope. Each end of the Pan array of each SCA was measured. From positions 2, 3, and 4, the reference cube was measured in autocollimation. In positions 1, 2, and 3, the fixed reference mirror was also measured in autocollimation. This provides an azimuth reference for those measurements. All elevation measurements are referred to the local vertical, which is automatically determined by the theodolite to an accuracy of 0.5 arc seconds. The azimuth accuracy is the same as for the elevation axis. Experience of the operators has shown that sightings of the same target are repeatable to approximately ± 1 arc second.

For the purpose of alignment, the frame of reference for the detector lines of sight is defined as follows: The *Z*-axis is the normal to the +*Z* face of the reference cube. The *Y*-axis is in the plane determined by this normal and the normal to the +*Y* face of the cube (which is orthogonal to the +*Z* normal to within 1 arc-second). The *X*-axis is orthogonal to the other two, forming a right-handed coordinate system.

Since the ALI was not situated with its *X*-axis exactly vertical during the present measurements, the angular readings had to be transformed to the cube frame of reference. Angular readings are first converted into vectors in the laboratory frame. The vectors in the laboratory frame were transformed to the reference cube frame by a rotation matrix. Application of the rotation matrix to the sighting vectors results in the cube-referenced vectors as listed in TABLE 3-12. For convenience, the corresponding azimuth and elevation angles are listed as well.

TABLE 3-12

Direction Vectors in the Cube Frame

Vectors	Reference Axis			Angles (degrees)	
	X	Y	Z	Azimuth	Elevation
Pan Points					
1 Right	-0.003259	-0.133084	0.991099	7.6479	-0.1867
1 Left	-0.003270	-0.119690	0.992806	6.8743	-0.1873
2 Right	-0.008552	-0.120270	0.992704	6.9080	-0.4900
2 Left	-0.008561	-0.106914	0.994231	6.1377	-0.4905
3 Right	-0.003295	-0.107339	0.994217	6.1620	-0.1888
3 Left	-0.003309	-0.093965	0.995570	5.3918	-0.1896
4 Right	-0.008577	-0.094509	0.995487	5.4233	-0.4915
4 Left	-0.008586	-0.081046	0.996673	4.6488	-0.4919
Cube Faces					
+Z	0.000000	0.000000	1.000000	0.0000	0.0000
+Y	0.000000	1.000000	0.000000	-90.0000	0.0000
-Y	0.000052	-1.000000	-0.000035	90.0020	0.0030

The positions sighted on the focal plane through the theodolite are all within the MS/Pan detector array, and do not correspond with the axes of the ALI telescope. In contrast, the *relative* lines of sight derived from the end-to-end Ronchi images are based on the telescope axes. We next needed to relate the telescope axes to the ALI reference cube axes.

We see in TABLE 3-12 a set of eight vectors called "Pan points." These correspond with relative lines of sight of detectors at the ends of the Pan array of each SCA. From the LOS map file, we take the Y (cross-track) position of each end detector, and the average X (in-track) position of the odd and even end detectors to be the nominal sighted location. Using the fitted telescope focal length, the eight unit LOS vectors in the telescope frame were constructed. They are listed in TABLE 3-13.

TABLE 3-13

Direction Vectors in the Telescope Frame

Vectors	Optical Axis		
	X	Y	Z
Pan Points			
1 Right	0.003131	-0.129842	0.991530
1 Left	0.003046	-0.116589	0.993176
2 Right	-0.002232	-0.117034	0.993125
2 Left	-0.002322	-0.103737	0.994602
3 Right	0.002957	-0.104093	0.994563
3 Left	0.002883	-0.090775	0.995867
4 Right	-0.002385	-0.091222	0.995828
4 Left	-0.002463	-0.077870	0.996960

Vectors in the telescope frame should be related to vectors in the cube frame by a three-dimensional rotation of coordinates. To within measurement uncertainties, all eight vector pairs should be related by the same transformation. We employed matrix algebra to find a least-squares solution for the rotation matrix R that performs that transformation:

$$R = \begin{pmatrix} 0.99915 & 0.00558 & -0.00570 \\ 0.00544 & 1.00072 & -0.00315 \\ 0.00689 & 0.00334 & 0.99999 \end{pmatrix}. \tag{1}$$

The R matrix is an approximation to the matrix for the small rotation from the telescope frame to the reference-cube frame. It represents small rotations about the *X*, *Y*, and *Z* axes, respectively. Let us call the three rotation angles α, β and γ. In spacecraft terms, these angles represent roll, pitch, and yaw, respectively. We find the following estimates for the three angles:

$$\alpha = \text{-}0.186 \pm 0.005 \text{ degees}$$

$$\beta = 0.361 \pm 0.034 \text{ degees}$$

$$\gamma = 0.004 \pm 0.316 \text{ degees}$$

The uncertainty in γ is much greater than for the other two angles, because that angle represents the rotation about the telescope axis, and the two ends of the MS/Pan array that was measured

with the theodolite are separated by only 3°. Uncertainty in that angle also leads to greater uncertainty in the β angle about the Y (elevation) axis.

Finally, we construct a rotation matrix to transform vectors from the telescope frame to the reference cube frame:

$$\text{DCB} = \begin{pmatrix} 0.99998 & 0.00007 & -0.00630 \\ -0.00009 & 0.99999 & -0.00324 \\ 0.00630 & 0.00324 & 0.99997 \end{pmatrix}. \qquad (2)$$

The three column vectors of the DCB rotation matrix represent the X, Y, and Z axes of the ALI telescope in the frame of the reference cube. This rotation matrix must be applied the detector LOS vectors to express them also in the reference cube frame.

3.1.2.4 Sample Images

In this section, we present a representative sampling of reconstructed ALI images. They have been system-corrected, using the radiometric and line-of-sight calibrations of the detectors, as described previously. The images are not geo-referenced, however. The images as shown here are selected from the JPEG-compressed browse image files. In our routine processing, the possible range of in-band radiances for each band is looked up, based on the solar zenith angle for the observation. For multispectral images, three bands are selected to be shown as red, green, and blue. True-color images use bands 3, 2, and 1 for the RGB triad. In order to bring out surface details with good contrast, but retain the wide dynamic range inherent in the data, a logarithmic scaling is applied for the 24-bit JPEG output. The radiances for 0% and 100% diffuse surface reflectance are used as scaling parameters for each selected color in the JPEG file. In this way, white surfaces (e. g. clouds) appear white in the browse images. The JPEG file can be opened in any good image-editing program, such as Adobe PhotoShop. We often make minor adjustments with the PhotoShop "Image > Adjust > Levels…" command, to further enhance surface detail, sometimes allowing bright clouds to saturate.

The first scene acquired by the ALI was of Alaska, just north of Anchorage, on November 25, 2000. It is shown in Figure 3-48. The solar zenith angle was approximately 85° for this data collection event. As a result, there is a very wide range of radiances in the scene, from the shadows to the snow-covered slopes facing the sun. The resolution and dynamic range of the ALI are brought out by the portion of the panchromatic image of Sutton seen in Figure 3-49.

Another panchromatic image is presented in Figure 3-50. It shows the downtown portion of Washington, D. C. The shadow of the Washington Monument is clearly visible in this image. A similar panchromatic image of Boston appears in Figure 3-55

Figure 3-51 and Figure 3-52 show two typical presentations of an ALI image of Cape Canaveral, Florida Figure 3-51 is the true-color image, and Figure 3-52 shows bands 4, 3, and 2 in false color. This selection is often used, since it highlights healthy vegetation in red. Additional true-color images are seen in Figure 3-53 (Yuma, Arizona) and Figure 3-54 (Oahu, Hawaii).

Figure 3-48. True-color image of Sutton, AK and the Matanooska River valley.

Figure 3-49. Selected portion of the panchromatic image of Sutton, AK

Figure 3-50. Panchromatic image of Washington, D. C.

Figure 3-51. True-color image of Cape Canaveral.

Figure 3-52. False-color image of Cape Canaveral. The red, green and blue components represent bands 4, 3, and 2, respectively. Healthy vegetation appears red.

Figure 3-53. True-color image of Yuma, Arizona and the Colorado river.

Figure 3-54. True-color image of Oahu, Hawaii

Figure 3-55. Panchromatic image of Boston.

In Figure 3-56, we present images of Lake Frome, South Australia in several different band selections. In the true-color image (bands 3-2-1), the dry lake bed appears in very light shades of gray. The SWIR bands 7-5-5' however, show dramatic variations as shades of blue, probably indicating the presence of water just below the surface.
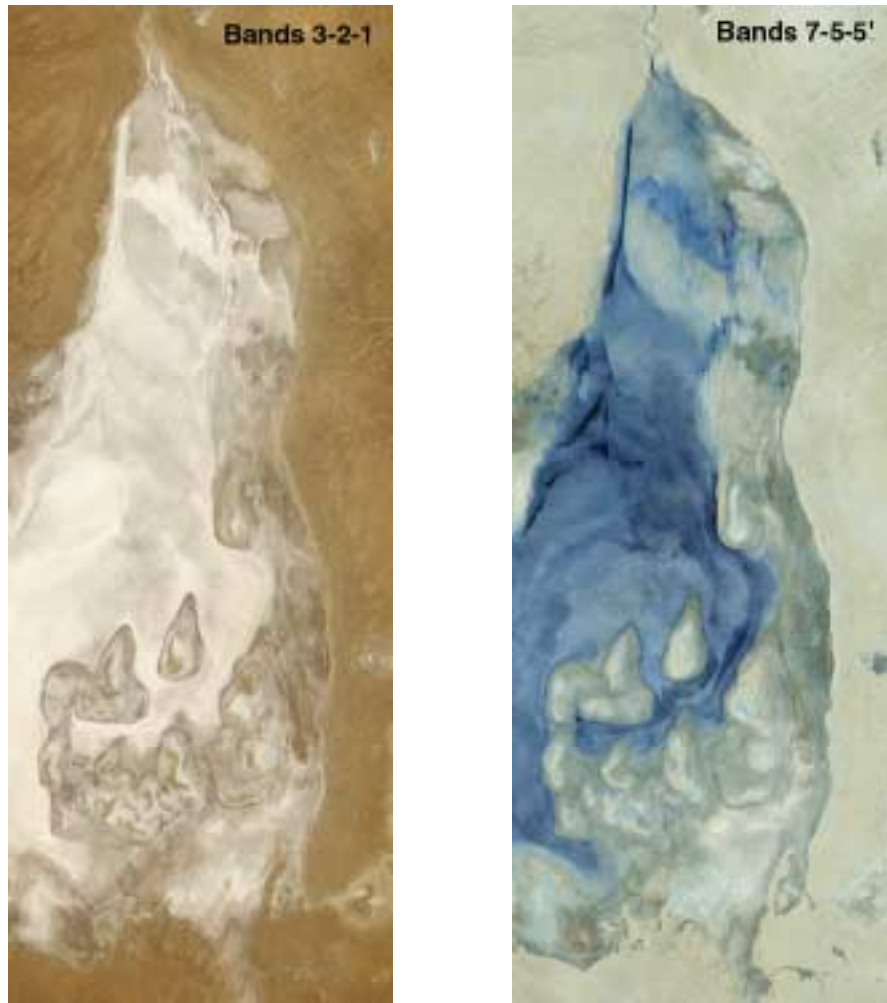
Figure 3-56. Multispectral images of Lake Frome, South Australia. The spectral bands represented by red, green, and blue, respectively, are indicated at the top of each image

Water in various forms appears in 3-57, which shows two views of Antarctica, near McMurdo Sound. In the true-color image on the left, it is difficult to distinguish snow, ice, and clouds. In the SWIR band image on the right however, snow and ice appear in shades of blue, while the clouds are white. A glacial stream appears distinctly darker, showing much less reflectance at the longer wavelengths.
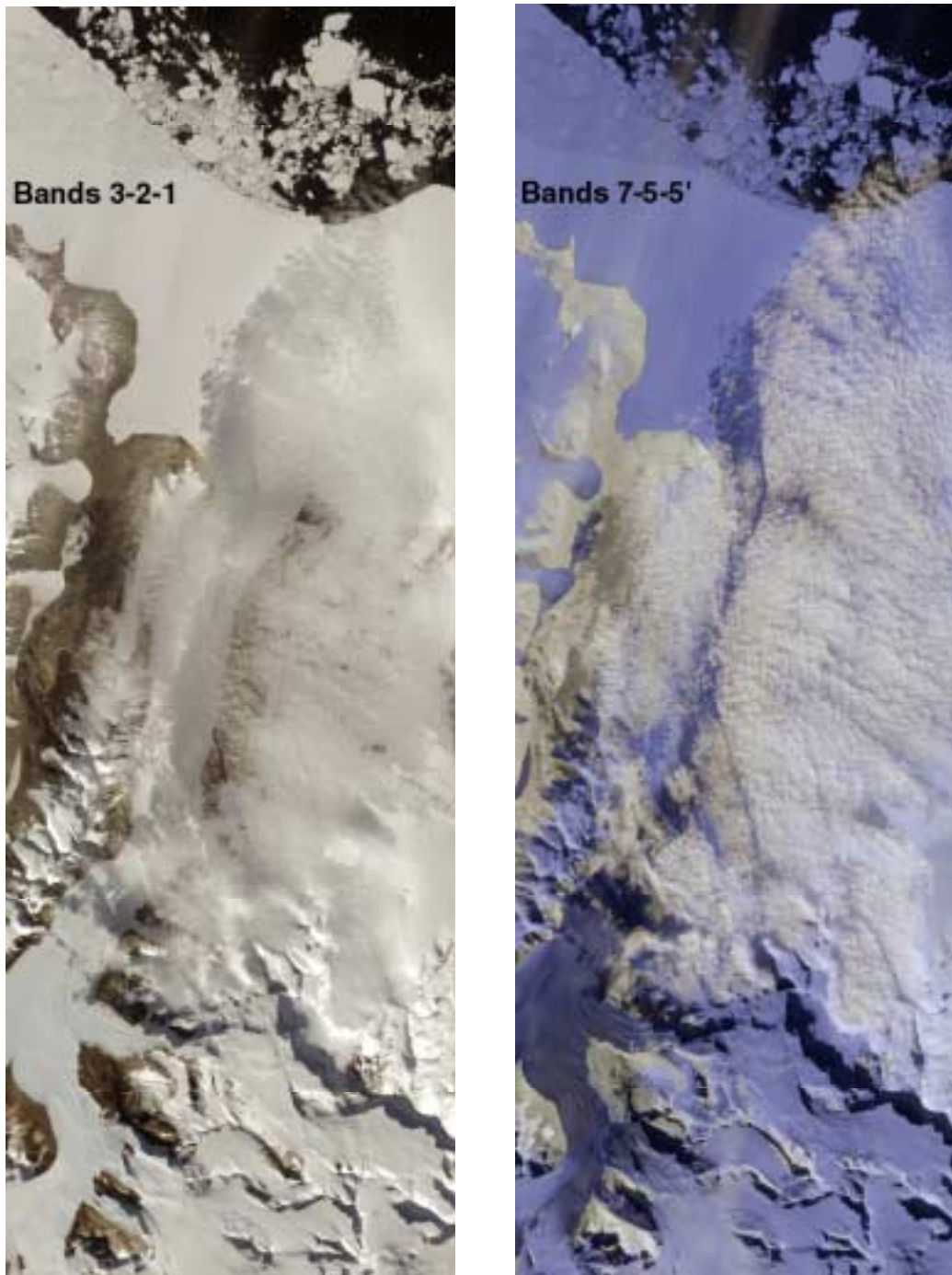
Figure 3-57. Multispectral images of Antarctica, near McMurdo Sound. A true-color image (bands 3-2-1) is on the right. The image on the left of the short-wave infrared bands clearly distinguishes snow, ice, and clouds.

3.1.3 Spectral Calibration

Included in the ALI ground calibration period was the system level spectral characterization of one of four focal plane Sensor Chip Assemblies (SCAs). This section provides a review of the techniques employed during spectral calibration and the results for the VNIR, SWIR and Panchromatic bands. These results are compared to subsystem measurements obtained before the instrument was assembled. Additional information may be found in the MIT/LL EO-1-2 project report.[18]

Table 3-14:
Spectral and spatial definitions for the ten EO-1 ALI bands.

Band	Wavelength (µm)	Ground Sampling Distance (m)
Pan	0.48 – 0.69	10
MS-1p	0.433 – 0.453	30
MS-1	0.45 – 0.515	30
MS-2	0.525 – 0.605	30
MS-3	0.633 – 0.69	30
MS-4	0.775 – 0.805	30
MS-4p	0.845 – 0.89	30
MS-5p	1.2 – 1.3	30
MS-5	1.55 – 1.75	30
MS-7	2.08 – 2.35	30

3.1.3.1   Focal Plane Construction

The spectral bands for each multispectral channel are defined by filters lying above the silicon and HgCdTe detectors. A cross sectional view of an individual SCA is provided in Figure 3-58 and a table of materials used in the filters is provided in Table 3-15. A three-piece sandwich design is used to construct the filters for bands 1p, 1, 2, and the panchromatic band. All other band filters use a single glass design. All glass segments are cemented together using Epotek 301 and the ten filters together form an assembly, which resides in a bezel, mounted directly above the detector arrays.
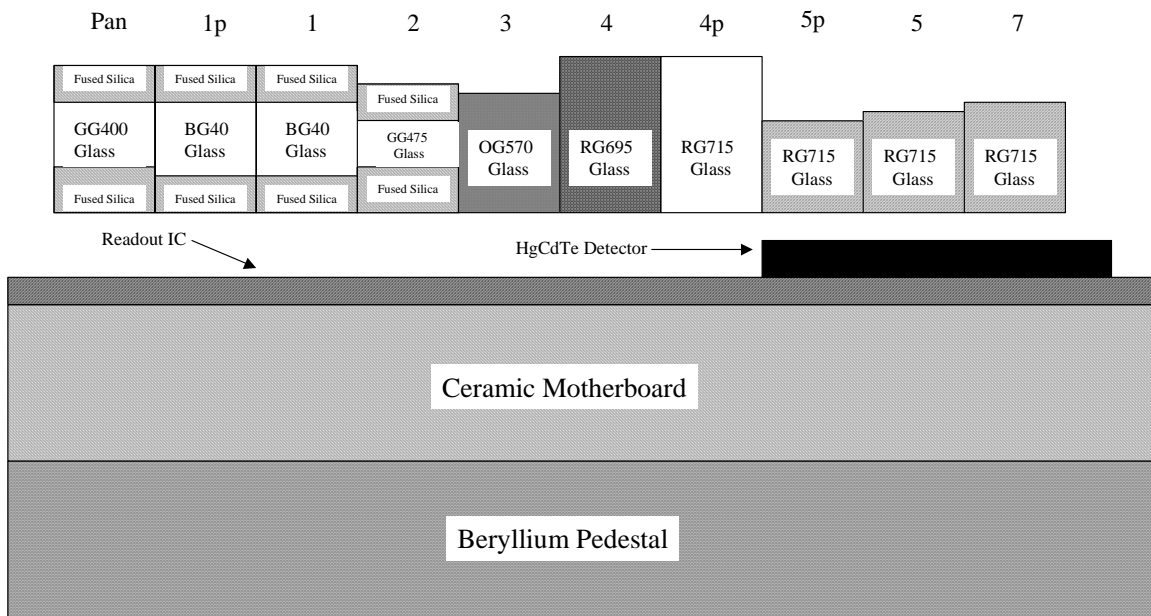
| Pan | 1p | 1 | 2 | 3 | 4 | 4p | 5p | 5 | 7 |

Fused Silica	Fused Silica	Fused Silica							
GG400 Glass	BG40 Glass	BG40 Glass	Fused Silica						
			GG475 Glass	OG570 Glass	RG695 Glass	RG715 Glass	RG715 Glass	RG715 Glass	RG715 Glass
Fused Silica	Fused Silica	Fused Silica	Fused Silica						

Readout IC

HgCdTe Detector

Ceramic Motherboard

Beryllium Pedestal

Figure 3-58. Focal plane array Sensor Chip Assembly cross-section.

Table 3.15:
Materials used for focal plane filter construction.

Band	Material
Pan	Fused Silica + GG400
1p	Fused Silica + BG40
1	Fused Silica + BG40
2	Fused Silica + GG475
3	OG570
4	RG695
4p	RG715
5p	RG715
5	RG715
7	RG715

3.1.3.2   Spectral Response Measurement Techniques

Spectral calibration of the Advanced Land Imager was conducted on both the subsystem and the system level.

3.1.3.2.1   Subsystem Level

The predicted system level spectral response for each band has been calculated analytically as the product of the spectral responses of individual ALI optical components. Component level spectral characterizations include measurements of witness sample detector responsivities by the Santa Barbara Research Center (now the Ratheon Infrared Center of Excellence), filter transmissions by Barr Associates, and M1-3 and F1 mirror reflectivities by SSG Incorporated.

3.1.3.2.2   System Level

System level spectral calibration of the fully assembled flight instrument was performed at Lincoln Laboratory under vacuum and operating at expected flight temperatures. A spectral collimator was used to project a monochromatic beam into the vacuum tank via a quartz window. Data were collected from 400 nm to 2500 nm to map both in-band and out-of-band response for pixels in each of the multispectral and panchromatic bands of SCA 3.

The collimator used during system level spectral characterization of the ALI may be divided into three sections: source, collimating optics, and beam monitor (Figure 3-59) The source is composed of a quartz tungsten halogen lamp assembly, monochromator, integrating sphere, and condensing lens. The halogen lamp assembly provides a stable broadband source and is used to fill the f/4 entrance cone of the monochromator. The wavelength and spectral bandwidth passed through the system are defined by the order sorting filters, diffraction gratings and slit widths of the *Oriel* MS257 monochromator. Upon exiting the monochromator, the beam was randomized into a uniform 0.5" diameter spot using a 2" diameter (I.D.) *Labsphere Spectralon* integrating sphere. A condensing lens (01 LPX 245) was positioned to expand the output of the integrating sphere and provide a 3" diameter field for calibration.
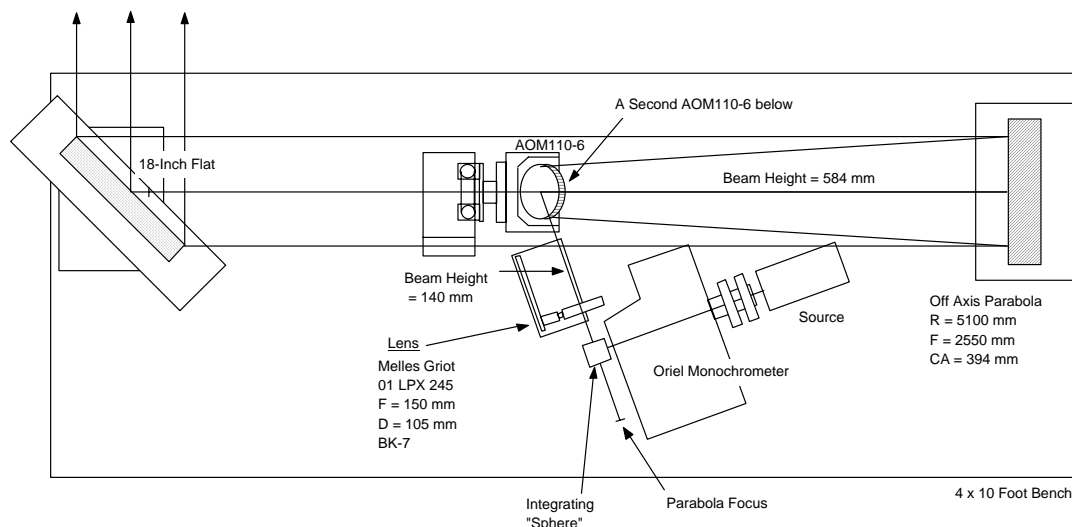
Figure 3-59: Collimator used during spectral calibration of the EO-1 Advanced Land Imager.

The primary component of the spectral collimating optics was a 17" diameter, 100" focal length off-axis parabola. This mirror was mounted such that its focus was colocated with the virtual image of the integrating sphere output formed by the condensing lens. Collimated radiation reflected from the parabola was directed into the vacuum tank window using a large (18" diameter) flat mirror. A light tent was positioned around the spectral collimator and an intricate baffling scheme was adopted to prevent stray light from contaminating the dim monochromatic output for this measurement.

The collimator also contained two reference detectors, used to monitor the beam stability and flux throughout spectral calibration of the instrument: a silicon detector for VNIR measurements and a lead sulfide detector for SWIR measurements. Each detector, located between the 18" flat mirror and the vacuum tank window, was chopped and a lock-in amplifier was used to accurately subtract dark current drift and background radiation.

System level spectral calibration data were collected in December 1998 and January 1999 in a class 1,000 clean room at Lincoln Laboratory. This calibration was conducted with the ALI as a fully assembled instrument in a thermal vacuum chamber at operational temperatures.

A DELL 266 MHz PC (Windows 95 platform) controlled the monochromator scanning and beam sampling using a GPIB interface and LabVIEW control software. For visible near infrared (VNIR) measurements (400-1000 nm) a spectral bandwidth and sampling interval of 2 nm was used. For short wave infrared (SWIR) measurements (1000-2500 nm) a spectral bandwidth and sampling interval of 4 nm was used.

Data collection consisted of iteratively sampling the beam with the reference detector and the ALI at each wavelength interval. Initially, a wavelength and bandpass are set by the monochromator. A translation stage then positions the silicon or lead sulfide detector and chopper between the18" flat mirror and vacuum tank window. After sampling the beam, the detector is moved to an out-of-beam position. All bands of the ALI then sample the monochromatic beam. Finally, a filter wheel, acting as a shutter between the light source and monochromator, blocks the incident beam to provide a dark ALI reference for each spectral sample.

3.1.3.3   Analysis

3.1.3.3.1   Subsystem Level

The generation of system level spectral response functions based on component level measurements must account for all elements that affect the response of an assembled instrument: mirror reflectivities, filter transmissions, and detector responsivities. Reduced witness sample data for each of these components were provided by each manufacturer as a part of MIT/LL quality control during instrument construction. Five VNIR and sixty SWIR detector responsivity measurements, 20 nm interval mirror reflectivity measurements, and 0.5 and 1nm interval filter transmission measurements were used in this analysis. Each of these data sets was interpolated onto a 1nm spectral sampling interval and the overall system level performance was calculated for each band as the product of component measurements as a function of wavelength, normalized to unity at the peak response.

3.1.3.3.2   System Level

Analysis of the ALI system level spectral calibration data was conducted at Lincoln Laboratory and centered on the normalization of a given pixel's response (dn) to account for beam intensity and vacuum tank window transmission artifacts as a function of wavelength (λ). Initially, the ALI pixel response is offset corrected by subtracting dark scene values for each wavelength. A plot of spectral transmission versus wavelength is then generated for a given pixel by accessing data for a particular spectral calibration run and the wavelengths covered at that time. Artifacts induced by the vacuum tank window are then removed by dividing the pixel's spectral response by the window's previously measured spectral transmission. Next, the varying intensity of the incident beam as a function of wavelength is accounted for by dividing the pixel spectral response by the beam intensity measured at each wavelength by the silicon or lead sulfide detectors. Finally, the spectral response of the reference detector itself is removed by dividing the beam intensity measurement by the detector's responsivity for the spectral range of interest. The above technique may be shown analytically using the following relation

$$S_P(\lambda) = \frac{A_P(dn, \lambda)\, R_d(\lambda)}{T_W(\lambda) F(\lambda)}.$$

Here, $S_P(\lambda)$ is the derived spectral response for pixel P as a function wavelength λ, $A_P(dn,\lambda)$ is the ALI focal plane response for pixel P as a function of wavelength , $T_W(\lambda)$ is the spectral transmission of the vacuum tank window, and $F(\lambda)$ is the measured reference detector response to the beam as function of wavelength. $R_d(\lambda)$ is the spectral responsivity of the detector used to measure the beam.

Once the above corrections are applied, the resulting spectral response function for a given pixel is normalized to unity at the peak response. Responses for 200 pixels are then averaged and compared to the theoretical spectral response of the ALI (generated from the component measurements).

3.1.3.4   Results

We have measured the system level spectral response function for each ALI VNIR, SWIR and panchromatic band. Figures 3-60 to 3-69 compare the measured spectral response functions near band cut-on and cut-off wavelengths to the theoretical response functions generated from component level measurements. We find excellent morphological agreement (<5% near peak transmissions) for all bands. The panchromatic band (Figure 3-69) in particular reveals good agreement between system and component level measurements despite intricate variability across this band's spectral bandpass. We also find the cut-on and cut-off wavelengths agree with subsystem level measurements to within 1 nm for VNIR bands and 2 nm for SWIR bands.
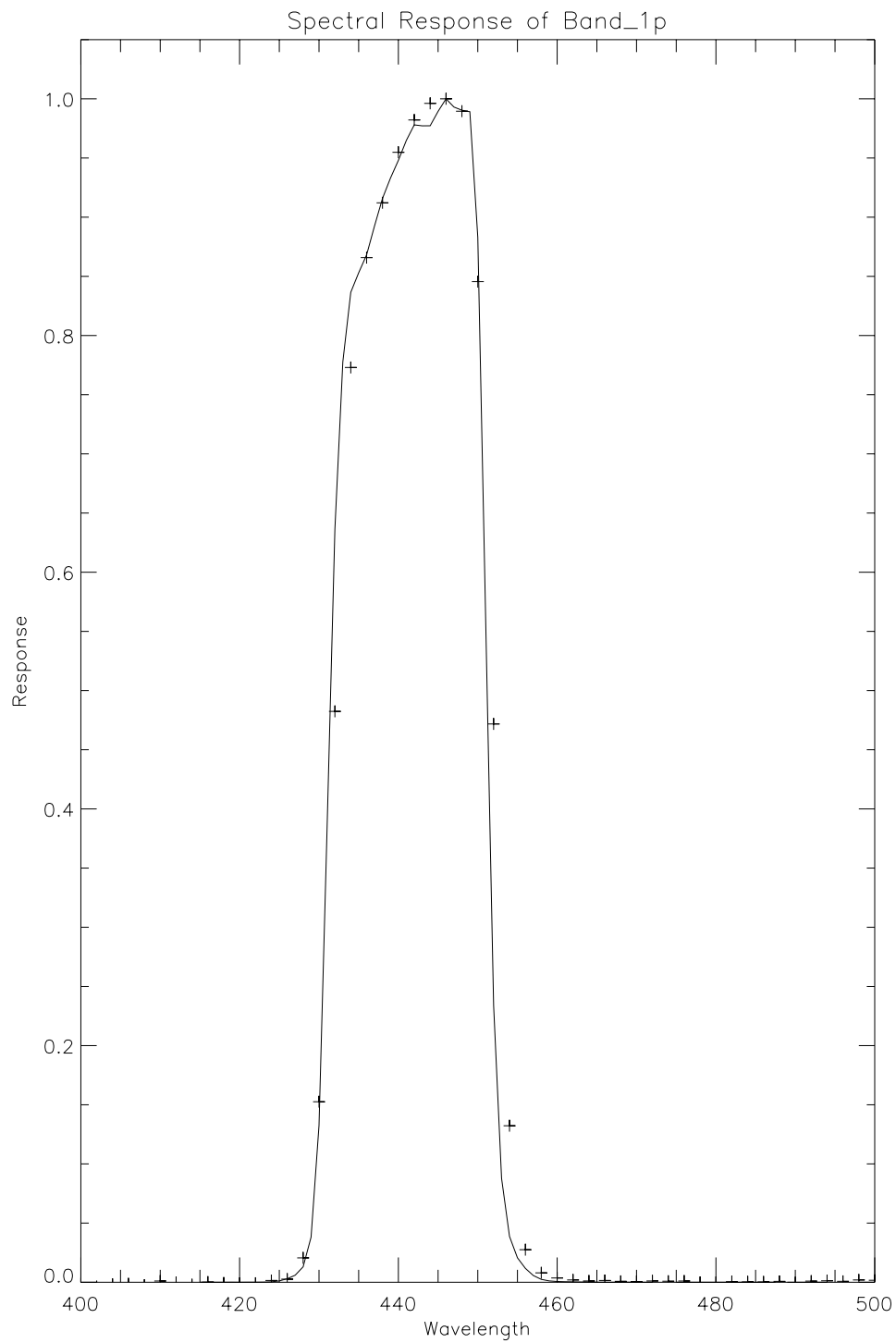
Figure 3-60. Spectral response of band 1p. The crosses represent the mean system level measured response for 200 pixels. The solid line represents data collected during subsystem level measurements.
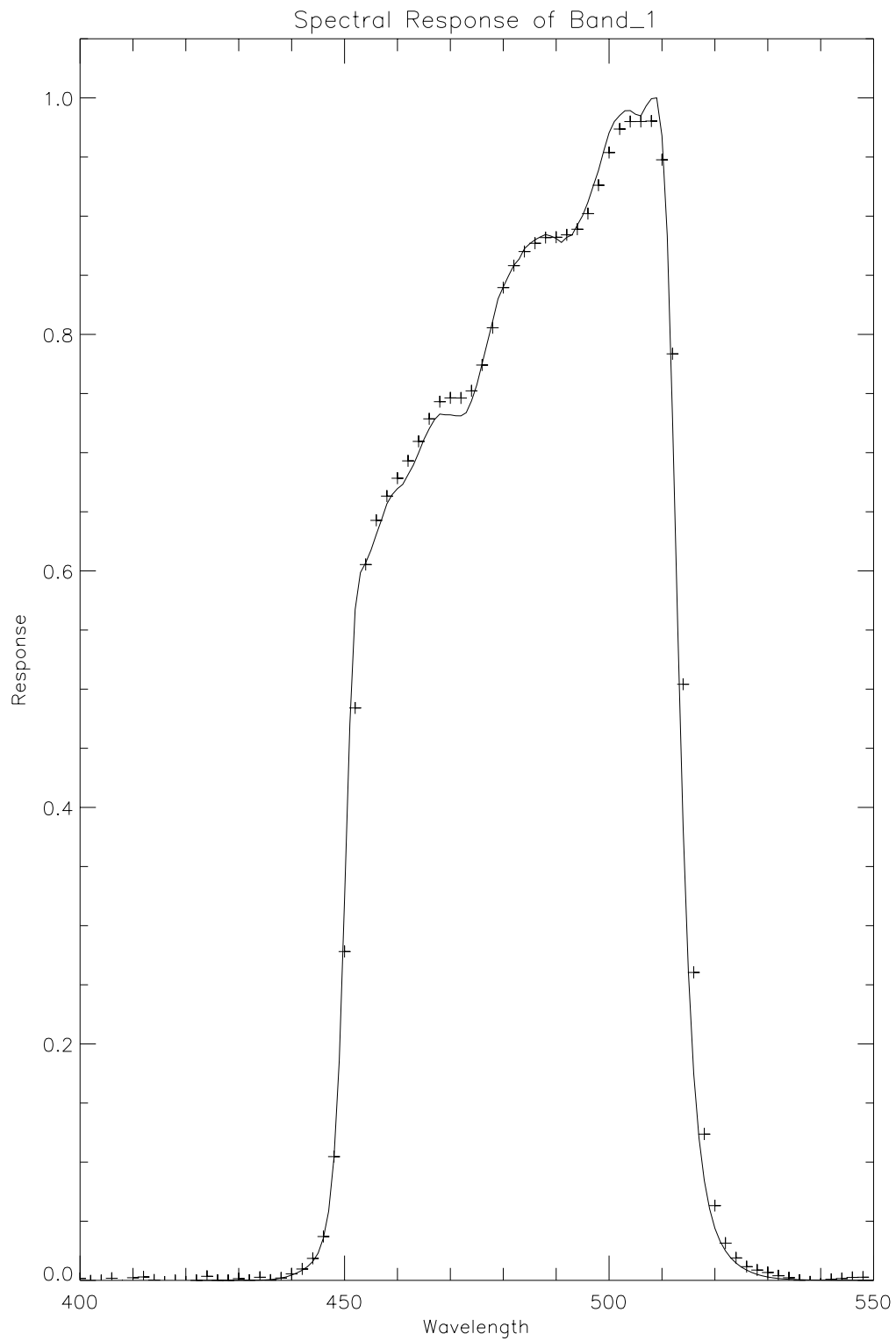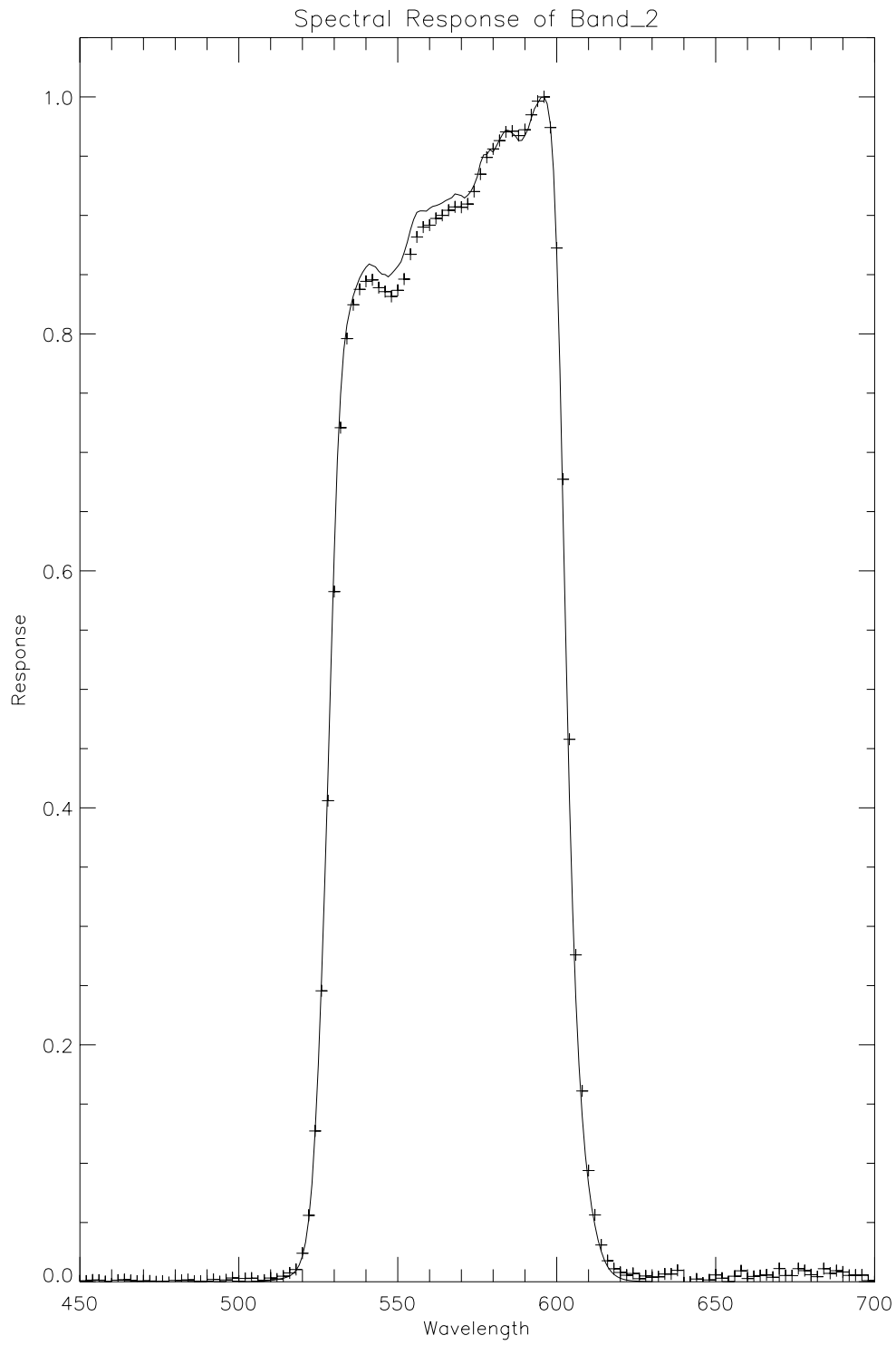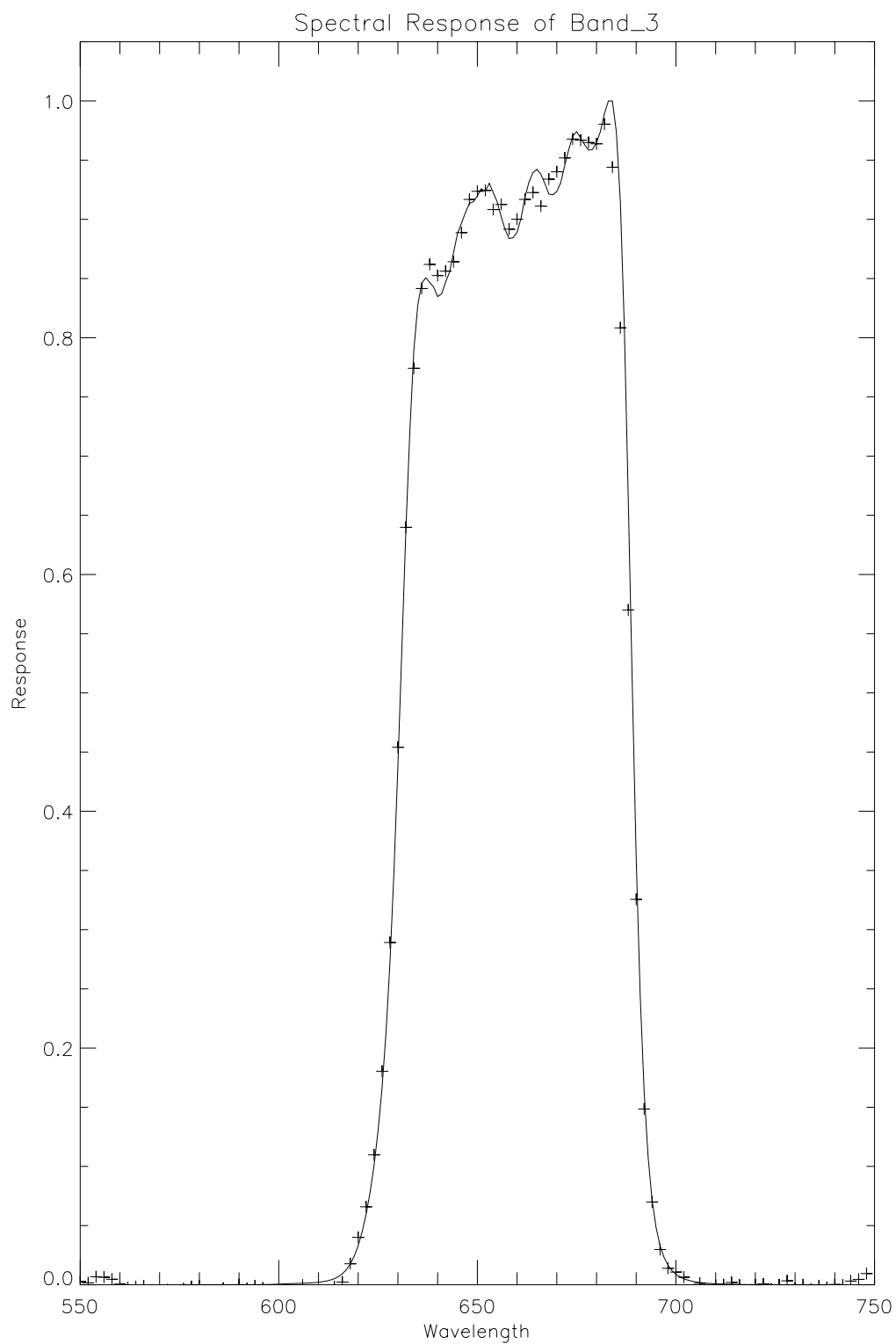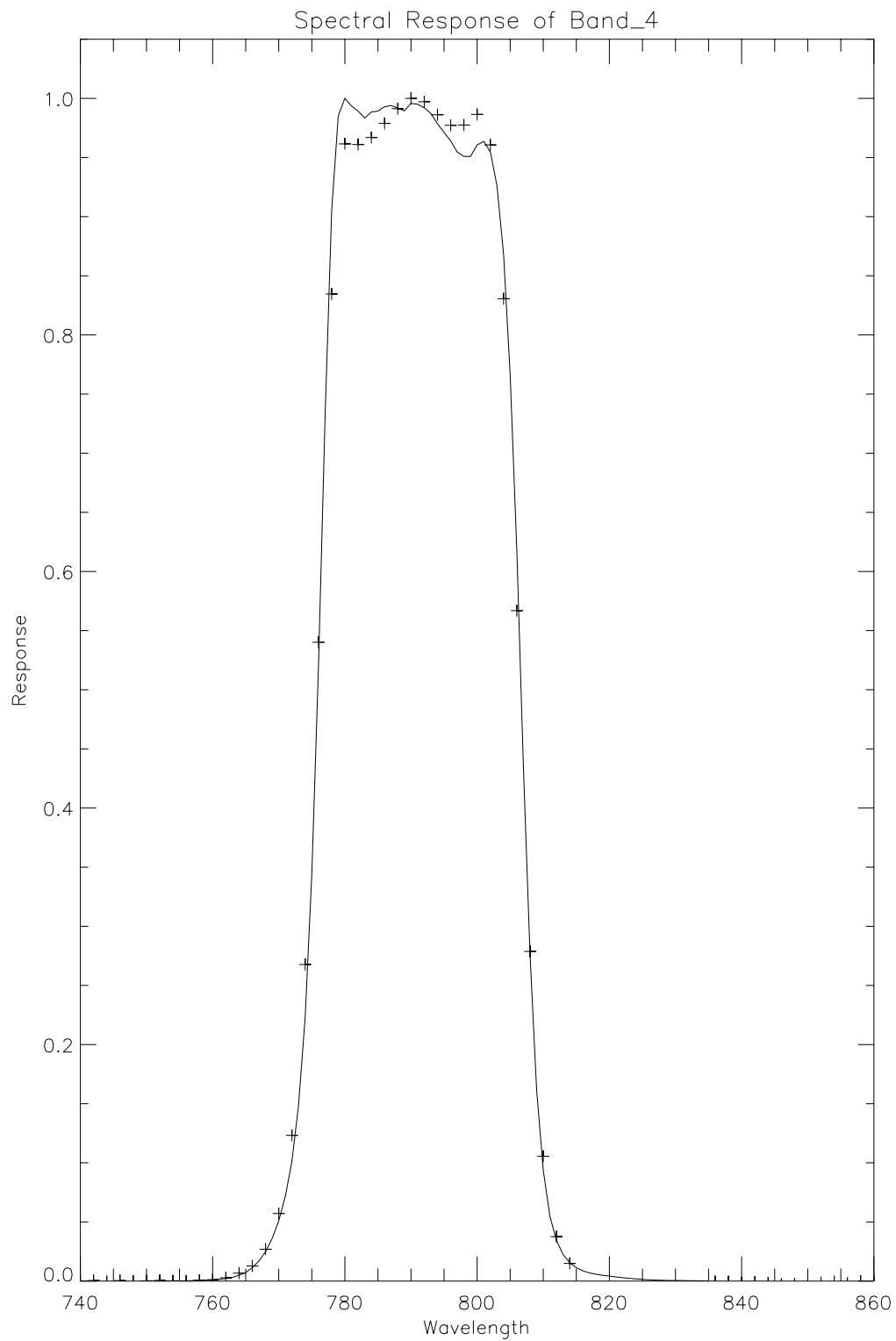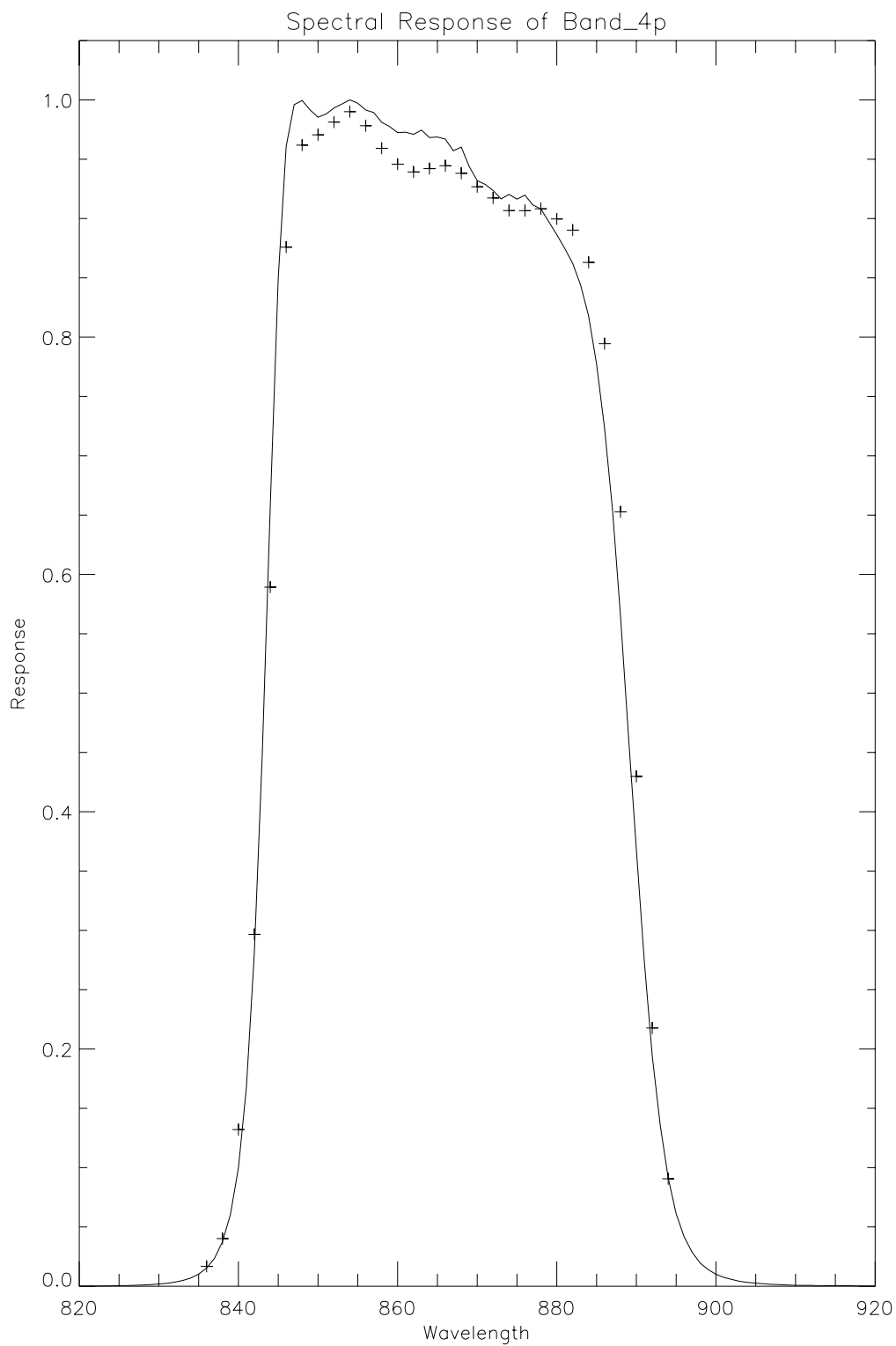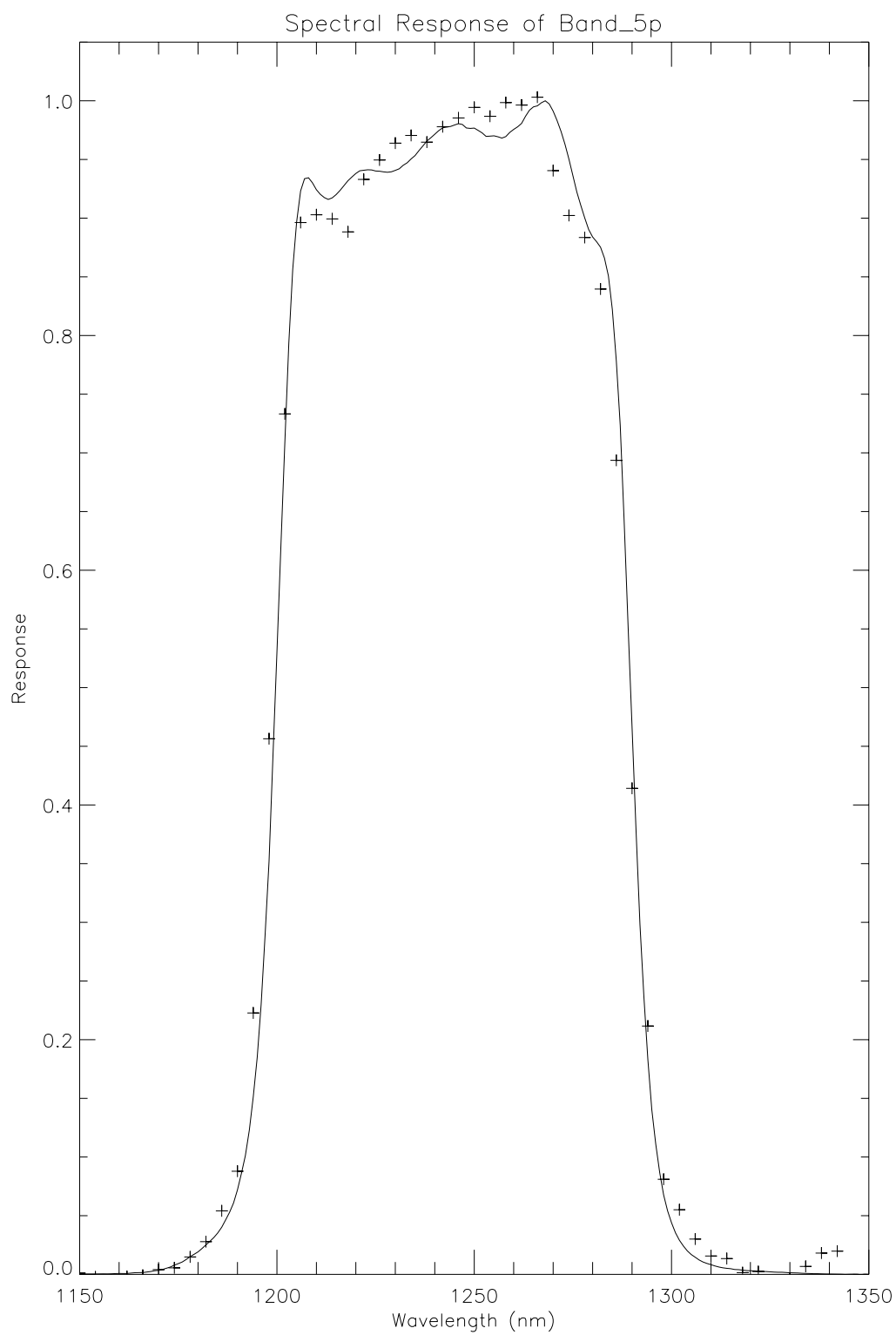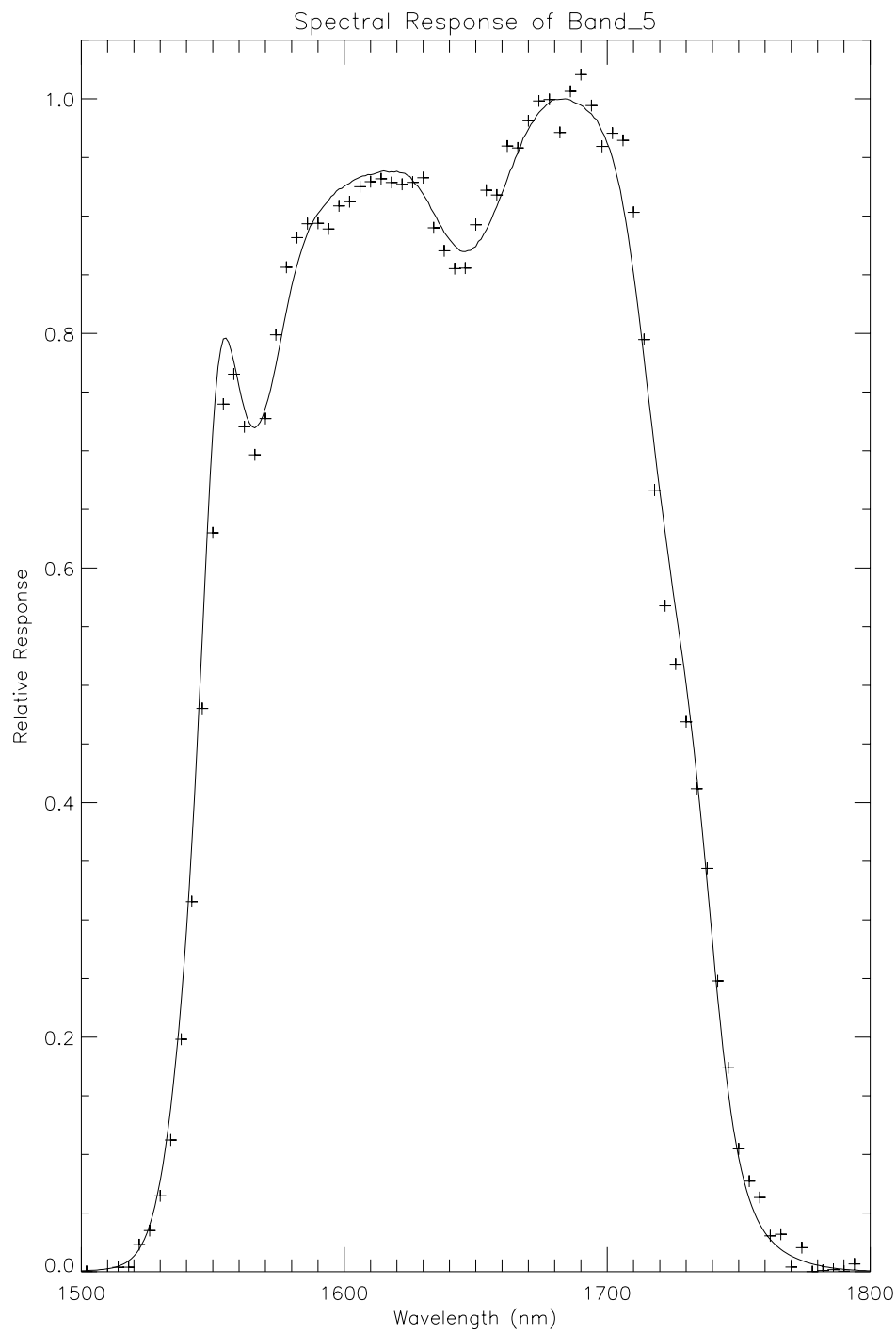
Figure 3-61. Spectral response of band 1. The crosses represent the mean system level measured response for 200 pixels. The solid line represents data collected during subsystem level measurements.
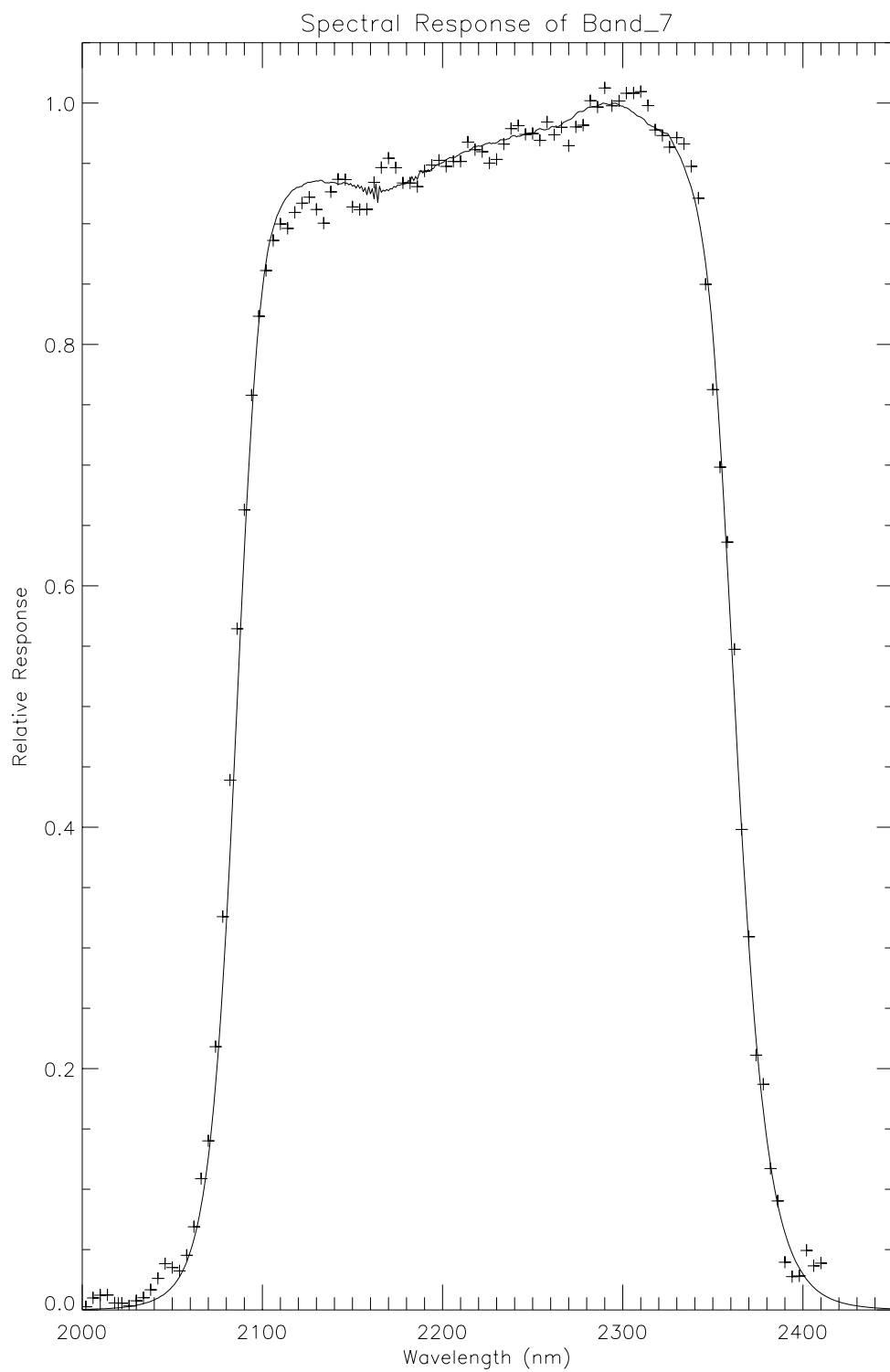
Figure 3-62. Spectral response of band 2. The crosses represent the mean system level measured response for 200 pixels. The solid line represents data collected during subsystem level measurements.
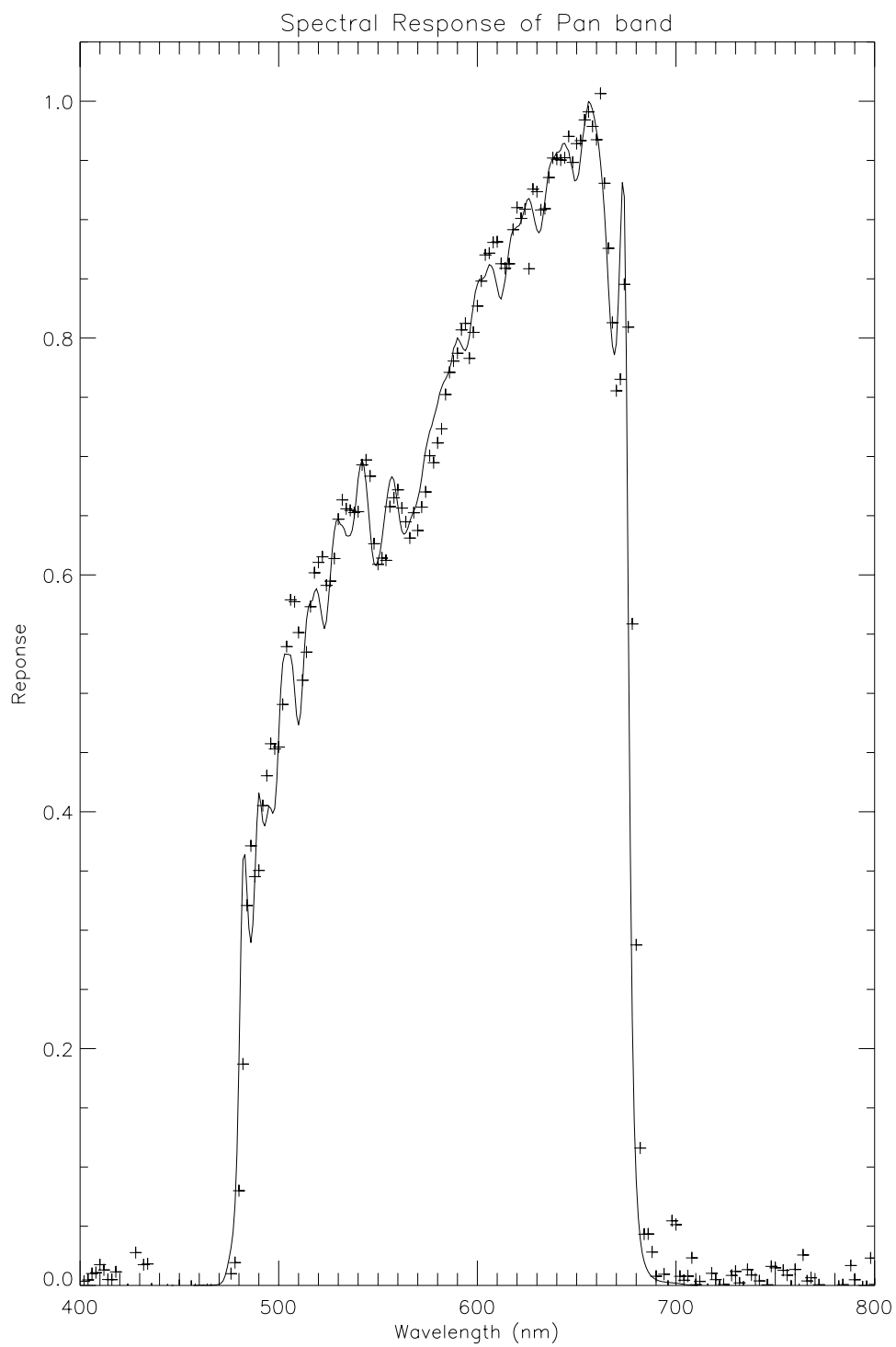
Figure 3-63. Spectral response of band 3. The crosses represent the mean system level measured response for 200 pixels. The solid line represents data collected during subsystem level measurements.

Figure 3-64. Spectral response of band 4. The crosses represent the mean system level measured response for 200 pixels. The solid line represents data collected during subsystem level measurements.

Figure 3-65. Spectral response of band 4p. The crosses represent the mean system level measured response for 200 pixels. The solid line represents data collected during subsystem level measurements.

Figure 3-66. Spectral response of band 5p. The crosses represent the mean system level measured response for 200 pixels. The solid line represents data collected during subsystem level measurements.

Figure 3-67. Spectral response of band 5. The crosses represent the mean system level measured response for 200 pixels. The solid line represents data collected during subsystem level measurements.

Figure 3-68. Spectral response of band 7. The crosses represent the mean system level measured response for 200 pixels. The solid line represents data collected during subsystem level measurements.

Figure 3-69. Spectral response of the panchromatic band. The crosses represent the mean system level measured response for 200 pixels. The solid line represents data collected during subsystem level measurements.
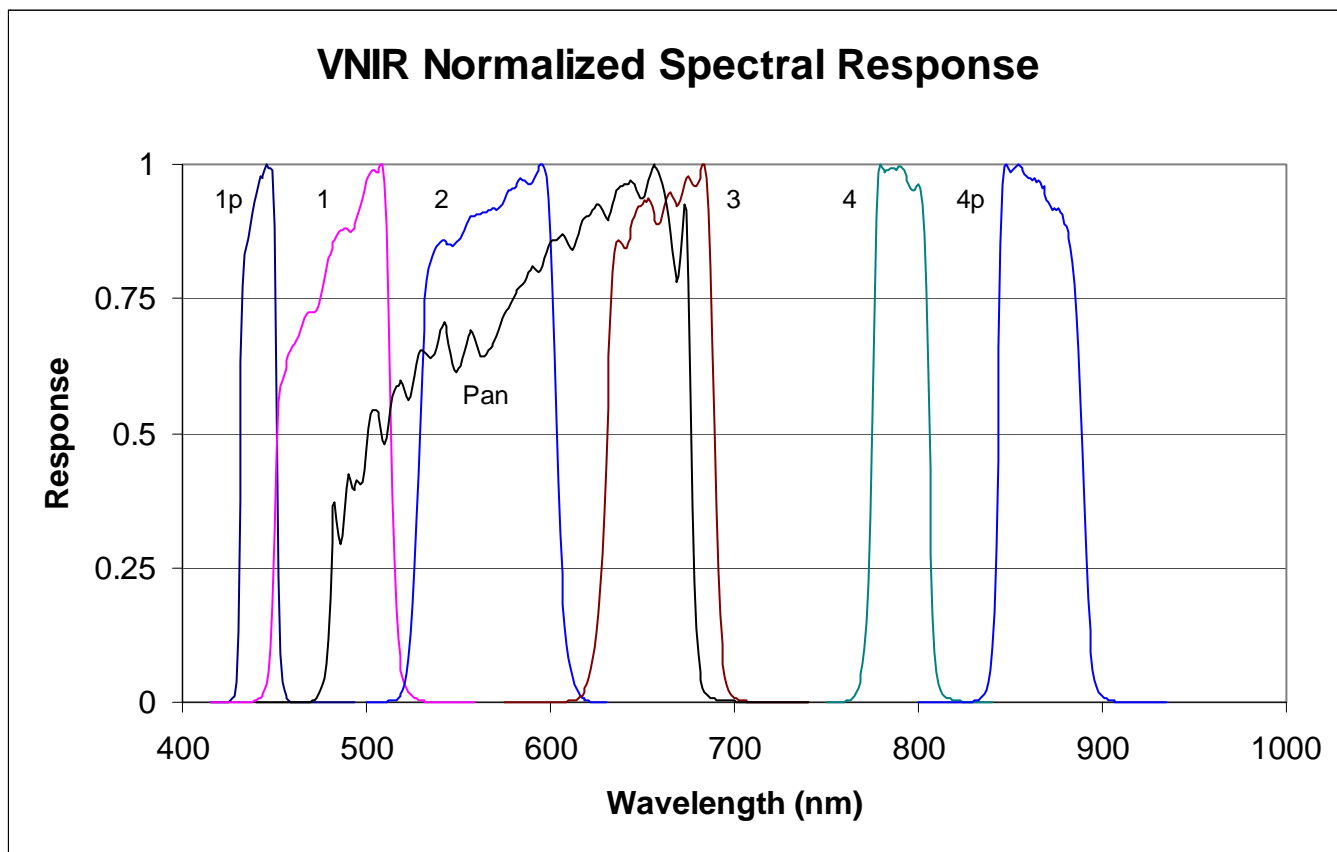
Figure 3-70. Normalized visible and near infrared spectral response functions based on subsystem level measurements.
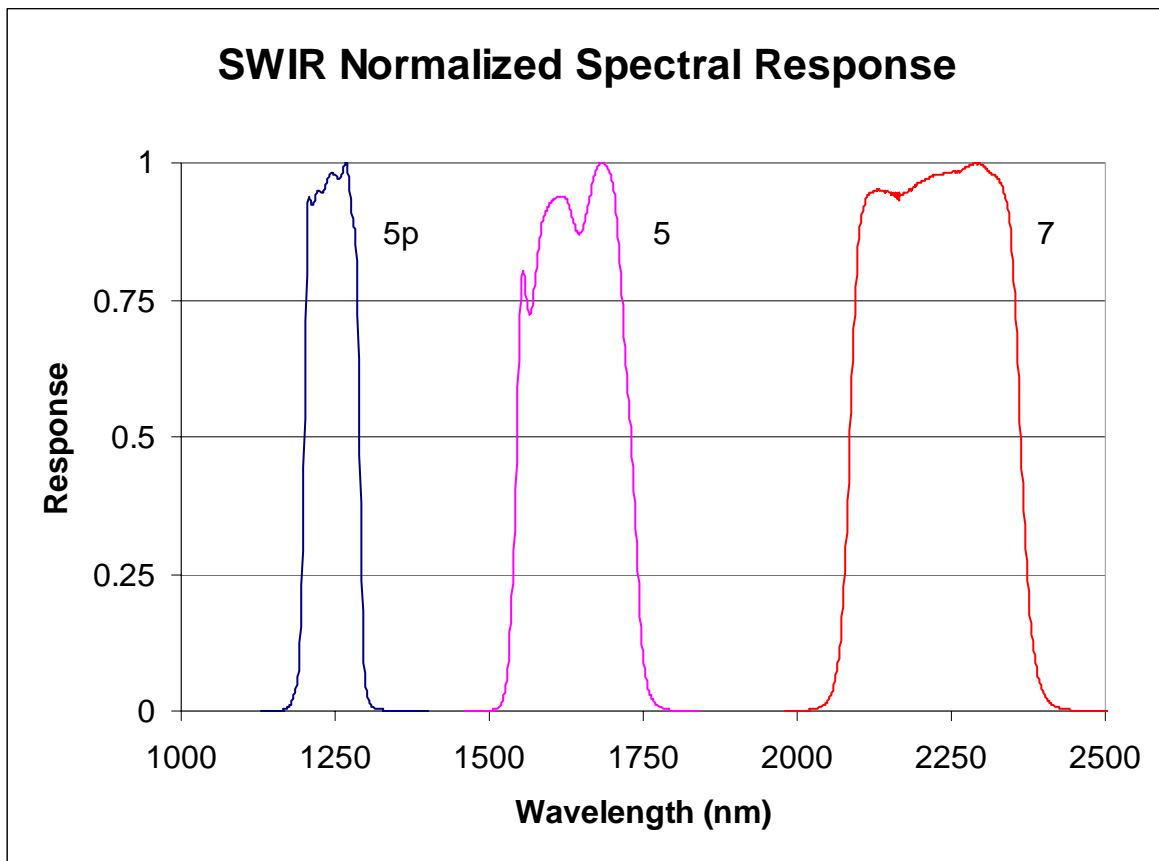
Figure 3-71: Normalized short wave infrared spectral response functions based on subsystem level measurements.

3.1.3.5 Discussion

We find the system level ALI VNIR, SWIR and panchromatic spectral response measurements are in excellent agreement with theoretical models generated from component measurements. We find the spectral response of the ALI to be primarily dependent on the spectral response of the band defining filters lying directly above the focal plane. Detector responsivities also have a small effect on the spectral response of this instrument. This is particularly true for bands with larger bandpasses, such as the panchromatic band. For this band, the gradually increasing efficiency of the silicon material must be accounted for to accurately predict the spectral response of the ALI. Finally, mirror response has little effect on the spectral response of the instrument above 500 nm, providing a global diminution of ~5% which is not a factor when band responses are normalized to unity. However, mirror reflectivities do fall off (down to 80%) below 500 nm and so must be properly accounted for when considering bands in this spectral range.

We have adopted response functions based on the finer spectrally sampled component measurements as the spectral response of the Advanced Land Imager for the VNIR, SWIR and panchromatic bands. These responses will be used to define the spectral bandpass for each band during the analysis of in-flight data. These responses have also been adopted for calculating the in-band radiance of each pixel during radiometric calibration of the ALI (see *Earth Observing-1 Advanced Land Imager: Radiometric Response Calibration*[19].)

An Excel file entitled 'EO1_ALI_SPECTRAL_RESP.XLS' has been generated and is available through the GSFC EO-1 project office. This file contains the in-band and out of band response of each ALI band listed in the above tables.

3.1.4   Radiometric Calibration

This section provides a review of the technique employed during radiometric calibration of the Advanced Land Imager and the results from the characterization of the radiometric response of each detector. Additional information may be found in MIT/LL E0-1-3 project Report [19].

3.1.4.1 Radiometric Calibration Technique

The technique we have adopted for the measurement of the radiometric response of each ALI detector consists of flooding the entrance aperture with a diffuse source of stable, broadband emission at various radiance levels and recording the output of the focal plane at each level. The source of diffuse emission is a (76.2 cm) diameter integrating sphere with a (25.4 cm) diameter output port manufactured by *Labsphere Inc*. (Figure 3-72). The sphere contains three internally mounted 150 watt and one externally mounted 125 watt halogen lamps. These lamps provide a combined radiance equal to 100% Earth-equivalent albedo for Bands 3, 4, 4p, 5p, 5, and 7 and the panchromatic band. Four additional externally mounted 300 watt xenon lamps were used to provide 100% Earth-equivalent albedo for Bands 1p, 1, and 2. Eight intermediate radiance levels were obtained through a combination of sequentially extinguishing lamps and de-rating one internal lamp current. Exercising a linear attenuator mounted between the external halogen source and the integrating sphere provided an additional eight levels. This GPIB commanded slide provided up to 256 aperture variations for an externally mounted source. A similar attenuator was also located between one of the externally mounted xenon sources and the sphere to provide more flexibility in selecting radiance levels for Bands 1p, 1 and 2.
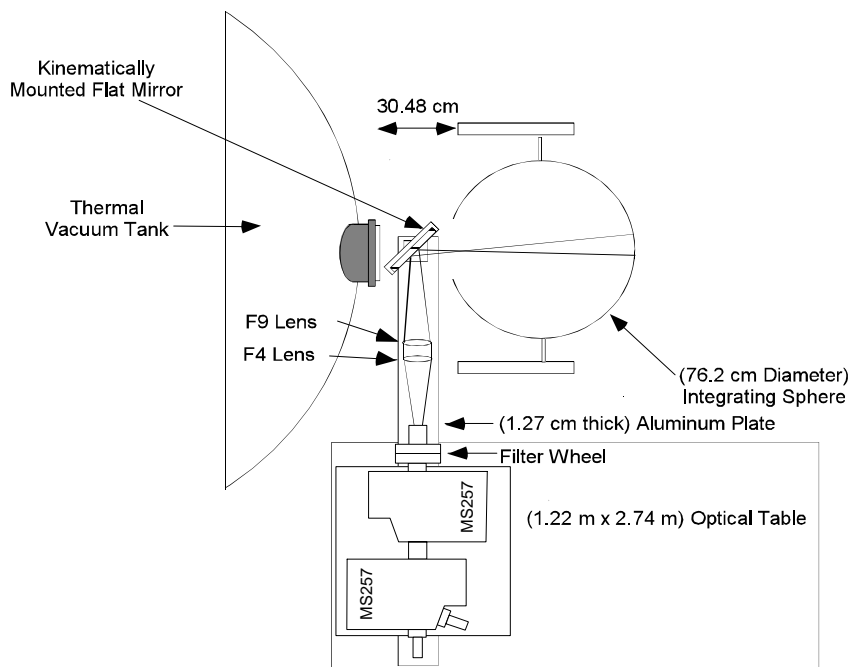

Figure 3-72. Integrating sphere and spectroradiometer used during radiometric calibration of the Advanced Land Imager

In order to provide absolute radiometric traceability to other sensors, a radiometric transfer standard system was constructed at Lincoln Laboratory (Figures 3-72 and 3-73). The principal components of the system are an irradiance source, traceable to the National Institute of Standards and Technology (NIST), and an *Oriel MS257* monochromator used as a spectroradiometer. The 250 watt irradiance source was mounted on a post with proper baffling to control stray light from the room and reflections from the source off other surfaces. A standard radiance scene was generated by placing a *Labsphere Spectralon* sheet 50 cm from the irradiance source. The monochromator field-of-view was limited to a 6.45 cm^2 region of the diffuse scene to maintain the traceability of the radiance source. A (15.24 cm) flat mirror was placed between the *Spectralon* diffuser and entrance slit of the monochromator for convenient location of the source. Alternately scanning the radiance scene produced by the standard lamp and various radiance levels output by the large integrating sphere, radiometric NIST traceability was established for the Advanced Land Imager. Additional near real-time monitoring of the sphere radiance level was accomplished by mounting the (15.24 cm) flat mirror on a (30.48 cm) post between the vacuum tank window and the integrating sphere. During radiometric calibration of the ALI, the mirror was removed and the response of the focal plane recorded. Between ALI data collections, the mirror was kinematically mounted on the aluminum bar, redirecting a portion of the sphere radiance into the entrance slit of the spectroradiometer. The radiance of the integrating sphere was measured from 300 to 2500 nm in 10 nm intervals with 5 nm full-width-half-maximum resolution. Finally, silicon and germanium detectors, mechanically mounted to the sphere wall, provided continuous broadband monitoring of the sphere stability.
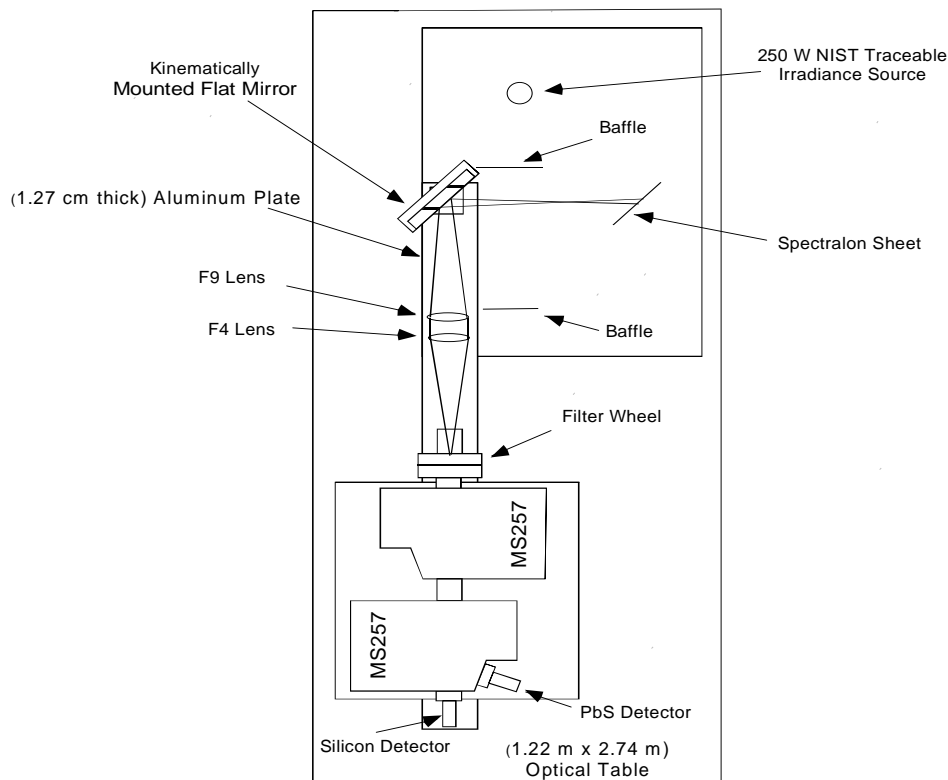

Figure -3-73. Radiometric transfer standard system built at Lincoln Laboratory.

A listing of contributing errors to the radiometric calibration technique at three wavelengths is provided in Table 3-16. The dominant factor in the VNIR spectral range is the NIST standard lamp. Near 1300 nm the repeatability of the lead sulfide spectroradiometer detector dominates the uncertainty in the measurement, followed closely by the standard lamp. Finally, at 2000 nm, the standard lamp provides the largest degree of uncertainty in the measurement.

Table 3-16
Radiometric Calibration Error Budget.

Source	1σ Error (%)		
	600 nm	1300 nm	2000 nm
NIST Standard Lamp	0.875	0.94	1.535
Spectralon Panel	0.67	0.67	0.67
Spectroradiometer Repeatability	0.67	0.67	0.67
Spectroradiometer Detectors	0.67	1.0	1.0
Integration Sphere Repeatability	0.33	0.33	0.33
Integrating Sphere Uniformity	0.67	0.67	0.67
Vacuum Window Transmission	0.33	0.67	0.67
ALI repeatability	0.33	0.33	0.33
Total (sum in quadrature)	1.7%	1.97%	2.32%

3.1.4.2   Data Collection

Radiometric data were collected in January 1999 in a class 1,000 clean room at Lincoln Laboratory. This calibration was conducted with the ALI as a fully assembled instrument in a thermal vacuum chamber at operational temperatures.

Selection of the integrating sphere radiance level and monitoring of radiance stability was coordinated by the ALI Calibration Control Node (ACCN), a LabVIEW-based personal computer operating on a Windows 95 platform. Commanding and housekeeping monitoring of the ALI was also controlled by the ACCN via a Goddard Space Flight Center-provided RS2000 Advanced Spacecraft Integration and Systems Test (ASIST) computer. Data acquisition was performed by a Unix-based Electrical Ground Support Equipment (EGSE1) computer. A Silicon Graphics Performance Assessment Machine (PAM) stored and processed focal plane data in real time for quick look assessment.

For each radiance level selected, the sphere was allowed to stabilize for one hour. A spectroradiometric scan of the sphere output from 300 – 2500 nm was then conducted after placing a (15.24 cm diameter) flat mirror between the sphere exit port and vacuum tank window to redirect the beam into the

monochromator. After the mirror was removed, the response of the focal plane was recorded for several integration periods [0.81 (0.27), 1.35 (0.45), 1.89 (0.63), 2.97 (0.99), 3.51 (1.17), and 4.05 (1.35) milliseconds for MS (Pan) detectors]. Finally, the ALI aperture cover was closed and reference dark frames were recorded for identical integration periods.

Data were collected with the ALI illuminated by a combination of halogen sources only, a combination xenon sources only, and a combination of halogen and xenon sources. Additional data were collected using the halogen sources only with the focal plane operating at two other possible operating temperatures (215 K and 225 K) to assess the effects of temperature on focal plane response.

3.1.4.3   Analysis

Analysis of the radiometric response of the Advanced Land Imager has been divided into three categories: VNIR, *leaky*, and SWIR. The VNIR and SWIR analysis was separated due to the differing detectors used in these bands (silicon for VNIR, HgCdTe for SWIR). The *leaky* detector category refers to Band 2 of SCA 4 and Band 3 of SCA 3. Odd detectors of Band 2, SCA 4 exhibit substantial optical or electrical cross-talk when detector 1149 is illuminated. Similarly, even detectors of Band 3, SCA 3 exhibit substantial optical or electrical cross-talk when detector 864 is illuminated. An empirical correction methodology has been developed to effectively remove all traces of the cross-talk and transfer detector responses of these bands into units of radiance. As a result, calibration results for odd detectors of SCA 4 Band 2 and even detectors of SCA 3 Band 3 will not be reviewed in this paper.

For VNIR and SWIR data, a linear function was fitted to the response of each detector to incident radiance after subtraction of the dark current. This fit may be expressed as

$$L_\lambda(B, I) = B_P[P_{illum,I} - P_{dark}].$$

Here, $L_\lambda(B,I)$ is the incident band weighted spectral radiance for Band B and sphere level I, B_p is the radiometric calibration coefficient for detector P (mW/cm^2/sr/μ/DN), $P_{illum,I}$ is the illuminated detector digital response for sphere level I, and P_{dark} is the dark detector digital offset.

$L_\lambda(B,I)$ was calculated knowing the output radiance of the integrating sphere, the spectral response of each band, and the spectral transmission of the vacuum tank window. This may be expressed analytically as

$$L_\lambda(B, I) = \frac{\int L_\lambda(\lambda, I)T_W(\lambda)S(b,\lambda)d\lambda}{\int S(b,\lambda)d\lambda}$$

Here, $L_\lambda(\lambda,I)$ is the spectroradiometrically measured output radiance of the sphere for level I, T_W is the spectral transmission of the vacuum tank window, and S is the normalized spectral response for Band B. The spectral response of each band used in this analysis was determined during the spectral calibration of the ALI (see *Earth Observing-1 Advanced Land Imager: Spectral Response Calibration [18]).*

An example of a linear fit to the data for detector 100 of Band 3 is provided in Figure 3-74. In this figure, 20 radiance levels were used to fit the detector response. The top graphic is an overlay of the data points and best-

fit linear function (the fit was anchored at zero incident radiance by inserting a synthetic data point of zero digital number (dn) for all detectors). The bottom graphic provides the errors to this fit for all radiometric levels. We find all VNIR, SWIR, and panchromatic radiometric response fits to agree with measurements to within ± 3.5% (peak to peak). This is within the error budget specified in Table 3-16.
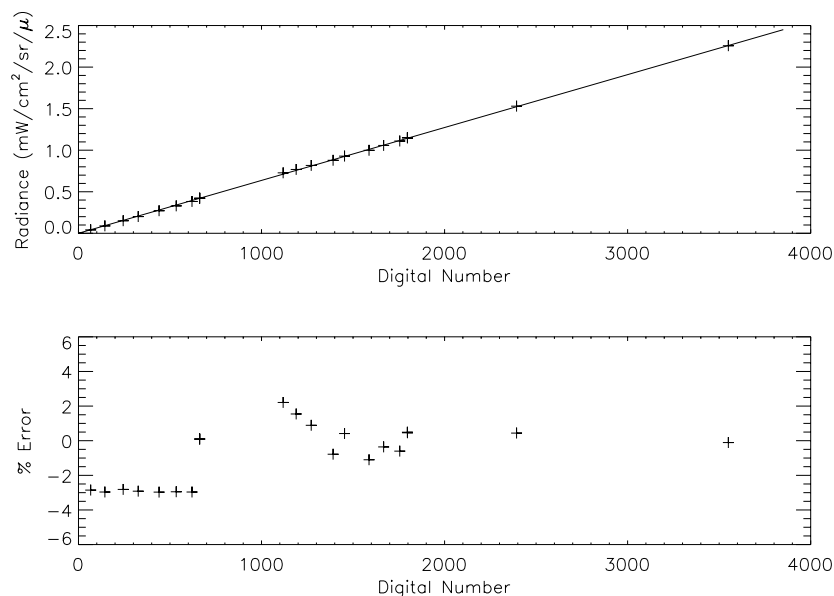

Figure 3-74. Example of linear fit to Band 3 detector 100 data.

3.1.4.4 Results

The radiometric response of each detector of every band was derived individually using the method defined above. From this calibration, the response coefficient, signal-to-noise ratio, saturation radiance, and dynamic range of the ALI focal plane have been determined. We report the results for a nominal integration time of 4.05 ms (1.35 msec for the Pan) and a focal plane temperature of 220 K. Results for other integration times and focal plane temperatures are reported elsewhere (see *Earth Observing-1 Advanced Land Imager: Radiometric Response Calibration Addendum).*

The response coefficient of each band is provided in Figures 3-75 to 3-84. Detectors 0 through 319 belong to SCA 1 (outboard), detectors 320 through 639 to SCA2, detectors 640 through 959 to SCA3, and detectors 960 through 1279 to SCA 4. SCA-to-SCA and detector-to-detector variability are evident in these figures.
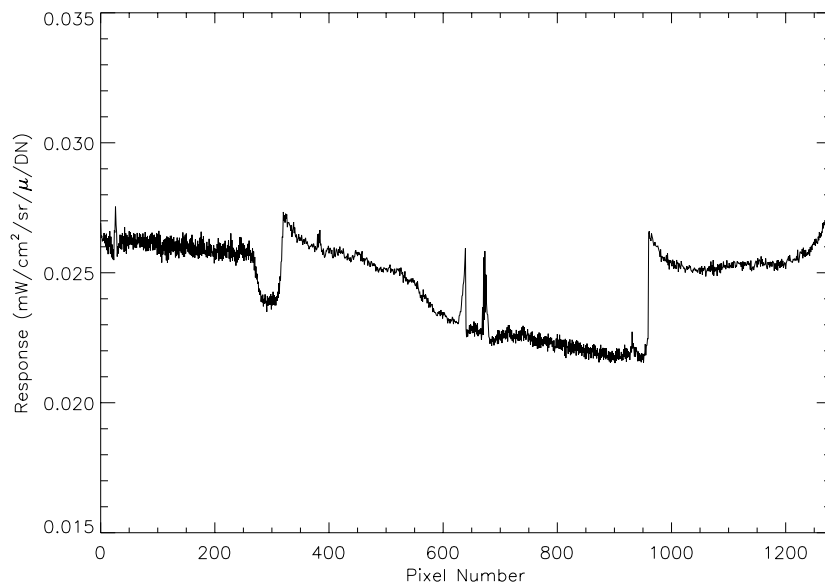
Figure 3-75. Radiometric calibration coefficients for Band 1p.
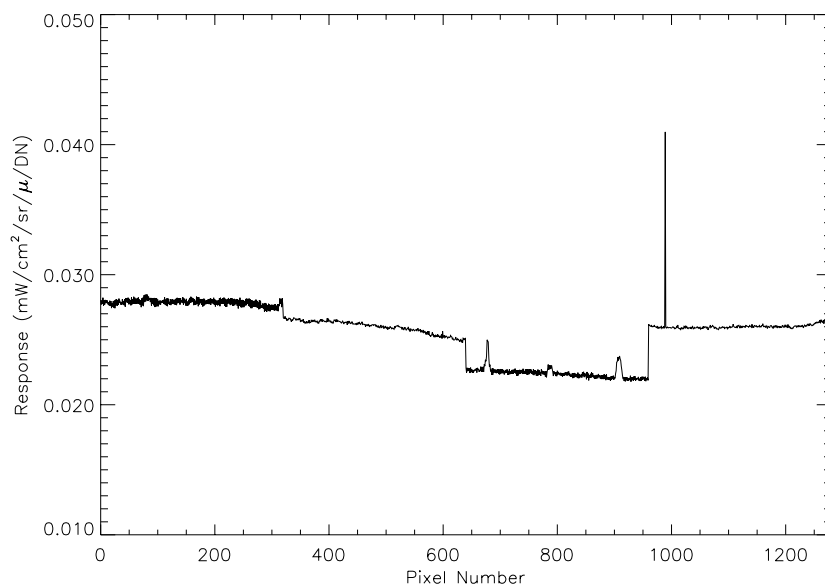
Figure 3-76. Radiometric calibration coefficients for Band 1.

Detector 989 of Band 1 has also been identified as having excessive dark current[13].
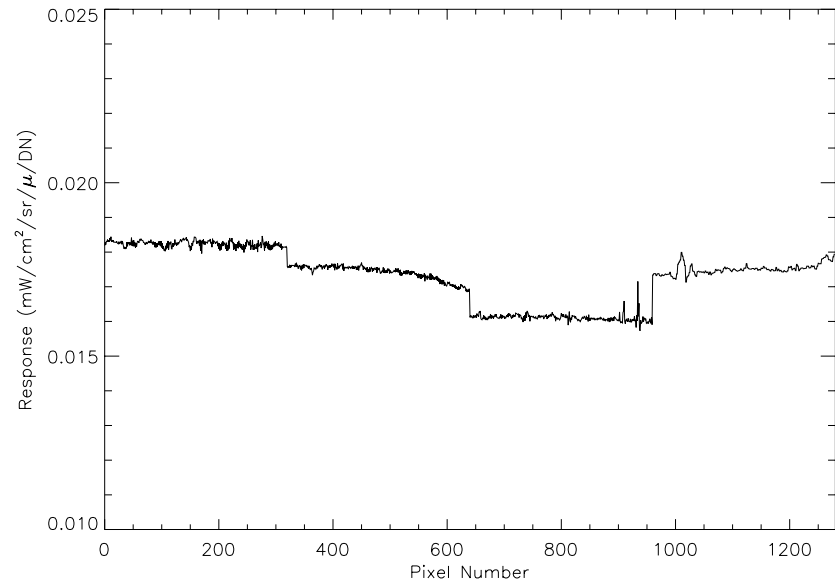
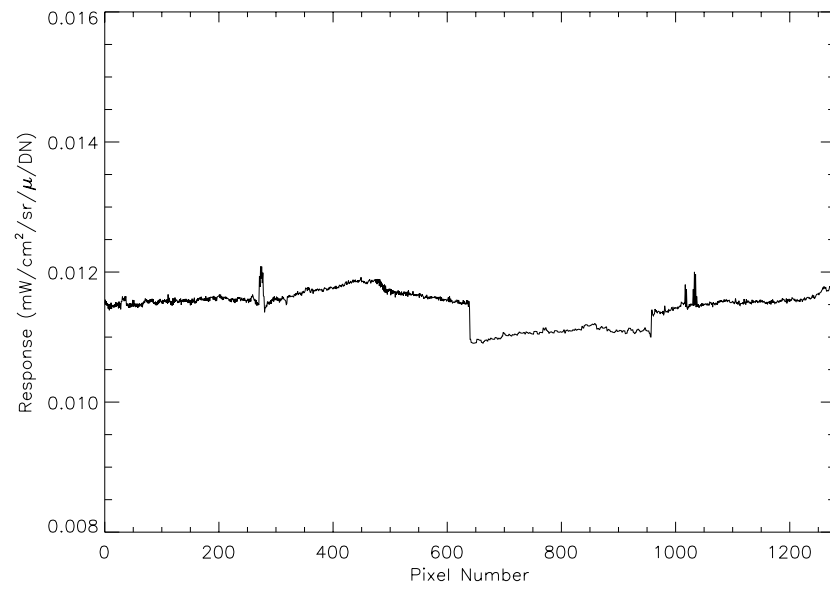*Figure 3-77. Radiometric calibration coefficients for Band 2.*

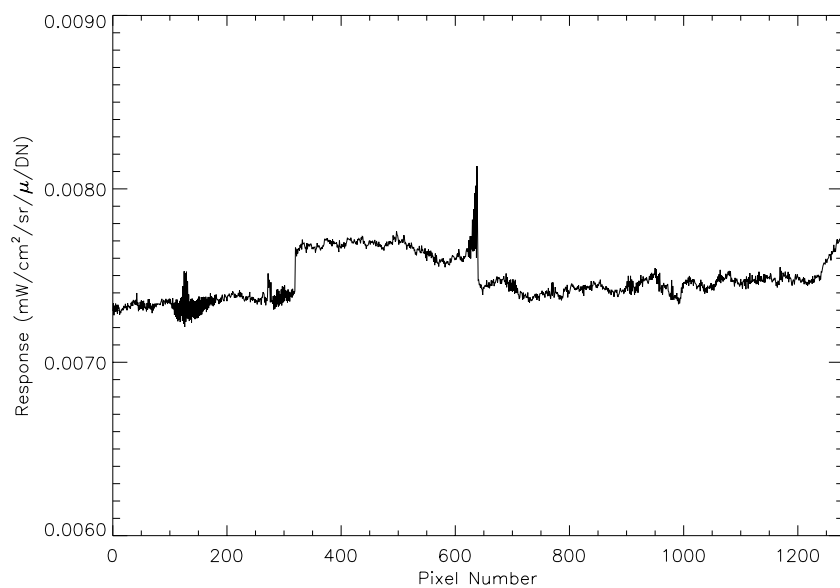*Figure 3-78. Radiometric calibration coefficients for Band 3.*

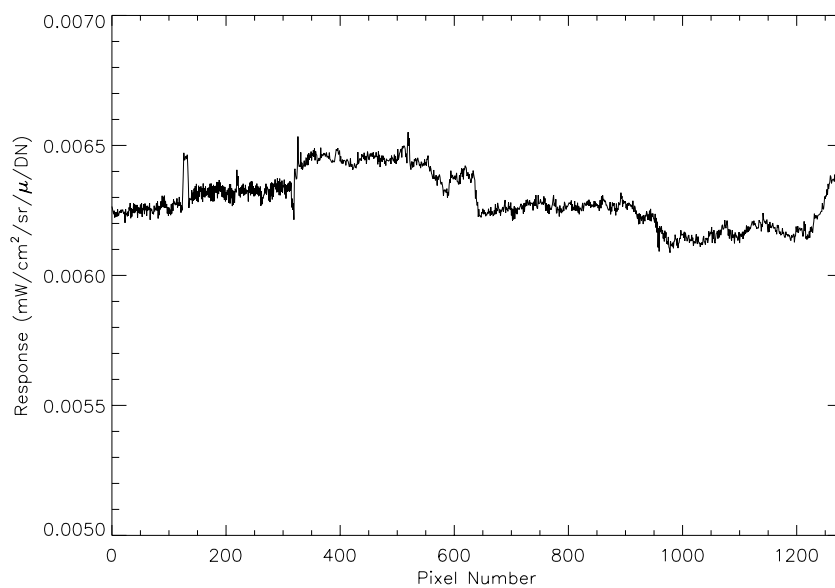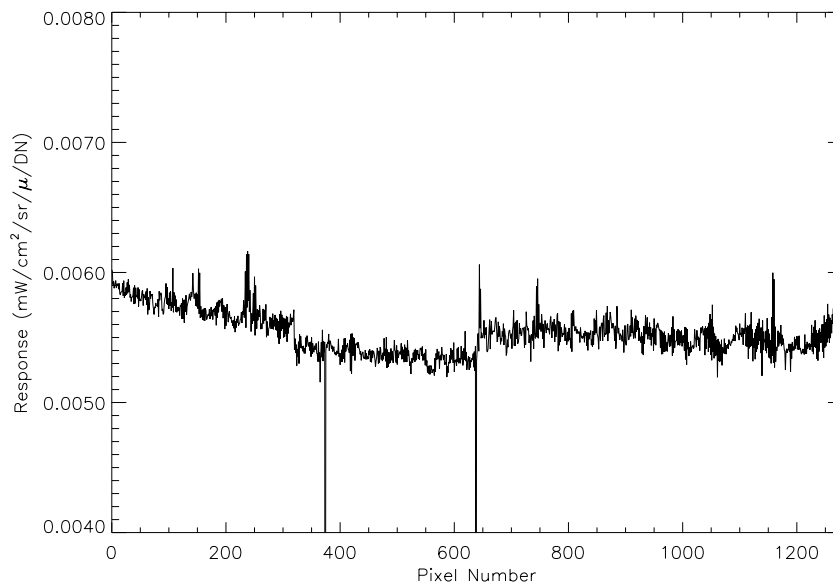*Figure 3-79. Radiometric calibration coefficients for Band 4.*

Figure 3-80. Radiometric calibration coefficients for Band 4p.

Figure 3-81. Radiometric calibration coefficients for Band 5p.

Detectors 374 and 638 of Band 5p have been classified as *inoperable detectors* that are saturated at all times [13]. Detector 365 has a larger than average dark current value.
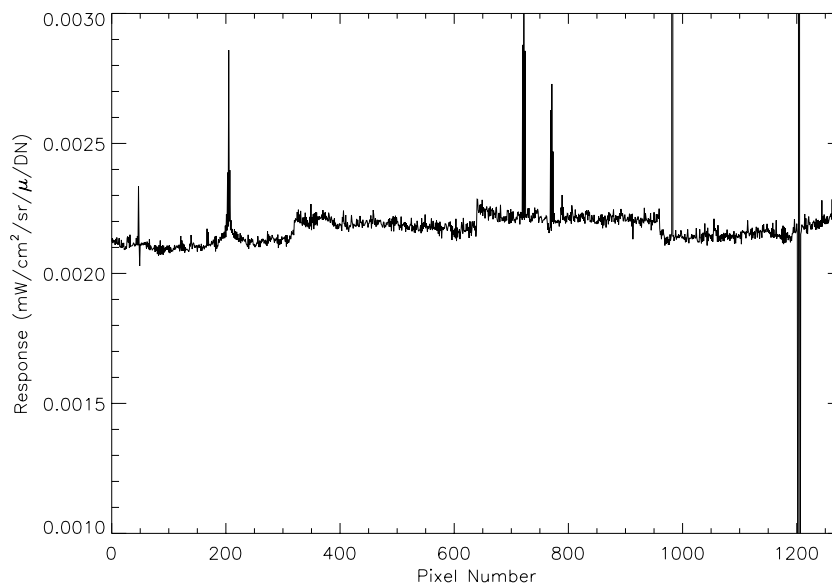
Figure 3-82. Radiometric calibration coefficients for Band 5.

Detector 982 is an inoperable detector that exhibits no variation in response with input signal. Detectors 1202, 1204, and 1206 are inoperable detectors that are saturated at all times [13]. Coefficient variations near detectors 200, 700, and 800 are not associated with any unusual noise or dark current characteristics for this band. Detectors 911 and 913 have larger than average dark current values.
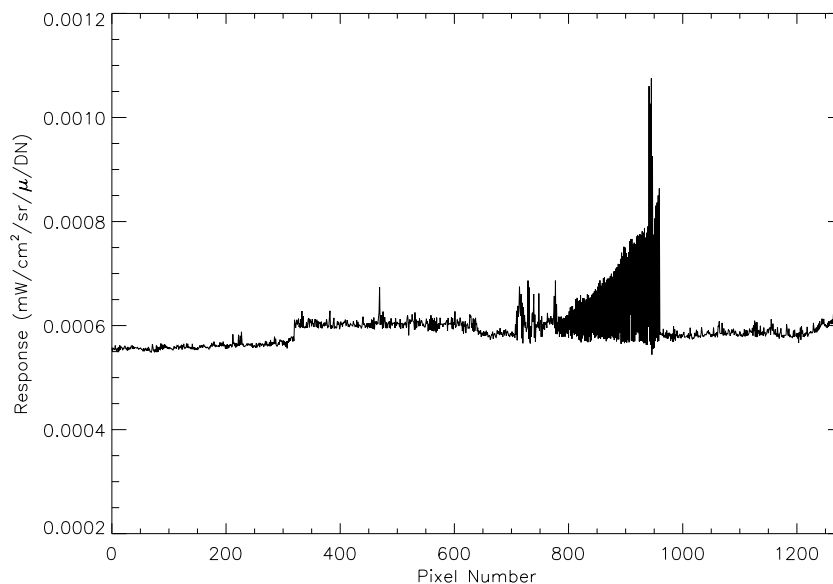
3-102

Figure 3-83. Radiometric calibration coefficients for Band 7.

The large differences present between odd and even detector calibration coefficients for SCA 3 detectors 800-960 are not associated with any unusual noise or dark current characteristics of Band 7.
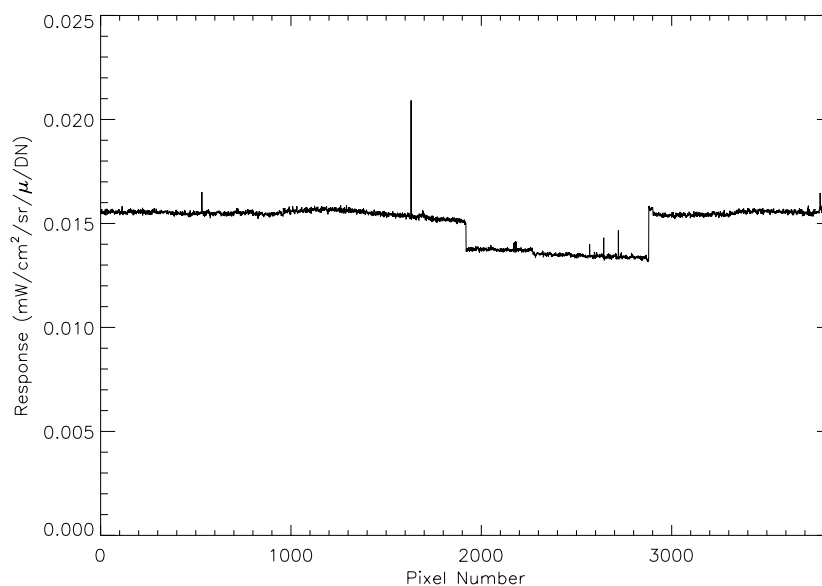

Figure 3-84. Radiometric calibration coefficients for the Panchromatic Band.

Detector 1631 of the panchromatic band has also been identified as having excessive noise[13].

3.1.4.5 Internal Reference Lamps

An internal reference source, located within the instrument telescope cavity, will act as a radiometric calibration transfer mechanism between ground and flight operations. This source consists of three Welch Allyn 997418-7 (modified) gas-filled lamps mounted on a small (2.03 cm) diameter integrating sphere (Figures 3-85, 3-86). Light emerging from the exit slit of the sphere passes through a BK 7 lens and infrared filter, is reflected off the ALI flat mirror, and floods the focal plane. The response of the ALI focal plane to these sources has been correlated to ground radiometric calibration. Additionally, extensive stability and lifetime testing for spaceflight operation was conducted at Lincoln Laboratory, and these sources have also been shown to be stable to within 1-2% over the two-year period between ground calibration and launch of the spacecraft.
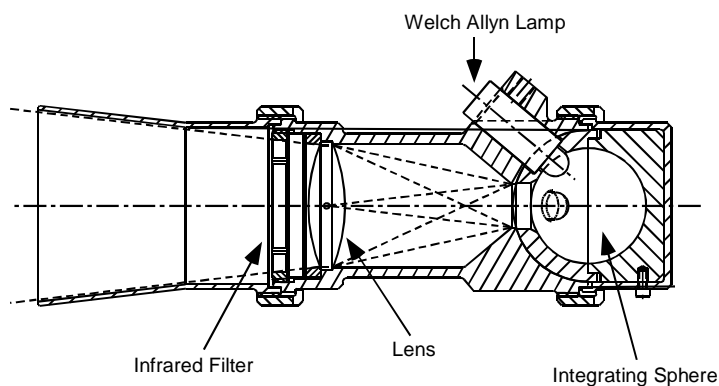

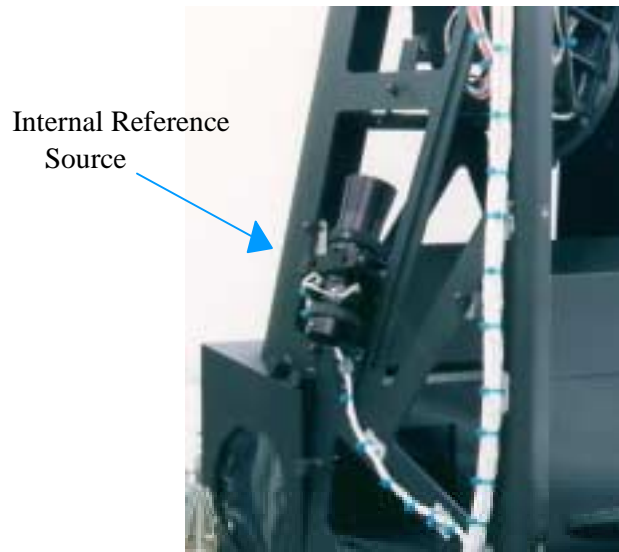*Figure 3-85. EO-1 ALI internal reference source.*

Figure 3-86. Photograph of internal reference source.

Daily in-flight radiometric checks of the instrument will be conducted by observing these internal reference sources. Following each observation, after the aperture cover has been closed, the three internal reference lamps are powered by the ALI Control Electronics. After an eight-second stabilization period the lamps are sequentially powered down in a staircase fashion, with two-second exposures between each step. In this manner, the focal plane will receive a three point radiometric reference after each observation.

3.1.4.6 Discussion

The radiometric response of the Earth Observing-1 Advanced Land Imager has been calibrated during ground testing at MIT Lincoln Laboratory. This calibration includes the investigation of the response, signal-to-noise ratio, saturation radiance, and dynamic range of each detector of every spectral band.

The results obtained in the analysis outlined in this report, along with results from the *leaky detector* analysis, have been incorporated into the calibration pipeline and will be used to radiometrically calibrate initial ALI flight data. As an example of this calibration, Figure 3-87 depicts a Band 4 image of Lincoln Laboratory before and after radiometric calibration is applied. Detector-to-detector and SCA-to-SCA variations, a result of dark current and response coefficient variations, are clearly evident in the data prior to calibration.

Figure 3-87. Band 4 image of Lincoln Laboratory. The image on the left is prior to radiometric calibration. The image on the right is after radiometric calibration.

Finally, results presented here will also be compared against data collected during on-orbit internal reference lamp monitoring and solar, lunar, and vicarious calibrations to track changes in ALI radiometric response over the lifetime of the mission.

3.2   ON-ORBIT TEST VALIDATION

The objective of on-orbit test validation is to show that the technology performs on-orbit as well as it did before launch. This is to verify that the conditions of the launch or the orbital environment do not significantly degrade the performance. For the Advanced Land Imager, we divide the on-orbit test validation into the spatial and the radiometric performance categories. Spatial validation of the ALI technology consists of demonstrating that the instrument yields clear, sharp images that may be accurately registered with features on the ground. Radiometric validation is to show that the in-band radiances reported in the radiometrically-corrected (Level 1R) data accurately represent the top-of-the-atmosphere radiances of the scene imaged.

3.2.1 Spatial Validation

The major aspects of spatial validation are to verify the modulation transfer function (MTF) and the detector lines of sight. The aspects spartial assessment of the SLD is also reviewed

3.2.1.1   Modulation Transfer Function

The MTF, or spatial transfer function (STF) which we prefer to use, was extensively calibrated at Lincoln Laboratory before integration with the spacecraft, as described in section 3.1.2. In the laboratory, it is possible to present a precisely defined object to the instrument, and to sample the image data much more finely than is done on-orbit. Our approach to MTF validation on-orbit is to use the spatial calibration data to simulate the instrument response to simple models of certain well-defined objects imaged from space. The simulated response is then compared to the actual response. If the two match well, the MTF is validated.

Objects that we have used to date for MTF validation are bridges, the moon, and stars. Bridges can provide a roughly uniform strip of radiance contrasting with the uniform darker water on either side. The lunar limb presents a sharp edge against dark space. Bright stars are essentially point sources that yield the instrument's point-spread function, albeit at a low sampling frequency.

An example of a bridge scan is shown in Figure 3-88. It is the Bronx Whitestone Bridge, seen in a scan of New York City on March 20, 2001. The dotted rectangle delineates the pixels we used to test the MTF of the ALI. Those pixels were projected onto an axis perpendicular to the bridge. The result is shown in Figure 3-89. The radiance along that axis was modeled as a step function, including the bridge, the water on each side, and the shadow of the bridge on the water. The expected system response to this model was computed using the spatial transfer function from our laboratory calibration. After an initial estimate of the radiances and edge locations was made, those parameters were refined by performing a least-squares fit of the computed response to the average projected pixel data. The resulting fitted response is shown in Figure 3-90. The close agreement between the fitted response and the pixel data indicates the validity of the calibrated STF.

Figure 3-88. Portion of the panchromatic image of New York City, scanned on March 20, 2001.
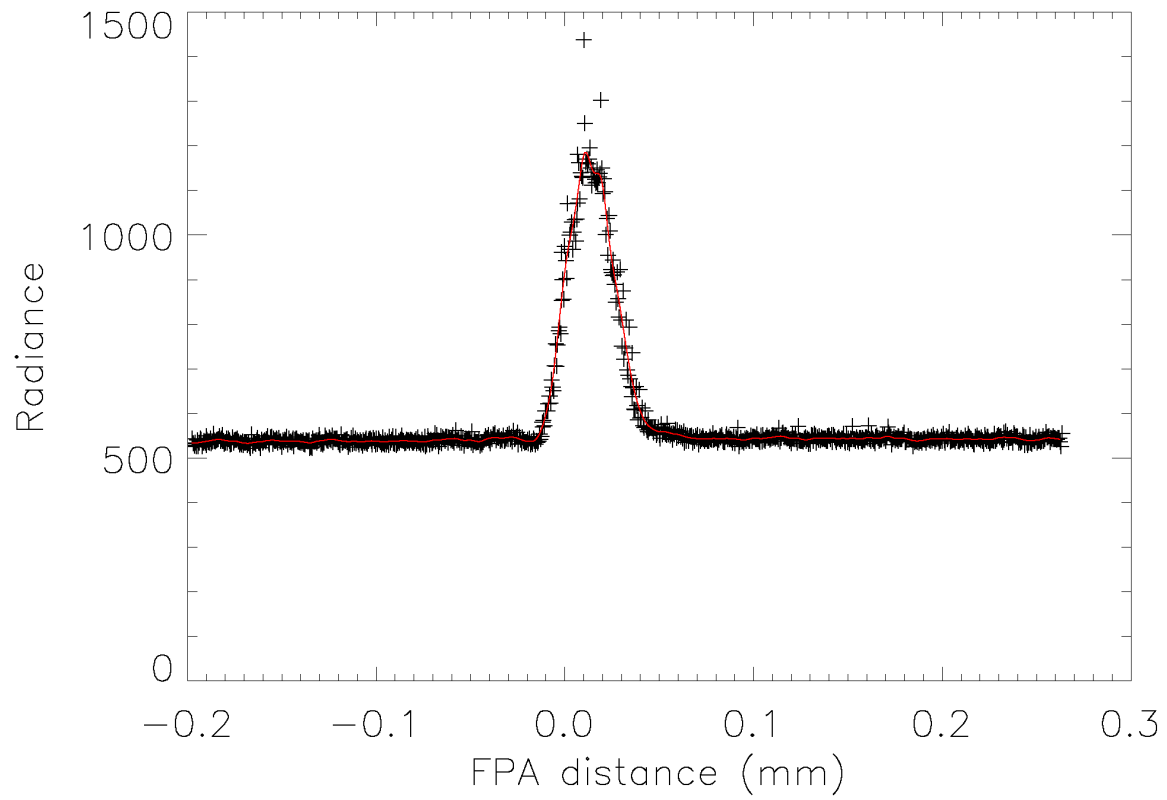
Figure 3-89. Panchromatic radiances of the region of interest shown in Figure 3-78, projected to the axis perpendicular to the Bronx Whitestone bridge. Crosses are the individual pixel data, and the curve represents a slightly smoothed average of the radiance vs. distance
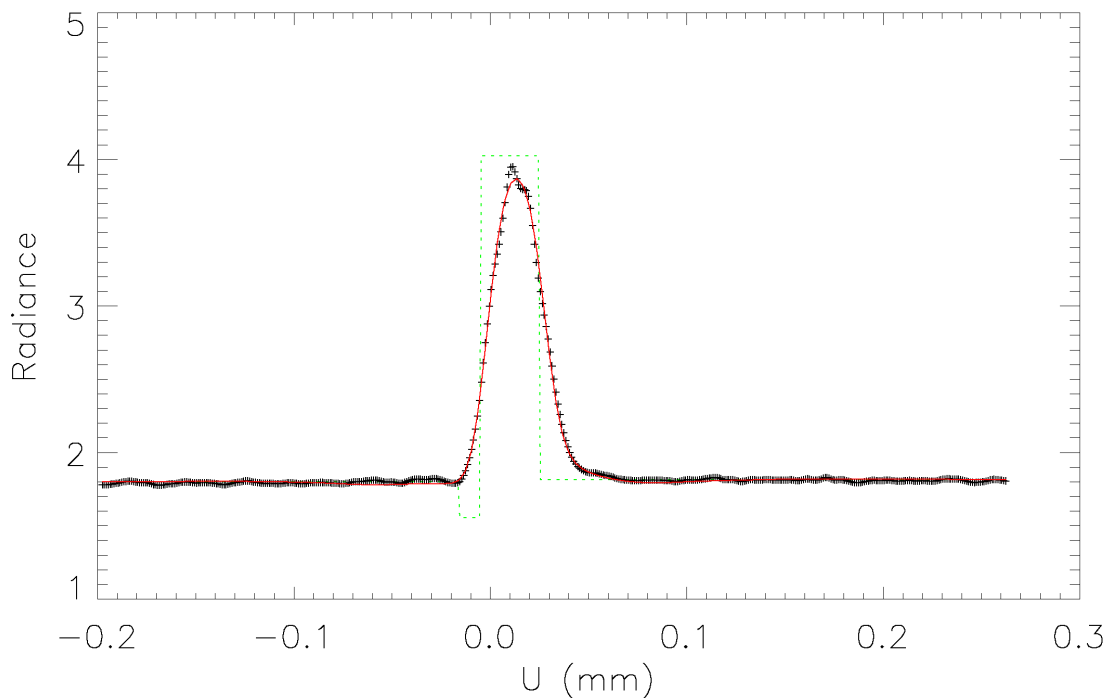
Figure 3-90. Radiance profile of the Bronx Whitestone Bridge. The crosses are the average panchromatic image data shown as the curve in Figure 3-89. , the dotted lines show the fitted radiance model, and the smooth curve is the computed instrument response.

As a further check on the model, the apparent width of the bridge was compared to the actual width as reported on a Web site (http://www.nycroads.com/crossings/bronx-whitestone/). To make certain of the scale of the image, the distance from the bridge to a small point of land on Throgs Neck was measured both in the Pan image (3.013 mm) and on a USGS map of the Flushing quadrangle (2.279 km). The transverse scale factor .7563 km/mm. The 29.3 µm fitted width of the bridge image corresponds to 22.15 m at the bridge. The reported width is 23.5 m.

A panchromatic image from a lunar calibration scan is seen in Figure 3-91. A small region of interest (ROI) along the southwest limb was selected. As for the bridge image, the pixel radiances in the ROI were projected onto an axis perpendicular to the limb. The result is shown in Figure 3-92. The figure also shows the panchromatic edge spread function computed from the MTF calibration data. Apart from a fall-off of lunar radiance inward from the limb, the agreement is close. In particular, the slope of the edge spread function matches the radiance data very well.

Figure 3-91. Panchromatic image of the first quarter moon, from a lunar calibration scan of Feb. 2, 2001.
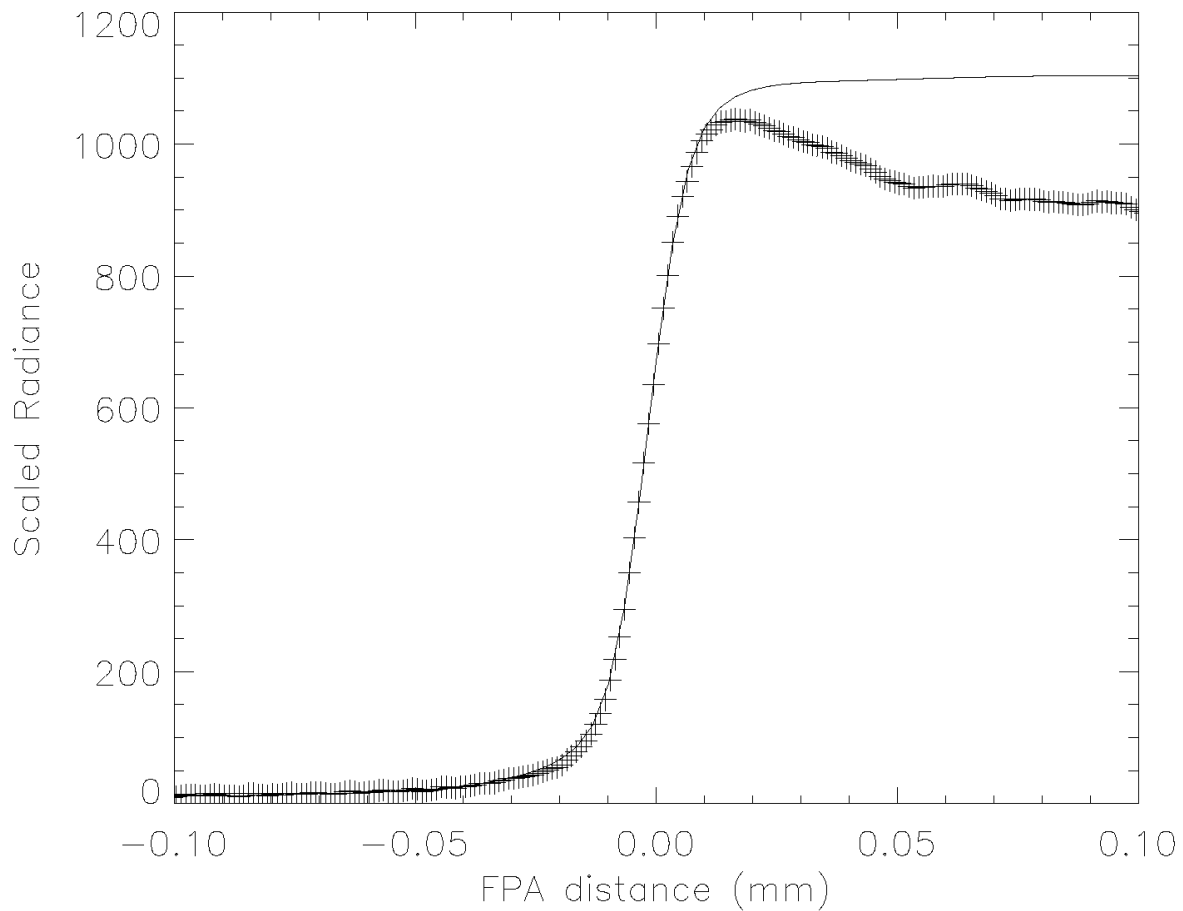
Figure 3-92. Scaled panchromatic radiance of the lunar limb as a function of distance perpendicular to the limb in the focal plane space. The crosses are the averaged data within the ROI, and the smooth curve is the computed ALI edge spread function.

A scan with SCA 4 across the 0.3 magnitude star Vega is presented in Figuren3-93. The scan was performed at one-fourth the nominal angular image speed of earth scenes. Thus the data are sampled four times per detector height in the scan direction. Figure 3-94 shows the panchromatic radiance profiles through the star in the in-scan and cross-scan directions. The crosses are the calibrated scan data, and the curves represent the point-spread function computed from the MTF calibrations and fitted to the scan data.
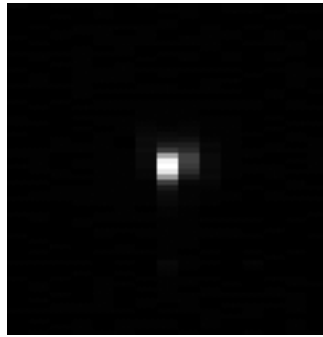
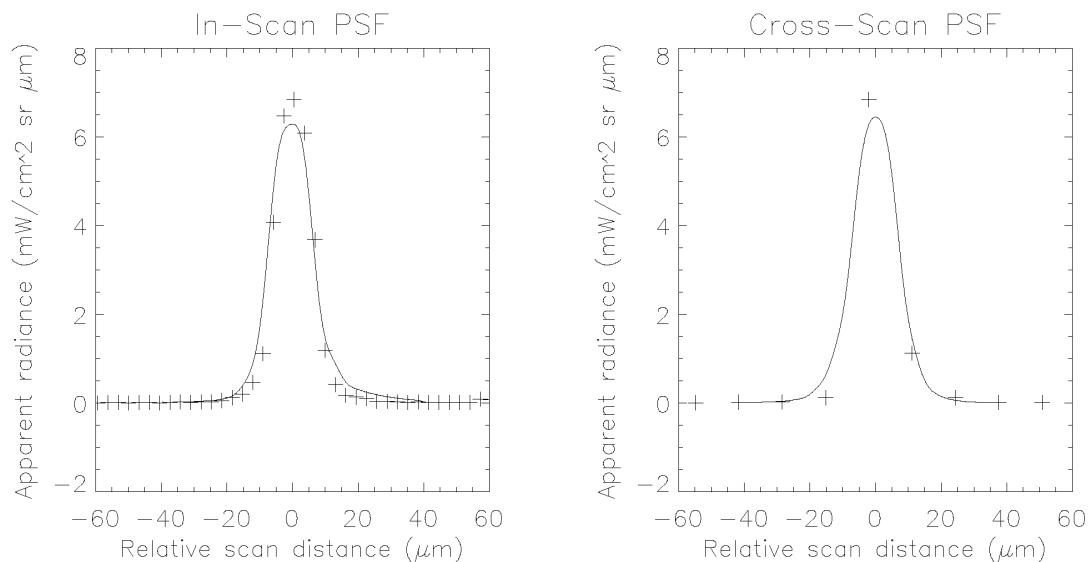*Figure 3-93. Panchromatic image of the star Vega. The scan direction is vertical here.*

Figure 3-94.Panchromatic radiance profiles of Vega in the in-scan (left) and cross-scan directions. Only one row or column of pixels through the center of the star's image is shown in each case (crosses). The curve is a fitted Pan point-spread function.

In the case of the Vega scan, we observe from Figure 3-94 that the instrument performance may be better than indicated by the laboratory calibrations. The fitted point-spread function appears to be noticeably wider than the actual image. A possible explanation for this discrepancy is that the focus shim of the ALI may not have been cut with the correct wedge angles. During MTF calibration, the focus error was measured at one point of the focal plane array, and this value was incorporated in the MTF model. If the plane of the detectors is actually at a slight angle to the

3-112

plane of best focus of the telescope, then images will be in better focus for some parts of the array than for others. This warrants further observations of a bright star, crossing different parts of the focal plane array, to ascertain if any truer estimate of the focus term should be incorporated in a revised MTF model.

3.2.1.2   Detector Lines of Sight

To date, the best indication we have of the validity of the detector line-of-sight map is the clarity of multispectral images reconstructed from the radiometrically-calibrated data. An example of these images is seen in Figure 3-95. Close inspection reveals no fringes of color that would indicate a misregistration of the spectral bands. There is also no sign of the boundaries of the individual SCA's. Thus the detector line-of-sight map is valid, at least down to the sub-pixel level.

Figure 3-95. False-color multispectral image of part of the South Island of New Zealand. Seen here are parts of the Rolleston Range, Lake Coleridge, and the Rakaia River. The red, green and blue components represent bands 7, 4, and 2, respectively. In this presentation, snow on the mountain peaks appears light blue, while clouds near the peaks are white.

The process we used to reconstruct images such as that in Figure 3-95 from Level 0 data is as follows: First, a radiometric calibration is performed on all of the data, to produce Level 1R files

in HDF format. Next, the speed and direction of the image motion across the focal plane are estimated, assuming that they are constant. This is done by cross-correlating the overlapping portions of the Pan images in neighboring SCA's. The geometric re-sampling procedure reads in the Level 1R data and shifts the odd detector data in time (frame number) to restore synchronous sampling. (This step is necessary because the Data Processing System at GSFC applies an odd/even shift in the Level 0 data to offset the staggered locations of the detectors on the focal plane. That makes the Level 0 and Level 1R data easier to view.) Finally, the re-sampling procedure applies the detector line-of-sight map to re-sample the data to an output image, at the same nominal resolution. The outputs of this process are a Level 1G file in HDF format for each SCA. Another procedure produces browse files in JPEG format for selected triads of multispectral bands or the Pan band. The JPEG images cover the full swath, and join the SCA's by omitting some redundant pixels that would otherwise overlap.

As previously stated, we see no evidence to date of errors in the detector line-of-sight map. The re-sampled images are clear and seamless. However, a full analysis of the band-to-band registration is yet to be done. If the bands were in perfect registration, then a satisfactory multi-band image could be constructed from the Level 1R data simply by shifting the bands by whole numbers of frames, representing their separations in the scan direction. This would not, however, take into account optical distortions or SCA location errors.

We have indirect evidence that the bands are in good registration. The procedure that estimates the image speed and direction generally finds the speed to be within a few percent of nominal, and the yaw angle to be a few milliradians or less. This is done solely with the Pan data. A multispectral image such as that in Figure 3-95 uses the speed and yaw from this Pan analysis, along with the line-of-sight map to place the other bands. Consider that the band 2 detectors are separated from the band 7 detectors by 4.8 mm in the scan direction. The band 7 detectors of adjacent SCA's are separated by 20.3 mm. Yet even at the line where the SCA's meet in the re-sampled image, the band-to-band and SCA-to-SCA registration is within 0.04 mm. For this to be true, both the line-of-sight map and the speed and yaw estimates have to be valid to better than two parts per thousand. This also indicates that the assumption of constant speed and direction is generally valid.

So far, Lincoln Laboratory has lacked the resources to produce geo-referenced Level 1G images. Our geometric re-sampling has relied on image data alone to estimate speed and yaw, rather than reading spacecraft telemetry. We have just begun to use the telemetry data for the simpler problem of deriving the Right Ascension and Declination of stars that were scanned. Apparent departures from the known positions are of order a few tenths of a degree. The discrepancies could result from pitch and roll offsets between the Attitude Control System (ACS) axes and the ALI axes, and from a temporal offset between the ACS readings and the image frame times. Further work should clear up these differences.

3.2.2 Radiometric Performance Assessment

The on-orbit radiometric performance assessment of the Advanced Land Imager consists of deriving radiometric performance characteristics of the instrument and comparing them to measured pre-flight or expected values [25, 26]. This assessment not only assists in ensuring the radiometric accuracy of data collected on orbit, but also assesses ground calibration accuracy, cleanliness of the environment during ground testing, and changes of the instrument response induced by the stresses of launch.

Although the absolute radiometric accuracy of all data collected by the ALI is critical for earth observations, sensitivity, saturation radiance, signal-to-noise ratio, and stability are also key attributes when assessing the technical merit of this instrument for future earth observing missions.

3.2.2.1   Sensitivity

The sensitivity of the ALI has been demonstrated by imaging several cities at night. Figure. 3-96 depicts a panchromatic image of Las Vegas at night on January 22, 2001. Clearly visible are lights from various hotels and casinos. This scene demonstrates the ALI is capable of detecting events with radiances of 0.033 mW/cm^2 sr μm for this band. Table 3-17 lists the sensitivities of each band, as determined from this image.
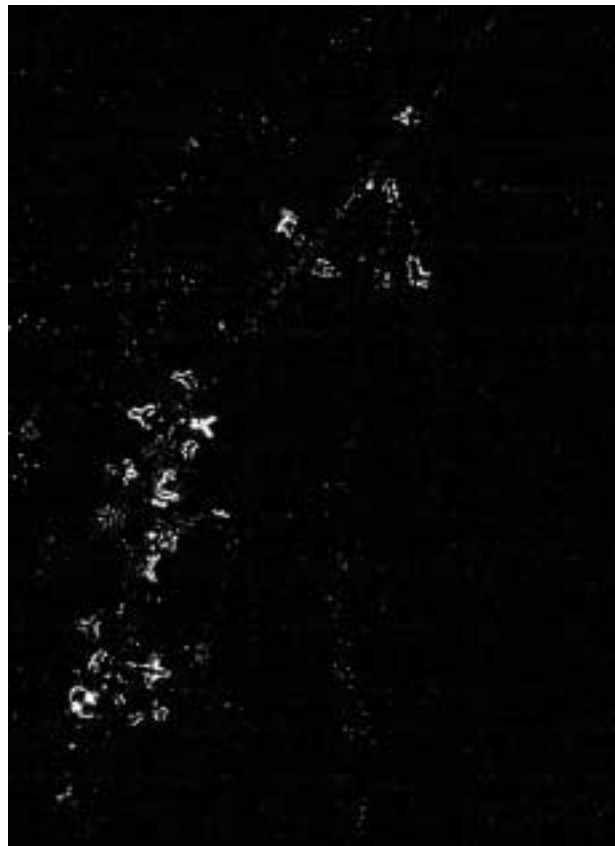

Figure 3-96. Panchromatic image of Las Vegas at night.

TABLE 3-17
ALI Sensitivity

Band	Radiance (mW/cm^2 sr μ)
1p	0.067
1	0.067
2	0.067
3	0.033
4	0.013
4p	0.013
5p	0.100
5	0.033
7	0.013
Pan	0.033

The good sensitivity of the ALI also extends the sources of on orbit sensitivity measurements to include extra-Terran planets and stars. When observed from orbit, these sources can serve as ideal extended and point-like sources that may be used for instrument calibration without the troublesome effects of the Earth's intervening atmosphere inherent in all Earth observations. During the first seven months of operations, the ALI has observed ten stars in the Pleiades star cluster as well as Vega and Rasalhague (Figure 3-98). The result of these measurements has pushed the ALI limiting magnitude to +6.5. Additional sensitivity observations include Venus, Saturn, and Jupiter (including the Jovian moons Io and Ganymede). Figure 3-97 is a collage of several celestial observations made to date.
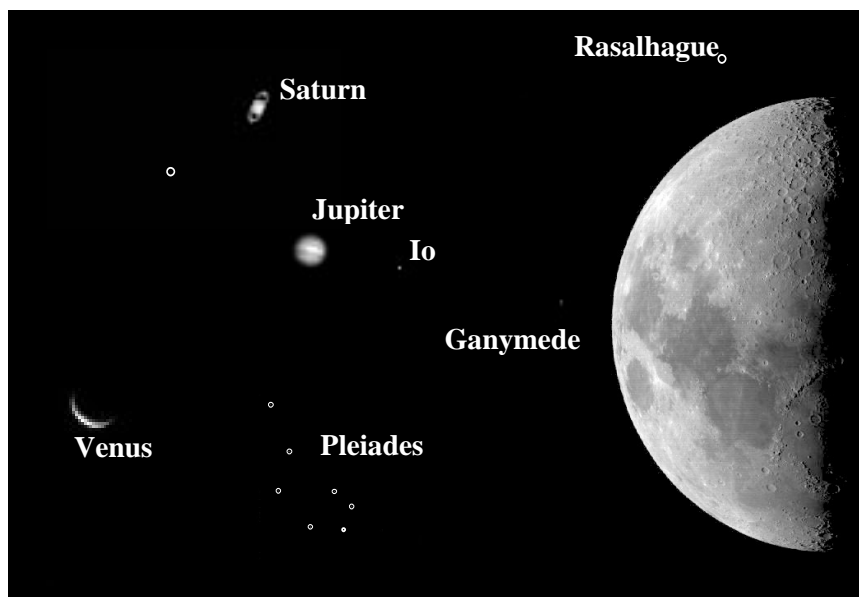

Figure 3-97. Celestial observations performed by the ALI

3.2.2.2 Saturation Radiance

The ALI was designed such that the focal plane would not saturate for mid-latitude summer scenes with 100% Earth equivalent albedo. These high saturation radiances will allow for the direct observation of clouds, snowfields, frozen rivers, and glaciers. The saturation radiances of the ALI have been checked on orbit by observing scenes with high albedo. Figure 3-98 depicts a Band 4,3,2 ALI observation of Hawaii, HI under partially cloudy skies. Figure 3-99 depicts a Band 4,3,2 image of East Antarctica. In each observation the high albedo regions are clearly resolved and not saturated. Table 3-18 lists the maximum radiance and number of counts in each band for each scene.

Figure 3-98. Band 4,3,2 image of Hawaii, HI.

Figure 3-99. Band 4,3,2 image of East Antarctica.

Table 3-18
Response of ALI to high albedo scenes.

Band	Hawaii HI (Clouds)		East Antarctica (Ice)	
	Radiance (mW/cm^2 sr μ)	Counts[1]	Radiance (mW/cm^2 sr μ)	Counts[1]
1p	24.52	1017	15.16	619
1	30.44	1189	18.25	705
2	28.36	1630	15.97	939
3	25.03	2052	13.71	1182
4	20.83	2705	10.68	1424
4p	17.83	2769	8.82	1423
5p	7.92	1492	1.85	342
5	3.43	1573	0.18	82
7	0.76	1246	0.043	72
Pan	27.67	1797	15.19	980

1=Maximum counts = 4095

3.2.2.3 Signal-to-Noise Ratio

The focal plane of the ALI has been designed to provide a signal-to-noise ratio for each band between four and ten times that of the Landsat ETM+. To check signal to noise ratios on-orbit, we have selected three regions of a data set, collected as a part of the on-orbit solar calibration sequence, representing low, medium, and high albedo scenes. Initially, this data is radiometrically calibrated using calibration coefficients derived during ground testing of the instrument at Lincoln Laboratory. Next, regions of constant radiance are identified. The signal to noise ratio for each region is then calculated for each band. Table 3-19 lists the derived signal to noise ratios for all bands.

TABLE 3-19
SIGNAL TO NOISE RATIO FOR VARYING RADIANCES.

Band	Radiance[*]	SNR	Radiance[*]	SNR	Radiance[*]	SNR
1p	4.78	151	14.79	339	34.92	520
1	5.55	245	17.08	572	41.1	1263
2	5.11	310	16.10	1001	38.28	1536
3	4.29	343	13.37	1039	31.99	1933
4	3.34	358	10.44	722	25.03	1123
4p	2.80	350	8.73	710	20.93	1145
5p	1.40	263	4.42	662	10.66	1258
5	0.68	341	2.15	1040	5.13	1606
7	0.22	274	0.68	912	1.63	1636
Pan	4.82	215	15.04	348	36.01	703

[*] $mW/cm^2\,sr\,\mu$

3.2.2.4 Absolute Radiometry

The absolute radiometric accuracy of the Advanced Land Imager defines the ability to make accurate, quantifiable measurements of a scene's radiance in each of the instrument's ten spectral bands. On-orbit, the absolute radiometric accuracy of any mission is challenged by stray light, instrument aging, and the space environment. We have adopted five independent calibration techniques in an attempt to establish and maintain the radiometric accuracy of the ALI over the duration of the mission: pre-flight calibration, solar calibration, lunar calibration, ground truth measurements, and intersatellite comparisons.

The basis for the on-orbit radiometric accuracy of the Advanced Land Imager is pre-flight calibration (Section 3.1.4). However, in order to assure the accuracy of these measurements and to assess changes in the instrument response over time, on-orbit calibration techniques are also required.

3.2.2.4.1 Solar Calibration

Solar calibration is the primary method of on-orbit radiometric calibration of the ALI. The solar calibration procedure, which is illustrated in Figure 3-100, involves pointing the ALI at the sun with the aperture cover closed. A motor-driven aperture selector in the aperture cover assembly moves an opaque slide over a row of small to increasingly larger slit openings and then reverses the slide motion to block all sunlight. A series of seven discrete aperture areas can be obtained. Just prior to solar calibration, a space grade Spectralon® diffuser plate is swung over the secondary mirror by a motor-driven mechanism. The diffuser reflectively scatters the sunlight that would otherwise impinge on the secondary mirror. The scattered sunlight exposes the FPA to irradiance levels equivalent to earth-reflected sunlight for albedos ranging from 0 to 100%.
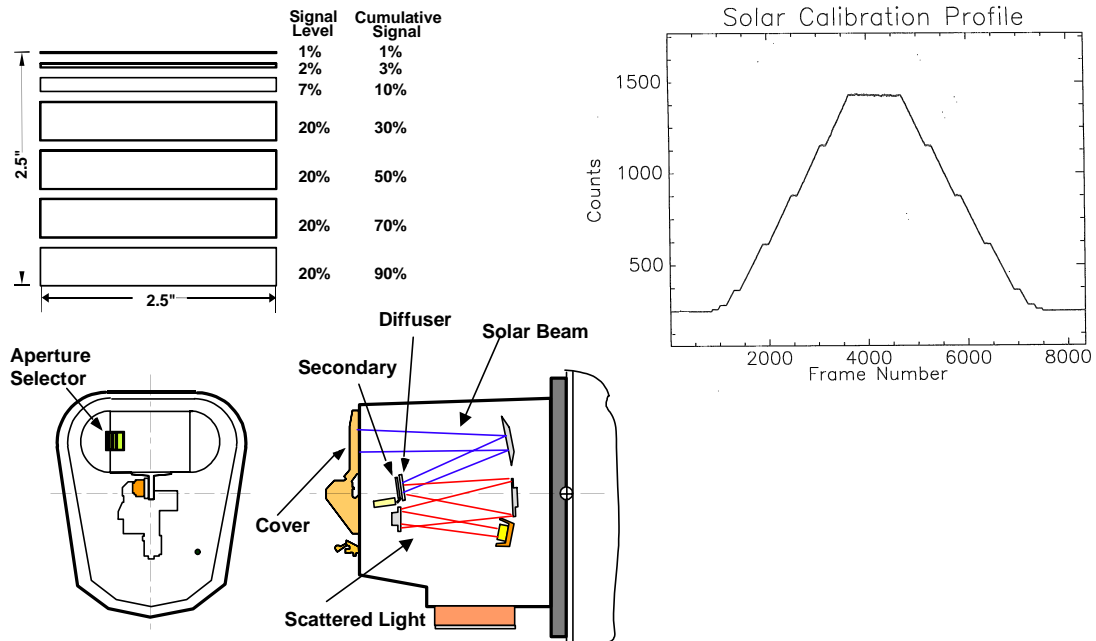
Figure 3-100. Illustration of the solar calibration mode and laboratory test data from a solar simulator.

During solar calibration the optical throughput differs from a normal data collection because the Spectralon BRDF replaces the reflectance of the secondary mirror. Measurements of the BRDF were made on a spare flight quality Spectralon disk over a spectral range of 400 to 900 nm and for the appropriate angles of incidence and reflection at NASA's Goddard Space Flight Center. Values outside this spectral range were estimated by assuming that they scale as the total hemispherical reflectance, which was measured by Labsphere®. The resulting BRDF is shown in Figure 3-101.
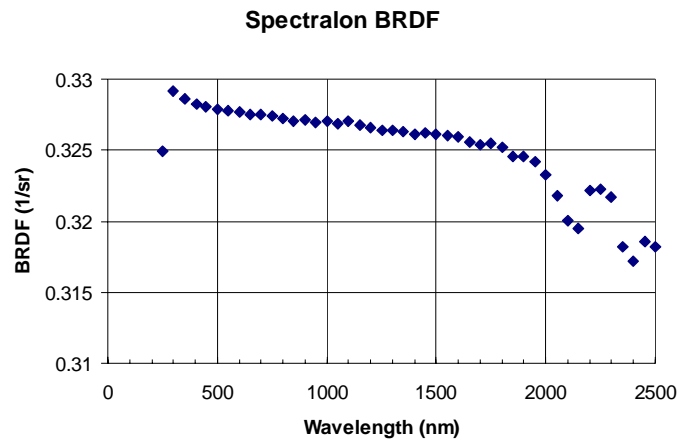
Figure 3-101. BRDF of diffuser located in front of the ALI secondary mirror used in the solar calibration model.

3-120

A detailed CODE V® optical analysis has provided the ratios of the irradiance at the FPA to the solar irradiance at the sub aperture for each position of the aperture selector. For a given sub aperture the FPA irradiance was shown to vary by 2% over the full 15º field of view and by less than 1% over the region populated by detectors. The irradiance at the FPA is thus a known function of the aperture slot opening and solar irradiance. This FPA irradiance corresponds to a known effective radiance at ALI entrance. The detector channel output corresponding to this effective radiance provides the solar calibration.

Two solar irradiance models have been used in the analysis: the MODTRAN 4.0 – CHKUR model, which is currently being used for all Landsat 7 solar calibration derived gains, and the World Radiation Center (WRC) model. The solar irradiance correction factor (F) that is used to account for the varying earth sun distance is given by the approximation:

$$F = [\ 1+e \ \cos((d-4)360/365)]^2 /[1-e^2 \ ]^2$$

where d is the day of the year and e = 0.01671 is the eccentricity of the earth's orbit. Finally, the ALI must be pointed at the sun such that all of the sunlight coming through the sub aperture falls on the Spectralon. The calculated margin of error in the ALI pointing is 0.5 degrees. Half of this error tolerance was allocated to the spacecraft and half to the ALI alignment.

The detector response during a solar calibration sequence consists of an approximately linear increase as the aperture opens with a series of constant responses during those times when the slide passes over a reference bar. These bars provide a set of seven calibrated response points. When the aperture cover reverses direction and closes, the pattern of response reverses and proceeds back down to zero. Typical examples of detector responses for each of the ten ALI spectral bands are shown in Figure 102.
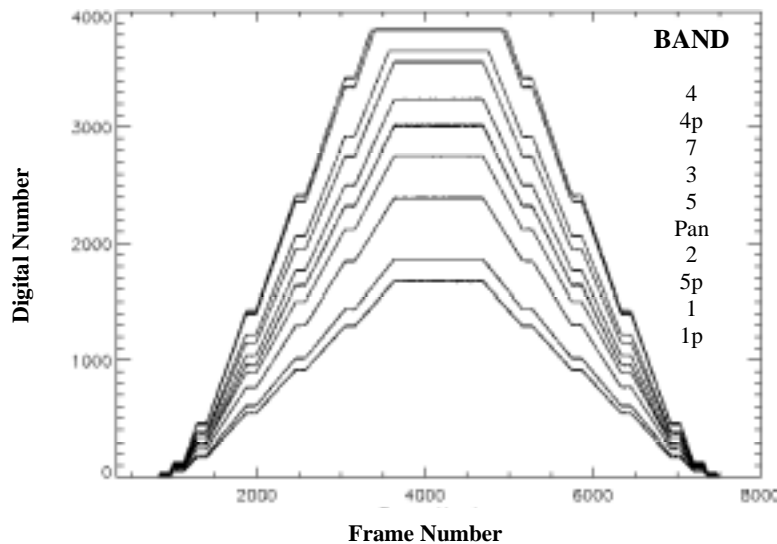

Figure 3-102. Measured detector responses for the ten ALI bands during a solar calibration.

The flux level at the maximum or seventh level corresponds approximately to a 100% albedo at a 30º solar zenith angle. For the data shown, only bands 4 and 4p saturate at this maximum input level. The estimated radiances using the pre-launch calibration for each band are normalized to the expected values from the solar model and are shown in Figure 3-103. These data are plotted at the mean wavelength of the band. Results for two solar irradiance models are shown. Notice the significant differences between the two models in the SWIR region.
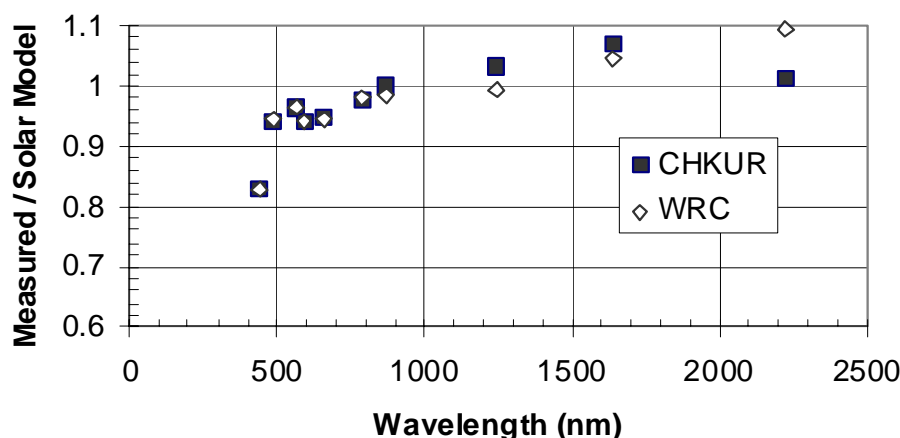
Figure 3-103. Ratios of measured radiances to calculated radiances from the solar model.

With the exception of band 1p, the solar and pre-launch calibrations agree to within the estimated uncertainties of the two independent techniques. The pre-launch calibration accuracy combined with the additional on-orbit effects of contamination is currently estimated to be less than 5% for all bands. The solar calibration uncertainty is currently estimated to be 5% in the VNIR bands and 7% in the SWIR bands. The larger uncertainty in the SWIR bands is due to both the uncertainty in the solar irradiance models and the BRDF of the Spectralon. The low response in band 1p is a significant discrepancy between the two calibration techniques. The solar calibration data exhibit two other interesting trends, which are of lesser significance. There is a general increase in the ratios with increasing wavelength as can be seen in Figure 3-103.

3.2.2.4.2 Lunar Calibration

Lunar calibration is another method of assessing the radiometric accuracy of the instrument. Since no absolute radiance measurement of the moon by ground teams or other satellites have been published, only relative comparisons of data in ALI bands to other sensors can be made at this time. Lunar calibration involves calculating the spectral irradiance of the moon for an ~7º phase angle and comparing the result to irradiance measurements obtained by the SeaWifs satellite for several of the ALI bands.

Lunar scans of the ALI have been conducted each month since January 2001. For each observation, the spacecraft is maneuvered to scan the moon in the in-track direction at ¼ the nominal scan rate in order to oversample the moon. Because the moon has ~ ½ º diameter, it is scanned four times – once per sensor chip assembly.

To calculate the lunar irradiance, the image is first radiometrically calibrated using the pre-flight calibration coefficients. A region of interest, narrowly circumscribing the moon, is then defined (Figure 3-104).

Figure 3-104. Image of the moon taken by the ALI on February 7, 2001. The circle surrounding the moon describes the regions used in the lunar irradiance calculations.

Summing the response within the circumscribed region, the spectral irradiance of the moon for each band may be calculated as

$$E_M(\lambda) = \frac{d\Theta\Delta}{fF} \sum L_P(\lambda)$$

Here, $E_M(\lambda)$ is the lunar spectral irradiance, $d\Theta$ is the ALI pitch rate during the scan (radians/second), Δ is the detector pitch, f is the ALI focal length, F is the frame rate (Hz), and $L_P(\lambda)$ is the measured lunar spectral radiance for detector P.

The lunar irradiance observed on February 7, 2001 is shown in Figure 3-105.
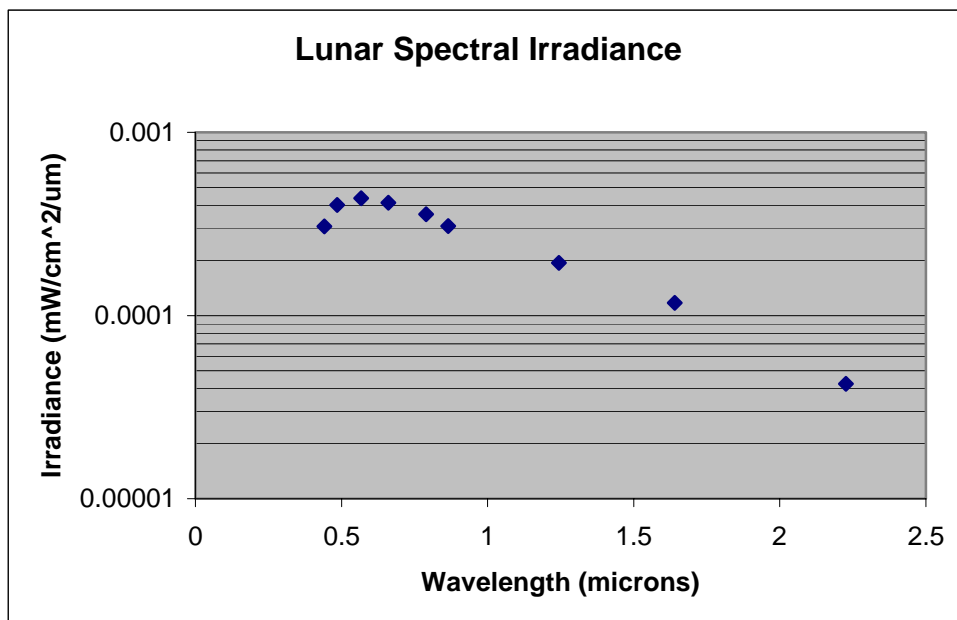
Figure 3-105. Inrradiance observed by the ALI during the February 7, 2001 lunar calibration scan.

Once the lunar spectral irradiance is measured, the ALI data is compared to SeaWifs data. The SeaWfis sensor has four bands equivalent to ALI bands 1p, 1, 2, 3, and 4p. Eliminating ALI data for other bands and normalizing to the measured SeaWifs response for Band 4p, the relative responses of the remaining bands may be obtained. Figure 3-106 shows the relative spectral irradiance measurements of SeaWifs to ALI, overlaid with the previous results from the solar calibration. Inspection of this figure reveals a remarkable agreement between the solar and lunar calibration results for all bands. All data agree to within 1% between these two independent techniques. This result immediately strengthens the results of solar calibration, validates the lunar and solar calibration approaches, and implies the slight drop in ALI response in the blue and significant drop for Band 1p is real.
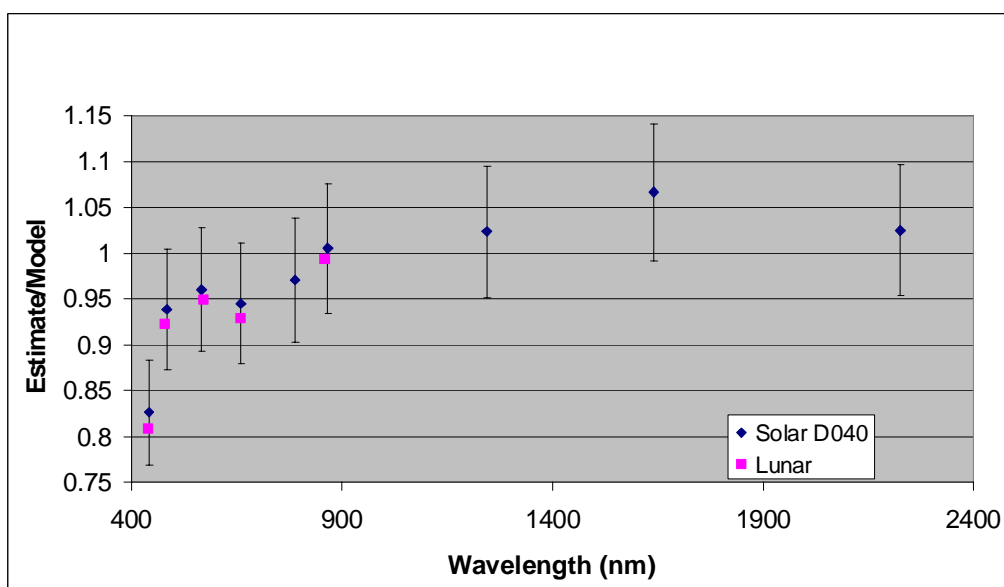
Figure 3-106. Results of solar and lunar radiometric calibrations.

3.2.2.4.3 Ground Truth Calibration

The next method of assessing the radiometric accuracy of ALI data hinges on ground truth measurements. This basic principle of this technique is to image a stable, flat, diffuse ground target using the ALI while simultaneously measuring reflectivity properties of the target region and local atmospheric conditions. The ground measurements can then be used to calculate the top of the atmosphere radiance seen by the ALI.

A large ground truth campaign was conducted in Argentina in February 2001 as a part of the EO-1 Science Validation Team performance assessment period. The results of the University of Arizona ground truth measurements at Barreal Blanco are overlaid with solar and lunar calibration measurements in Figure 3-107 [27]. The ground truth measurements agree with all solar and lunar calibration measurements within experimental error, except for Band 5. For this band, the measured ALI radiance is 15% higher than the expected level.
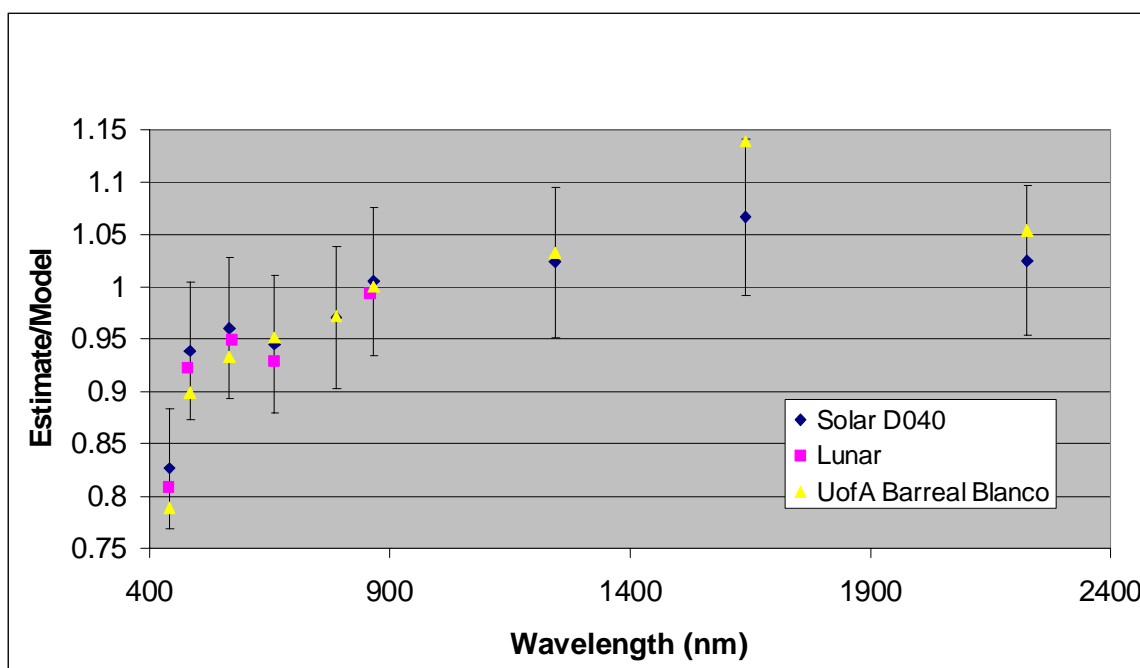
Figure 3-107. Results of solar, lunar, and ground truth radiometric calibrations.

3.2.2.4.4 Intersatellite Comparisons

The final method used in assessing the radiometric accuracy of the Advanced Land Imager is intersatellite comparison. The EO-1 spacecraft is orbiting the earth in a constellation of four spacecraft: Landsat 7 (10:01 AM descending node), EO-1 (10:02 AM), SAC-C (10:14 AM), and TERRA (10:42 AM). Since these spacecraft closely follow one another, a target can be imaged by instruments on all these satellites within a 41-minute period. This allows for an intercomparison of satellite data for flat, diffuse, stable regions.

To date, a comparison between EO-1 ALI and Landsat 7 ETM+ data have been conducted for three sights: the California Super Site (January 14, 2001), Railroad Valley (January 5, 2001), and Barreal

Blanco (February 22, 2001). For each of these observations, Bands 1, 2, 3, 5 and 7 of the ALI and ETM+ may be directly compared, due to the similarity of each instrument's spectral response. For all observations, the ALI measured radiance is consistently 2-4% lower than the ETM+ radiances for Bands 1, 2, and 3. Band 7 is consistently with ±2% of the ETM+ measurements. Finally, ALI Band 5 measurements are consistently 12-15% higher than ETM+ measured radiances. The results of the EO-1, Landsat 7 intercomparisons, along with other results are displayed in Figure 108. The intercomparison results are consistent with solar, lunar, and ground truth measurements for Bands 1, 2, 3, and 7. The intercomparison also agrees with ground truth data but disagrees with the solar calibration data for Band 5.
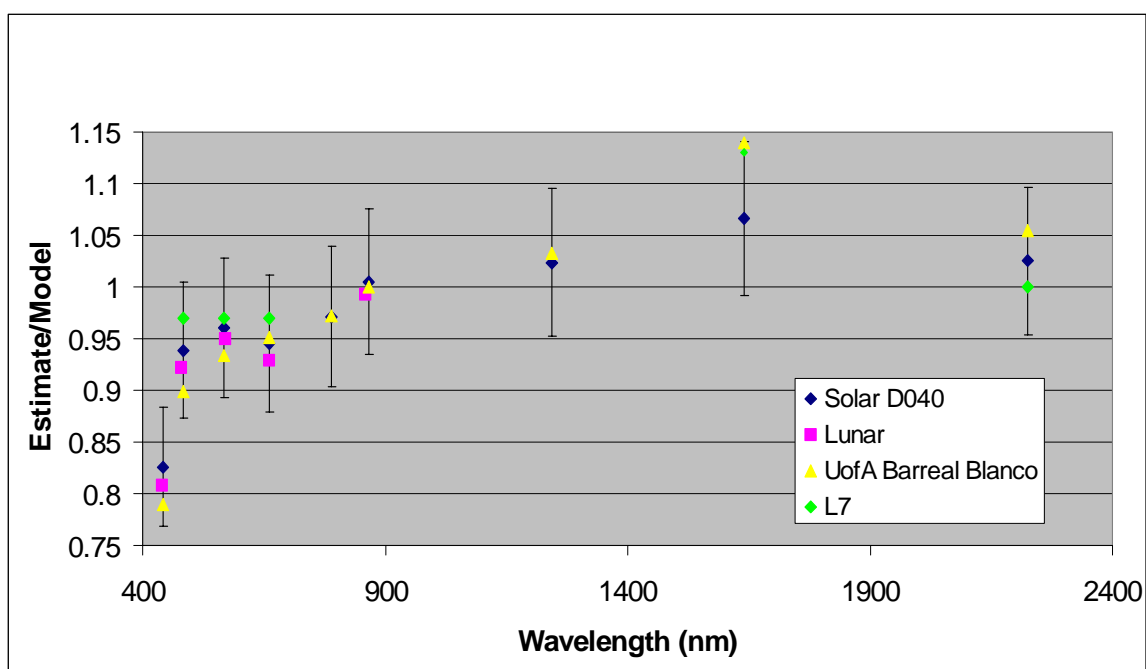
Figure 3-108. Results of solar, lunar, ground truth, and intersatellite radiometric calibrations.

3.2.2.5   Stability

The stability of the ALI has been measured on orbit using internal reference lamps and solar calibration measurements. However, instrument stability can become clouded by contamination of the focal plane. We have considered the periods unaffected by contamination to be the best times to measure the intrinsic stability of the instrument. This assumes than effects of contamination will not be experienced for future missions. The effects of contamination on the instrument response will be discussed in Section 3.3.3.

Internal reference lamp data has been collected at least once per day since the ALI was powered on orbit (November 25, 2000). To begin assessment of the ALI stability using this data, we select periods directly after ALI outgassing periods and label these as 'clean' periods. The ratio of 'clean' periods to the original 'baseline' internal reference lamp data collected on December 1, 2000 is then calculated.

Finally, the mean of each ratio is plotted as a function of days since launch. An example of internal reference lamps stability data for Band 1p is shown in Figure 3-109.
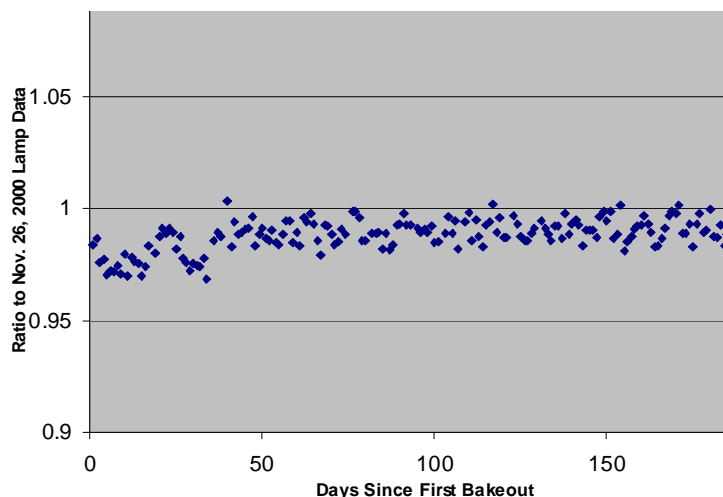

Figure 3-109. Band 1p stability of the ALI focal plane, flat mirror, and internal reference lamps during the first six months on orbit.

The internal reference lamp data suggest each band has been stable to within 2% during the first 200 days on orbit. However, one must recall that these lamps only reflect off the ALI flat mirror and flood illuminate the focal plane. Therefore, this result should only be applied to these regions of the instrument.

Another technique to measure the stability of the instrument uses solar calibration data. Using this data, stability of instrument M1, M3, and flat mirrors, as well as the solar diffuser and focal plane may be assessed. For this analysis, solar calibration data collected on June 15 has been specified as the 'baseline' data. All other data are considered 'test' data. The first step in assessing the ALI stability using this technique is to account for the $1/r^2$ effect introduced into each data set by the varying distance between the sun and the earth over time. The ratio of 'test' data to 'baseline' data, for the same aperture selector level, are then calculated for each period. Finally, the mean of each ratio is plotted as a function of days since launch. An example of solar calibration stability data for Band 1p is shown in Figure 110. This data suggests each band has been stable to within 1.5% since January 9, 2001.
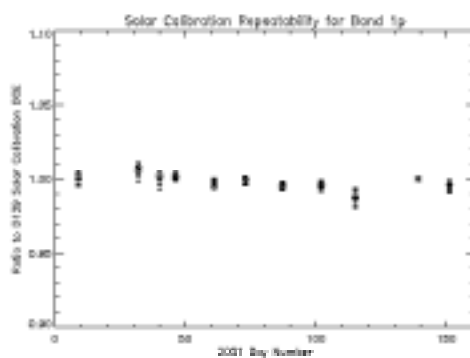

Figure 3-110. Band 1p stability of the ALI focal plane, M1mirror, M2 mirror, flat mirror, and solar diffuser panel during the first six months on orbit.

The radiometric performance of the Advanced Land Imager has been investigated using several on-orbit techniques. Excellent sensitivity has been demonstrated by imaging cities at night as well as stars and extra-Terran planets. Stability measurements indicate the instrument has been stable to within 2% since launch for all bands.

Solar, lunar, ground truth, and intersatellite radiometric measurements all agree within experimental error in the VNIR and suggest a slight drop in the blue response from pre-flight calibration measurements. Additionally, solar and lunar calibration data indicate a significant drop in Band 1p response.

Possible sources of the VNIR disagreement include 1) poor pre-flight calibration, 2) contamination, and 3) stray light. Poor pre-flight calibration is unlikely because the Goddard produced Landsat Transfer Radiometer (LXR) was used to measure the radiance emitted by the integrating sphere used for pre-flight calibration at Lincoln Laboratory. These measurements agreed to within 2% for all LXR bands and integrating sphere levels. This agreement adds strength to the validity of the pre-flight calibration measurements.

Contamination is another possible source of radiometric error. Problems with focal plane contamination were recognized early in the characterization of the ALI at Lincoln Laboratory (Section 3.1.1). Additionally, the instrument was exposed to 18 months of ground testing at Swales Aerospace and Goddard Space Flight Center after being integrated with the spacecraft. Although no direct evidence of contamination was observed during this period, prolonged exposure to a test environment leave paths for contamination to intervene.

A third source of radiometric error is stray light. During the construction of the flight telescope, SSG informed Lincoln Laboratory that it was having difficulty meeting the specification of the mirrors' figures and finish within schedule and budget. The program directed SSG to concentrate efforts on the mirror figure in order to make the flight schedule and validate all ALI technologies. Subsequently, the telescope was delivered with excellent mirror figure but with poor finish on the primary and tertiary surfaces. A ray tracing analysis of the flight telescope by Lambda Research suggested stray light would significantly affect the Band 1p and 1 radiometric accuracy of the instrument.

The principle components of stray light can be described by first defining a reference detector. Detectors whose fields of view are within three degrees of the reference detector's field are then considered neighbors. Sources of stray light may then be described as 1) scattering from the reference detector's field of view into those of its neighbors, 2) scattering from neighboring detectors' fields of view into the that of the reference detector, and 3) scattering of scene radiance off the black surfaces surrounding the secondary mirror into the fields of all detectors. A model of the expected effect from these components was developed and may be expressed analytically as

$$\Delta L_R = \{\sigma_B / [1 - \sigma_T + (\sigma_P + \sigma_B)]\}\{L_B - L_R\}$$

Here, ΔL_R is the percent error in the true radiance of a reference detector's scene, σ_T is the percent of the reference detector radiance scattered into the neighboring detector fields, σ_P is the percent of the scene radiance scattered by the black paint into the reference detector, σ_B is the percent of the neighboring radiance scattered into the reference detector, L_B is the radiance observed by the neighboring detectors, and L_R is the radiance of the region observed by the reference detector. Inspection of this relation indicates that if regions observed by the reference detector are brighter than the neighboring regions, the net effect is a loss in measured radiance as signal is scattered out of the field of view. Conversely, is a reference detector observes a region much dimmer than its neighbors, the net effect will be an increase in apparent radiance as signal is scattered into the field of view.

The effect of the stray light model described above for calibration targets has been plotted, along with the results of on-orbit radiometric calibrations, in Figure 3-111.
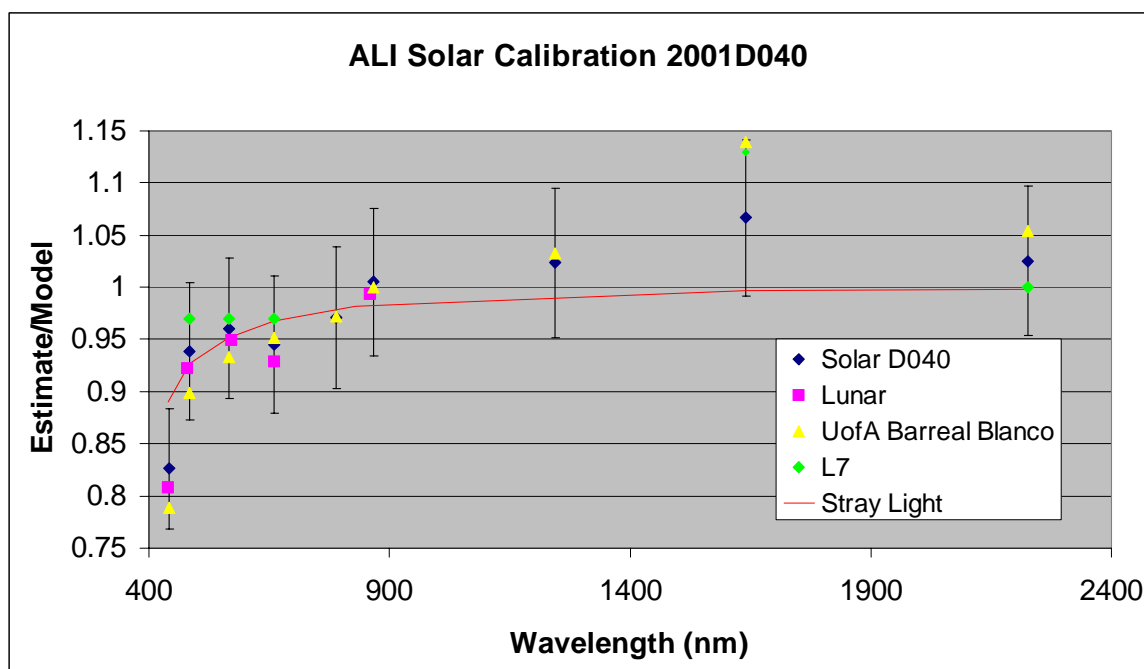

Figure 3-111. Overlay of ALI stray light model and results of on-orbit radiometric calibration.

Inspection of this figure reveals stray light effects track the slight drop in radiometric response in the blue observed in the ALI data. However, it does not explain the significant drop in the Band 1p response or the discrepancy observed in the Band 5 response observed in the flight data. These areas will be the focus of future work.

3.3　On-Orbit Usage Experience

The ALI has undergone significant testing during the first seven months in orbit. This section provides a summary of the electrical and mechanical operations, detector trending, and contamination monitoring between November 21, 2000 and June 21, 2001.

3.3.1 Electrical and Mechanical Operations

3.3.1.1　ALI Electronics

On November 25, 2000 (Day 5 of the mission) the ALI was powered for the first time on orbit. As of June 21 2001, the ALI Control Electronics (ALICE) has been powered continuously for 4990 hours. The focal plane electronics (FPE) is only powered during data collection events or DCEs. 1154 DCEs have been collected for a total FPE powered time of 154 hours.

3.3.1.1.1　Mechanisms and HOPAs

The ALI has three mechanisms and six High Output Paraffin Actuators or HOPAs. The primary mechanism is the aperture cover. The aperture cover has been exercised 1229 times. During solar calibrations, the solar diffuser and aperture selector mechanisms are exercised. These mechanisms have been used 10 times.

The HOPAs are used as launch latches for the aperture cover (2) and solar diffuser (1), and as failsafe latches for the aperture cover (2) and solar diffuser (1). One aperture cover and one solar diffuser launch latch were successfully deployed on November 25, 2000.

3.3.1.1.2　Internal Reference Lamps

The internal reference lamps are used as focal plane stability as well as contamination build-up monitors. Until May 15, 2001 these lamps were exercised as a part of each data collection event. In order to preserve the life of the Krypton bulbs in the event of an extended mission, the lamps are now exercised one or two times per day. As of June 21, 2001 the internal reference lamps had been exercised 851 times. Trending data for periods when the focal plane is not contaminated indicate that the internal reference lamps have been stable to within 1% for all bands.

3.3.2　Detector Trending

The trending of focal plane dark current data has been used to assess detector stability. In this section, we present noise and dark current stability trending and contrast mean values with those determined from pre-flight characterization. Dark current stability over one-half orbit period is also investigated.

3.3.2.1　Dark Current and Noise Trending for the First 60 Days

This section provides detector noise and dark current trending results of the Advanced Land Imager during its first sixty days in orbit (November 21, 2000 – January 19, 2001).

Data are trended for each of the ten spectral bands and each of the four sensor chip assemblies. Additional information may be found on the EO-1-7 project report [22].

3.3.2.1.1 Methodology

The noise and dark current of the Advanced Land Imager have been trended using dark current data collected as a part of daily Earth scene observations. During a typical data collection event or DCE, two seconds of dark current are collected before and after the Earth scene is imaged. These dark currents are used to establish baselines for all detectors for the corresponding observation and are also used to monitor the noise of the focal plane over time. For each DCE, the data from the second two-second dark period is used for the trending in this report[*].

The focal plane has been divided into several sections for this analysis, owing to the different noise and dark current produced by different detectors. For the noise analysis, the focal plane is divided by band and SCA. For the dark current analysis, odd and even detectors are treated separately for all bands. Results for the Panchromatic band have been additionally divided by tri-reads (each Panchromatic detector is read three times for each Multispectral detector read. Each tri-read results in a different dark current value for each detector.). Finally, SCA 4 for the SWIR bands has been divided into four sections to account for the enhanced dark current values observed near detector 1200.

For each data collection event, the noise has been calculated as the mean of individual detector noise values and the dark current has been calculated as the mean of individual detector dark current values.

Data collection event numbers, calendar dates and days since launch are provided as a reference in Table 3-20.

---

[*] All SWIR detectors have a transient effect associated with the initial data collected following the focal plane turn-on. Additionally, ground processing sometimes requires fill data to be added to the end of each data set. As a result, the first and last twenty-five frames from all data sets have been excluded from trending analysis.

Table 3-20
Data Collection Event Dates

Year	GMT Day	Day[*]	Data Collection Event Count
2000	330	5	1-3
	331	6	4
	336	11	5-6
	337	12	7-8
	338	13	9-10
	339	14	11-12
	340	15	13-14
	341	16	15-17
	342	17	18-20
	343	18	21
	344	19	22-23
	345	20	24-27
	346	21	28-29
	347	22	30-32
	348	23	33-36
	349	24	37-41
	350	25	42-44
	351	26	45-46
	352	27	47-51
	353	28	52-54
	354	29	55-59
	355	30	60-63
	356	31	64-66
	357	32	67-70
	358	33	7174
	359	34	75-79
	360	35	80-87
	361	36	88-92
	362	37	93-98
	363	38	99-103
	364	39	104-110
	365	40	111-116
	366	41	117-119
2001	001	42	120-123
	002	43	124-129
	003	44	130-137
	004	45	138-143
	005	46	144-150
	006	47	151-154
	007	48	155-159
	008	49	160-164
	009	50	165-168
	010	51	169-172
	011	52	173-178
	012	53	179-185
	013	54	186-192
	014	55	193-198
	015	56	199-203
	016	57	204-207
	017	58	208-213
	018	59	214-217
	019	60	218-224

[*]Since launch.

The results of the ALI focal plane noise trending are provided in Figures 3-112 to 3-121 and Table 3-21. Each figure depicts the results of an individual band. Within each figure, the results for each sensor chip assembly are provided. Table 3-21 lists the mean and standard deviation of noise values, grouped by bands, in a similar fashion.

The mean noise value levels for all bands and SCAs is less than 1 digital number, except for the Panchromatic Band on SCA 3 (1.15 digital numbers) and Band 7 SCAs 1, 2, and 4 (1.06, 1.09, and 1.01 digital numbers, respectively). The standard deviation of detector noise is less than 0.05 digital numbers for all VNIR bands and SCAs. The repeatability of some SWIR SCAs is slightly higher with a maximum standard deviation of 0.099 digital numbers for Band 7, SCA 2.

The apparent systematic increase in detector noise across several spectral bands for some particular DCEs is the result of focal plane outgassing performed at the times of those observations. All ALI detectors were heated to 270 K five times during the first sixty days in orbit to drive-off contaminant build-up on the focal plane filter surfaces. This heating resulted in increased detector dark current and noise, particularly in the short wave infrared bands (5p, 5, 7). Outgassing periods correspond to DCE numbers 55, 140, 160, 190, and 219.
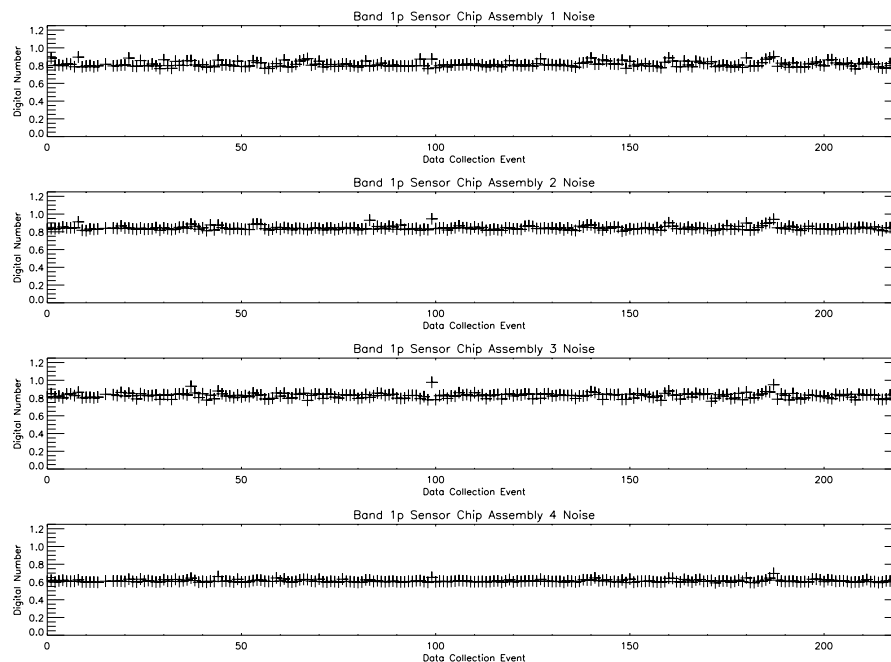
Figure 3-112. Noise trending for Band 1p. Detector outgassing occurred near DCE 55, 140, 160, 190, and 219.
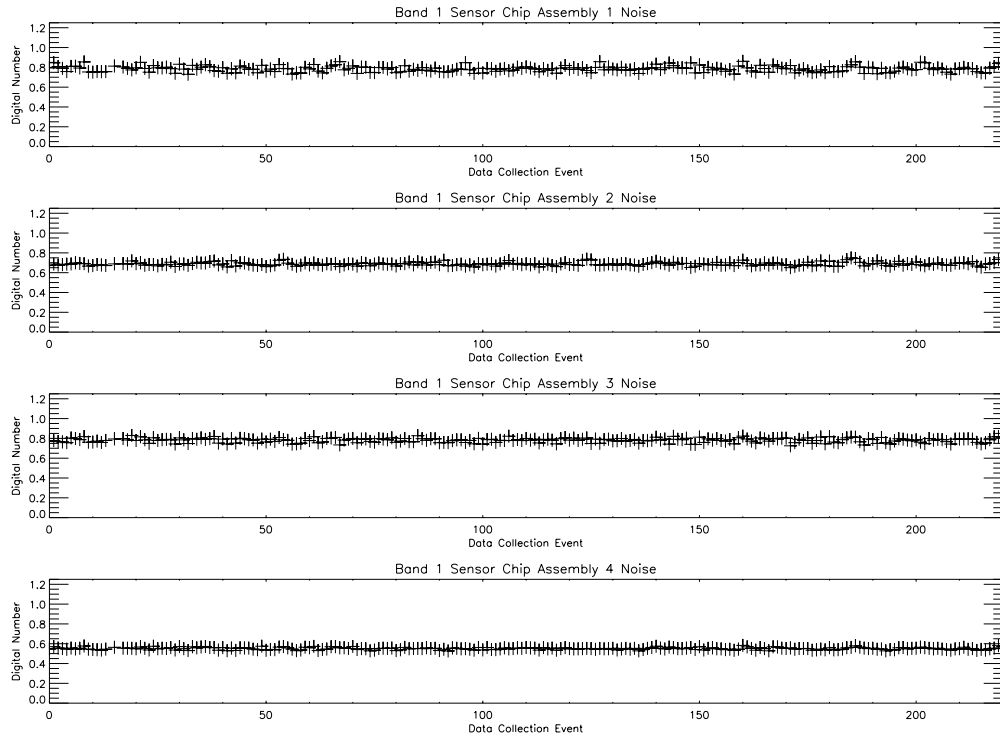
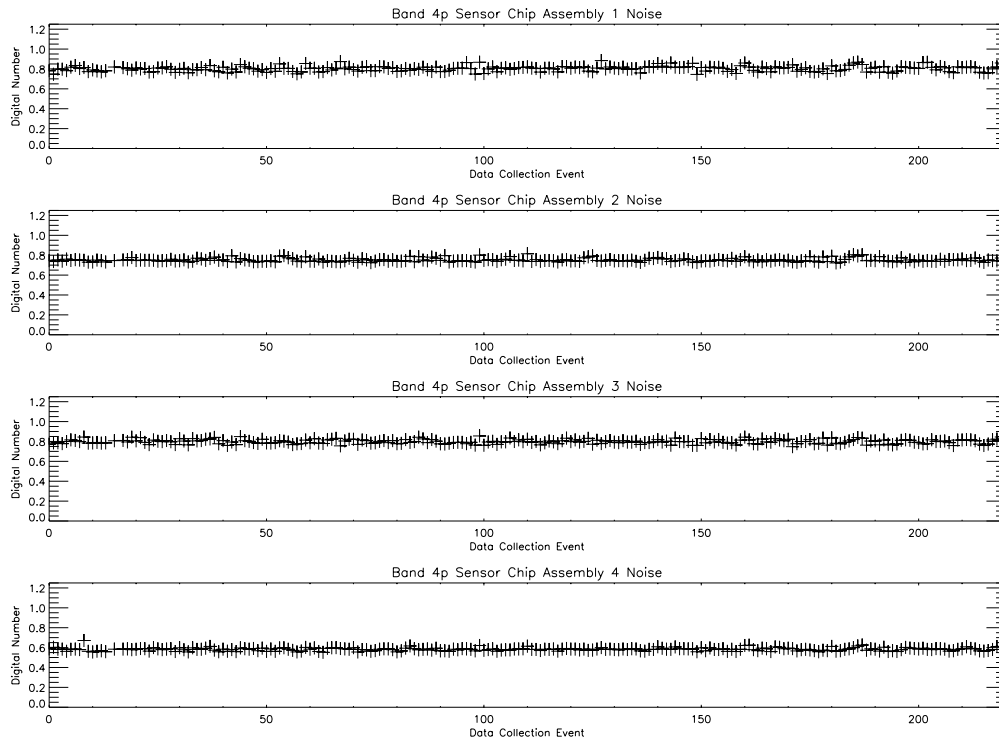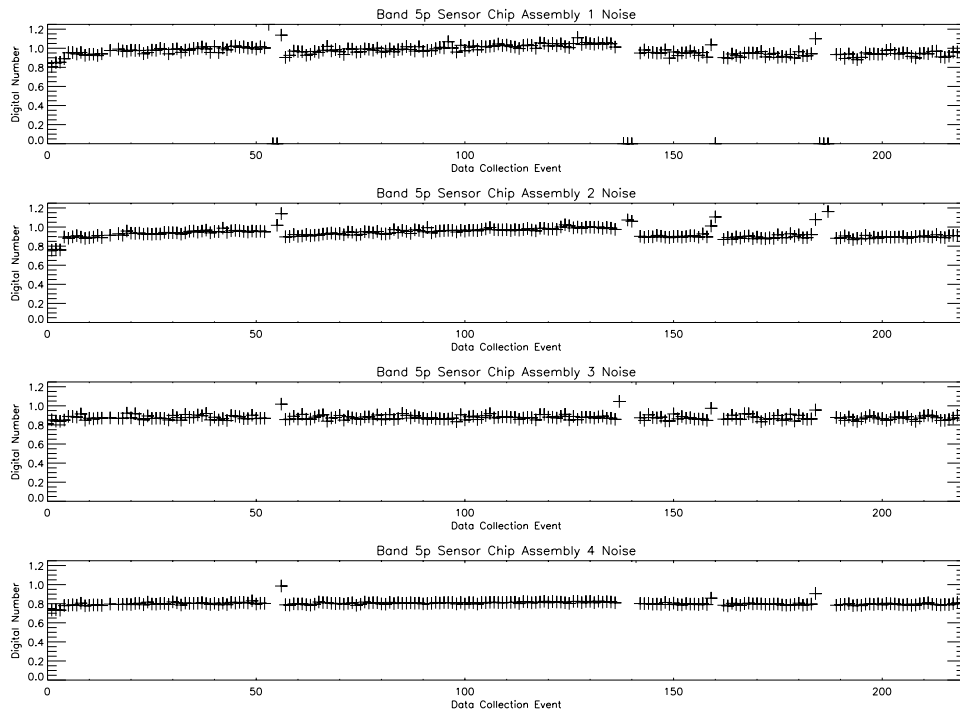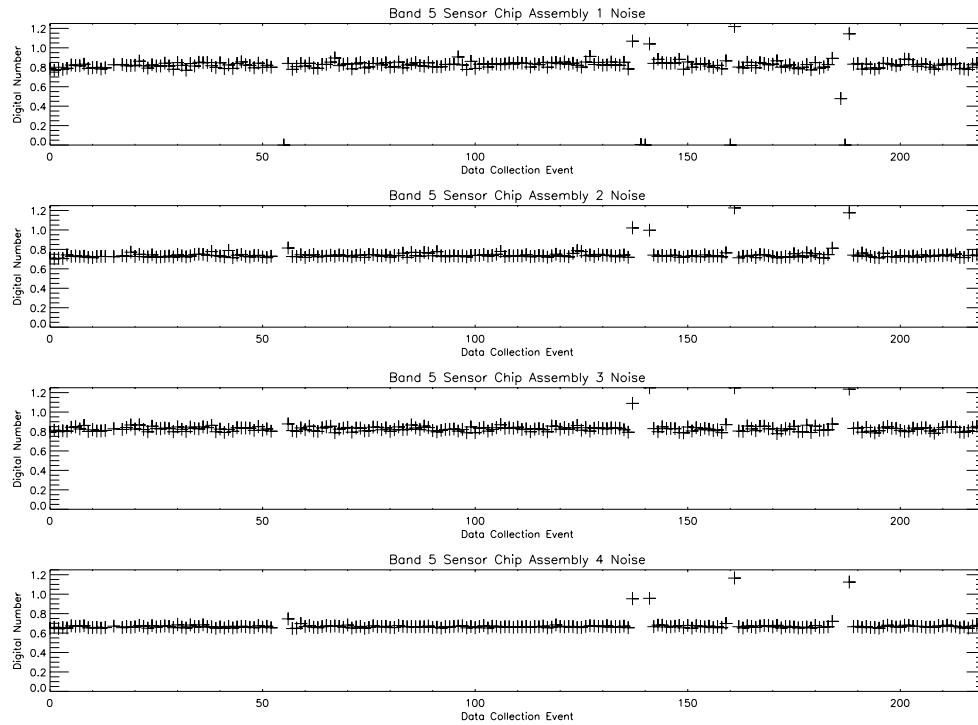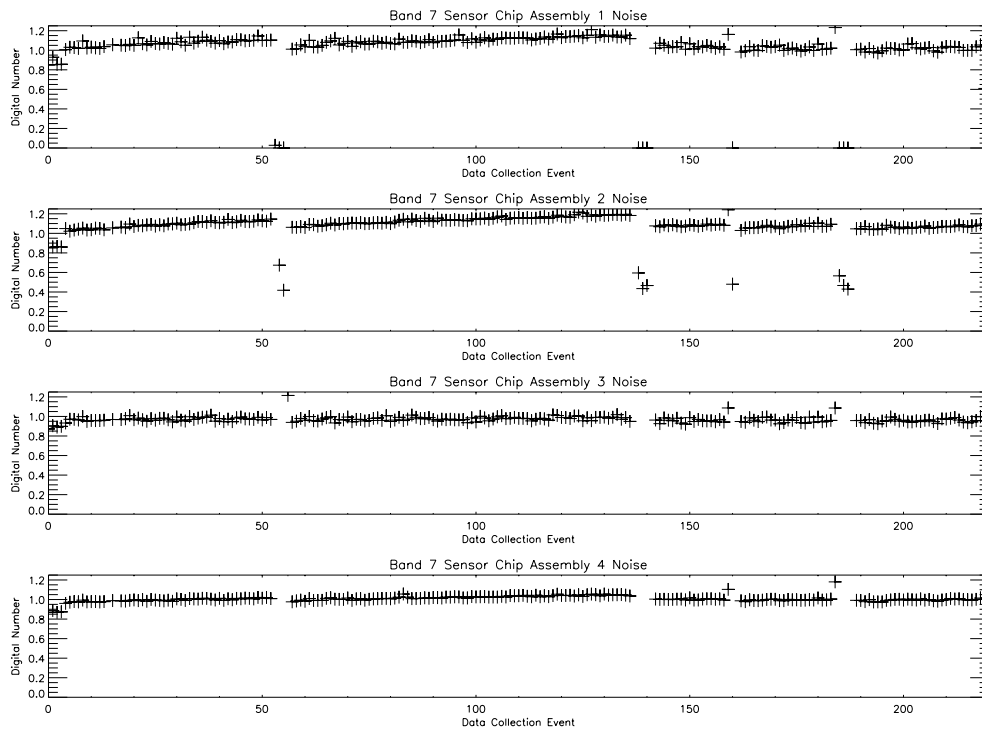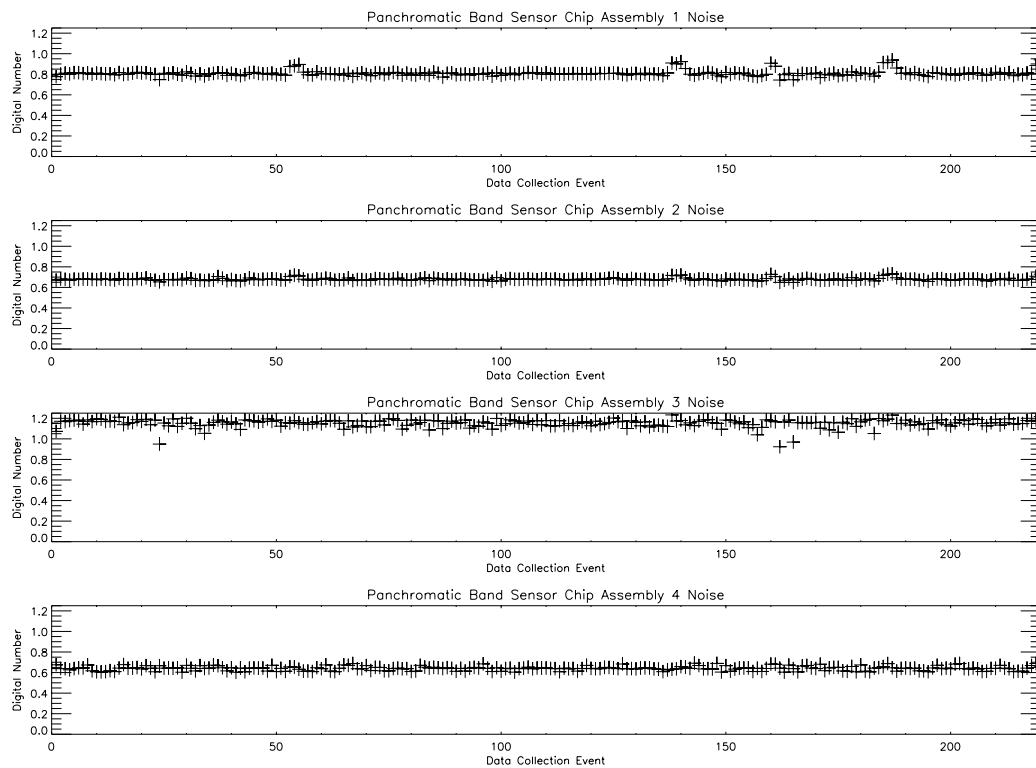*Figure 3-113. Noise trending for Band 1. Detector outgassing occurred near DCE 55, 140, 160, 190, and 219.*
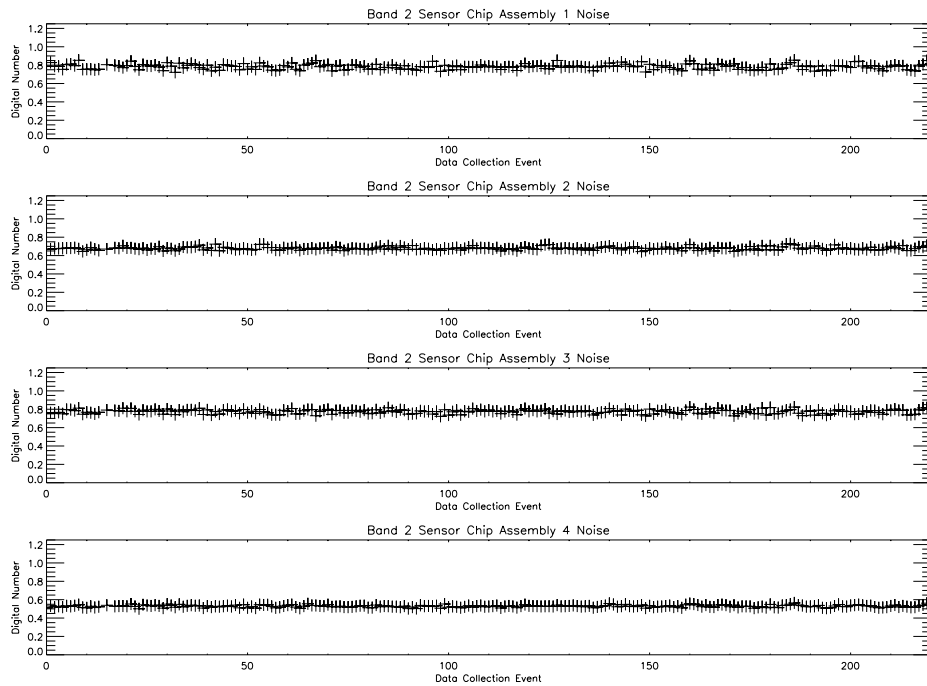
Figure 3-114. Noise trending for Band 2. Detector outgassing occurred near DCE 55, 140, 160, 190, and 219.
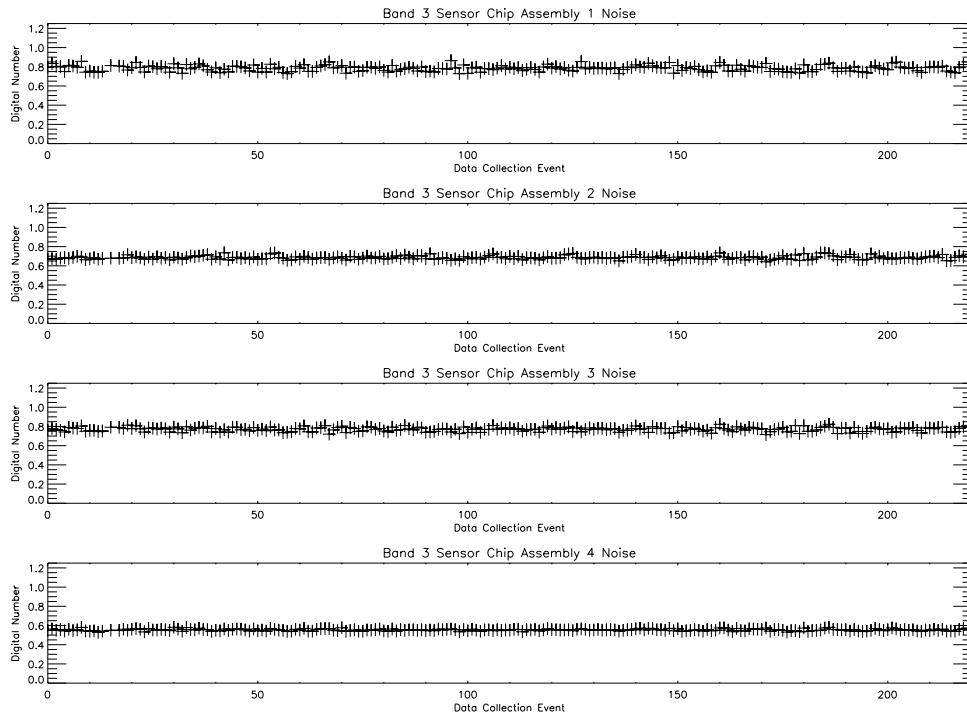
Figure 3-115. Noise trending for Band 3. Detector outgassing occurred near DCE 55, 140, 160, 190, and 219.
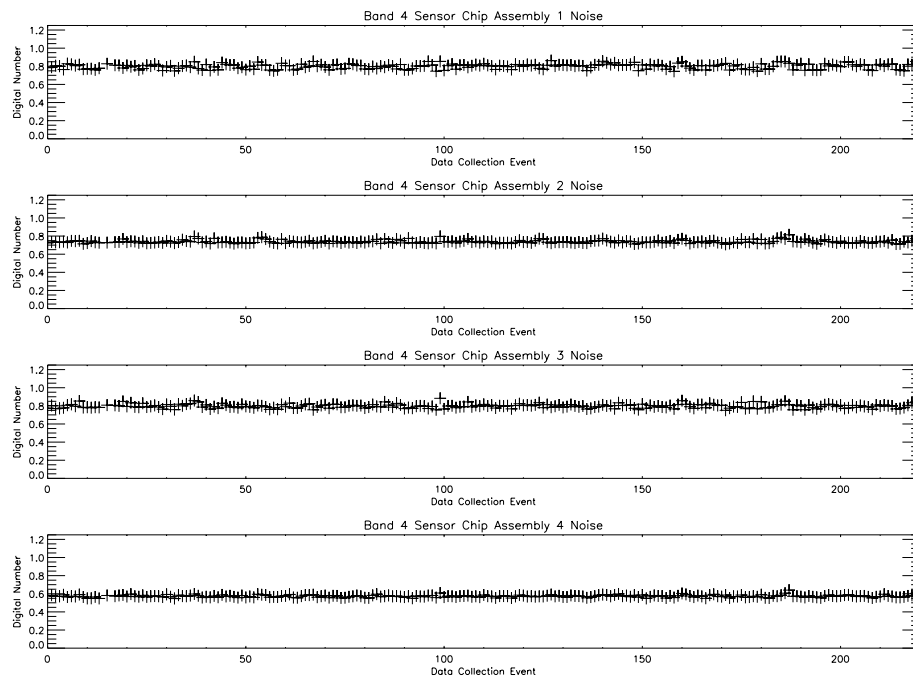
Figure 3-116. Noise trending for Band 4. Detector outgassing occurred near DCE 55, 140, 160, 190, and 219.

Figure 3-117. Noise trending for Band 4p. Detector outgassing occurred near DCE 55, 140, 160, 190, and 219.

Figure 3-118. Noise trending for Band 5p. Detector outgassing occurred near DCE 55, 140, 160, 190, and 219.

3-137

Figure 3-119. Noise trending for Band 5. Detector outgassing occurred near DCE 55, 140, 160, 190, and 219.

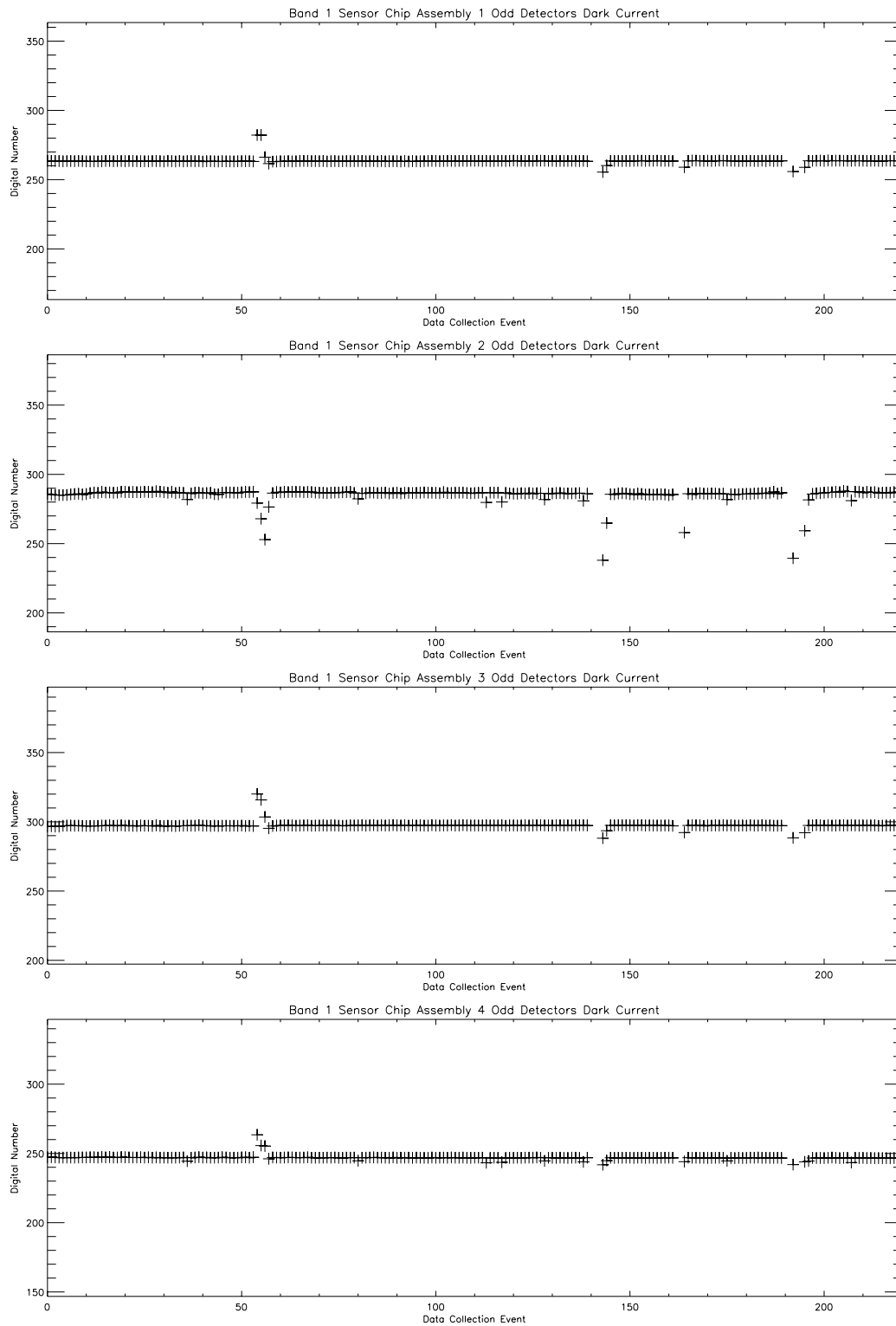*Figure 3-120. Noise trending for Band 7. Detector outgassing occurred near DCE 55, 140, 160, 190, and 219.*

Figure 3-121: Noise trending for the Panchromatic Band. Detector outgassing occurred near DCE 55, 140, 160, 190, and 219.

Table 3-21
Noise Trending Statistics

Band	SCA	Preflight Mean (Digital Number)	Flight Mean (Digital Number)	Flight Std. Deviation (Digital Number)
1p	1	0.88	0.81	0.030
1p	2	0.86	0.84	0.022
1p	3	0.91	0.83	0.028
1p	4	0.60	0.61	0.014
1	1	0.83	0.78	0.029
1	2	0.73	0.69	0.017
1	3	0.87	0.78	0.021
1	4	0.54	0.55	0.012
2	1	0.82	0.78	0.028
2	2	0.70	0.68	0.017
2	3	0.84	0.77	0.022
2	4	0.53	0.53	0.012
3	1	0.83	0.78	0.030
3	2	0.72	0.69	0.018
3	3	0.85	0.77	0.022
3	4	0.55	0.55	0.010
4	1	0.86	0.80	0.029
4	2	0.77	0.74	0.019
4	3	0.88	0.80	0.022
4	4	0.57	0.57	0.013
4p	1	0.85	0.80	0.027
4p	2	0.78	0.75	0.018
4p	3	0.87	0.80	0.022
4p	4	0.58	0.58	0.016
5p	1	0.92	0.97	0.042
5p	2	0.83	0.94	0.031
5p	3	0.92	0.88	0.021
5p	4	0.75	0.81	0.025
5	1	0.87	0.83	0.035
5	2	0.75	0.74	0.035
5	3	0.89	0.83	0.037
5	4	0.67	0.70	0.024
7	1	0.99	1.06	0.068
7	2	0.90	1.09	0.099
7	3	0.98	0.97	0.031
7	4	0.90	1.01	0.037
Pan	1	0.80	0.81	0.029
Pan	2	0.67	0.68	0.013
Pan	3	1.05	1.15	0.039
Pan	4	0.64	0.64	0.021

3.3.2.1.3   Dark Current Trending

The results of the ALI focal plane dark current trending for Bands 1p, 1, 2, 3, 4, 4p are provided in Figures 3-122-3-133. Each figure depicts the results of an individual band. Within each figure, the results of odd and even detectors for each sensor chip assembly are provided. The results of dark current trending for Bands 5p, 5, and 7 are provided in Figures 3-134 to 3-139. Each figure depicts the results of an individual band. Within each figure, the results of odd and even detectors for each sensor chip assembly are provided. SCA 4 is further divided into four quadrants, owing to the rapid change in dark current near the previously identified 'hot spot' near detector 1200 [21]. Finally, the results of dark current trending for the Panchromatic Band are provided in Figures 3-140 to 3-145. Each figure depicts the results of an individual tri-read. Within each figure, the results of odd and even detectors for each sensor chip assembly are provided.

Table 3-22 lists the mean and standard deviation of dark current values, grouped by bands, in a similar fashion.
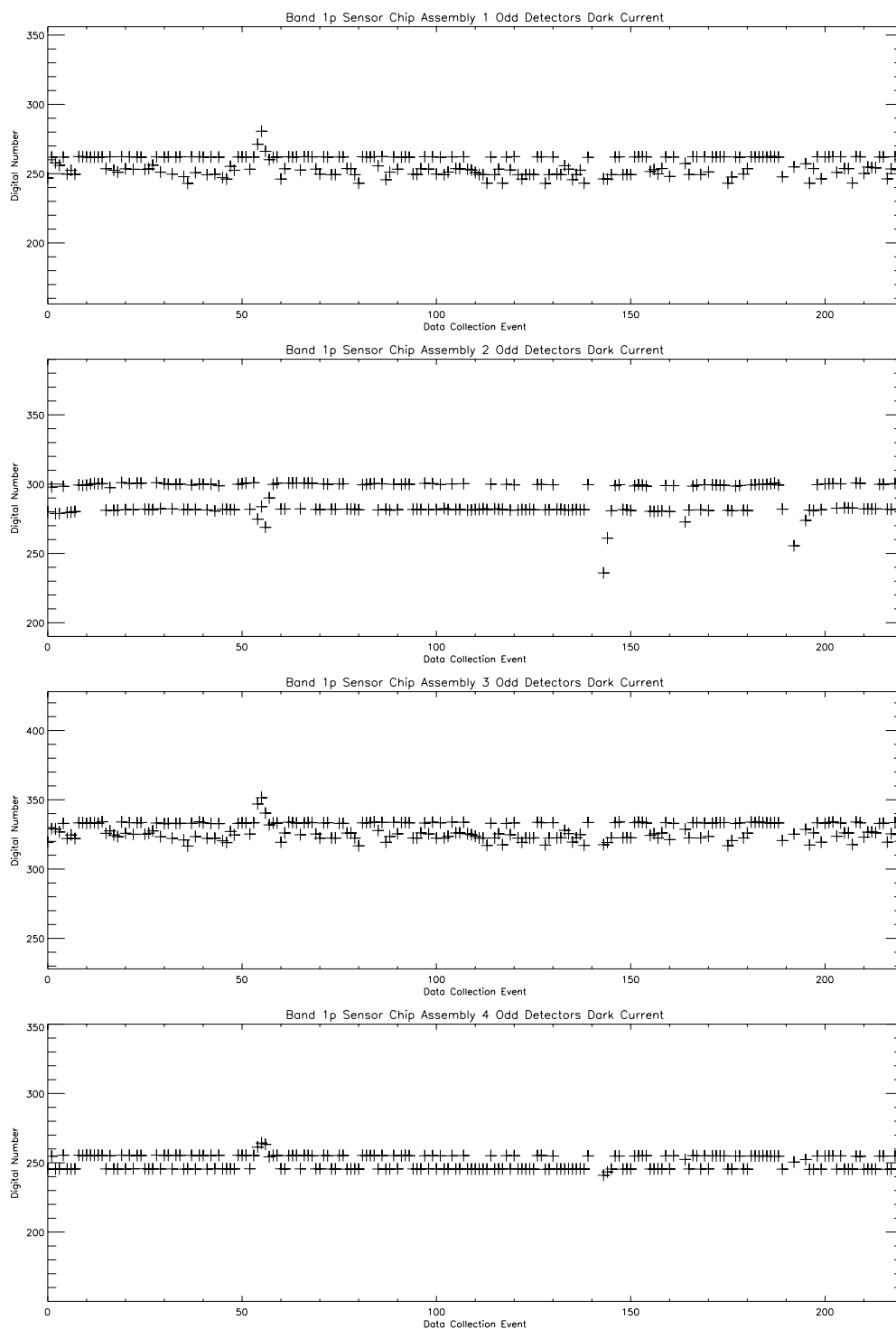
Figure 3-122. Dark current trending for Band 1p odd detectors. Detector outgassing occurred near DCE 55, 140, 160, 190, and 219.

Figure 3-123. Dark current trending for Band 1p even detectors. Detector outgassing occurred near DCE 55, 140, 160, 190, and 219.
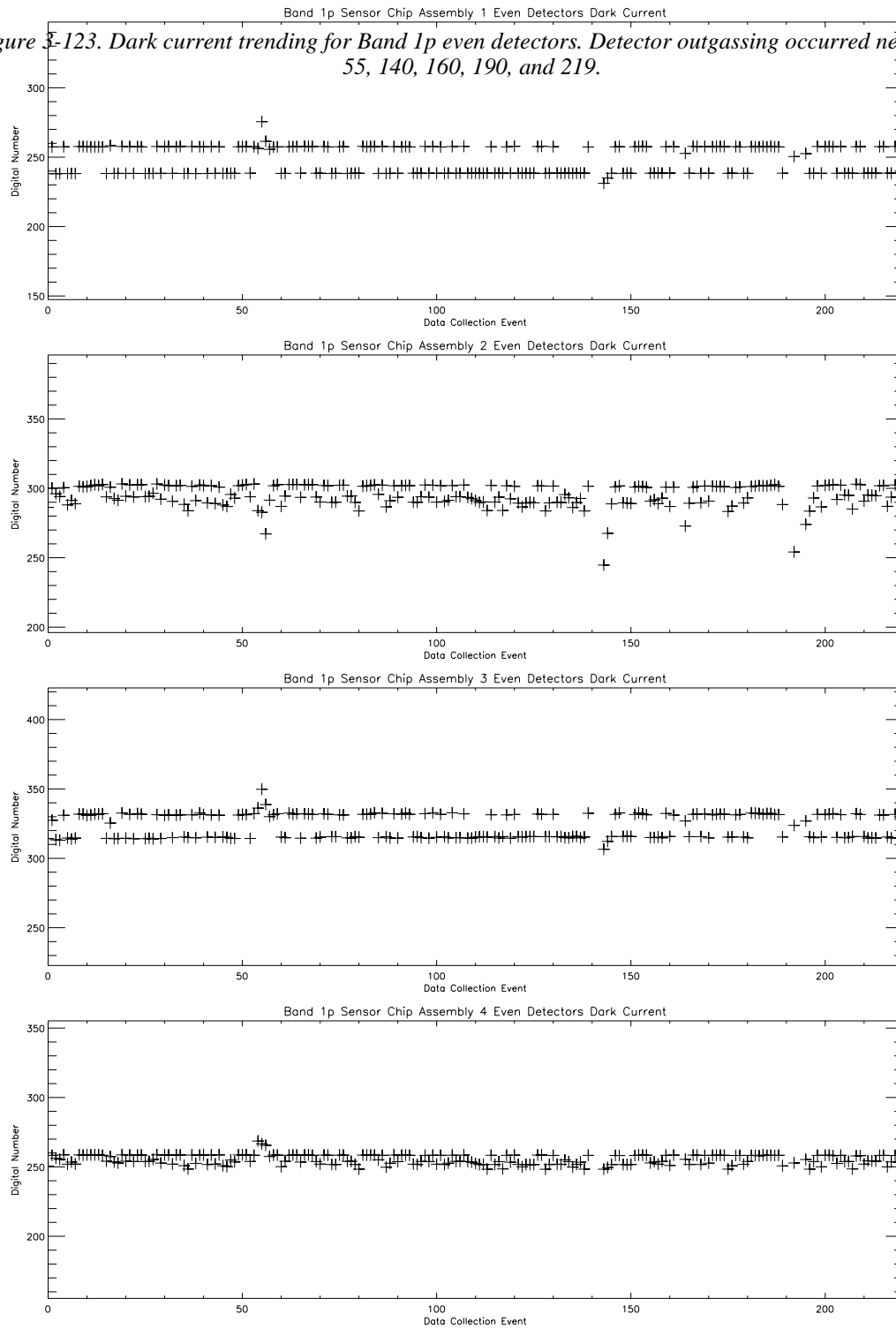
Figure 3-124. Dark current trending for Band 1 odd detectors. Detector outgassing occurred near DCE 55, 140, 160, 190, and 219.
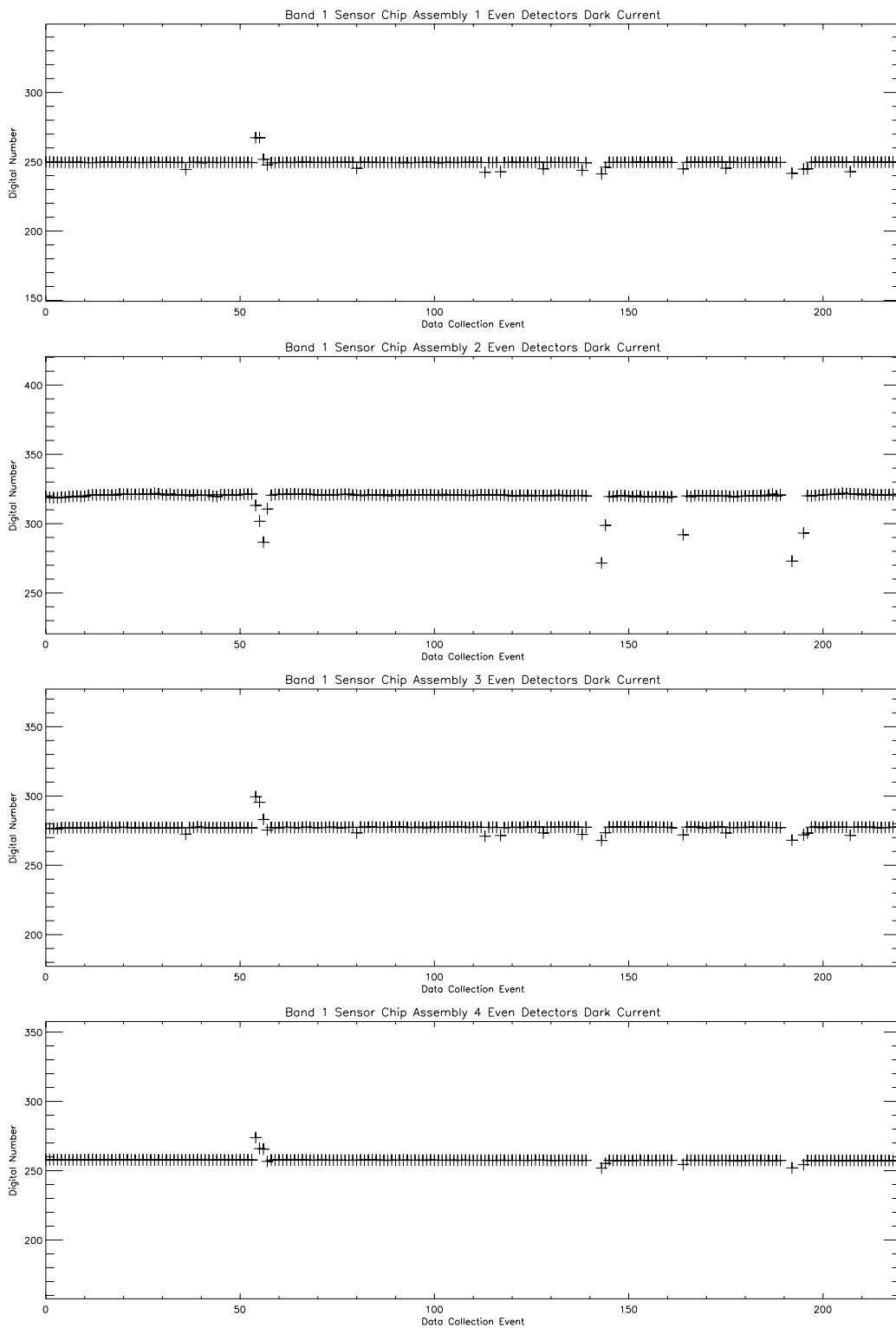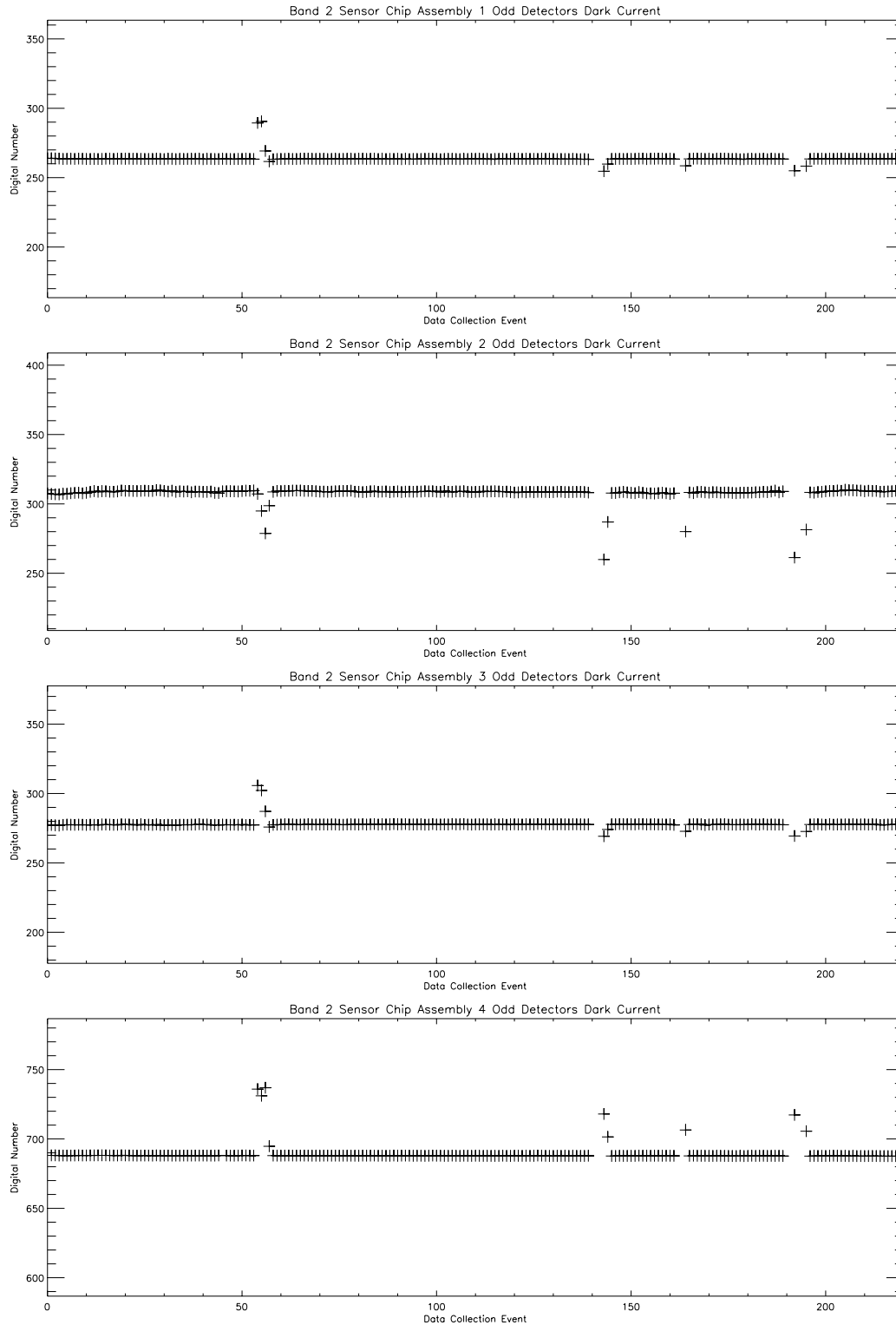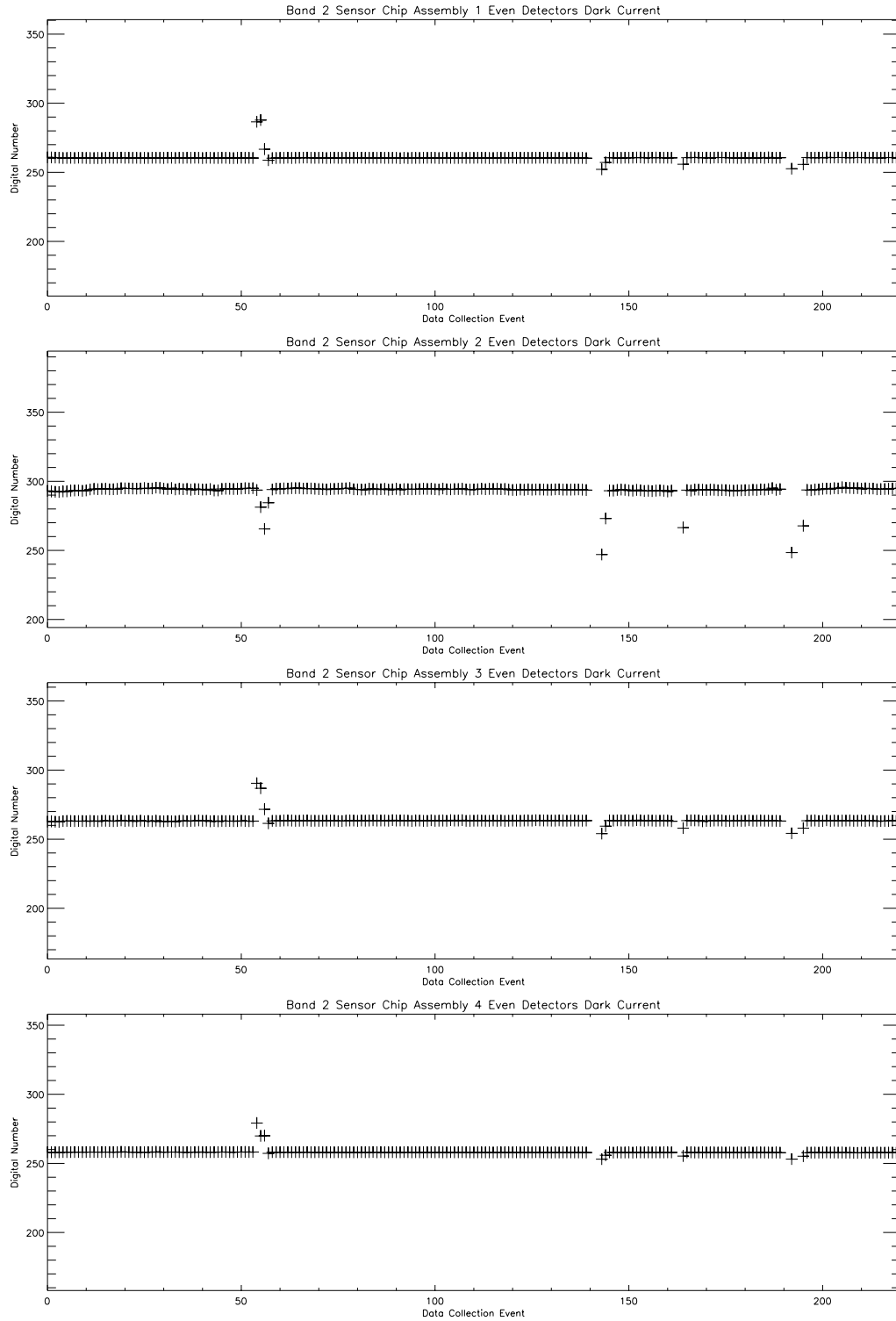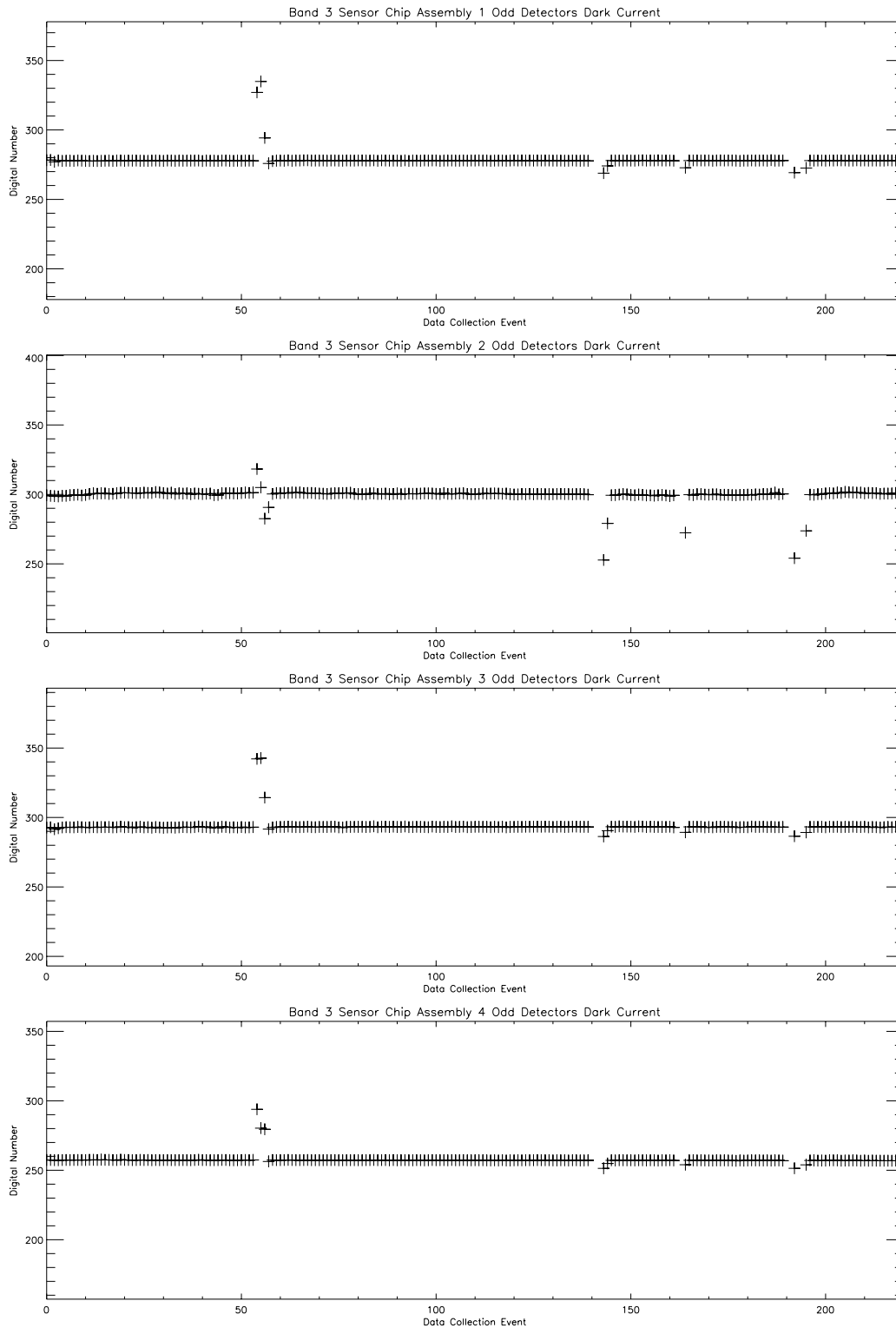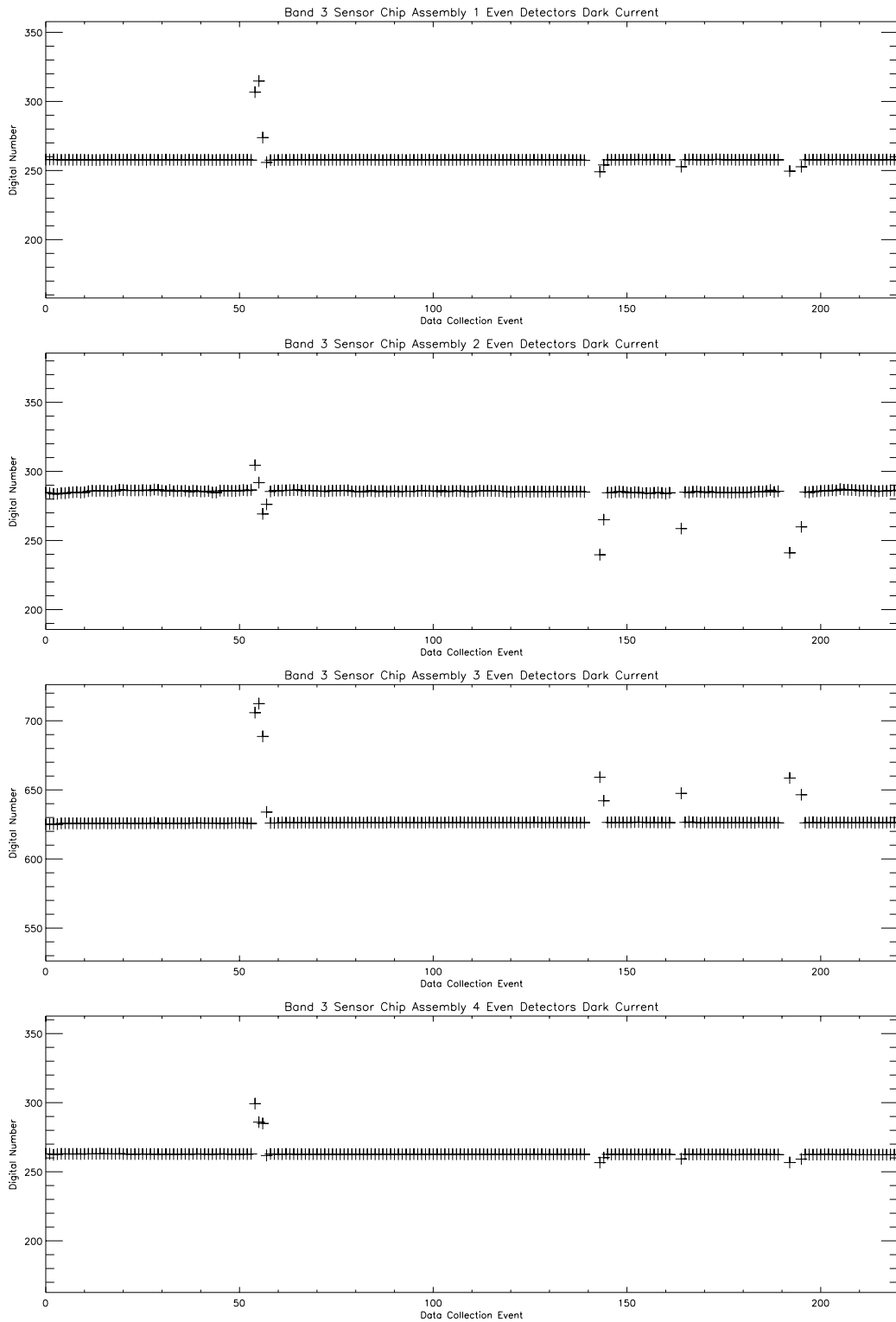
Figure 3-125. Dark current trending for Band 1 even detectors. Detector outgassing occurred near DCE 55, 140, 160, 190, and 219.
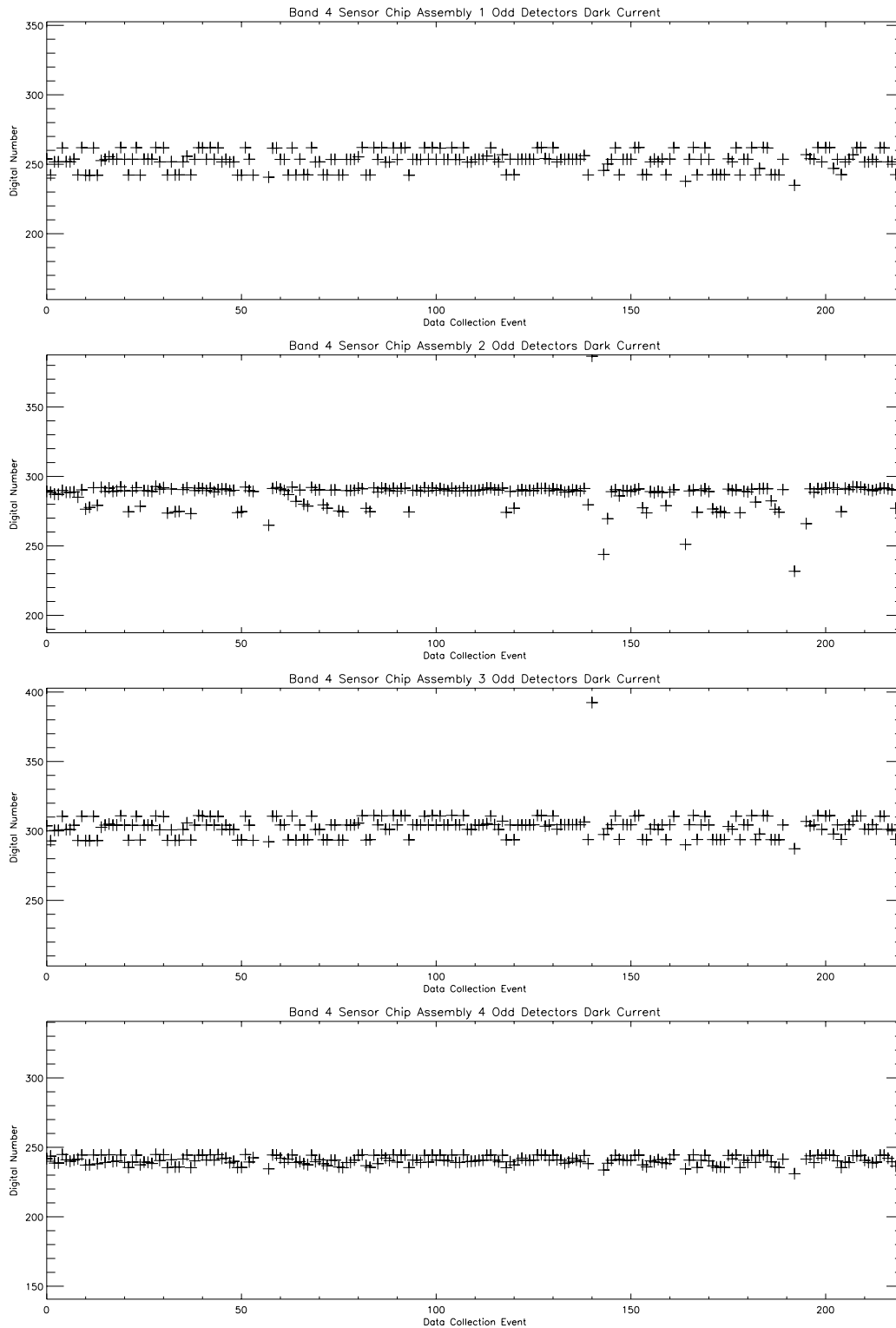
Figure 3-126. Dark current trending for Band 2 odd detectors. Detector outgassing occurred near DCE 55, 140, 160, 190, and 219.
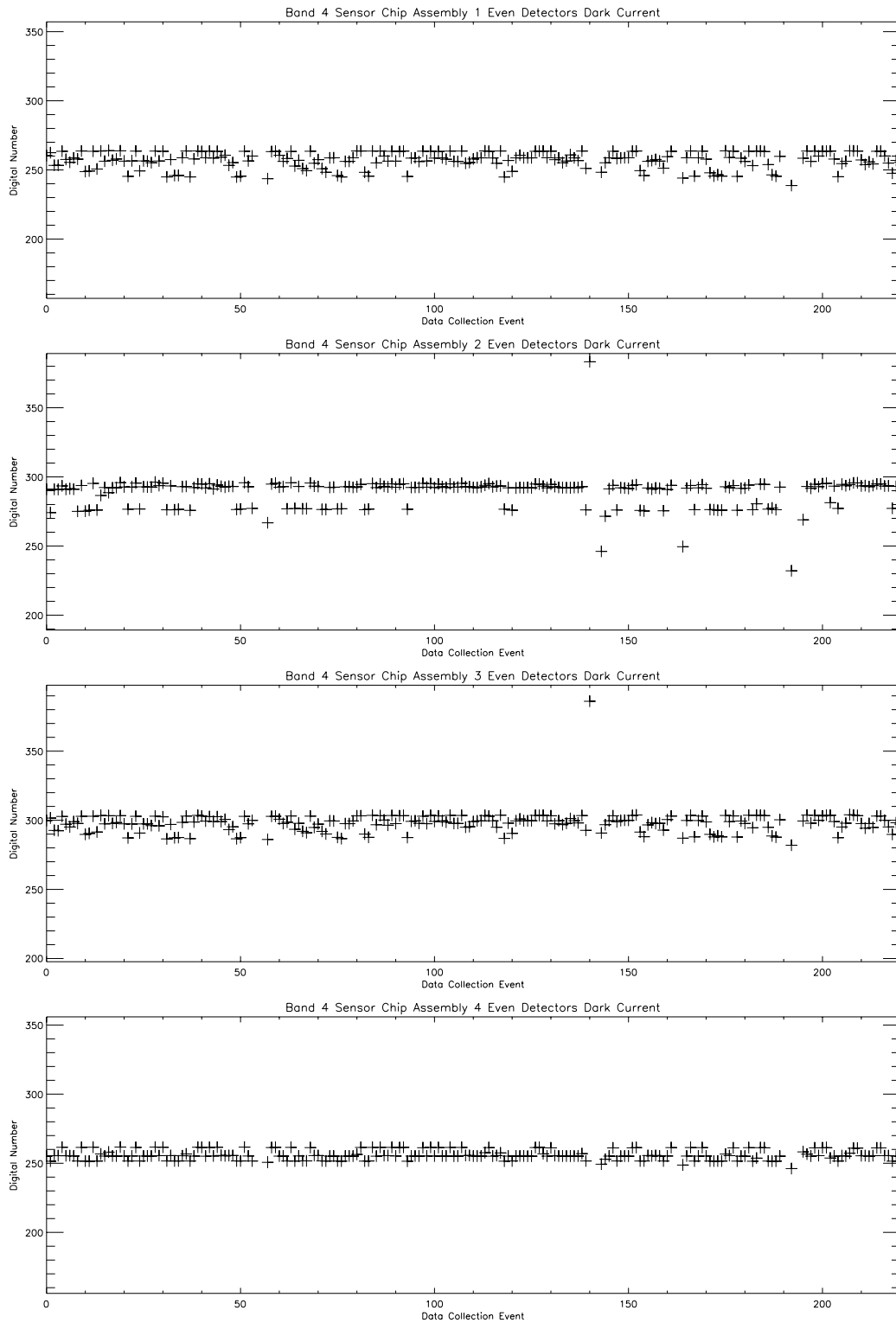
Figure 3-127. Dark current trending for Band 2 even detectors. Detector outgassing occurred near *DCE 55, 140, 160, 190, and 219.*
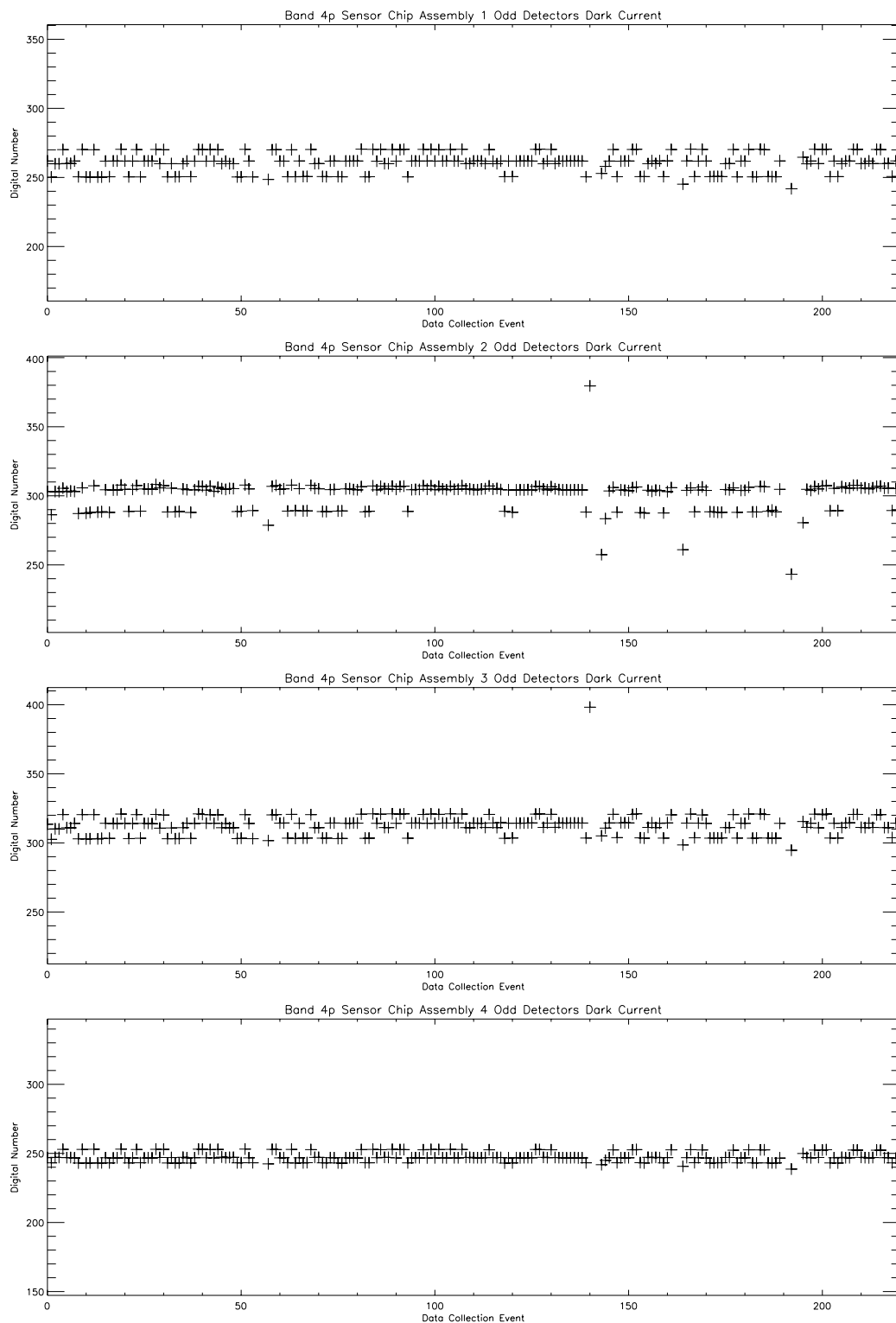
Figure 3-128. Dark current trending for Band 3 odd detectors. Detector outgassing occurred near DCE 55, 140, 160, 190, and 219.

Figure 3-129. Dark current trending for Band 3 even detectors. Detector outgassing occurred near DCE-55, 140, 160, `90, and 219

Figure3-1 30. Dark current trending for Band 4 odd detectors. Detector outgassing occurred near DCE 55, 140, 160, 190, and 219.
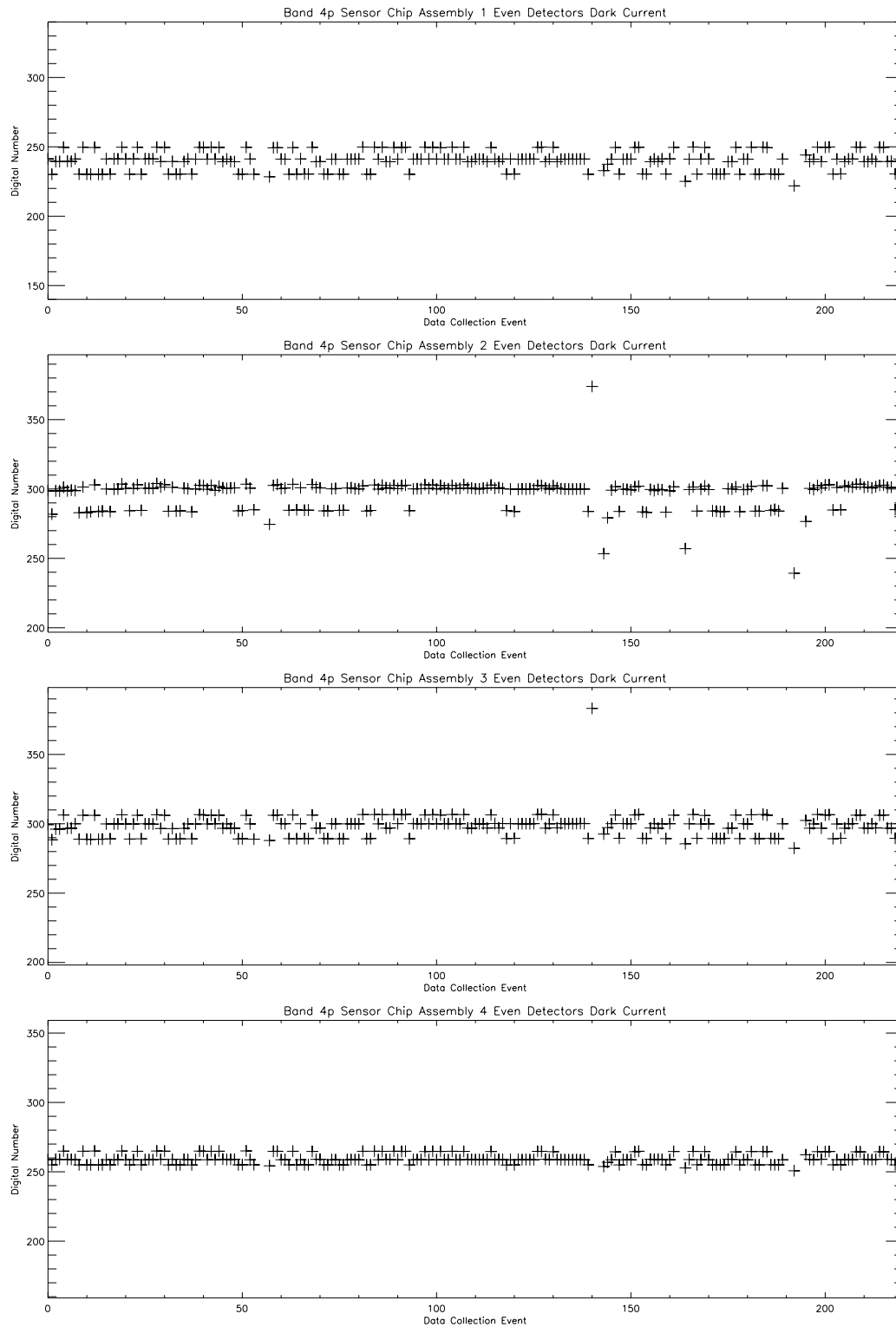
Figure 3-131. Dark current trending for Band 4 even detectors. Detector outgassing occurred near DCE 55, 140, 160, 190, and 219.

Figure 3-132. Dark current trending for Band 4p odd detectors. Detector outgassing occurred near DCE 55, 140, 160, 190, and 219

Figure 3-133. Dark current trending for Band 4p even detectors. Detector outgassing occurred near DCE 55, 140, 160, 190, and 219.
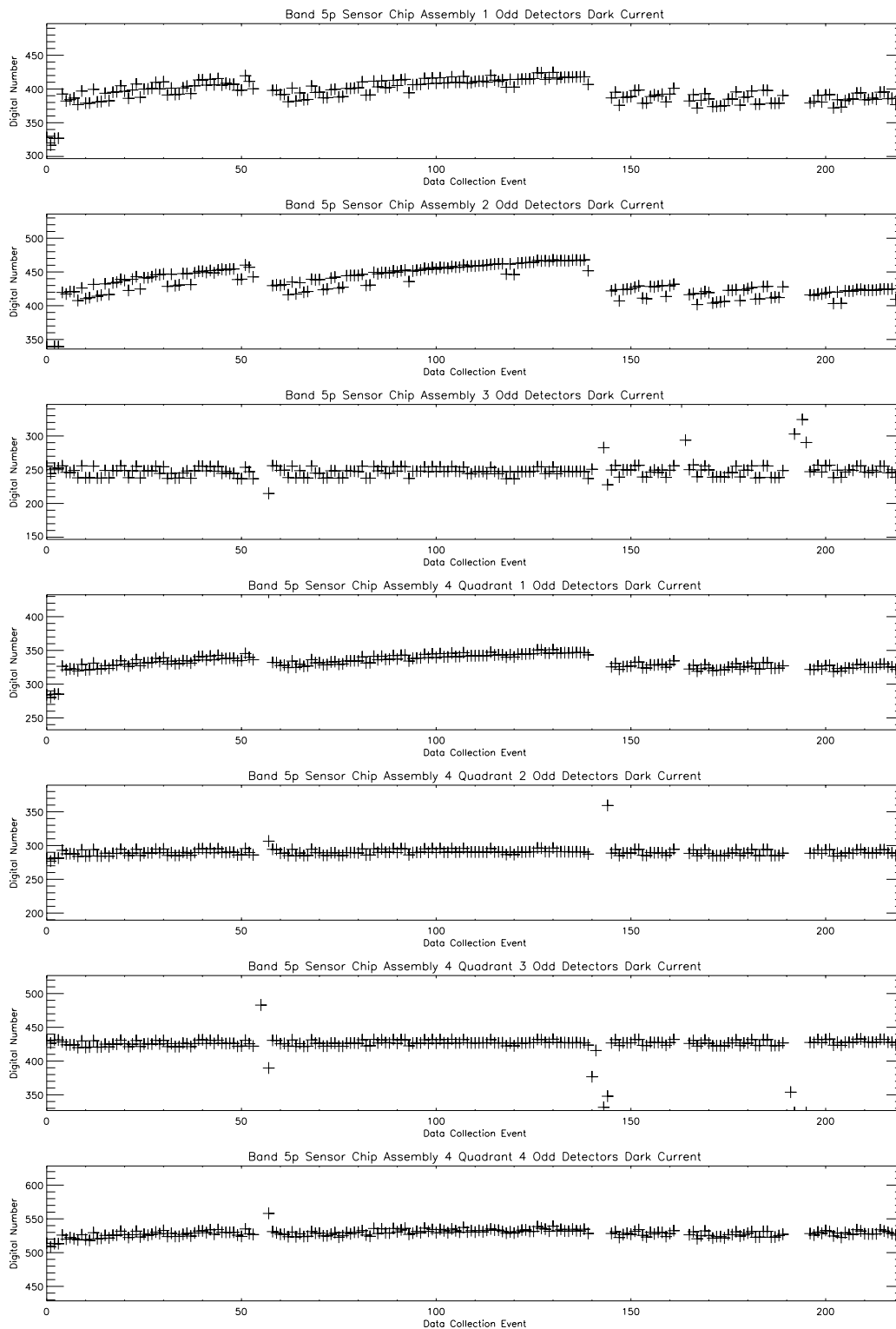
Figure 3-134. Dark current trending for Band 5p odd detectors. Detector outgassing occurred near DCE 55, 140, 160, 190, and 219.
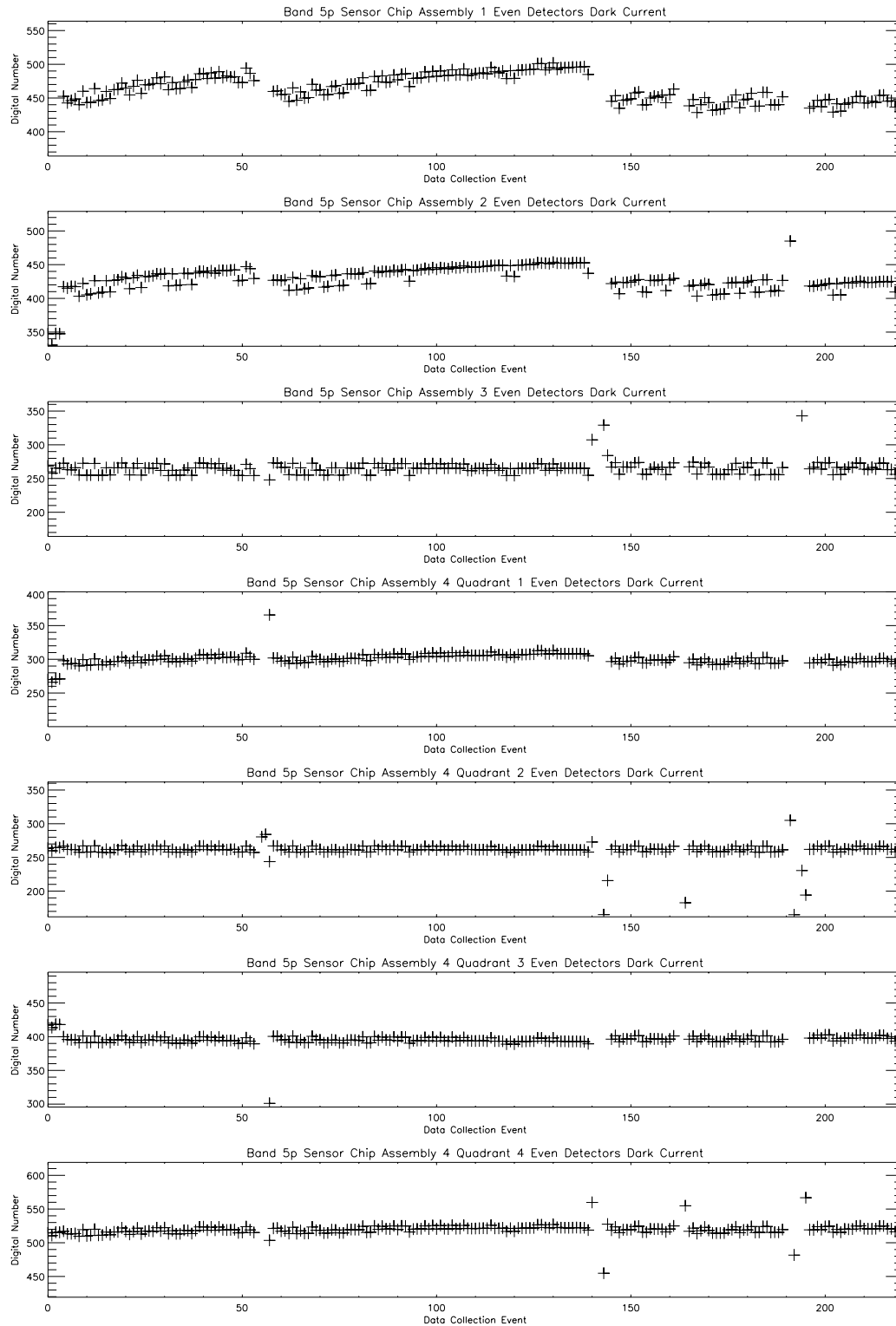
3-154

Figure 3-135. Dark current trending for Band 5p even detectors. Detector outgassing occurred near DCE 55, 140, 160, 190, and 219.
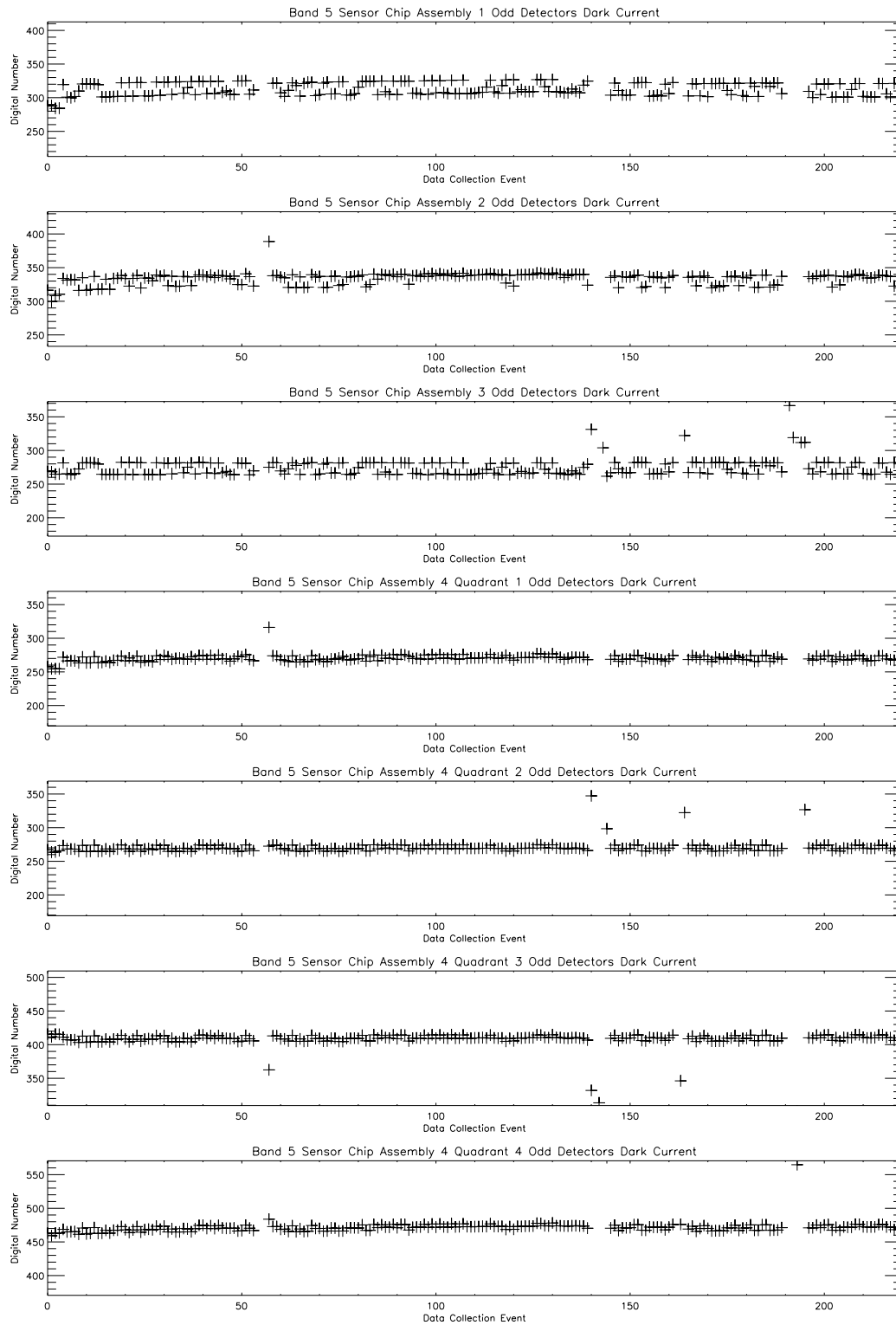
Figure 3-136. Dark current trending for Band 5 odd detectors. Detectors outgassing occurred near DCE 55, 140, 160, 190 and 219.
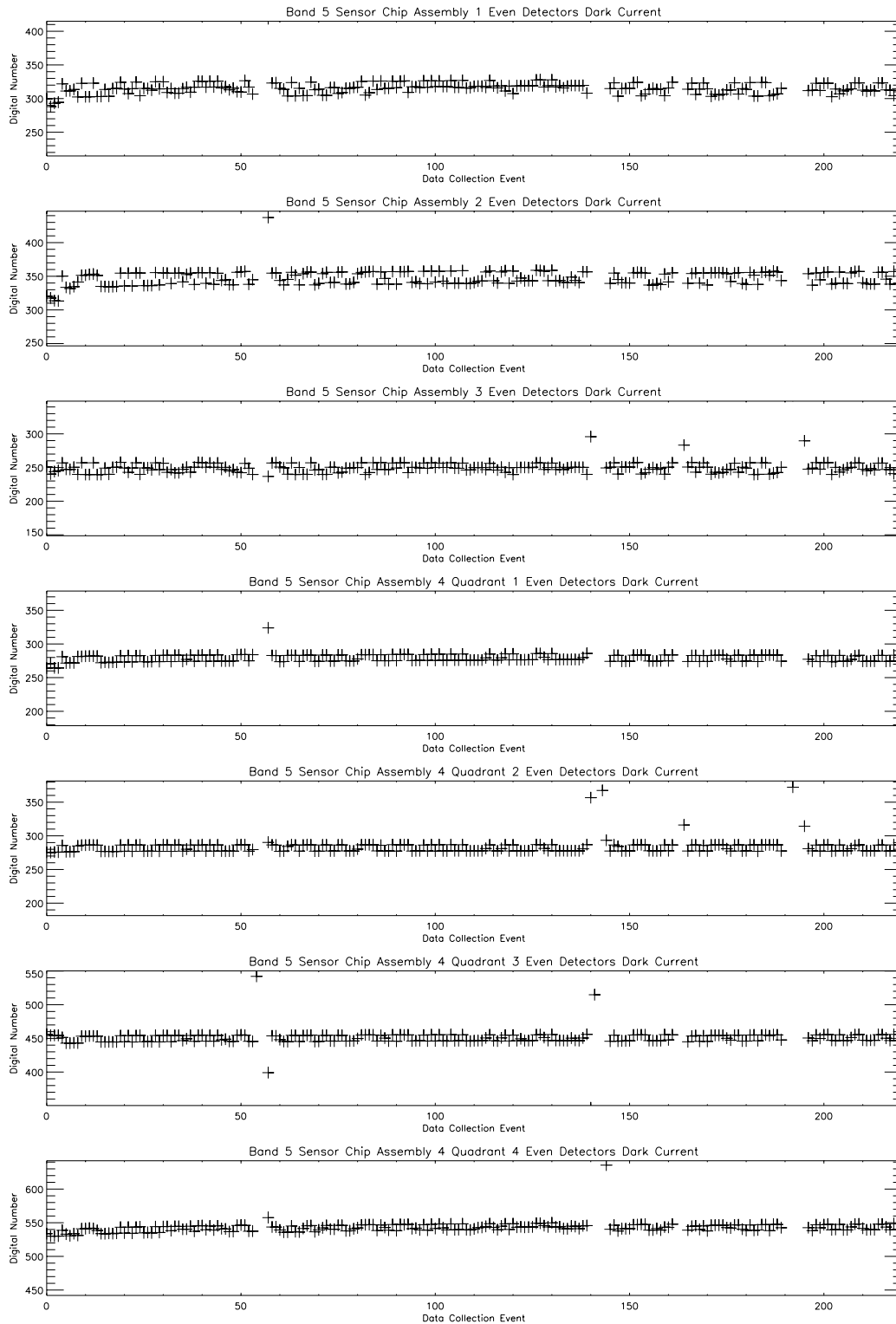
Figure 3-137. Dark current trending for Band 5 even detectors. Detector outgassing occurred near DCE 55, 140, 160, 190, and 219.
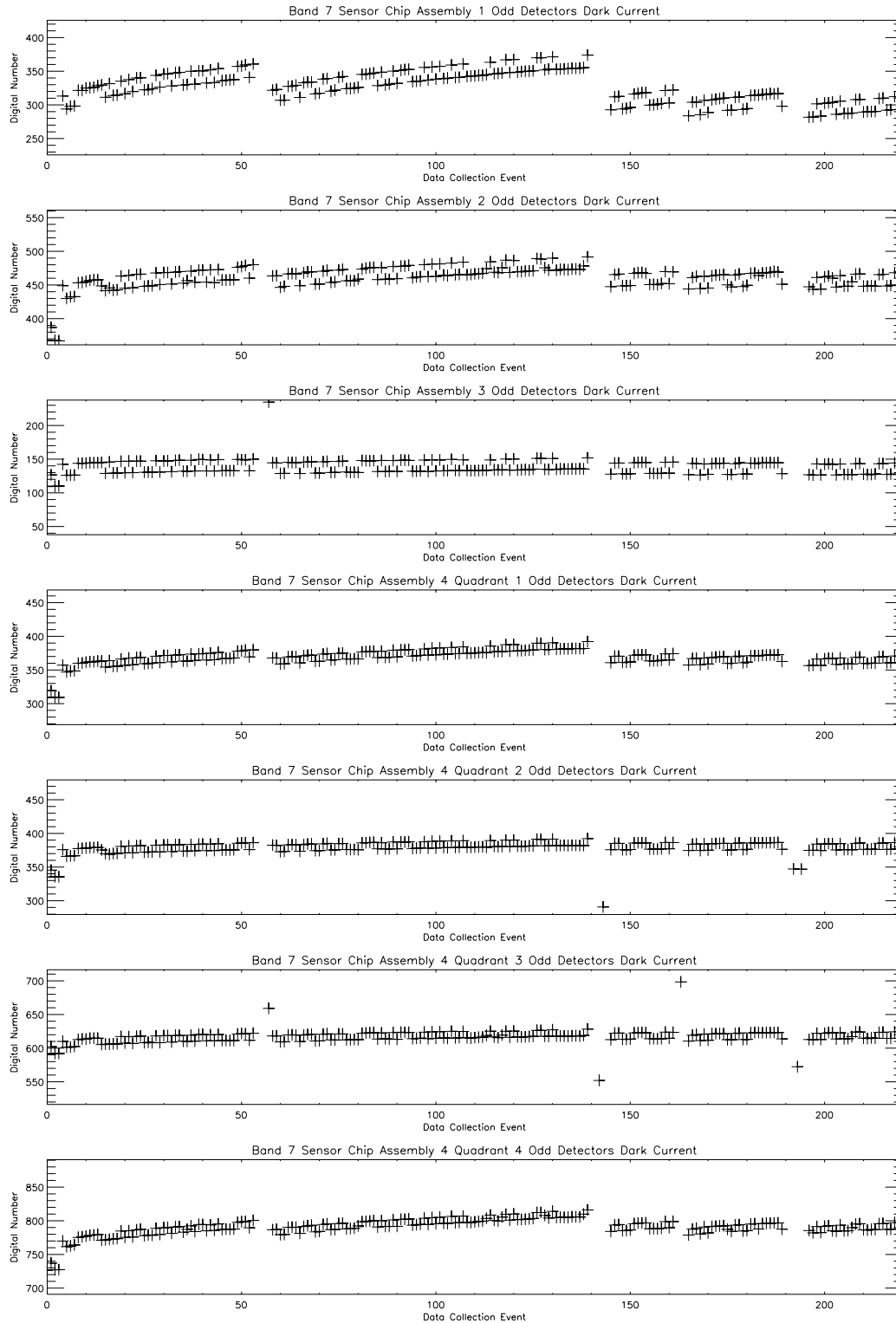
Figure 3-138. Dark current trending for Band 7 odd detectors. Detector outgassing occurred near DCE 55, 140, 160, 190 and 219.
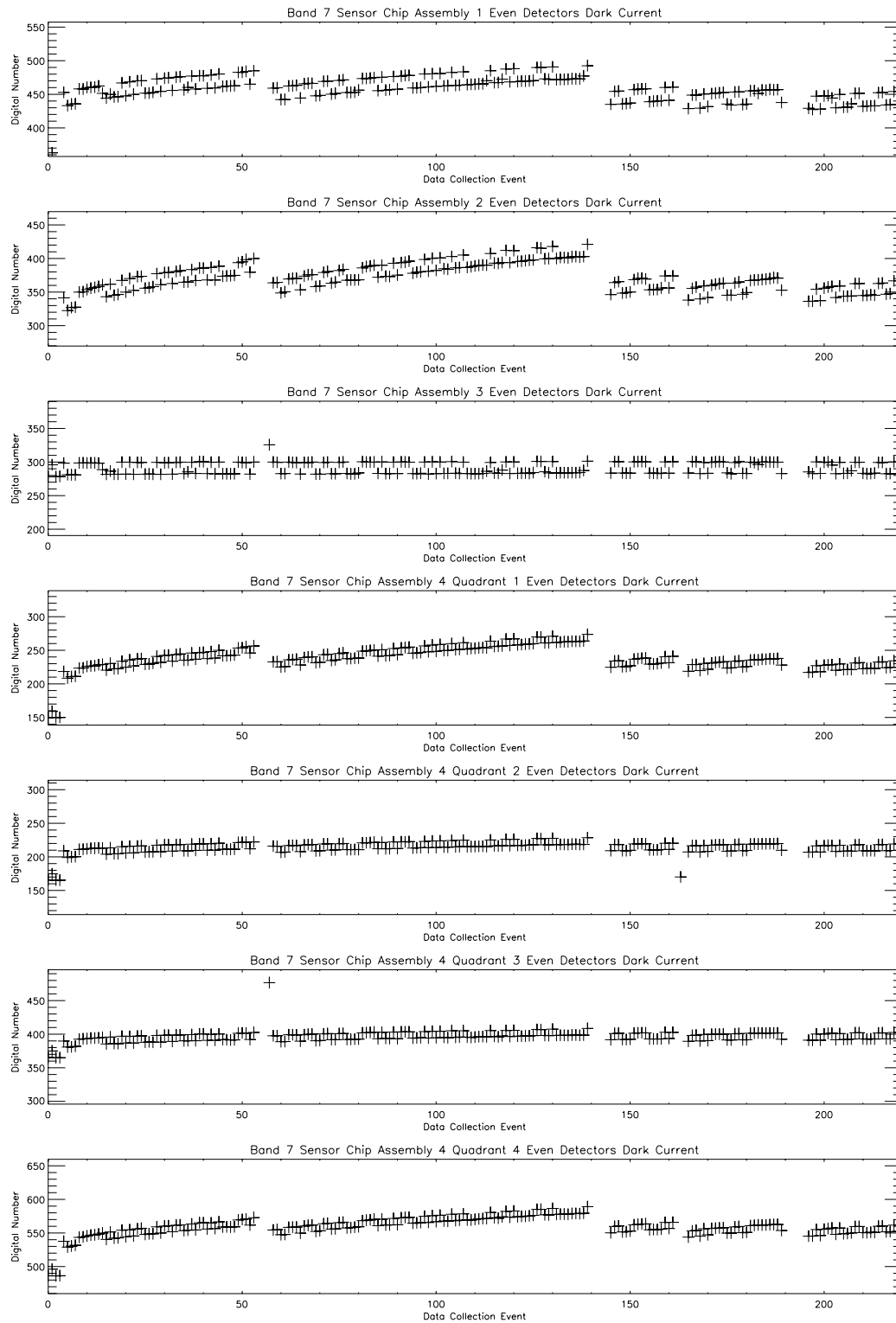
3-158

Figure 3-139. Dark current trending for Band 7 even detectors. Detector outgassing occurred near DCE 55, 140, 160, 190, and 219.

3-159

Figure 3-140. Dark current trending for Panchromatic Band tri-read #1 odd detectors. Detector outgassing occurred near DCE 55, 140, 160, 190, and 219.
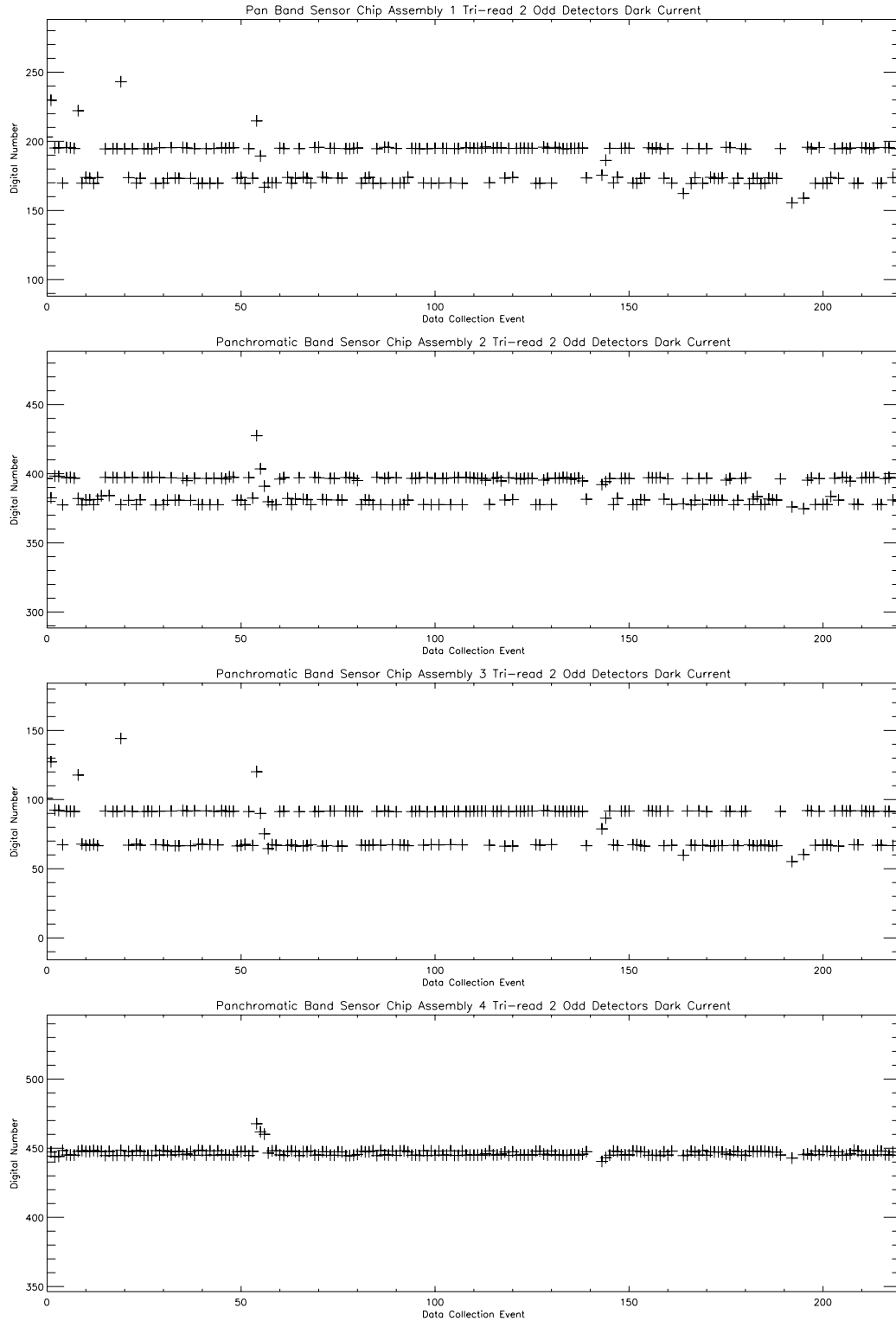
Figure 3-141. Dark current trending for Panchromatic Band tri-read #2 odd detectors. Detector outgassing occurred near DCE 55, 140, 160, 190, and 219
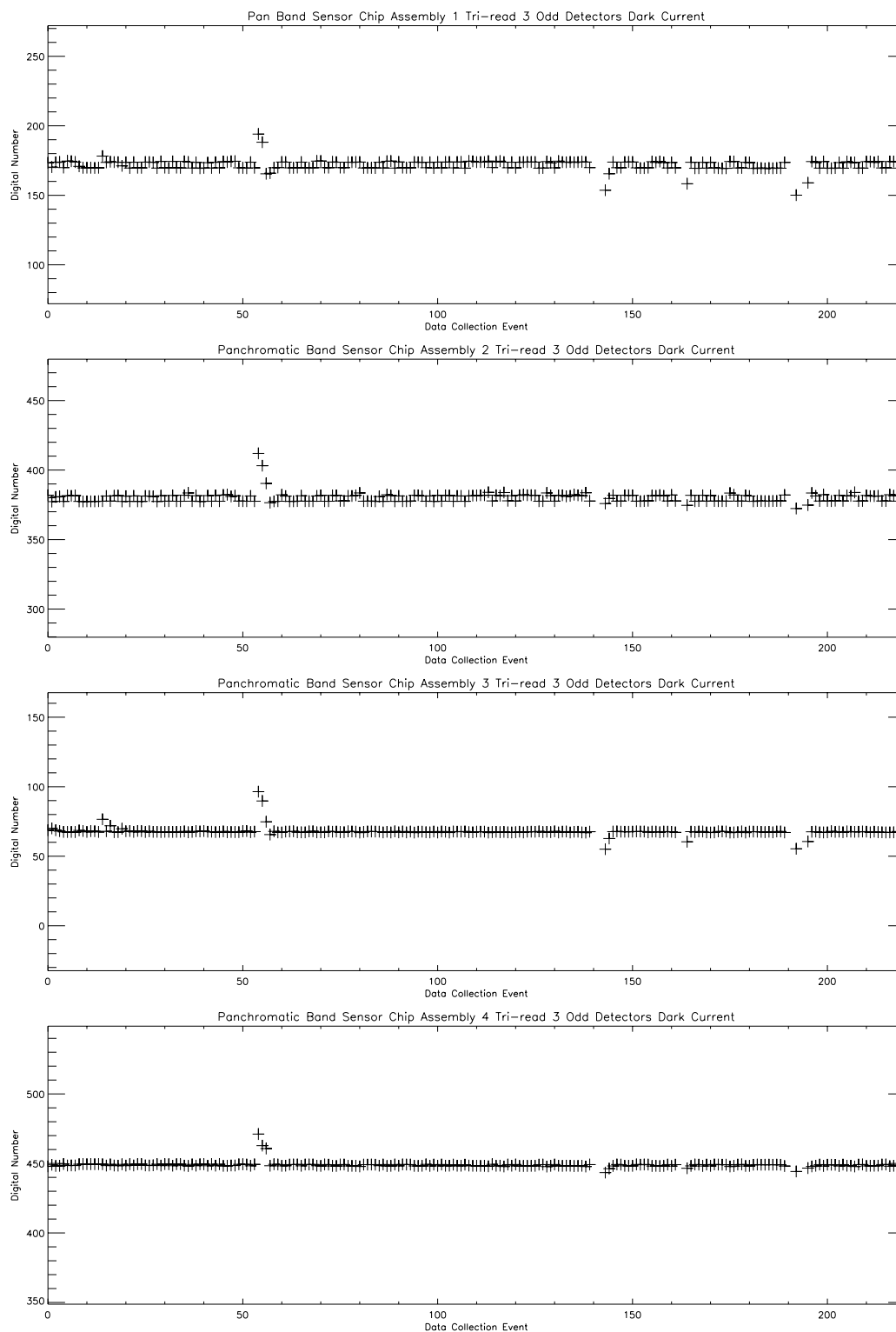
Figure 3-142. Dark current trending for Panchromatic Band tri-read #3 odd detectors. Detector outgassing occurred near DCE 55, 140, 160, 190, and 219.

Figure 3-143. Dark current trending for Panchromatic Band tri-read #1 even detectors. Detector outgassing occurred near DCE 55, 140, 160, 190, and 219.

Figure 3-144. Dark current trending for Panchromatic Band tri-read #2 even detectors. Detectors outgassing occurred near DCE 55, 140, 160, 190, and 219.
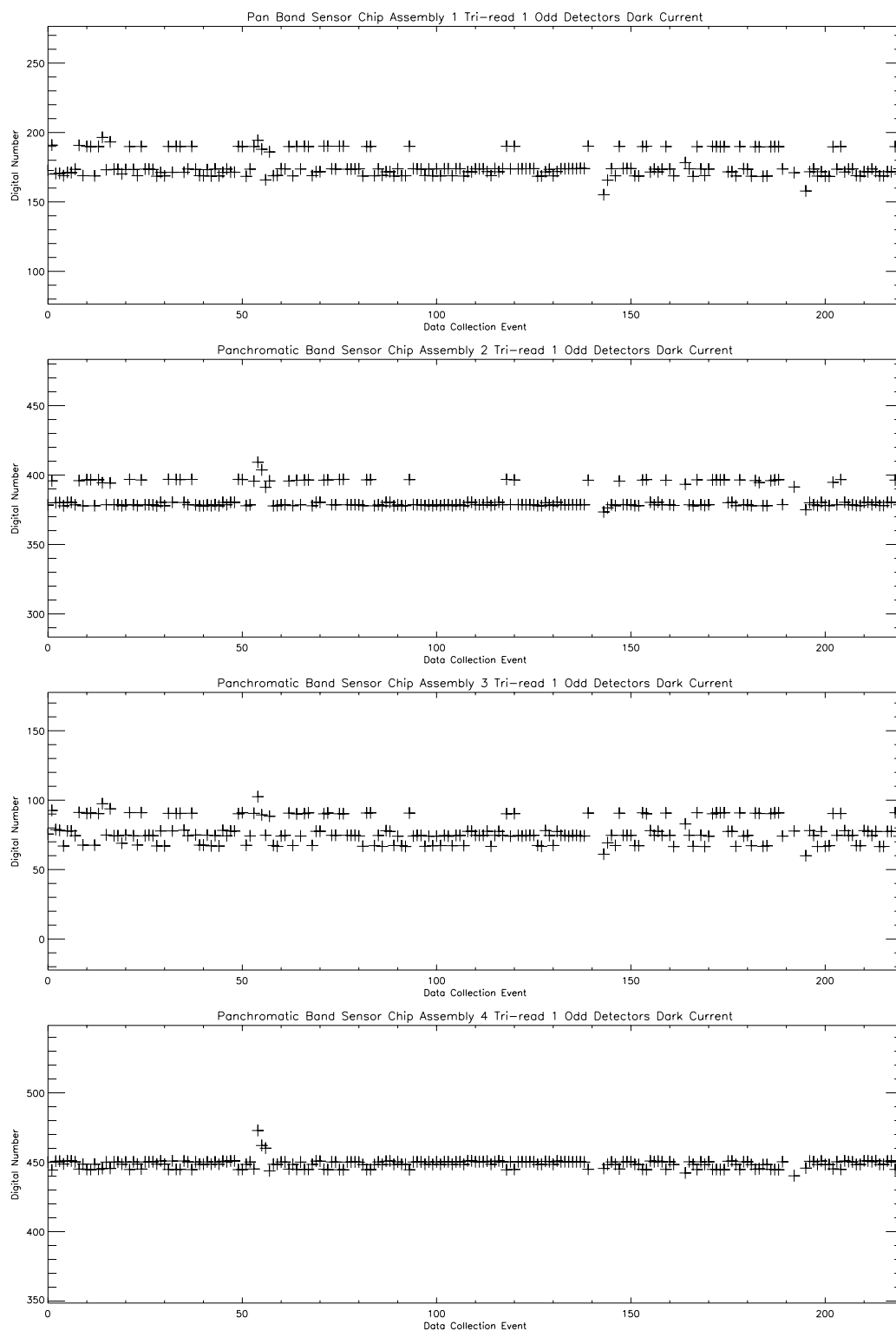
Figure 3-145. Dark current trending for Panchromatic Band tri-read #3 even detectors. Detector outgassing occurred near DCE 55, 140, 160, 190, and 219.
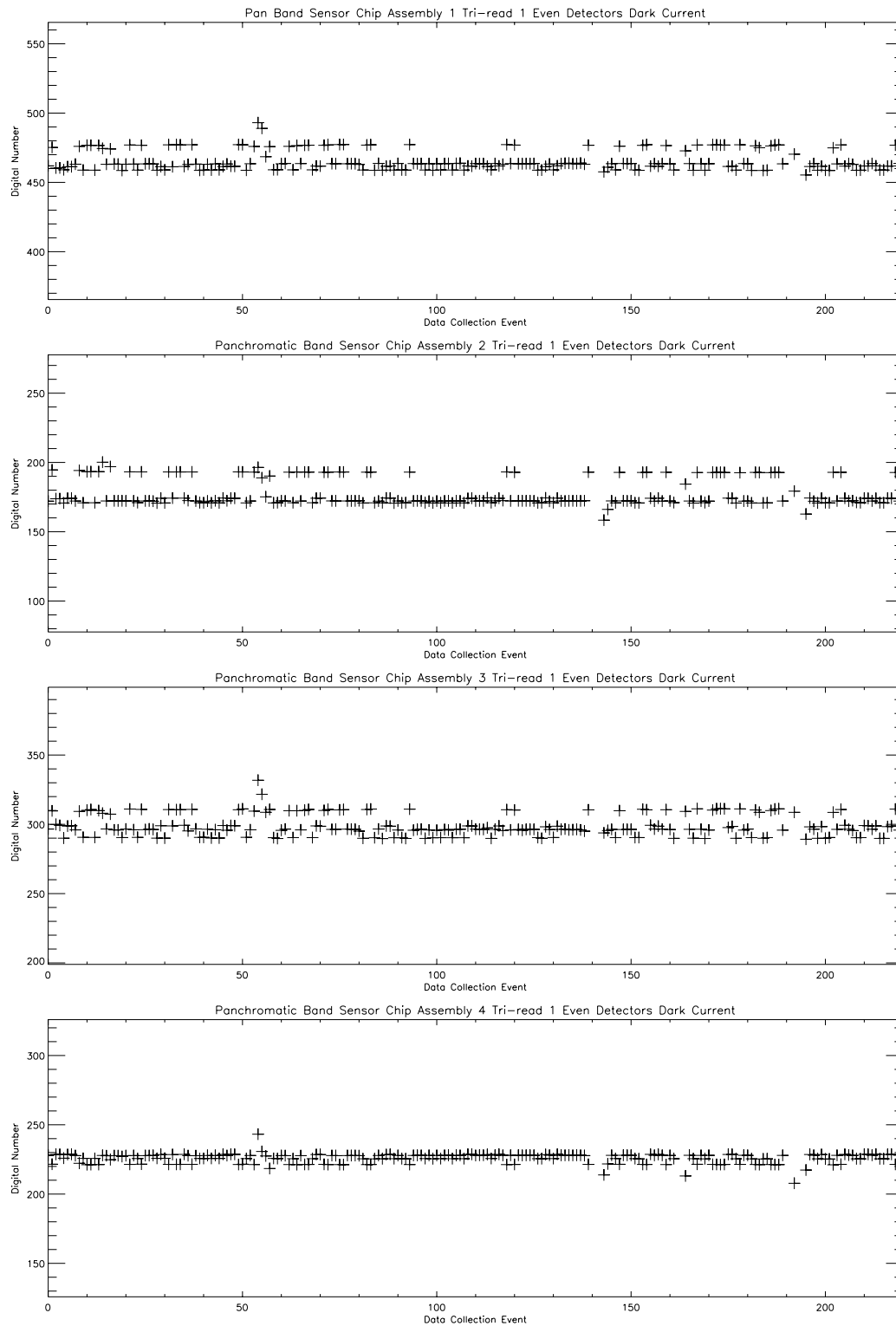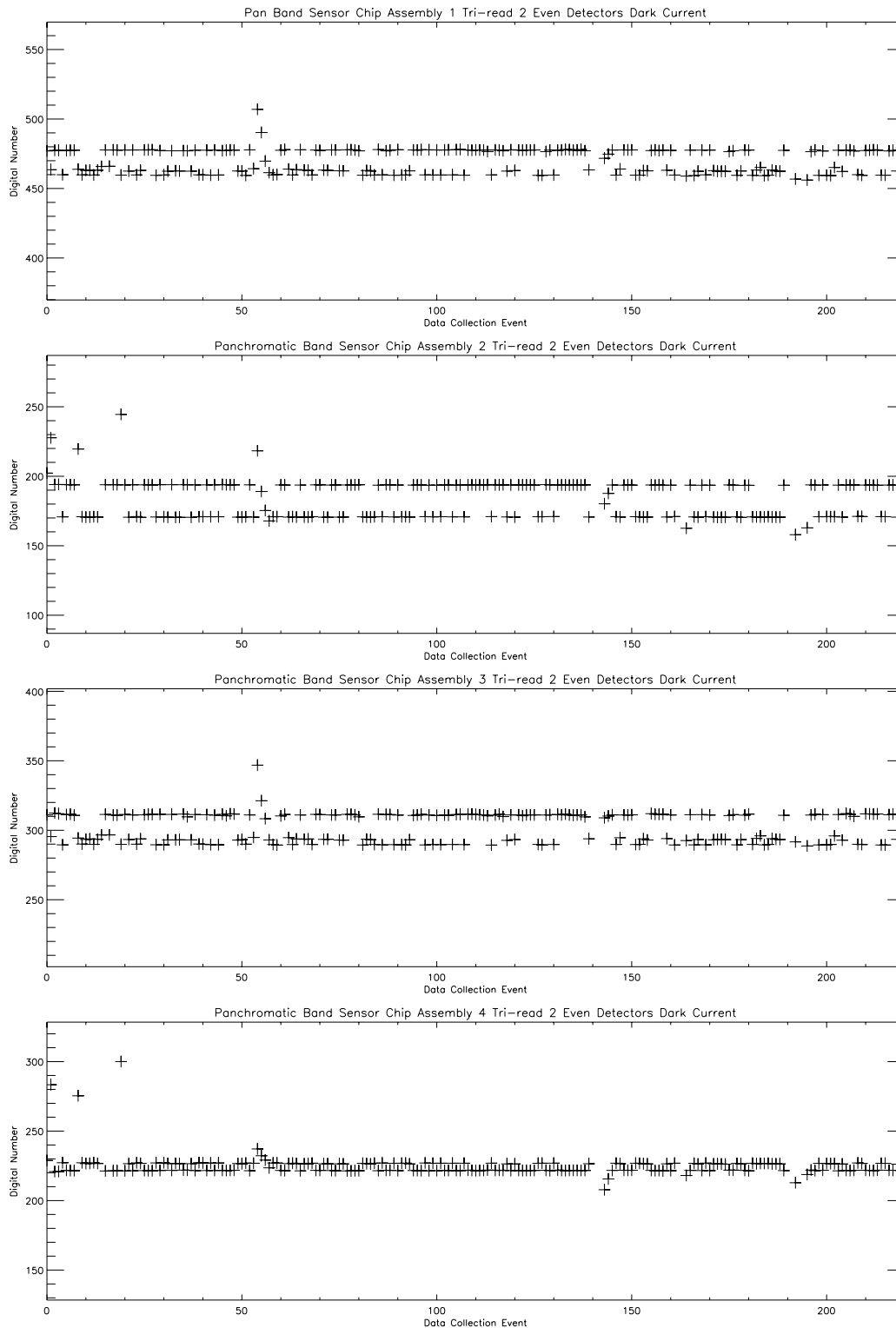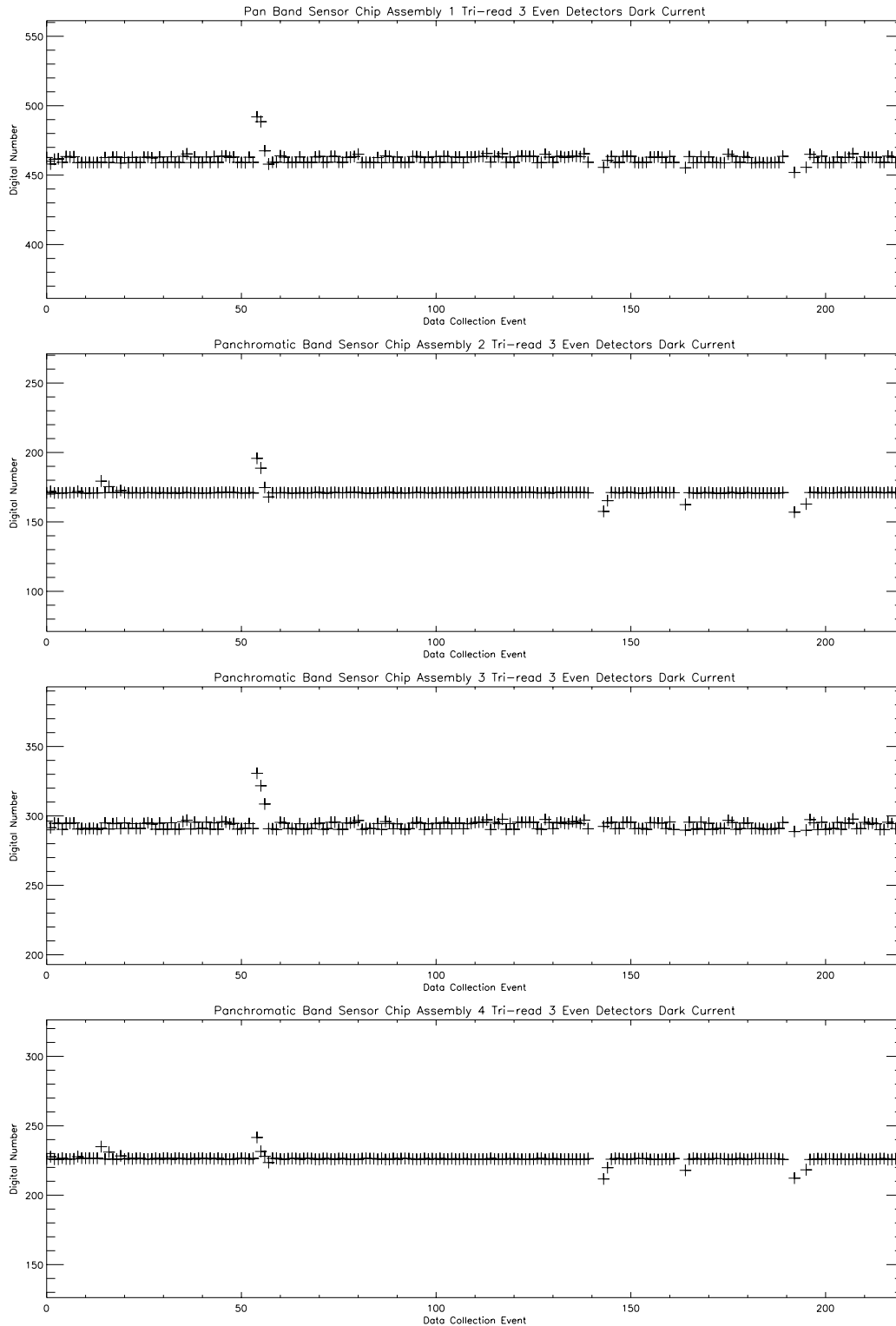
3-165

Table 3-22
Dark Current Trending Statistics

Band	SCA	Preflight Mean (Digital Number)	Flight Mean (Digital Number)	Flight Std. Deviation (Digital Number)
1P	1E	238.0	247.4	9.6
1P	1O	248.0	256.0	6.3
1P	2E	290.1	296.1	6.0
1P	2O	282.6	290.1	9.2
1P	3E	315.7	322.8	8.4
1P	3O	321.9	328.0	5.5
1P	4E	251.6	255.2	3.3
1P	4O	246.1	250.0	4.8
1	1E	248.2	249.3	1.2
1	1O	261.8	263.4	0.2
1	2E	318.2	320.5	0.6
1	2O	285.0	286.3	1.3
1	3E	277.7	277.1	1.1
1	3O	297.3	297.3	0.2
1	4E	257.0	257.6	0.2
1	4O	246.1	246.8	0.6
2	1E	259.5	260.5	0.1
2	1O	262.7	263.5	0.1
2	2E	292.0	294.2	0.6
2	2O	306.0	308.8	0.6
2	3E	263.6	263.3	0.2
2	3O	277.8	277.6	0.2
2	4E	257.4	258.0	0.2
2	4O	686.7	686.7	0.2
3	1E	256.9	257.7	0.1
3	1O	277.3	277.9	0.2
3	2E	283.8	285.6	0.6
3	2O	298.0	300.4	0.6
3	3E	625.2	626.2	0.3
3	3O	293.4	300.4	0.6
3	4E	261.6	262.6	0.2
3	4O	256.3	257.2	0.2
4	1E	258.6	257.1	5.8
4	1O	254.3	252.6	6.7
4	2E	292.5	289.2	7.3
4	2O	289.4	287.5	5.9
4	3E	299.9	297.7	5.1
4	3O	305.0	302.8	6.0
4	4E	255.3	255.9	3.4
4	4O	240.4	240.7	2.9
4P	1E	241.5	240.0	6.7
4P	1O	262.6	260.6	6.8
4P	2E	300.6	296.8	7.4
4P	2O	304.8	301.1	7.4

Band	SCA	Preflight Mean (Digital Number)	Flight Mean (Digital Number)	Flight Std. Deviation (Digital Number)
4P	3E	301.0	298.2	6.1
4P	3O	314.5	301.1	7.4
4P	4E	258.9	259.1	3.4
4P	4O	246.8	247.2	3.3
5P	1E	405.9	464.0	26.2
5P	1O	361.7	396.8	17.2
5P	2E	385.9	429.0	18.9
5P	2O	377.6	435.9	23.7
5P	3E	283.8	264.1	6.0
5P	3O	269.8	246.7	6.0
5P	4EQ1	282.7	300.1	7.1
5P	4EQ2	263.4	261.9	3.1
5P	4EQ3	403.8	395.7	4.6
5P	4EQ4	509.7	519.2	4.0
5P	4OQ1	301.1	332.4	11.1
5P	4OQ2	285.4	289.5	3.7
5P	4OQ3	426.5	426.7	3.4
5P	4OQ4	510.5	528.4	4.9
5	1E	307.7	314.8	7.6
5	1O	293.5	312.7	9.9
5	2E	347.9	346.6	9.5
5	2O	340.0	333.1	8.2
5	3E	261.2	248.6	5.6
5	3O	272.1	272.7	7.9
5	4EQ1	276.3	278.6	4.7
5	4EQ2	281.4	281.5	4.5
5	4EQ3	441.0	450.3	4.3
5	4EQ4	535.8	542.0	4.6
5	4OQ1	270.0	269.7	4.0
5	4OQ2	272.4	269.2	3.1
5	4OQ3	406.4	409.5	3.2
5	4OQ4	465.6	470.6	3.9
7	1E	382.3	457.5	22.1
7	1O	235.7	325.7	31.2
7	2E	242.3	369.8	30.1
7	2O	389.1	461.1	17.9
7	3E	300.1	290.6	8.4
7	3O	140.2	137.8	8.8
7	4EQ1	164.5	238.7	18.9
7	4EQ2	181.2	214.1	9.0
7	4EQ3	371.1	395.9	6.9
7	4EQ4	483.0	559.7	15.6
7	4OQ1	318.4	368.8	12.2
7	4OQ2	359.6	379.5	8.4
7	4OQ3	599.1	616.4	6.5
7	4OQ4	726.7	790.8	13.7
PAN	1ET1	465.7	465.5	6.8

Band	SCA	Preflight Mean (Digital Number)	Flight Mean (Digital Number)	Flight Std. Deviation (Digital Number)
PAN	1ET2	479.2	469.8	8.2
PAN	1ET3	465.3	461.2	2.2
PAN	1OT1	176.6	176.4	8.4
PAN	1OT2	197.2	188.1	9.0
PAN	1OT3	175.9	172.0	2.2
PAN	2ET1	172.4	177.7	9.3
PAN	2ET2	193.8	186.9	8.0
PAN	2ET3	171.5	171.1	0.8
PAN	2OT1	381.8	383.3	7.7
PAN	2OT2	396.2	388.8	8.7
PAN	2OT3	378.5	379.7	2.1
PAN	3ET1	295.8	298.9	7.3
PAN	3ET2	311.3	301.8	9.8
PAN	3ET3	295.4	293.0	2.3
PAN	3OT1	74.0	77.6	8.6
PAN	3OT2	91.9	84.2	8.4
PAN	3OT3	67.5	67.6	0.9
PAN	4ET1	226.3	225.9	2.8
PAN	4ET2	229.5	228.4	2.7
PAN	4ET3	224.5	226.2	0.9
PAN	4OT1	448.8	448.6	2.4
PAN	4OT2	451.4	446.3	1.4
PAN	4OT3	447.3	448.7	0.5

3.3.2.1.4   Discussion

The magnitude and repeatability of the EO-1 Advanced Land Imager focal plane noise were excellent during the first sixty days in orbit. The magnitudes presented in Table 3-21 are consistent with those calculated during pre-flight calibration of the instrument [21]. The trending indicates little change in noise levels throughout this period, except during times when the focal plane was being warmed-up for outgassing.

The magnitude of the ALI focal plane dark current was as expected during the first sixty days in orbit. The magnitudes presented in Table 3-22 are consistent with those calculated during pre-flight calibration of the instrument[6]. Band 2 SCA4 odd detectors and Band 3 SCA 3 even detectors have increased dark current levels compared to the corresponding even and odd detectors respectively. This is due to the influence of previously identified leaky detectors in these bands. Additionally, all SWIR bands exhibit enhanced dark current levels for a region of SCA 4 that is associated with a previously identified 'hot spot' in the focal plane.

Analysis of dark current data indicates excellent stability of all dark current levels within a given observation. However, dark current level variability as high as 30 digital numbers for Bands 1p, 4, 4p, 5p, 5, 7, and the Panchromatic band has been observed from one observation to another and is not well understood at this time. A small (20-50 digital numbers) increase in dark current is also observed in Bands 5p and 7 over the course of the first 150 DCEs. More frequent outgassing (once per week) since then has reduced this drift to less than 10 digital numbers.

Additional changes in noise and dark current levels are observed during times when the focal plane was being heated for outgassing. However, even during these periods, all Visible and Near Infrared bands (1p, 1, 2, 3, 4, 4p) and the Panchromatic Band indicate little change in detector dark current levels. This is undoubtedly the result in differing dark current characteristics between the silicon (VNIR) and HgCdTe (SWIR) detector materials.

The results presented here will serve as baselines for noise and dark current trending during the remainder of the EO-1 mission.

3.3.2.2 *Dark Current Stability over One-half Orbit Period*

Employing a pushbroom imaging method, the ALI does not have the luxury of observing periodic dark reference periods during each scan that wiskbroom imaging systems enjoy. As a result, dark current measurements of the ALI focal plane can only be performed when the aperture cover is closed, during eclipse, or when viewing deep space. Furthermore, under normal operating conditions, a Landsat type instrument will collect imagery for a great majority of the portion of the orbit illuminated by the Sun. To characterize the dark current stability of the ALI focal plane and hence the required frequency of dark current reference periods for Landsat class missions, a sequence of special dark current collections was performed during the first sixty days on orbit. This section documents the results of this dark current stability test. Additional information may be found in the MIT/LL EO-1-6 Project Report [23].

3.3.2.2.1 *Data Collection*

The data collected for this study occurred on January 3, 2001. In preparation for this special dark current test, the focal plane was powered and allowed to warm-up for 4 minutes. Once thermally stabilized, the focal plane remained powered for over 40 minutes and two-seconds of data were collected every 5 minutes with the aperture cover closed.

3.3.2.2.2 *Analysis*

The mean dark current level of each detector of the ALI focal plane is determined for each of the nine dark current collections. A linear fit is then performed on each detector's dark current data. The fitted function is then subtracted from the original dark data and the mean and standard deviations for the *flattened* data are then calculated. Any detector with a standard deviation greater then 1.5 digital numbers is then categorized as a 'non-linear drifter'.

3.3.2.2.3 *Results*

The results of the thermal drift analysis are provided in Figures 3-146 to 3-157. For each figure, the overall linear drift and the standard deviation of the *flattened* data for each detector are provided. All VNIR bands and the Panchromatic band exhibited less than one digital number drifting during the forty minute period. These bands also exhibited residual drifting of less than 0.5 digital numbers, after linear drifting is subtracted. All SWIR bands exhibited up to 30 digital numbers of linear drifting. However, all but twenty-four SWIR detectors exhibited less than 1.5 digital number of residual drifting (Table 3-23). Twelve of these detectors were previously identified as exhibiting anomalous dark current or noise characteristics during ground calibration[6]. The distribution of SWIR detectors as a function of non-linear drifting threshold (0.5, 1.0, 1.5, 2.0, 2.5, and 5.0 digital numbers) is provided in Figures 3-158 to 3-160. Only the previously identified anomalous detectors exhibit non-linear drifting greater than 2.3 digital numbers.
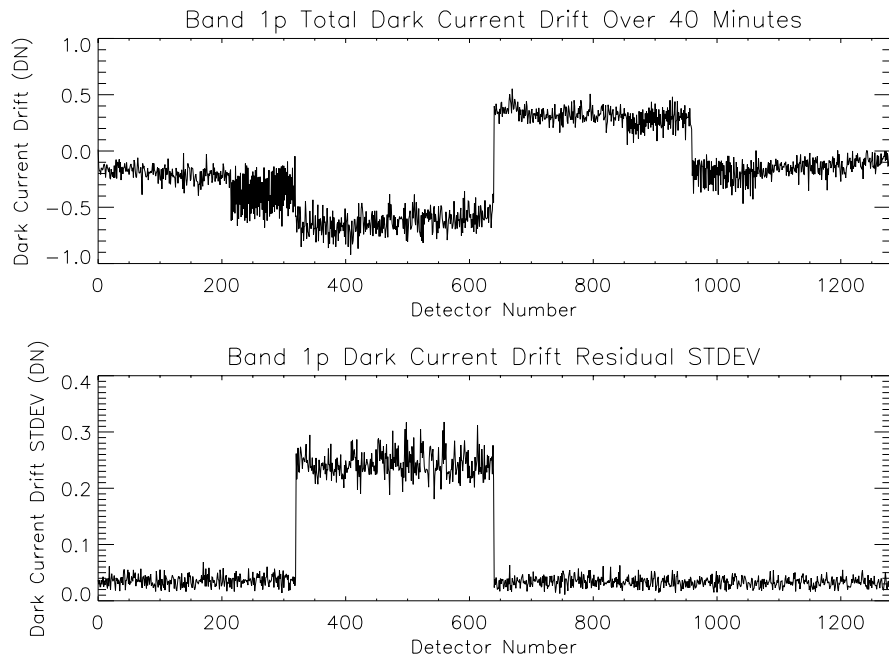
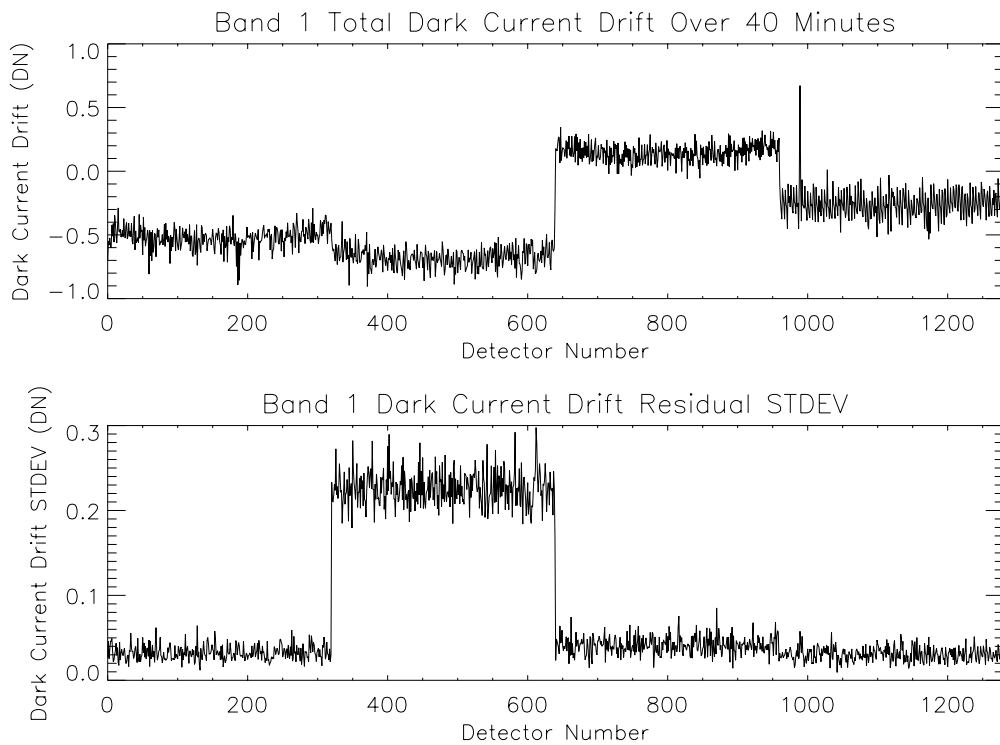*Figure 3-146. Dark current drift for Band 1p.*
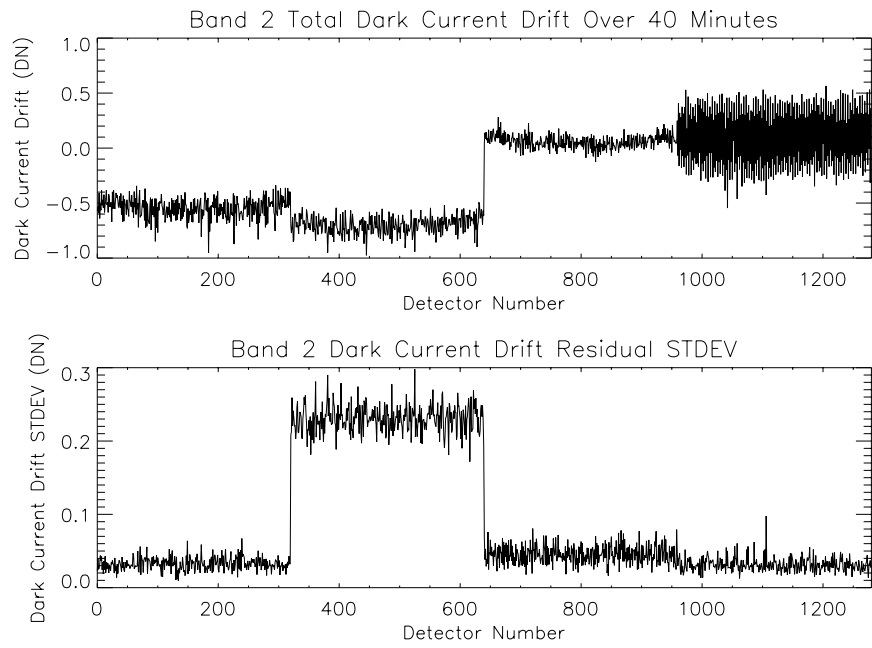

Figure 3-147. Dark current drift for Band 1

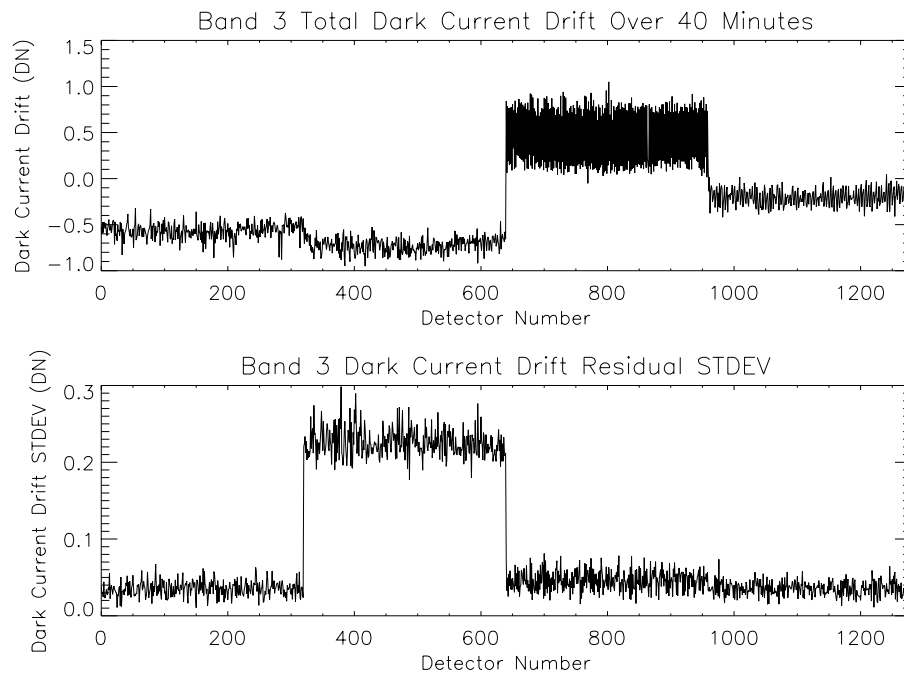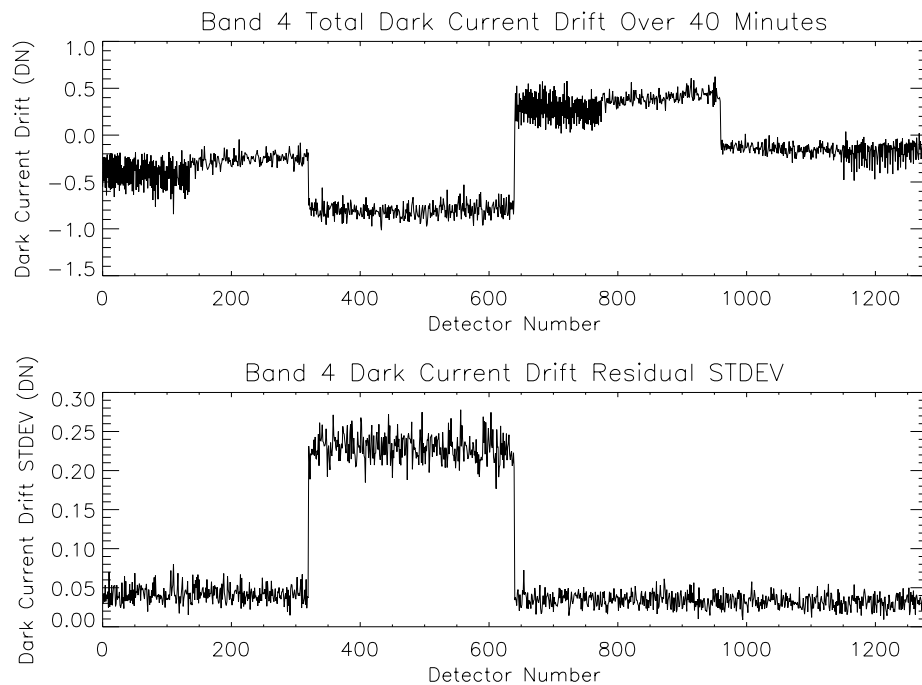*Figure 3-148. Dark current drift for Band 2*

Figure 3-149. Dark current drift for Band 3.

Figure 3-150. Dark current drift for Band 4.

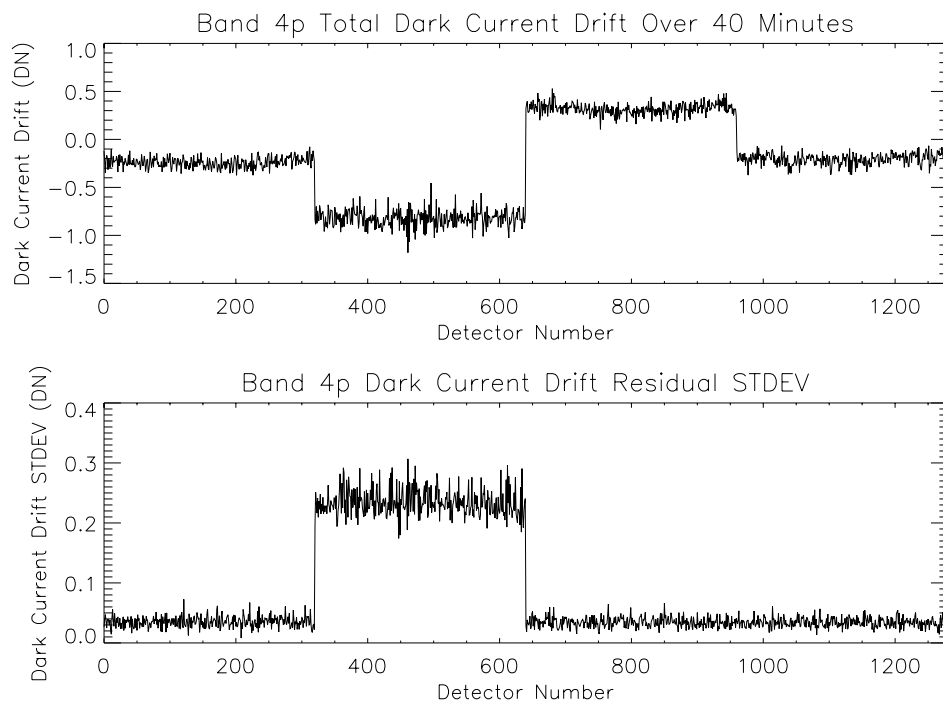
Figure 3-151. Dark current drift for Band 4p.

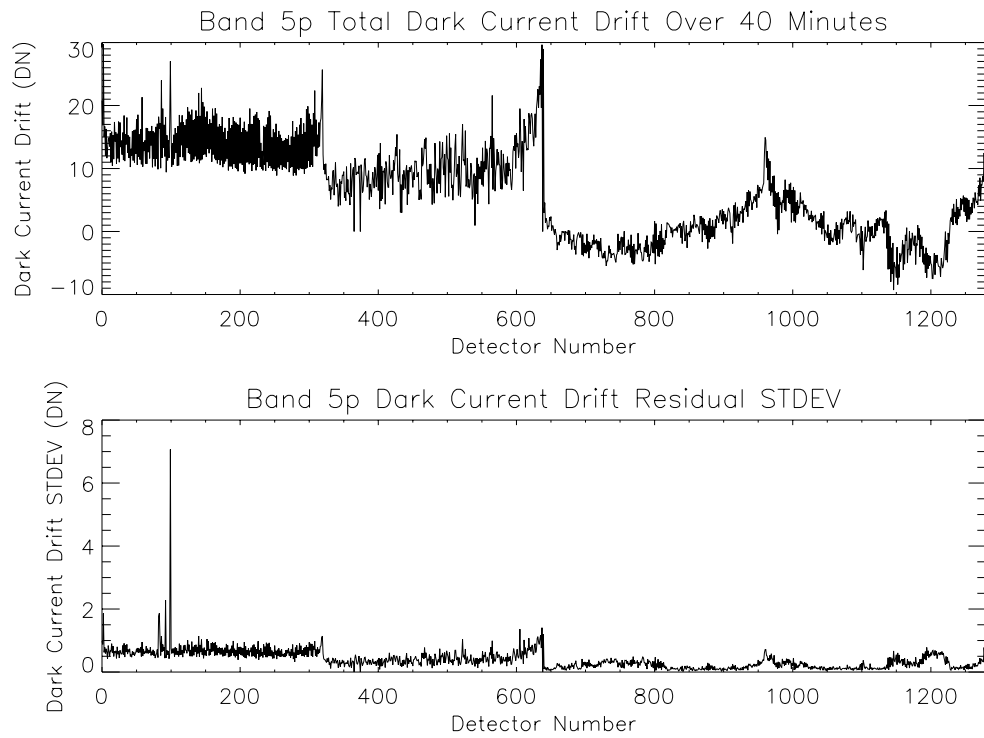Band 5p Total Dark Current Drift Over 40 Minutes

Band 5p Dark Current Drift Residual STDEV

Figure 3-152. Dark current drift for Band 5p.

Band 5 Total Dark Current Drift Over 40 Minutes

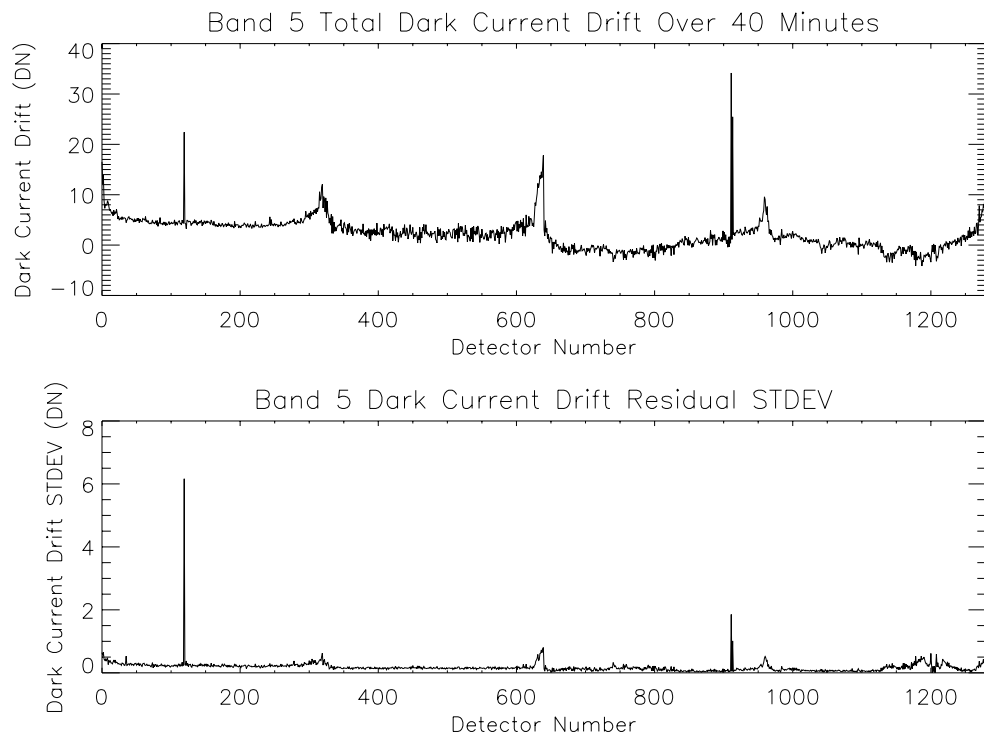Band 5 Dark Current Drift Residual STDEV
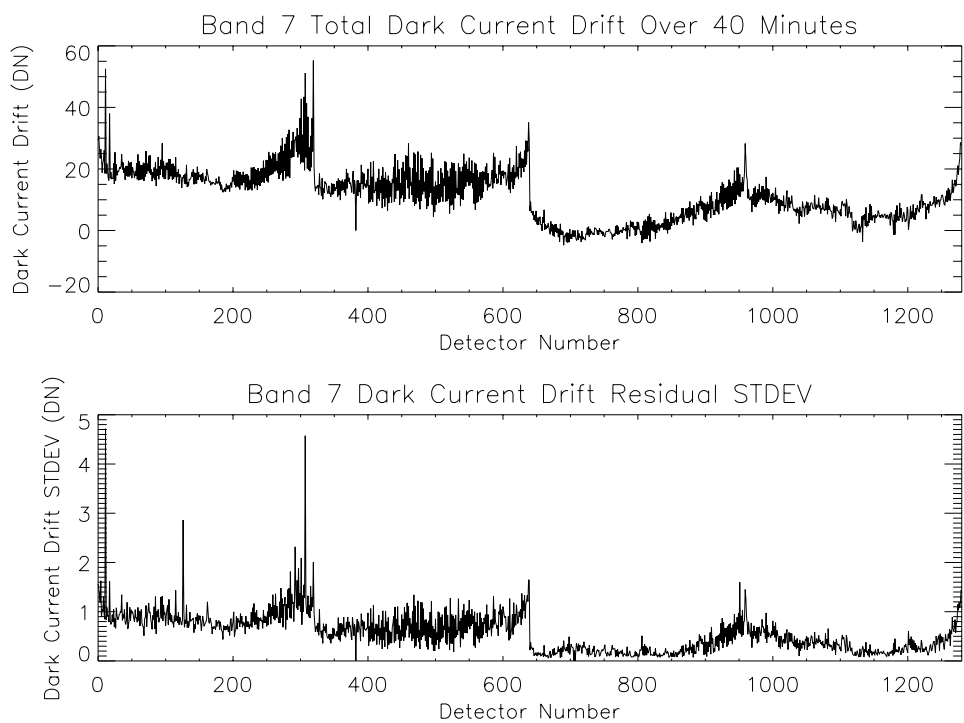
Figure 3-153. Dark current drift for Band 5.

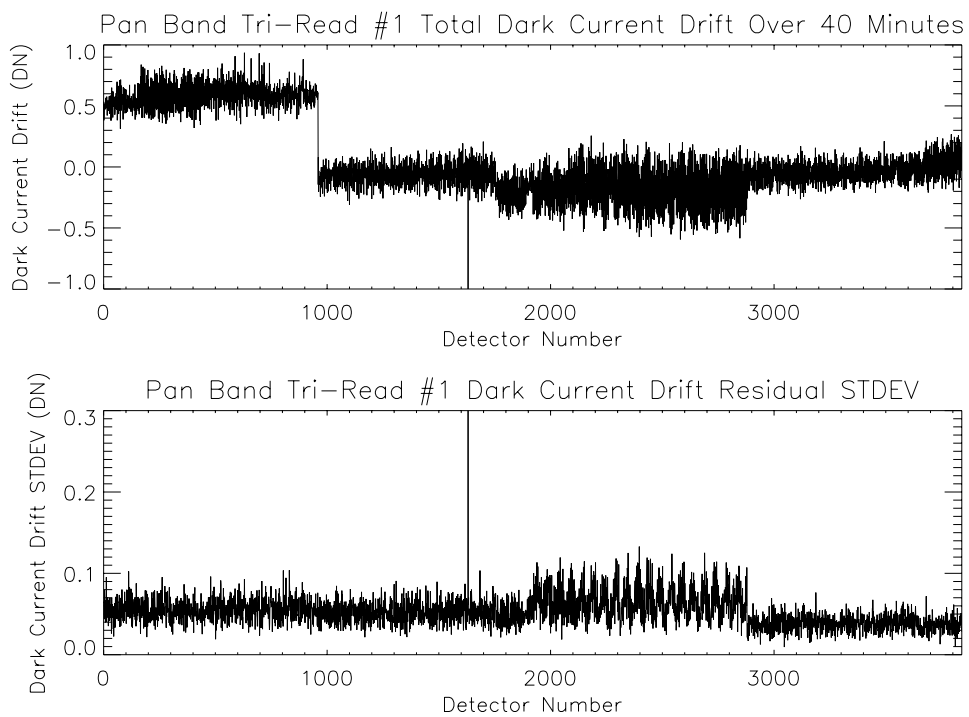*Figure 3-154. Dark current drift for Band 7.*

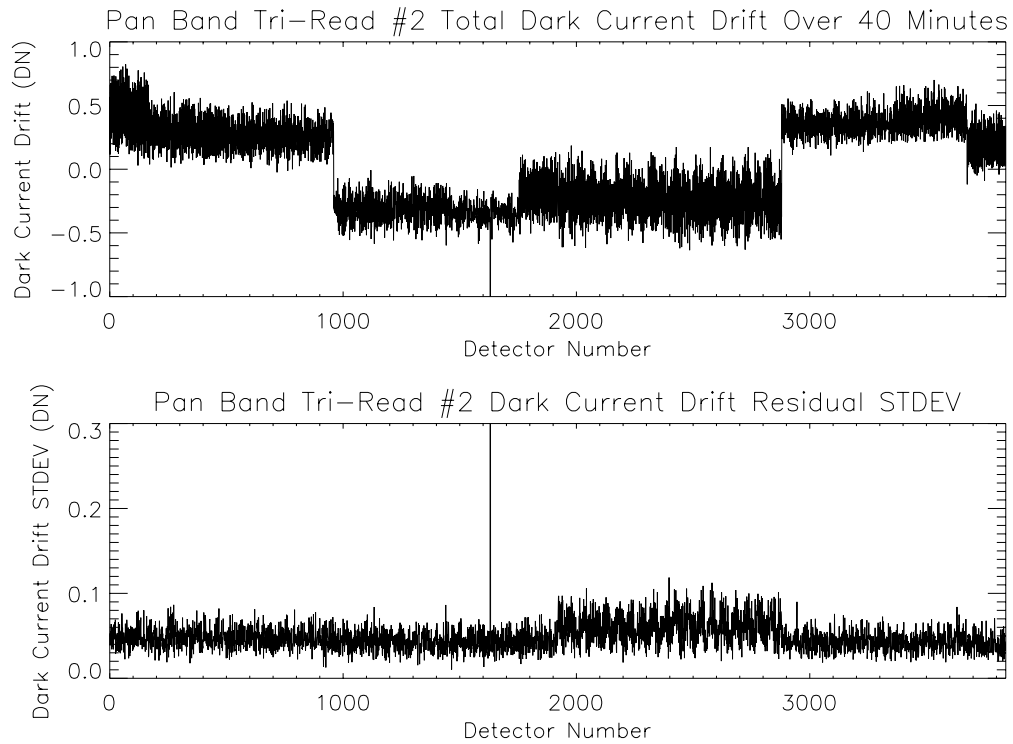*Figure 3-155. Dark current drift for Panchromatic Band tri-read #1.*

Figure 3-156. Dark current drift for Panchromatic Band tri-read #2.
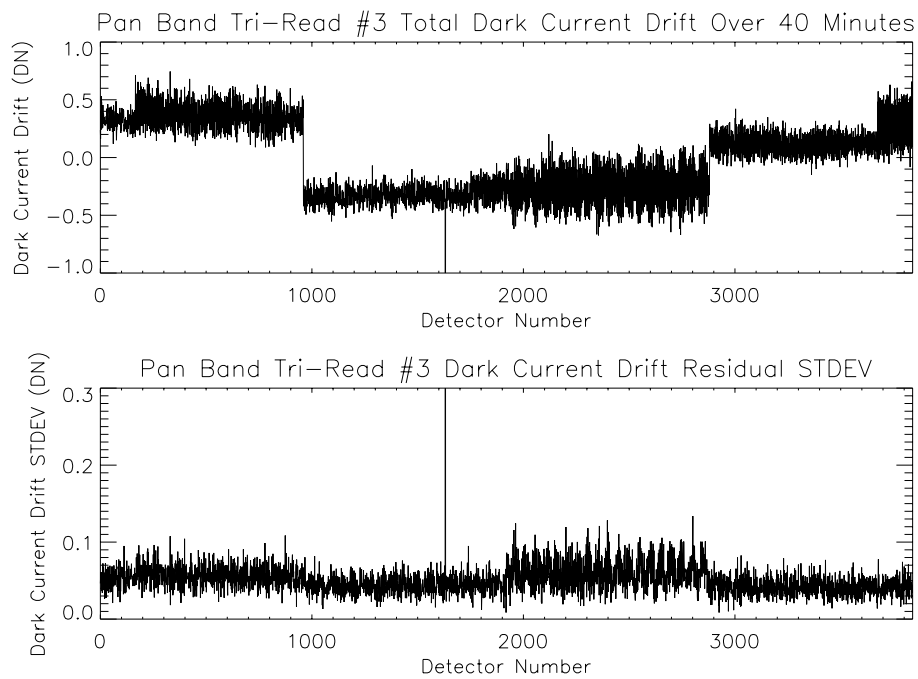

Figure 3-157. Dark current drift for Panchromatic Band tri-read #3.
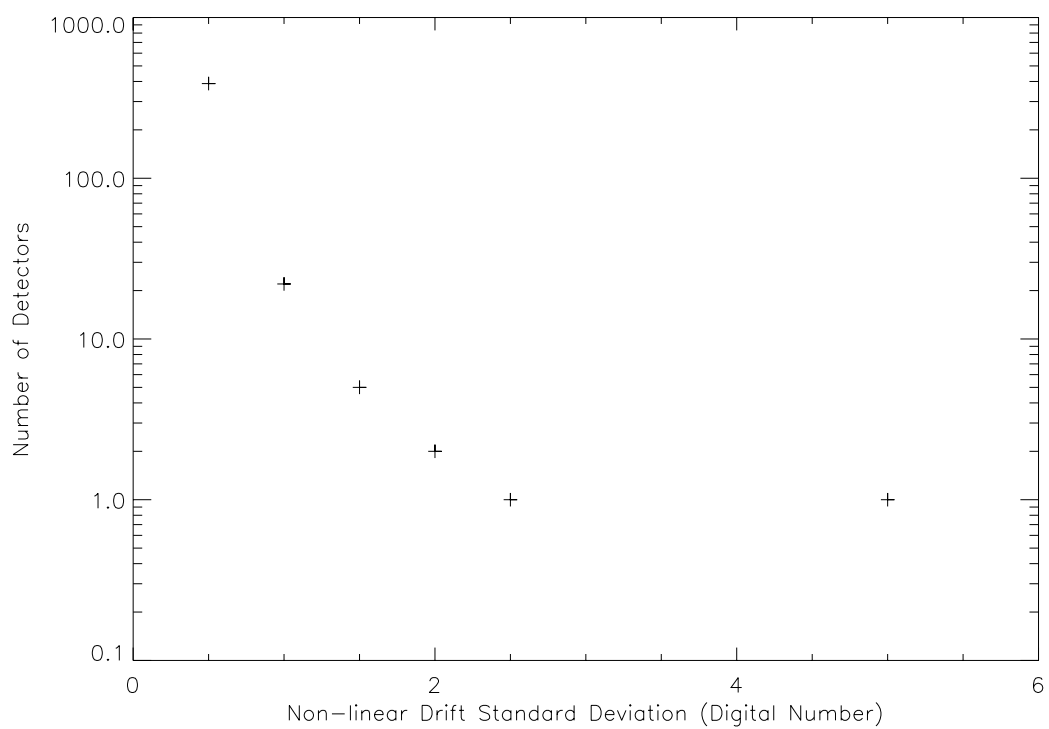
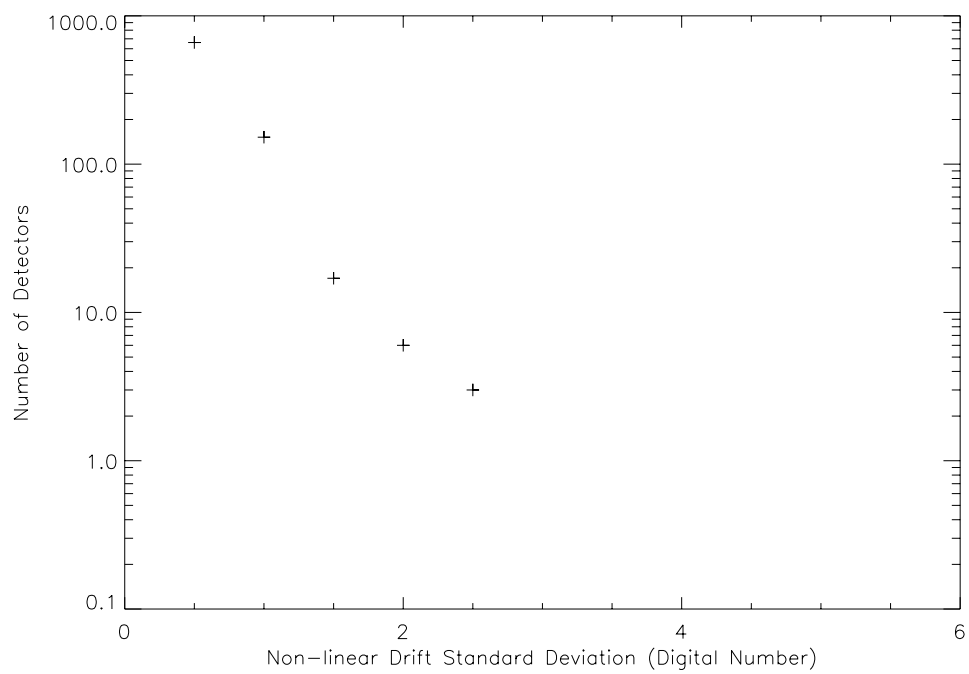*Figure 3-158. Dark current non-linear drift distribution for Band 5p.*

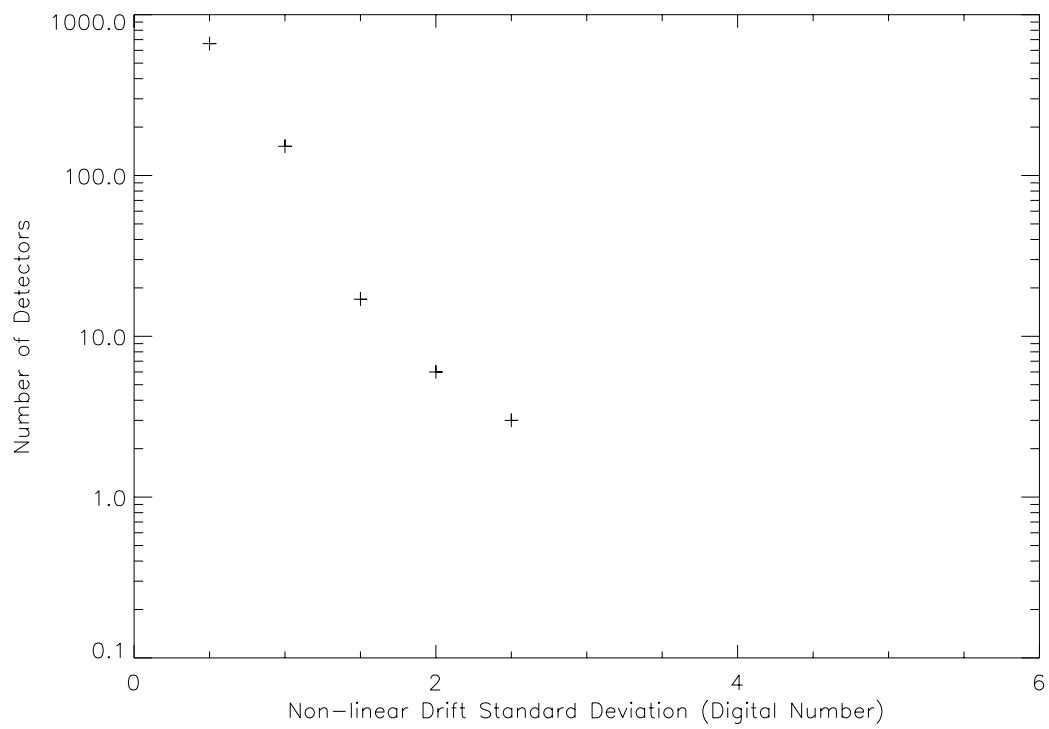*Figure 3-159. Dark current non-linear drift distribution for Band 5.*

Figure 3-160. Dark current non-linear drift distribution for Band 7.

Table 3-23
Detectors with non-linear drifting greater
than 1.5 digital numbers over a 40-minute period.

Band	Detector Number	Residual Drift (Digital Number)
5p	2	1.86
5p	82	1.77
5p	83	1.87
5p	92	2.28
5p	99	7.07
5	119	6.16
5	911	1.86
7	0	1.57
7	4	1.63
7	11	4.72
7	17	1.61
7	126	2.86
7	285	1.81
7	292	2.32
7	295	1.64
7	297	1.88
7	301	2.09
7	305	1.55
7	307	4.58
7	315	1.52
7	319	2.01
7	638	1.65
7	639	1.64
7	951	1.60

3.3.2.2.4   Discussion

The above analysis indicates all of the active VNIR and Panchromatic detectors of the EO-1 Advanced Land Imager focal plane are stable to within 1 digital number over a period of forty minutes. However, all of active SWIR detectors exhibit some drifting during this period. Fortunately, 99.4% of these detectors drift linearly and may be easily accommodated through a linear interpolation of dark current measurements obtained as the instrument exits eclipse near the North Pole and enters eclipse near the South Pole. An additional 0.3% exhibit less than 2.3 digital numbers of nonlinear drifting over the 40 minute period. The worst detector drifts by 7.1 digital numbers but has been previously identified as having excessive white and pseudo-random noise[6].

The effect of non-linear drifting will result in the inaccurate subtraction of dark current levels during observations. This will become most evident in regions of poor illumination or low reflectivity (e.g. water). This uncertainty will result in detector-to-detector striping which is dependent on the amount of signal produced by the scene and the amount of non-linear drifting by the detector.

3.3.3 Focal Plane Contamination

Contamination on orbit has been monitored using the internal reference lamps. Figures 3-161 to 3-164 provide a history of focal plane contamination since launch for the panchromatic band. Figures 3-161 and 3-162 depict the mean and standard deviation of the ratio of lamp data collected for each day relative to the December 1, 2000 data. As is clearly evident, significant contamination build-up was observed during the first 30 days on orbit. However, once the bakeout frequency was increased to once every six days, the amount of contamination was significantly restricted. Figures 3-163 and 3-164 depict the mean and standard deviations as above, but only for the fourth day after each bakeout. As can be seen, the rate of contamination build-up significantly decreased over the first 15 bakeout periods. Since then, the bakeout frequency has decreased to once every 10 days.

Contamination build-up on the focal plane will continue to be monitored for the duration of the EO-1 mission and the bakeout frequency will be adjusted to maintain radiometric effects below 1%.
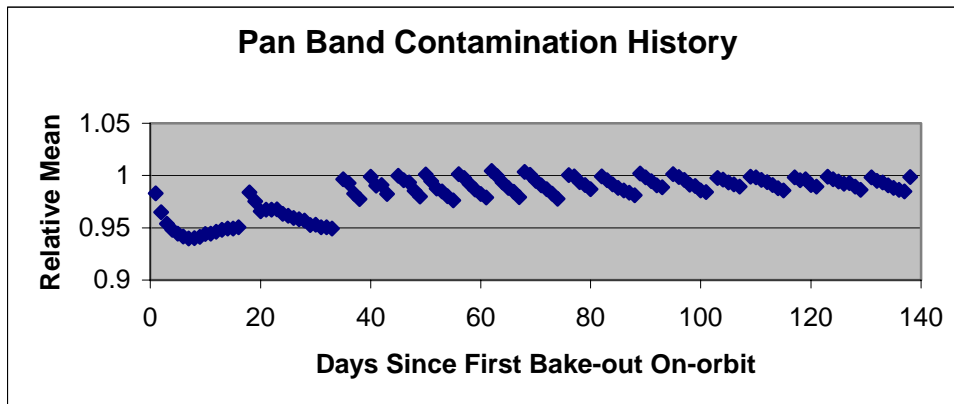

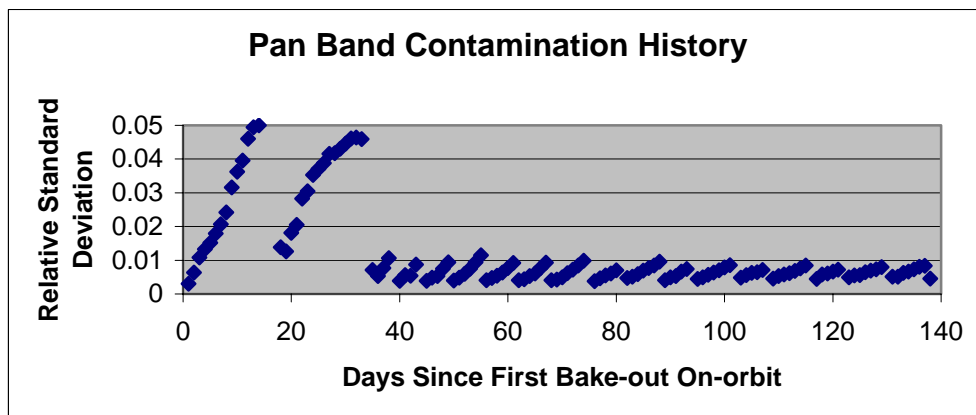*Figure 3-161. Pan Band on-orbit contamination history.*

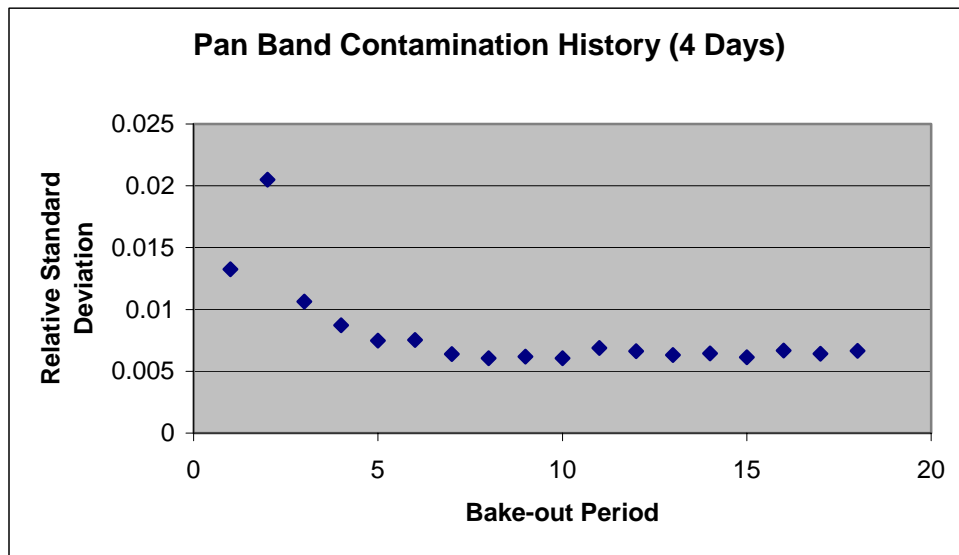*Figure 3-162. Pan Band on-orbit contamination history.*

Figure 3-163. Pan Band on-orbit contamination history.
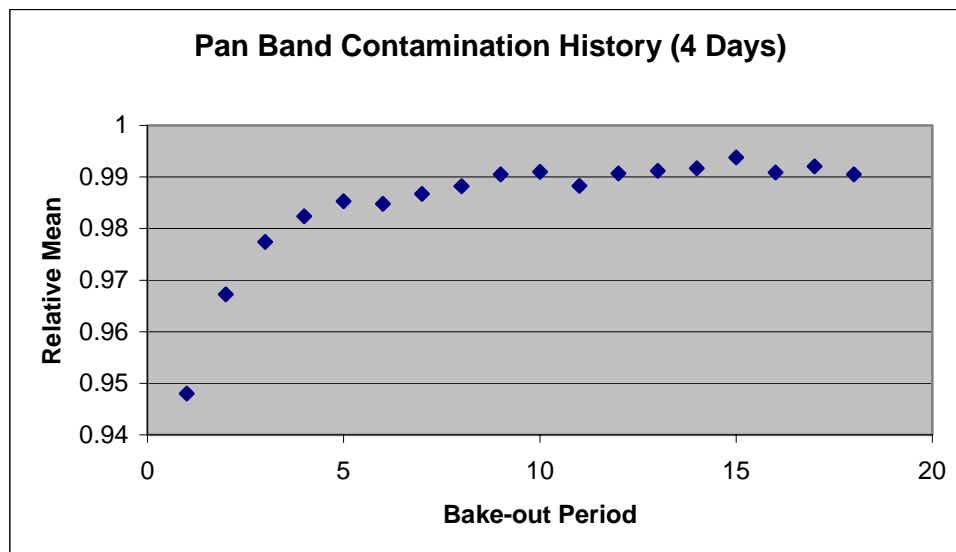
Figure 3-164. Pan Band on-orbit contamination history.

4. CONTACT INFORMATION

Below are the contacts' names, program roles and e-mail addresses.

- Dr. Jeff A. Mendenhall, ALI System Engineer, mendenhall@ll.mit.edu
- Dr Don E. Lencioni, ALI Instrument Scientist, lencioni@ll.mit.edu
- Dr David R. Hearn, ALI Instrument Analyst, drhearn@ll.mit.edu
- Dr Steve E. Forman, ALI Payload Manager, sforman@ll.mit.edu
- Ms Jenifer Evans, ALI Calibration Pipeline development, jenifer@ll.mit.edu
- Dr Costas J. Digenis, ALI Program Manager, digenis@ll.mit.edu

The mailing address for all of the above is:

Massachusetts Institute of Technology

Lincoln Laboratory

244 Wood Street

Lexington, MA 02420-9185.

5. SUMMARY

The Advanced Land Imager (ALI) was developed at Lincoln Laboratory under NASA's New Millennium Program (NMP). The instrument concept incorporates a number of innovations addressing the needs and science goals of NASA's Earth Science Enterprise. The program objective is to develop and flight test advanced technologies that will increase the performance and reduce the cost of future land imaging instruments. Lincoln Laboratory had a major role in the instrument design that was refined further during the Preliminary System Design study performed in collaboration with NASA's Goddard Space Flight Center (GSFC).

Following an instrument definition phase in mid-FY96, Lincoln Laboratory began development of the ALI. The instrument has multispectral imaging capabilities and contains a silicon carbide (SiC) optical system with wide field of view (1.25° by 15°), a partially populated focal plane system, an onboard calibration system, and the ancillary structural, thermal, and electrical components required to form an integrated unit. ALI was flown into space aboard the first Earth Observing satellite (EO-1) which was launched on November 21, 2000. Swales Aerospace developed the spacecraft and provided the essential support functions such as attitude control and onboard power.

The key attributes of ALI are that it is smaller in both size and weight than the Enhanced Thematic Mapper (ETM+) of Landsat 7, by a factor of four, and requires less power to operate, by a factor of five. It has a total of nine Multispectral (MS) bands plus a Panchromatic band, three more than ETM+, but does not have the thermal band. It has increased sensitivity by a factor varying from four to ten depending upon the band. The spatial resolution of the MS bands is the same as that of ETM+ (30 m) but it is better in the Pan band (10 m versus 15 m).

Lincoln Laboratory was assisted in the development of ALI by two subcontractors: Raytheon/Santa Barbara Remote Sensing (SBRS), who developed the focal plane assembly, and SSG, who developed the telescope. The instrument was assembled and aligned at Lincoln Laboratory and underwent electrical and environmental testing at the proto-flight level. It was then calibrated under thermal vacuum and delivered to NASA/GSFC in March 1999. Lincoln Laboratory supported the spacecraft integration and test activities providing on-site support, data acquisition, analysis, and evaluation. A Calibration Pipeline, based on the instrument ground calibration data, was provided to NASA/GSFC at the beginning of the flight test program.

The analysis of the data collected during the instrument ground calibration has been completed. The results have been documented in a series of reports listed in the references. Briefings to the sponsor and industry and conference presentations have been made and will continue throughout the year to implement technology transfer.

ALI has been functionally validated in space collecting up to ten scenes per day, as commanded. Lincoln Laboratory is using the flight data to conduct the instrument performance assessment and comparisons with other imagers (e.g., Landsat7). These comparisons have been very favorable for ALI, demonstrating the instrument's increased sensitivity and spatial resolution. An updated version of the Calibration Pipeline, reflecting the results of the on-orbit calibrations, has been delivered to NASA and is being used for flight data calibration. The

Calibration Pipeline includes routines for correcting various image artifacts. The science data is used to generate calibrated, spatially reconstructed earth scenes for dissemination to other investigators.

The telemetry data is being used for instrument parameter trending and overall health assessment. So far, the instrument has shown excellent stability. Since ground testing of the assembled instrument in thermal vacuum, it was observed that some contaminant gradually accumulates on the cold focal plane. To deal with the problem, heaters have been provided to warm up the focal plane and boil off the contaminant. This operation is carried out every ten days and lasts for about twenty hours. While the focal plane is warm, SWIR data cannot be taken due to the increased noise, however the VNIR data are good. Spacecraft issues that can be addressed through ALI include assessment of jitter and absolute pointing accuracy by earth scene measurements and yaw correction methodology. These investigations are in progress.

Work has already begun at NASA to define the Landsat Data Continuity Mission (LDCM) which is expected to be based on the ALI technologies. Lincoln is participating in this effort, by assisting NASA in the development of the procurement specifications, and by being available to serve as a technical consultant to the eventual developer.

6. REFERENCES

1. "Landsat 7 System Specification," Revision K, NASA Goddard Space Flight Center, 430-L-0002-K, July 1997.

2. D. E. Lencioni and D. R. Hearn, "New Millennium EO-1 Advanced Land Imager," *International Symposium on Spectral Sensing Research*, San Diego, Dec. 13-19, 1997.

3. C. J. Digenis, D. E. Lencioni, and W. E. Bicknell, "New Millennium EO-1 Advanced Land Imager," *SPIE Conference on Earth Observing Systems III*, San Diego, California, July 1998.

4. J. A. Mendenhall, D. E. Lencioni, D. R. Hearn, and A. C. Parker, "EO-1 Advanced Land Imager preflight calibration," Proc. SPIE, Vol. 3439, pp. 390-399, July 1998.

5. J. A. Mendenhall, D. E. Lencioni, D. R. Hearn, and A. C. Parker, "EO-1 Advanced Land Imager in-flight calibration," Proc. SPIE, Vol. 3439, pp. 416-422, July 1998.

6. W. E. Bicknell, C. J. Digenis, S. E. Forman, and D. E. Lencioni, "EO-1 Advanced Land Imager," *SPIE Conference on Earth Observing Systems IV*, Denver, Colorado, 18 July 1999.

7. D. E. Lencioni, D. R. Hearn, J. A. Mendenhall, and W. E. Bicknell, "EO-1 Advanced Land Imager calibration and performance," *SPIE Conference on Earth Observing Systems IV*, Denver, Colorado, 18 July 1999.

8. D. R. Hearn, J. A. Mendenhall, and B. C. Willard, "Spatial calibration of the EO-1 Advanced Land Imager," *SPIE Conference on Earth Observing Systems IV*, Denver, Colorado, 18 July 1999.

9. J. A. Mendenhall and A. C. Parker, "Spectral calibration of the EO-1 Advanced Land Imager," *SPIE Conference on Earth Observing Systems IV*, Denver, Colorado, 18 July 1999.

10. J. A. Mendenhall, D. E. Lencioni, and A. C. Parker, "Radiometric calibration of the EO-1 Advanced Land Imager," *SPIE Conference on Earth Observing Systems IV*, Denver, Colorado, 18 July 1999.

11. J. Evans and H. Viggh, "Radiometric Calibration Pipeline for the EO-1 Advanced Land Imager," *SPIE Conference on Earth Observing Systems IV*, Denver, Colorado, 18 July 1999.

12. B. C. Willard, "Wide field-of-view Schmidt-sphere imaging collimator," *SPIE Conference on Earth Observing Systems IV*, Denver, Colorado, 18 July 1999.

13. H. Viggh, J. Mendenhall, R. Sayer, J. S. Stuart, and M. Gibbs, "An Automated Ground Data Acquisition and Processing System for Calibration and Performance Assessment of the EO-1 Advanced Land Imager," *SPIE Conference on Earth Observing Systems IV*, Denver, Colorado, 18 July 1999.

14. H. Viggh, J. S. Stuart, R. Sayer, J. Evans, and M. Gibbs, "Performance Assessment Software for the EO-1 Advanced Land Imager," *SPIE Conference on Earth Observing Systems IV*, Denver, Colorado, 18 July 1999.

15. D. E. Lencioni, C. J. Digenis, W. E. Bicknell, D. R. Hearn, and J. A. Mendenhall, "Design and Performance of the EO-1 Advanced Land Imager," *SPIE Conference on Sensors, Systems, and Next Generation Satellites III*, Florence, Italy, 20 September 1999.

16. D. R. Hearn, "EO-1 Advanced Land Imager Modulation Transfer Functions," *MIT Lincoln Laboratory Technical Report 1061*, 22 March 2000.

17. J. A. Mendenhall et al., "Earth Observing-1 Advanced Land Imager: Instrument and Flight Operations Overview," MIT/LL Project Report EO-1-1, 23 June 2000.

18. J. A. Mendenhall, D. P. Ryan-Howard., "Earth Observing-1 Advanced Land Imager: Spectral Response Calibration," MIT/LL Project Report EO-1-2, 20 September 2000.

19. J. A. Mendenhall, D. E. Lencioni, J. B. Evans, "Earth Observing-1 Advanced Land Imager: Radiometric Response Calibration," MIT/LL Project Report EO-1-3, 29 November 2000.

20. D. R. Hearn, "Earth Observing-1 Advanced Land Imager: Detector Line-of-Sight Calibration," MIT/LL Project Report EO-1-4, 29 December 2000.

21. J. A. Mendenhall, "Earth Observing-1 Advanced Land Imager: Dark Current and Noise Characterization and Anomalous Detectors," MIT/LL Project Report EO-1-5, 7 May 2001.

22. J. A. Mendenhall, M. D. Gibbs, "Earth Observing-1 Advanced Land Imager Flight Performance Assessment: Noise and Dark Current Trending for the First 60 Days," MIT/LL Project Report EO-1-7, 1 June 2001.

23. J. A. Mendenhall, "Earth Observing-1 Advanced Land Imager Flight Performance Assessment: Investigating Dark Current Stability Over One-half Orbit Period During the First 60 Days," MIT/LL Project Report EO-1-6, 1 July 2001.

24. D. R. Hearn et al., "EO-1 Advanced Land Imager Overview and Spatial Performance Assessment", IGARSS 2001, Sydney, 9 July 2001.

25. J. A. Mendenhall et al., "Initial Flight Test Results from the EO-1 Advanced Land Imager: Radiometric Performance", IGARSS 2001, Sydney, 9 July 2001.

26. D. E. Lencioni, J. A. Mendenhall, D. P. Ryan-Howard, "Solar Calibration of the EO-1 Advanced Land Imager", IGARSS 2001, Sydney, 9 July 2001.

27. Bigger, S. F., Private Communication, May 2001.